Université catholique de Louvain
Faculté des Sciences Appliquées
LABORATOIRE DE TÉLÉCOMMUNICATIONS
ET
TÉLÉDÉTECTION

B - 1348 Louvain-la-Neuve Belgique

Multiuser communications over frequency selective wired channels and applications to the powerline access network

Thierry Sartenaer

Thesis presented for the Ph. D. degree in
Applied Sciences

Jury:

Luc Vandendorpe (UCL) - Supervisor
Paul Delogne (UCL)
Jérôme Louveaux (Technische Universiteit Delft)
Marc Moeneclaey (Universiteit Gent)
Gregori Vázquez Grau (Universitat Politècnica de Catalunya)
Jean-Didier Legat (UCL) - Chairman

September 2004

Remerciements

L'on raconte que la section 'remerciements' est de loin la section la plus lue et la plus commentée des thèses de doctorat. Je profite donc de l'auditoire inespéré qui m'est offert ici pour encourager le lecteur de passage à persévérer dans sa lecture. Qu'il sache que les huit chapitres qui vont suivre ont demandé six années de dur labeur, alors que cette modeste page n'a nécessité que quelques minutes de rédaction!

Ma première pensée est destinée à la mémoire de mon père. Durant toute sa vie, il a transmis à ses enfants le goût des études, la soif de connaissances, la curiosité intellectuelle. Autant de moteurs indispensables à la finalisation d'une thèse de doctorat.

Un merci tout particulier est adressé à mon promoteur, Luc Vandendorpe, qui m'a enseigné (avec patience) le métier de chercheur et m'a éclairé de ses nombreux conseils. Sa compétence et son enthousiasme à toute épreuve furent salutaires.

Merci à Paul Delogne pour son aide énorme et la grande qualité de ses conseils.

Je tiens aussi à remercier les membres de mon jury pour leurs critiques constructives et leur contribution à l'amélioration de ce texte.

Je n'oublierai jamais la formidable ambiance qui règne au sein du laboratoire TELE. Plusieurs de ses membres sont devenus aujourd'hui de grands amis. En particulier, David Lemaire, Jérôme Louveaux et Antoine Dejonghe furent des compagnons de bureau exceptionnels. Quant à François Horlin, mes zygomatiques ne sont pas près d'oublier son passage en TELE!

Merci à Murielle pour son infinie patience et son soutien de tous les instants. Enfin, merci à Louis, Noël et Henri d'avoir été si sages pendant que leur papa rédigeait son 'gros livre'!

Abstract

The low-voltage power distribution network is considered today as a serious candidate to provide residential customers with a high-speed access to communication services such as Internet. Outdoor Power-Line Communications (PLC) systems represent an alternative to the other classical 'last-mile solutions' such as ADSL, cable modems, or wireless access systems. The outdoor powerline channel is made of the interconnexion of various buried or aerial multiconductor cables, providing connectivity between the central PLC modem (installed at the medium-voltage/low-voltage transformer) and a number of remote PLC modems (installed at customer premises).

We developed an accurate powerline channel simulation tool based on the Multiconductor Transmission Line theory. This tool is able to predict the end-to-end channel responses on the basis of the multiconductor cable structure and the network topology. The obtained channel responses are strongly frequency-selective due to the cable losses and to the various reflections at cable derivations and unmatched terminations.

Then the issue of optimal resource allocation in a multiuser environment was addressed in the light of the Multiuser Information Theory. Simultaneously active users are in competition for the limited resources that are the power (constrained by electro-magnetic compatibility restrictions) and the bandwidth (in the range of 1 to 10 MHz for outdoor PLC). The concept of multiuser balanced capacity was introduced to characterize the optimal resource allocation providing the maximum data rates with fairness constraints among the subscribers.

The optimal PLC system was shown to require the shaping of the signal spectrum in the transmitters, and successive decoding in the receiver. A generic multiple access scheme based on Filter Banks (FB) was proposed, which offers the required spectral shaping with limited degrees of freedom. Classical multiple-access techniques (TDMA, CDMA, OFDMA) can be obtained by selecting the appropriate FB. The Minimum-Mean-Square-Error Decision-Feedback Joint Detector was shown to approach the performance of the optimal successive decoding receiver. Practical implementations were discussed and compared, with a special concern about complexity issues.

Finally, the robustness of the proposed system against channel estimation and timing synchronization errors was addressed. The problem of multiuser

timing synchronization was introduced, and practical multiuser timing error detectors were proposed.

Contents

List of Figures

List of Tables

Chapter 1

Introduction

1.1 Powerline communications

Digital communications over powerlines is an old idea that dates back to the early 1920s. For some decades, the omnipresent power grid has been used for low-speed data communications [1]. Many different standardized or proprietary systems have been used for the transmission of control and management signals (e.g. remote meter reading) by power supply companies. However, the powerline has largely been dismissed as being too noisy and unpredictable to be useful as a practical high-speed communication channel.

A significant change occurred when the last telecommunication monopolies were ended by 1998. In the same time, major advances in the fields of modulation, coding and detection enabled the design of efficient broadband communication systems over powerlines. The idea of exploiting the low-voltage (LV) power grid to provide broadband Internet access to residential customers has been proposed as an alternative to the other classical 'last-mile solutions' such as ADSL, cable modems, or wireless access systems. LV powerline communication (PLC) networks have a tree-like topology, with a PLC modem installed at the medium-voltage/low-voltage (MV/LV) transformer and providing connectivity to all premises in the neighbourhood. The architecture of the LV PLC network has to be optimized for the special characteristics of the distribution grid, which changes from one geographic area to another, considering the number of households per transformer and the distance from the transformer to the customer premises. When larger distances are involved, as it is the case in European topologies, intermediate repeaters are typically needed to regenerate the signal from the head-end and provide adequate coverage in every customer outlet.

There is also growing interest in the prospects of reusing in-building powerline cables to provide a broadband LAN within the home or office. The major advantage offered by powerline-based home networks is the availability of an existing infrastructure of wires and wall outlets, so new cable installation is not required. The user can employ home networking devices for connecting several computers, sharing printers, or sharing a broadband Internet connexion.

Another important field of research is the use of the MV network for communication purposes. It can be used as a backbone to connect the low-voltage transformer stations to the Internet if conventional backbone networks, like fiber optic cables, are missing. MV lines have their own characteristics for communication: they are typically less noisy, and have fewer branches and taps than LV lines, so the environment is less hostile for communications and longer distances can be achieved. The problem with MV lines is that special couplers are needed for injecting the signal in the line to ensure that the mains voltage does not damage the equipment.

1.1.1 The power distribution grid

The hierarchical structure of the power distribution grid is basically the same in every country :

- High voltage (HV, above 36 kV) powerlines, emanating from power plants, form a wide-meshed long-distance nationwide transportation network.

- Medium voltage (MV, ranging from 1 kV to 36 kV) powerlines, constituting a finer meshed network, bring electrical power into cities, towns, and villages.

- Low voltage (LV, below 1 kV) powerlines ensure the final distribution to customer premises. The LV grid represents a very fine-meshed network, precisely adapted to the density of consumer loads.

From an MV/LV transformer, power is distributed over buried or aerial multiconductor cables to the customer premises, where they end on a panel board, from which the indoor wiring to various appliances and wall sockets starts.

In the European power supply network, a given MV/LV transformer can provide power to several hundred households. Typically, between 3 and 10 service cables emerge from one transformer substation, forming a tree-like structure. Three phases are provided, with a voltage of 400 V from phase to phase and 230 V from phase to neutral. The neutral conductor is usually grounded. In most European countries, all three phases and the neutral are brought to the customer's panel board: thus, the service cables generally include 4 conductors. In some countries, however, only one phase and the neutral are supplied to the buildings.

The U.S. power supply network has a different structure. The MV distribution circuit consists of a three phase main trunk. Depending on the load, a two-phase or one-phase tap extends into load areas. In direct neighbourhood to buildings, single-phase transformers provide the LV, which is immediately passed to the buildings' panel board. As a consequence, the length of the LV segment is usually less than 300 m, with 1 to about 10 customers per transformer. The secondary side of the transformer provides 240 V with a grounded center tap, and the customer receives power over three wires with 2 x 120 V or 240 V. Standard loads are connected to the 120 feeds while large loads use the 240 V level.

1.1.2 The powerline channel

Adequate channel models (including various classes of channel frequency responses and a complete noise scenario) are required to assess the performance of a PLC system. Unfortunately, these models have not been standardized yet, so there is no widely accepted model similar to COST models for mobile radio channels or ANSI/ETSI models for DSL channels.

The PLC channel presents a number of technical challenges. Frequency-dependent attenuation is caused by conductor and dielectric losses. Signals do not propagate along a single path, but suffer from reflections caused by impedance mismatches at line discontinuities. Hence, the PLC channel can be considered as a multipath environment with frequency-selective attenuation. Roughly speaking the channel transfer function has a low-pass characteristic, with deep notches at some frequencies. The degree of branching is responsible for increasing attenuation as each tap absorbs a certain amount of the transmitted power. Multipath reflections result in dispersion of the time domain signal. This can be characterized by the delay spread, which is the total time interval during which signal reflections with significant energy arrive at destination from the origin. Time dispersion generates intersymbol interference, which has to be handled by adequate equalization structures in the receiver.

Furthermore, the channel frequency responses are slowly time varying, although at certain moments they can change abruptly due to changes in the load distribution on the line, typically when electric appliances are connected and disconnected. As a consequence, the channel response should be continuously monitored by the transmitter/receiver, and transmission and/or detection parameters should be adapted to the channel change.

The most widely used model for the channel transfer function $H(f)$ is the multipath model proposed by Philipps [2] and Zimmermann [3] :

$$H(f) = \sum_{i=1}^{N} g_i \; e^{-(a_0 + a_1 f^k)\, d_i} \; e^{-2\pi j f \tau_i}$$

where d_i and τ_i are the length and delay of the N relevant propagation paths, g_i is the weighting factor for path i, and $\{a_0, a_1, k\}$ are model parameters to be adjusted. The exponent k has typical values ranging from 0.5 to 1, while the number of paths N is generally in the range of 5-50. This model was validated in the frequency range of 500 kHz to 30 MHz. It is valid for both outdoor and indoor PLC channels. The indoor lines are shorter, but they suffer from strong branching : the number of relevant paths is then usually higher while the attenuation associated with each path is smaller. Actually, the proposed model is the result of a top-down approach : the various parameters need to be determined through measurements. As such, it is not suitable for the computation a priori of the actual transfer function of a given link. Alternative models, based on the multiconductor transmission line theory (MTL), have been proposed in the case of indoor [4] and outdoor [5] channels. With these bottom-up models, it is possible to compute a priori and deterministically the transfer function of any PLC link, on the basis of the network topology and the cable characteristics.

In contrast to most other "well designed" communication channels, powerlines do not represent additive white Gaussian noise (AWGN) channels. The interference scenario is rather complex. The noise sources can be divided into 3 classes :

- *Colored background noise* is caused by common household appliances. It has a fairly low power spectral density which, however , significantly increases towards lower frequencies. The average PSD varies in the range between -140 and -125 dBm/Hz and remains stationary over periods from minutes to hours. The resulting PSD is actually the sum of numerous low-power noise sources.

- *Narrowband noise* is made of continuous wave signals with amplitude modulation, mainly produced by ingress of broadcast stations operating in the medium and shortwave bands. The mean interference level varies with the time of the day.

- *Impulsive noise* can be subdivided into three classes. Firstly, periodic impulsive noise synchronous to the mains frequency are caused by some domestic appliances such as light dimmers. They have a repetition rate of 50 or 100 Hz (60 or 120 Hz in the U.S.) and are of short duration (10-100 μs). Secondly, periodic impulsive noise asynchronous to the mains frequency is caused by switching power supplies. The spectrum repetition rate is generally in the range from 50 to 200 kHz. Finally, aperiodic and asynchronous impulsive noise is caused by transients due to switching within the network. The impulse duration ranges from several microseconds to a few milliseconds with a power spectral density than can exceed by 50 dB the level of the background noise at some frequencies. This kind of noise may occur at irregular intervals and contains considerable energy. It considerably affects high-speed communication, in such a way that complete symbols or even bursts of symbols cannot be decoded by the receiver. This has to be taken into account in the design of a complete and effective PLC system. Asynchronous impulsive noise is characterized by three random variables : amplitude, impulse width, and interarrival time. The statistical distribution of these parameters has been established through measurement campaigns. This allowed the derivation of a mathematical model [6] for the synthesis of asynchronous impulsive noise in realistic powerline channel emulation systems. Fortunately, even in heavily disturbed environments, it was found that the occurrence of the asynchronous impulsive noise concerned less than 1 percent of the time.

1.1.3 Electromagnetic compatibility, standards and regulations

Electromagnetic compatibility with respect to existing wireless services (fixed radio services, broadcasting, amateur radio, nautical radio, mobile radio, etc.) is a major issue in the elaboration of a universal PLC standard. The problem is that power cables and networks have been designed for the purpose of efficient power distribution at frequencies of 50 or 60 Hz, and certainly not for for the transmission of communication signals at frequencies of up to 20 or 30 MHz.

The high-frequency PLC signals are injected in differential mode. Differential mode currents are equal in magnitude and flow in opposite directions on the conductors. Balanced lines are necessary to achieve signal propagation in the desired differential mode. A lack of network or cable symmetry (defined in terms of impedance between conductors and ground) leads to unwanted common mode conversion. Common mode currents flow in parallel on all conductors, while the return current flows into the ground. These common mode currents are responsible for electromagnetic radiation. Actually, the powerlines operate as more-or-less efficient antennas.

Two classes of solutions can be investigated to minimize signal radiation from PLC networks. Firstly, the symmetry of the lines used for HF signal transmission should be exploited as far as possible, or even improved by network conditioning. In the access segment (assuming the distribution of three phases to the customers), a better symmetry is generally obtained by injecting the signals between two phases rather than between a phase and neutral. This solution is not applicable to indoor networks (two wires plus ground protective) where the signal injection is necessarily between phase and neutral. HF filters have also been proposed to keep HF signals on the useful propagation paths and prevent them from entering unused portions of the power network. Secondly, the power spectral density (PSD) of transmitted PLC signals should be reduced. For a given total power, this means that the signal spectrum should be spread as much as possible in the available bandwidth. As the channel transfer function decreases rapidly with frequency, spectrum spreading lowers the transmission efficiency. Actually, the mandatory restriction of the transmitted signal PSD represents a fundamental limitation to the performance of practical PLC systems. Unintentional radiation may occur from several sources in parallel. For this reason, the specification of a radiation limit should not be restricted to a single PLC device.

As PLC systems can be considered as unintentional radiators, licensing (i.e. frequency assignment through an authority) is not required, but PLC signal emissions must be compliant with current EMC limits. On the international level, a PLC standard (IEC 61000-3-8) [7] exists for frequencies below 525 kHz. At higher frequencies, the CISPR 22 publication [8] specifies limits for information technology equipments, and distinguishes between power supply ports and telecommunication ports. The disturbance potential of the device under test is measured through an artificial network emulating real-world network conditions. An adaptation of this standard to the special case of PLCs is underway. On the European level, a frequency range from 3 to 148.5 kHz, the so-called 'CENELEC-band' [9], is available for low speed PLC (up to 100 kbits/s) according to standard EN50065. For higher frequencies, a CENELEC/ETSI joint working group has been set up [10] to develop EMC requirements for wired transmission networks, including PLCs. This standard covers emission limits and measurement methods for all types of communications networks to ensure that the various technologies are treated equally. Various limits of electrical field levels at a distance of 3 meter of the network are currently proposed by different European countries at frequencies of up to 30 MHz. In the U.S., the use of PLC is regulated by the FCC Part 15 [11], which distinguishes between frequencies below and above 490 kHz. Compared to the proposed European limits, the American standard is highly generous for high-speed PLC. In Japan, a national standard regulates the frequency range 10-450 kHz, while PLC is currently not allowed at higher frequencies.

The disturbance potential of the PLC system is measured through the impact of PLC signals on a standard AM broadcast receiver. For that purpose, the emitted electromagnetic field is measured within a bandwidth of 9 kHz, which represents the usual AM radio receiver bandwidth, by means of a standardized magnetic loop antenna placed at a specific distance of the PLC network. The whole frequency range (from some kHz up to 30 MHz) has to be investigated. In order to determine how PLC signals symmetrically fed into the power supply network are converted into unwanted radiation, the concept of decoupling factor $K(f,d)$ was proposed. It can be regarded as a transfer function between the communication signals on the lines as input and the inadvertently radiated field as output, summarizing the impact of all parameters that influence this transfer function. Typical values of $K(f,d) = 10^{-3}/m$ have been reported for a distance of $d = 3$ meter. According to [12], the maximum PSD of transmitted PLC signals can reasonably be assumed to be in the range of -65 to -40 dBm/Hz.

Another important issue is the EM compatibility of different PLC systems. The coexistence of both the PLC access systems and different indoor systems requires a clear frequency separation. The current proposition is to dedicate the frequency range below 10 MHz to the access domain, and to assign frequencies above 10 MHz with no upper limit to indoor use. The fundamental reason of this proposal is that frequencies above 10 MHz are not usable in the access domain due to the lowpass characteristic of the channel responses. As indoor channels are much shorter, there is sufficient bandwidth above 10 MHz for most of the high-speed applications.

The frequency bands available for outdoor PLC transmission are not yet standardized. Most probably they will be in the range of 500 kHz to 10 MHz. The lower frequencies are dedicated to existing low-speed services (such as applications working in the CENELEC-band) while the higher frequencies will be allocated to indoor PLC systems. A possible solution is the 'chimney approach', which consists of allocating several narrow and not-contiguous bands to PLC systems at frequencies that are not used intensively by wireless services. Another solution is to use the whole frequency range for PLC, but with a lower PSD. Within international bodies such as the PLCforum (www.plcforum.org), which is a leading international association that represents the interests of manufacturers, energy utilities, and research organizations active in the field of PLC, frequency band standards have been proposed [12]: band A (0.5-20 MHz), band B (0.5-10 MHz) and band C (equivalent to B but excluding major broadcast and amateur radio frequencies).

1.1.4 Coding and modulation

The selection of an adequate modulation scheme for PLC must account for four major factors :

- The frequency-selective (and slowly time-varying) nature of the channel
- The interference scenario including narrowband interference and strong impulsive noise
- The multiuser aspect of the system, with many customers that request an access to the same physical medium simultaneously
- Regulatory constraints with regard to EMC, that limit the transmitted PSD

Three classes of modulation techniques are usually cited in the context of broadband PLC :

- *Single-carrier modulation* is an attractive proposition from the complexity point of view. If PLC transmission is only allowed in a small number of non-contiguous frequency bands, single-carrier modulation can be used separately in each band. Powerful detection and equalization techniques are needed to combat intersymbol interference. The deep frequency notches present in the channel transfer function prevent the use of linear equalizers. On the other hand, optimal symbol (MAP) or sequence (Viterbi) detectors exhibit a computational complexity that increases exponentially with the length of the impulse response, which is considerable in the powerline channel. Reduced-complexity versions of these detectors can be investigated. Another solution is the MMSE decision-feedback equalizer. Measures should be taken to avoid catastrophic error propagation caused by impulsive noise, and to allow the tracking of channel parameters.

- *Spread-spectrum* techniques, in particular DS-CDMA, make use of a code sequence that spreads narrowband signals over a wider bandwidth. Spread-spectrum techniques are naturally robust to narrowband interference. Moreover, CDMA is well-suited to multiuser systems including several users possibly with different rate demands. Like for single-carrier techniques, a robust channel equalization is required.

- *Multicarrier modulation*, in particular OFDM, is particularly well-suited for PLC. The information symbols are transmitted in parallel on many orthogonal subcarriers occupying a narrow subband. Using a cyclic-prefix extension technique, the effect of the channel on each subcarrier is transformed into a simple complex gain which depends on the channel transfer function evaluated at the subcarrier frequency. Hence, a frequency-selective channel becomes equivalent to a set of multiple flat-fading subchannels, and equalization of the data simply amounts to a normalization by a complex scalar. Using multilevel modulations, the bit rates on each subcarrier can be matched to the specific channel conditions, by the so-called bit loading technique. This aspect is important in the PLC context as the channel transfer function presents deep notches and also because of the narrowband noise. Moreover, the PSD of the transmitted signal can be shaped by selecting an appropriate subset of carriers, which is important in order to comply with the EMC requirements. The main drawback of the OFDM system is the need for the cyclic prefix whose duration depends on the channel memory, which is quite long in PLC channels. Time domain equalizers (TEQ) are commonly used in single-user OFDM systems to shorten the length of the equivalent channel impulse response. A multiple access method based on OFDM, the so-called 'OFDMA', can be investigated, but it is not compatible with the TEQ technique.

The multiuser aspect is generally handled by the medium access control (MAC) layer. The channel is made available for a given customer in specific portions of the time. A better performance can be expected from advanced multiple access techniques like CDMA or OFDMA, by which several customers are allowed to use their channel simultaneously.

A choice should be made of either a robust solution providing a sufficient quality for a wide range of variations of the channel parameters, or an adaptive one. Obviously, since the characteristics of the powerline channel change over time (sometimes abruptly), a better performance can be expected when the transmission parameters can be adapted to the channel conditions. Furthermore, the nominal channel transfer function is also strongly dependent on the specific network topology and the position of the customer modem, which definitely requires an adaptive system able to provide a customized solution for a wide range of PLC configurations.

Finally, powerful coding techniques are required to ensure reliable communications in the extremely noisy PLC medium. A large range of coding and decoding techniques have been considered in a PLC context, a review can be found in [13].

1.1.5 The HomePlug standard

In 2001, an industrial standards organization called the HomePlug Powerline Alliance (www.homeplug.org), originally founded by 13 major companies, announced the completion of the HomePlug 1.0 specification [14] for a 14 Mbits/s in-home powerline networking technology based on OFDM. HomePlug compliant products are today available on a large scale in the consumer market. They appear as a competitive alternative to Ethernet and Wi-Fi (IEEE 802.11x) solutions. The HomePlug Powerline Alliance is now establishing a 100 Mbits/s class in-home powerline networking standard, called HomePlug AV, to provide distribution of data, video and audio signals throughout the home.

The HomePlug 1.0 standard specifies the physical (PHY) and medium access control (MAC) layers of the protocol stack. To overcome the hostile PLC environment, adaptive OFDM with a cyclic prefix (CP) extension and bit loading has been adopted. The frequency band is approximately 4.3 to 20.9 MHz, that is a bandwidth of roughly 17 MHz. Actually the band from 0 to 25 MHz is divided into 128 evenly spaced carriers, of which 84 fall within the band used. Some subcarriers are left unused in the amateur radio bands. The tone map can be adapted to support regulatory requirements of different countries. Compliance with radiated power requirements has resulted in -50 dBm/Hz of transmission PSD in the USA (FCC Part 15), and -80 dBm/Hz in the amateur radio bands. One OFDM symbol comprises 256 IFFT samples plus 172 samples for the cyclic prefix, and the sample rate is 50 MHz. Channel estimation is used by the transmitter to detect channel conditions and adapt the transmission parameters by avoiding poor subcarriers and by selecting an appropriate modulation method and coding rate for the remaining subcarriers. Active modems perform channel estimation at least once every 5 seconds. Three variants of phase shift keying (PSK) modulation are used: coherent binary PSK, differential BPSK, and differential quadrature PSK. Both turbo product codes and Reed-Solomon concatenated with convolutional codes are used for forward error correction (FEC), in conjunction with interleaving and automatic repeat request (ARQ) techniques. The bit rate can vary from 1 Mbit/s to 14 Mbits/s practically continuously according to the number of usable carriers, modulation methods, and coding rate. Burst transmission is used, i.e. short frames of 20 to 160 OFDM symbols are transmitted by the different modems. A preamble and frame control combination are used as delimiters that start and end the frames, for the purpose of synchronization and control. Only the payload portion of the frames is adapted to channel conditions. The MAC protocol is a modified multiple access with collision avoidance (CSMA/CA) protocol with priority signaling. The modems communicate with each other freely, without any centralized coordination. Encryption techniques are used to ensure the confidentiality of the transmission.

1.1.6 PLC systems in the access segment

The feasibility of powerline broadband transmission in the access segment has been demonstrated through many independent field trials. Proprietary technologies have been deployed up to now, with a vast range of modulations and system architectures. Moreover, the structure of the powerline network itself has a strong impact on the design of appropriate PLC systems. The proposed LV access systems are sometimes extended to the MV segment, or even into the indoor home network. Reports of specific PLC trials can be found in [15] (Europe) an [16] (United States), for example.

One of the leaders in the field of broadband access PLC systems is DS2 (Design of Systems on Silicon, www.ds2.es). Their products can currently achieve speeds up to 45 Mbits/s, and a next generation of 200 Mbits/s PLC chipsets is announced. A high-speed modem (Head End), containing the DS2 chipset, is installed in the MV/LV transformer. Each transformer contains either an Internet router or an ATM concentrator, enabling the link with a large broadband network. A telephone operator (PTT) supplies the broadband network. Each customer site requires a powerline modem (Customer Premises Equipment or CPE), again containing the DS2 chipset. The use of a gateway between the powerline modem and a LAN at the customer premises enables several users to connect and share the high-speed connection. The selected modulation is again adaptive OFDM with cyclic prefix extension. Multilevel quadrature amplitude modulation (QAM) is used on the more than 1000 subcarriers. The system continuously monitors the channel attenuation and noise level with a very high spectral resolution. Information from these measurements is used to adapt the modulation parameters per carrier in real time in order to keep the bit error rate to the desired level. If the signal quality falls beyond acceptable levels in a part of the spectrum, the affected carriers are not used to send information. The frequencies used by the system can be configured from 2 to 34 MHz, and are adapted according to channel conditions and to the evolving standards and regulations in place in different countries. The transmitted PSD can be shaped with deep notches of more than 30 dB at any frequency and with any bandwidth. Fast channel estimation and a robust timing and frequency synchronization scheme are implemented. Several interrelated and configurable FEC algorithms (including soft-decision decoding and Reed-Solomon decoding) are used to match the quality-of-service requirements.

1.2 Outline of the thesis and contributions

In this work, a simplified communication scenario is considered, that represents some of the key aspects of the global PLC scenario, but not all of them :

- **Multiuser** communications are considered. This implies that many users (up to 20 users in this work) wish to establish a communication with the head-end simultaneously. This aspect raises a number of questions regarding the optimal way of sharing the resources (power, time, frequency) among the active users, the impairment caused by the other-user signals to the quality of a given-user link, and the need for a fairness control mechanism in a scenario where the quality of the different user channels can be very heterogeneous. The head-end is located at the MV-LV transformer while the different user modems are physically distributed along the powerline. The uplink (communication from the user modems toward the common head-end) and the downlink (communication from the common head-end towards the user modems) are considered separately. A simple time-division duplex scheme is assumed. The network structure is illustrated in Figure 1.1.

- The channel transfer functions are **frequency-selective**. The frequency-selectivity is caused by cable losses, and mainly by the multipath effect in a strongly branched network. Intersymbol interference (ISI) results from the long impulse responses and calls for efficient equalization techniques. In a multiuser context, multiple-access interference (MAI) cannot be avoided and joint detection is required. Furthermore, the transmitted spectrum should be optimized according to the channel selectivity.

- Other important hypotheses are related to the assumption that the communication system is operated on **wired channels**:

  - Only the lower frequencies are available for efficient transmission, due to the lowpass characteristics of the cable responses. *Baseband transmission* is thus basically considered in this work. Actually, the available frequency spectrum does not extend down to the zero frequency, but rather in a range from F_0 to $F_0 + B$, where B is the effective bandwidth, and F_0 is much smaller than B. The system is thus 'quasi-baseband' and the use of a carrier is not required. *Carrierless* solutions are investigated, i.e. passband signals are directly produced in the digital domain before digital-to-analog conversion.
  - The power budget of the communication system is primarily dictated by *EMC restrictions.* As the signal bandwidth B is extremely large as compared to that of the wireless services that must be protected by the EMC requirements, the fundamental power limit is put on the *power spectral density* of the transmitted signal. As several transmitters can be active simultaneously,

the restriction can be applied on the signal-sum rather than on each individual signal.

- The channel transfer function is *slowly time-varying*. It is assumed that the channel responses remain approximately constant over periods of several thousands of symbols. Channel estimation is performed during the communication setup and channel tracking is performed periodically. Both transmitter and receiver are assumed to have a quasi-perfect knowledge of the channel responses. The resource allocation algorithm and the design of an efficient joint detection structure rely on this channel knowledge.
- Synchronization issues are restricted to the problem of *multiuser timing synchronization* as the communication system is of the carrierless type. Like for the channel estimation, the timing parameters are assumed to be estimated at the communication setup, and tracking is ensured during transmission with the appropriate structure.

The *noise scenario* considered in the sequel is the simple additive white Gaussian noise (AWGN) channel. The effects of narrowband noise and impulsive noise are discarded. Finally, the issue of channel coding is not considered in this work.

This thesis is structured as follows.

The first logical step is the characterization of the transmission environment, which includes the derivation of the channel transfer functions and the identification of the noise scenario. Tools for the computation of powerline channel responses are developed in **chapter 2**. This is actually the only chapter of this thesis that is specifically dedicated to the powerline scenario : the other chapters have a general scope and can be applied to a wide range of multiuser frequency-selective channels. For the first time, the powerline cables used in the LV access segment are modeled with the formalism of the *multiconductor transmission lines (MTL) equations*. Maxwell's equations are firstly solved in the cross-section of some typical powerline cables, which provides the distribution of the electromagnetic fields associated with the propagation of TEM waves in the cable structure. From these distributions, and considering lossy conductors and dielectrics, multidimensional lineic capacitance, lineic inductance, lineic resistance and lineic conductance parameters are derived. The MTL equations are then

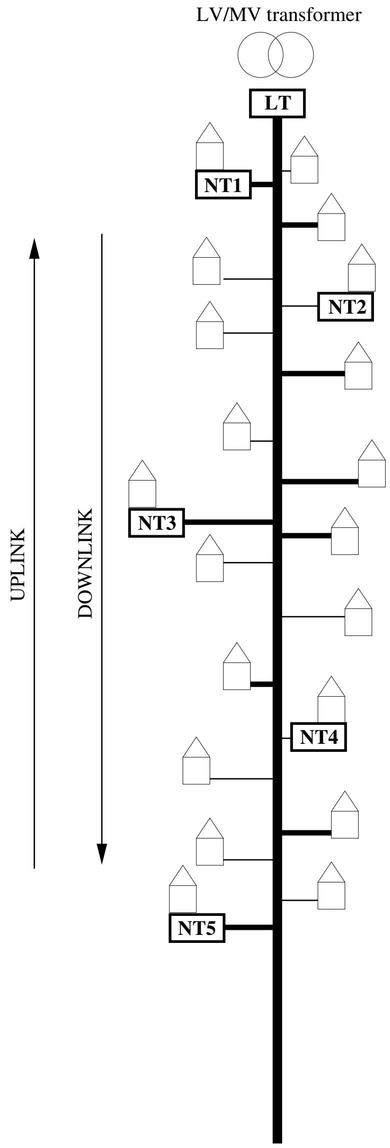

Figure 1.1: *The powerline access network: uplink and downlink transmission*

solved, and their solutions are shown to correspond to a number of propagation eigenmodes that are characterized by well defined distributions of voltages and currents on the conductors, with a common propagation factor $e^{-\gamma_n z}$. The lineic attenuation, phase velocity and characteristic impedance associated with the different eigenmodes are studied as a function of the conductor geometry and the material properties. The impulse response associated with a simple cable segment is derived. The analysis is then extended to the case of complex power distribution networks including a main distribution cable and a number of derivation cables, with specific terminations. Adequate mathematical methods, based on the multidimensional scattering matrix formalism, are derived to allow the computation of the end-to-end transfer function associated with a given communication link. A specific example of a 300 meter long network, with 20 derivations and three different types of cables, is analyzed in detail. Finally, a simple and intuitive multipath channel model is proposed. Results were published in [5, 17].

The next logical step is the derivation of the best performance that can be expected from the proposed channels, in terms of maximum throughput. This problem is analyzed in the light of multiuser information theory, which is the object of **Chapter 3**. The set of simultaneously achievable data rates is known to be the capacity region, which is a convex volume in the K-dimensional space, where K is the number of active users. An original concept, *balanced capacity*, is firstly introduced as a fair method for the distribution of individual data rates to the different users competing for the limited resources. The optimal power allocation problem is solved in the multiuser memoryless channel scenario. Explicit solutions for the optimal sharing of a total power between K users are derived for the downlink (broadcast channel) and the uplink (multiple access channel). An iterative algorithm for the computation of the maximum balanced rates is derived. The case of a multiuser frequency-selective channel is then addressed. Several types of power constraints are proposed and the associated capacity regions are compared. Explicit expressions of the optimal power allocations (among the users and among the frequency spectrum) are derived. Efficient algorithms are proposed for the computation of maximum balanced rates. The specific case of an individual power constraint is shown to be much more complex to handle, and an alternative suboptimal algorithm is proposed, based on the Iterative Multiuser Water-Filling algorithm. Then, the problem of FDMA capacity computation is addressed. It consists in distributing the power to the different users in mutually exclusive frequency bands. Results are finally presented for a 20-user powerline access network. This study has been partly presented in [18].

In **Chapter 4**, practical modulation schemes are proposed. The selected modulation has to be flexible enough in order to allow an efficient multiple access. Furthermore, a generic framework is called for, that allows the comparison of the classical modulation methods proposed in the context of PLC: single-carrier, CDMA and OFDM. The proposed general solution is based on the parallel modulation of a number of signature waveforms by mutually independent sequences of QAM symbols. The signature waveforms are assumed to be mutually orthogonal, and constitute a paraunitary filter bank (FB). Every user is provided with the ability to modulate any subset of waveforms. An adequate signature allocation algorithm implemented in the head-end computes the optimal signature allocation among the users. Single-carrier, CDMA and OFDM are obtained by selecting the appropriate FB. The effect of the frequency-selective channels on the transmitted signals is analyzed, and the received signal is assumed to be sampled at a fractional rate. IIR and FIR observation models, relating the received sequences of samples to the transmitted symbol sequences, are derived. The idea of CAP modulation (Carrierless Amplitude-Phase) is extended to CAP-FB, allowing the definition of a generic FB-based passband transmission scheme. Two variants are finally described. Firstly, CAP-CDMA with long codes is a multiple access scheme where each user is allocated a single time-varying binary signature code. With this method, the signature allocation algorithm is not needed any more, and every user is ensured to obtain an average performance level. Secondly, cyclic-prefixed block transmission, traditionally restricted to multicarrier (OFDM), is extended to the general FB-based transmission scheme.

Chapter 5 is dedicated to the derivation of practical joint detection structures. First of all, the effect of the selected modulation scheme on the multiuser capacity region is investigated. The matched filter bound (MFB) is derived as an alternative upper bound on the optimal performance that can be expected from real detectors. Infinite linear and decision-feedback (DF) minimum mean square error (MMSE) joint detectors are presented. Their performance is computed and compared to the multiuser capacity. Their FIR counterparts are derived, and the computational complexity associated with the coefficient computation is analyzed. The scenario of CAP-CDMA with long codes is analyzed separately, and reduced-complexity algorithms for the computation of MMSE joint detectors suited to long-code CDMA are proposed. Finally, cyclic-prefixed equalization structures are analyzed and performance is compared for different FBs. Original results related to multiple access and joint detection have been presented in [19, 20, 21, 22, 23, 24, 25, 26, 27].

The previous chapter assumed a perfect channel knowledge and a perfect timing synchronization. Actually, both parameters (channel coefficients and sampling time) are permanently estimated and tracked. In **Chapter 6**, the impact of non-ideal timing synchronization and non-ideal channel estimation on the signal-to-noise ratio at the output of the joint detectors is analyzed. The idea of timing sensitivity is introduced, and explicit methods for the computation of the timing sensitivity in a FB-based transmission system are proposed. Results on this topic can be found in [28].

Finally, **Chapter 7** addresses the problem of multiuser timing estimation. The average multiuser decision-directed (DD) Cramèr-Rao lower bound is derived. Both feedforward and feedback joint timing error tracking structures are introduced. Two practical timing error detectors are adapted to the multiuser FB-based transmission system: the early-late detector and the symbol rate (Mueller and Müller) detector. The associated results have been partly presented in [29].

Chapter 2

Channel model

2.1 Introduction

The design of communication systems, the choice of modulation and coding schemes, and the evaluation of performance require the knowledge of the end-to-end channel response in a wide range of frequencies.

In this chapter, a theoretical framework is proposed for the modeling of underground powerline access networks. A very important feature of the powerline cables is their multiconductor nature. In the light of multiconductor transmission lines theory [30], it appears that specific propagation eigenmodes may be defined for each type of cable. These correspond to specific distributions of voltages and currents that propagate with their own phase velocity and lineic attenuation, independently from each other. This aspect is generally ignored in the current publications related to measurement results [31].

A generic simulation tool was designed, that consists of several levels of abstraction :

- At the first level, Maxwell's equations are applied to the cable structure, leading to finding the distribution of the EM fields in the cable cross-section, together with charges and currents on the surface of each conductor. Conductors usually have large sections and are rather close to each other: this leads to the so-called 'proximity effect' and an heterogeneous charge distribution along each conductor surface. Considering an arbitrary cable geometry, the numerical resolution of the Laplace equation in the transverse plane provides the relevant information.

- At the second level, for a given class of metals and dielectrics, the classical primary parameters R, L, C and G are computed. Considering multi-dimensional voltages and currents, these parameters are not simple scalars but square matrices.

- At the third level, the multi-dimensional transmission line equations are solved, providing the definition and secondary parameters of the cable eigenmodes. This step implies the solution of an eigenvalue problem. With these results, a given cable segment may be modeled by a multi-dimensional scattering matrix providing transmission and reflection coefficients for each propagation mode.

- At the last level, the whole powerline access network is considered. It generally consists of a main distribution cable starting at the medium-voltage low-voltage transformer, and lying below the streets with derivation cables providing the final connection to the various subscriber buildings. Broadband modems may be connected on these termination points, just before the power meter, and transmit and/or receive digital signals to/from the central office. Cascading different cable segments, modeling the various network terminations with adequate multi-dimensional loads, and managing the derivation points finally provides the desired end-to-end channel responses.

In order to offer a better intuition on the obtained channel responses, a multipath channel model is also proposed. This model provides a very close approximation of the exact channel responses, as soon as some simplifying hypotheses are assumed. The impulse response of a cable segment, including dielectric losses and conductor losses, is firstly analyzed as a function of the segment length. The network topology is then considered, and the respective effects of derivations and terminations are analyzed to provide a multipath description of the channels. Finally, the cable losses are combined with the multipath formulation to obtain the approximated global channel responses.

2.2 Primary parameters

2.2.1 EM fields in a multiconductor structure

We consider the general case of a transmission line with N_c+1 conductors $\mathcal{C}_n$ with $n \in [0 \cdots N_c]$, where the first conductor $\mathcal{C}_0$ acts as a screen surrounding the others. The cross-section of the line is defined in the plane $(\vec{u}_x, \vec{u}_y)$

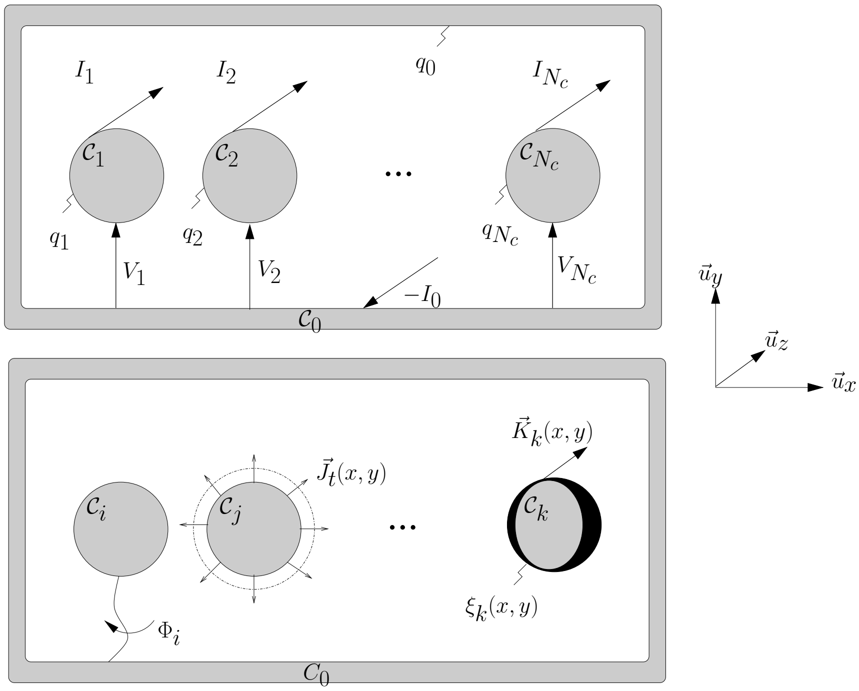

Figure 2.1: *Multiconductor structure*

whereas the longitudinal axis is aligned on $\vec{u}_z$. The dielectric medium between the conductors is supposed to be homogeneous with a dielectric constant κ. With perfect conductors, the solution of Maxwell's equations leads to the definition of TEM (Transverse Electro-Magnetic) waves propagating along $\vec{u}_z$. We define N_c *wire voltages* V_n with $n \in [1 \cdots N_c]$ with the shield conductor as the common reference, and $N_c + 1$ *wire currents* I_n with $n \in [0 \cdots N_c]$ such that $\sum_{n=1}^{N_c} I_n = -I_0$. The conductors $\mathcal{C}_n$, voltages V_n and currents I_n are illustrated in Figure 2.1.

In a so-called 'voltage-mode', voltage V_i is put to 1 while the V_j's are let to 0 with $j \neq i$. To obtain the expression of the fields in this TEM configuration, we have to solve the static EM problem corresponding to the 2-dimensional Laplace equation:

$$\nabla_t^2 \, \Phi_i(x, y) = 0 \tag{2.1}$$

with the boundary conditions:

$$\Phi_i(x, y) = \begin{cases} 1 & \text{if } (x, y) \in C_i, \; i \neq 0 \\ 0 & \text{if } (x, y) \in C_j, \; j \neq i \end{cases} \tag{2.2}$$

Once the potential function $\Phi_i(x, y)$ is known, the static transverse electric and magnetic fields $\vec{e}_t^{(i)}(x, y)$ and $\vec{h}_t^{(i)}(x, y)$ in the dielectric medium can be computed as follows:

$$\begin{aligned} \vec{e}_t^{(i)}(x, y) &= -\nabla_t \, \Phi_i(x, y) && (2.3) \\ \vec{h}_t^{(i)}(x, y) &= \frac{1}{\eta} \vec{u}_z \times \vec{e}_t^{(i)}(x, y), && (2.4) \end{aligned}$$

where $\eta = \sqrt{\mu/\varepsilon} = Z_0/\sqrt{\kappa}$ denotes the dielectric intrinsic impedance, and $Z_0 = 377\ \Omega$. The field phasors along the transmission line are given by $\vec{E}_t^{(i)}(x, y, z) = \vec{e}_t^{(i)}(x, y)\ e^{\pm\gamma z}$ and $\vec{H}_t^{(i)}(x, y, z) = \vec{h}_t^{(i)}(x, y)\ e^{\pm\gamma z}$.

The superficial charge and current densities $\xi_k^{(i)}(x, y)$ and $K_n^{(i)}(x, y)$ on the surface of the n-th conductor are then given by:

$$\begin{array}{lllll} \xi_n^{(i)}(x, y) & = \varepsilon |\vec{e}_t^{(i)}(x, y)| & = -\varepsilon \frac{\partial \Phi_i(x,y)}{\partial n_n}, & (x, y) \in \mathcal{C}_n \\ K_n^{(i)}(x, y) & = |\vec{n}_n \times \vec{h}_t^{(i)}(x, y)| & = v\ \xi_n^{(i)}(x, y), & (x, y) \in \mathcal{C}_n \end{array} \qquad (2.5)$$

where $v = 1/\sqrt{\varepsilon\,\mu} = c/\sqrt{\kappa}$ is the light velocity in the dielectric and $c = 3.10^8$ m/s. As the cross-section of the conductors is generally not small as compared with the distance between them, we have to be aware that the distribution of these charges and currents at the surface of each conductor may be largely non-uniform. The net charges $q_n^{(i)}$ and currents $I_n^{(i)}$ on a given conductor are obtained by integration on the contour $\mathcal{C}_n$:

$$q_n^{(i)} = \oint_{\mathcal{C}_n} \xi_n^{(i)}(x, y)\, dl \qquad\qquad I_n^{(i)} = \oint_{\mathcal{C}_n} K_n^{(i)}(x, y)\, dl \qquad (2.6)$$

Finally, the magnetic flux $\phi_n^{(i)}$ through an arbitrary line joining $\mathcal{C}_0$ and $\mathcal{C}_n$ is:

$$\begin{aligned} \phi_n^{(i)} &= \int_{(x_0,y_0)\in\mathcal{C}_0}^{(x_n,y_n)\in\mathcal{C}_n} \vec{n}\ .\ \mu \vec{h}_t^{(i)}(x, y)\, dl && (2.7) \\ &= \frac{\mu}{\eta} \left[\Phi_i(x_n, y_n) - \Phi_i(x_0, y_0)\right] = \frac{1}{v}\, \delta_{in} && (2.8) \end{aligned}$$

Figure 2.1 illustrates the superficial charge and current densities defined in (2.5), as well as the magnetic flux given by (2.8).

The different quantities $x^{(i)}$ defined above are valid for a given voltage mode i. More generally, the voltage distribution on the conductors will be arbitrary and given by the column vector $\underline{V}$. By the superposition principle, the corresponding quantities will be given by $x = \sum_{i=1}^{N} V_i \, x^{(i)}$.

The solution of the static EM problem (2.1)-(2.2) can be obtained numerically for an arbitrary configuration of the line cross-section. The computation of the charge density profile $\xi_n^{(i)}(x, y)$ on each conductor contour $\mathcal{C}_n$ and for each voltage mode i is actually sufficient to derive the primary parameters of the multiconductor transmission line. In the method proposed by [32], each conductor contour is approximated by a polygon with a large number of sides carrying a uniform charge density, and the densities on each side have to be found in order to recover the original boundary conditions given by (2.2). Figure 2.2 displays the charge density profiles $\xi_n(x, y)$ obtained with this method, for three types of voltage configurations. The multiconductor structure considered here includes 4 circular inner conductors and 1 circular screen. The bold lines give the conductor contours. The numbers inside each inner conductor give the wire voltage V_n (in volts) with respect to the external conductor. The line segments normal to the conductor contours give the local charge (and current) densities. Segments outside the conductors correspond to positive charges while segments inside the conductors correspond to negative charges. The three voltage configurations used here actually correspond to the *eigenmodes* of the multiconductor cable, as will be explained in Section 2.3.

2.2.2 Capacitance and external inductance

The capacitance matrix $\underline{\underline{C}}_w$ gives the global relation between the net charges q_n on the N_c inner conductors and the wire voltages V_n :

$$\begin{bmatrix} q_1 \\ \vdots \\ q_{N_c} \end{bmatrix} = \left[\underline{\underline{C}}_w\right] \begin{bmatrix} V_1 \\ \vdots \\ V_{N_c} \end{bmatrix} \tag{2.9}$$

From the definition of the voltage modes, it clearly appears that:

$$\left(\underline{\underline{C}}_w\right)_{n,i} = q_n^{(i)} = -\varepsilon \oint_{\mathcal{C}_n} \frac{\partial \Phi_i(x, y)}{\partial n_n} \tag{2.10}$$

From the relations above, it can easily be shown that the voltages and currents are related by :

$$v \, \underline{\underline{C}}_w \, \underline{V} = \underline{I} \tag{2.11}$$

for any progressive wave (i.e. with a propagation factor $e^{-\gamma z}$).

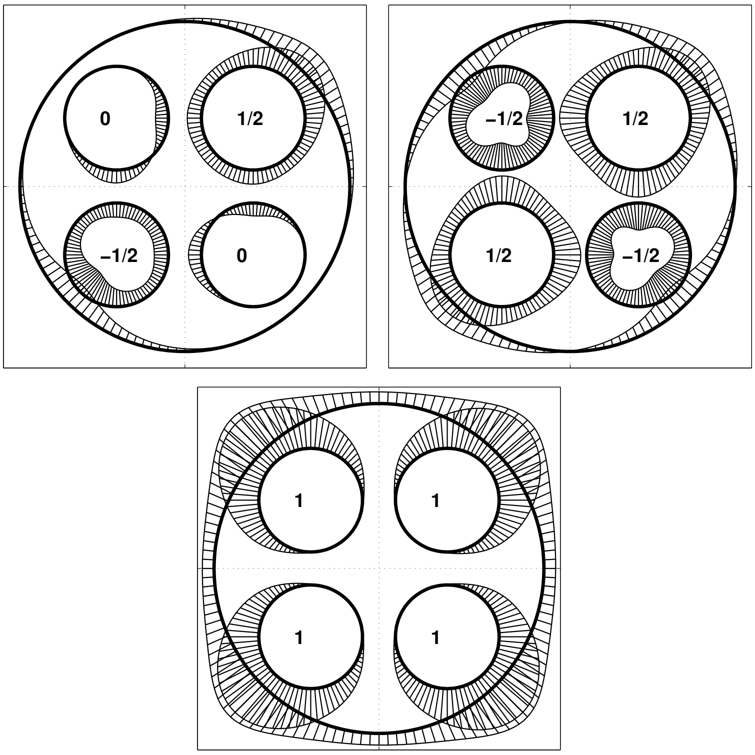

Figure 2.2: *Distribution of local currents for a unit line voltage in the different propagation modes : differential (up), phantom (middle) and common mode (down)*

The external inductance matrix $\underline{\underline{L}}_w$ gives the global relation between the magnetic fluxes ϕ_n and the wire currents I_n :

$$\begin{bmatrix} \Phi_1 \\ \vdots \\ \Phi_{N_c} \end{bmatrix} = \left[\underline{\underline{L}}_w\right] \begin{bmatrix} I_1 \\ \vdots \\ I_{N_c} \end{bmatrix} \tag{2.12}$$

From (2.8), it appears that $\underline{\phi} = 1/v\,\underline{V}$. By (2.11), this implies the next relation between the capacitance and inductance matrices:

$$\underline{\underline{L}}_w\,\underline{\underline{C}}_w = \frac{1}{v^2}\underline{\underline{E}}_{N_c} = \underline{\underline{C}}_w\,\underline{\underline{L}}_w \tag{2.13}$$

where $\underline{\underline{E}}_{N_c}$ is the identity matrix of size N_c. The counterpart of equation

(2.11) is :

$$v \,\underline{\underline{\mathrm{L}}}_w \,\underline{\mathrm{I}} = \underline{\mathrm{V}} \tag{2.14}$$

for any progressive wave.

2.2.3 Dielectric losses

Non perfect dielectrics are characterized by a complex permittivity $\varepsilon = \varepsilon' - j\,\varepsilon''$. The imaginary part ε'' encompasses both conduction and polarization losses. A transverse conduction current flowing between the conductors dissipates a part of the wave power. The conduction current density in the medium is given by $\vec{J}_t(x,y) = \omega\,\varepsilon''\,\vec{e}_t(x,y)$. Integrating around each inner conductor, we obtain the net transverse current per unit length :

$$I_{tn} = \oint_{\mathcal{C}_n} \vec{J}_t(x,y).\vec{n}\,dl = \omega\,\varepsilon''\frac{1}{\varepsilon'}\,q_n = \delta_d\,\omega\,q_n \tag{2.15}$$

where the dielectric loss angle δ_d is defined as $\mathrm{tg}(\delta_d) \approx \delta_d = \varepsilon''/\varepsilon'$. Figure 2.1 illustrates the conduction current density around conductor $\mathcal{C}_j$.

The conductance matrix $\underline{\underline{\mathrm{G}}}_w$ gives the relation between the transverse conduction currents I_{tn} and the wire voltages V_n :

$$\begin{bmatrix} I_{t1} \\ \vdots \\ I_{tN_c} \end{bmatrix} = \left[\underline{\underline{\mathrm{G}}}_w\right] \begin{bmatrix} V_1 \\ \vdots \\ V_{N_c} \end{bmatrix} \tag{2.16}$$

Inserting (2.15) into (2.9), it follows that the conductance matrix is given by :

$$\underline{\underline{\mathrm{G}}}_w = \delta_d\;\omega\,\underline{\underline{\mathrm{C}}}_w. \tag{2.17}$$

2.2.4 Conductor losses

In this section, we take into account the skin effect caused by the finite conductivity of the conductors. Non perfect conductors have a finite conductivity σ_n with $n \in (0\cdots N_c)$. It follows that a longitudinal electric field appears at the surface of the conductors:

$$\vec{e}^{(i)}_{z,n}(x,y) = \eta_n\,K^{(i)}_n(x,y) \qquad\qquad (x,y) \in \mathcal{C}_n \tag{2.18}$$

with η_n the metal surface impedance:

$$\eta_n = \sqrt{\frac{j\,\omega\,\mu_n}{\sigma_n}} = (1+j)\,R_{mn} = \frac{(1+j)}{\sigma_n\,\delta_n}. \tag{2.19}$$

$\delta_n = \sqrt{\frac{1}{2\omega\mu_n\sigma_n}}$ and $R_{mn} = \sqrt{\frac{\omega\,\mu_n}{2\,\sigma_n}}$ are the skin depth and surface resistance associated with the n-th conductor.

In a small perturbation approach, we assume that the transverse fields and related quantities are unaffected by the skin effect. On the other hand, longitudinal fields must be re-computed as they change from zero to a finite value.

To define the resistance matrix $\underline{\underline{\mathrm{R}}}_w$, the direct use of the longitudinal voltage drop induced along the line by the current flow is not a valid approach as this voltage drop is not uniquely defined. Indeed, the longitudinal fields $\vec{e}_{z,n}(x,y)$ and current densities $K_n(x,y)$ are largely non-uniform on each conductor contour. To keep a classical transmission line formalism, we introduce a kind of 'mean longitudinal voltage drop' per unit length $\underline{\mathrm{U}}$ such that:

$$\underline{\mathrm{U}} = \underline{\underline{\mathrm{R}}}_{wc}\,\underline{\mathrm{I}} \tag{2.20}$$

where $\underline{\underline{\mathrm{R}}}_{wc}$ is a complex matrix. The complex power dissipated in the conductors per unit length is given by:

$$P_c = \frac{1}{2}\underline{\mathrm{I}}^*\underline{\mathrm{U}} = \frac{1}{2}\begin{bmatrix} I_1^* & \cdots & I_{N_c}^* \end{bmatrix}\left[\underline{\underline{\mathrm{R}}}_{wc}\right]\begin{bmatrix} I_1 \\ \vdots \\ I_{N_c} \end{bmatrix} \tag{2.21}$$

To obtain a valid expression of the resistance matrix, the last quantity has to be the same as the complex power corresponding to the transverse component of the Poynting vector $\vec{S}(x,y)$. This can be computed as:

$$-\vec{n}_n\,.\,\vec{S}(x,y) = \frac{1}{2}\vec{e}_l(x,y)\times\vec{h}_t^*(x,y) \tag{2.22}$$

$$= \frac{1}{2}\eta_n|K_n(x,y)|^2 = \frac{v^2\,\eta_n}{2}|\xi_n(x,y)|^2 \tag{2.23}$$

The corresponding complex power is obtained by integrating on each contour and summing the contributions of the N_c+1 conductors:

$$P_c = \frac{v^2}{2}\sum_{n=0}^{N_c}\eta_n\oint_{\mathcal{C}_n}|\xi_n(x,y)|^2\,dl \tag{2.24}$$

This quantity must be calculated for an arbitrary voltage configuration $\underline{\mathrm{V}}$. Let us introduce a matrix $\underline{\underline{\mathrm{A}}}$ whose entry (i,j) is defined as:

$$\left(\underline{\underline{\mathrm{A}}}\right)_{i,j} = v^4\sum_{n=0}^{N_c}\eta_n\oint_{\mathcal{C}_n}\xi_n^{(i)}(x,y)\,\xi_n^{(j)}(x,y)\,dl \tag{2.25}$$

The complex power is now:

$$P_c = \frac{1}{2v^2}\,\underline{V}^*\underline{\underline{A}}\,\underline{V} = \frac{1}{2}\,\underline{I}^*\left[\underline{\underline{L}}_w^*\underline{\underline{A}}\,\underline{\underline{L}}_w\right]\underline{I} \tag{2.26}$$

where relation (2.14) was used. Comparing expressions (2.21) and (2.26), we finally obtain the resistance matrix as:

$$\underline{\underline{R}}_{wc} = \underline{\underline{L}}_w^*\underline{\underline{A}}\,\underline{\underline{L}}_w. \tag{2.27}$$

From the expression of η_n, it appears that this matrix is complex with the imaginary part equal to the real part. This matrix indeed encompasses both the resistance matrix $\underline{\underline{R}}_w$ corresponding to conductor losses and the internal inductance matrix which has to be added to the external inductance matrix $\underline{\underline{L}}_w$ previously calculated:

$$\underline{\underline{R}}_{wc} = (1+j)\,\underline{\underline{R}}_w \tag{2.28}$$

It should be observed that each of the $N_c + 1$ conductors plays a role in the computation of the lineic resistance matrix. Whatever the voltage configuration, local currents are induced along the contour of each conductor, which implies power dissipation, even if the mean current integrated along the corresponding contour is zero. Consider for instance the distribution of local currents given by the first scheme in Figure 2.2. The net currents I_n are zero for conductors $\mathcal{C}_1$ and $\mathcal{C}_3$ (with wire voltages equal to 0), and for the external conductor $\mathcal{C}_0$. Local currents are generated, however, in these three conductors, which contributes to power dissipation.

2.3 Secondary parameters

2.3.1 Multiconductor line equations

Transmission line equations may be written in matrix form:

$$\frac{d\underline{I}}{dz} = -\left[\underline{\underline{y}}\right]\,\underline{V} \qquad\qquad \frac{d\underline{V}}{dz} = -\left[\underline{\underline{z}}\right]\,\underline{I} \tag{2.29}$$

where $\underline{\underline{y}}$ and $\underline{\underline{z}}$ are lineic admittance and impedance matrices. The solution to these equations is given in [33]. After derivation and elimination, these equations transform into:

$$\frac{d^2\underline{I}}{dz^2} = \left[\underline{\underline{y}}\,\underline{\underline{z}}\right]\underline{I} \qquad\qquad \frac{d^2\underline{V}}{dz^2} = \left[\underline{\underline{z}}\,\underline{\underline{y}}\right]\,\underline{V} \tag{2.30}$$

As results from electromagnetic reciprocity, $\underline{\underline{y}}$ and $\underline{\underline{z}}$ are symmetric matrices, and $\underline{\underline{y}}\,\underline{\underline{z}}$ and $\underline{\underline{z}}\,\underline{\underline{y}}$ are the transposed of each other. As a consequence, they have the same eigenvalues. Let γ_m^2, with $m \in \{1, \cdots, M\}$ be the M distinct eigenvalues of $\underline{\underline{y}}\,\underline{\underline{z}}$ and $\underline{\underline{z}}\,\underline{\underline{y}}$, with $M \leq N_c$. Each eigenvalue γ_m^2 has an algebraic multiplicity $\pi(m)$ with $\sum_m \pi(m) = N_c$. Multiple eigenvalues generally appear when the considered transmission line presents some kind of symmetry, which is the case for many powerline cables.

Equations (2.30) have a set of N_c linearly independent solutions, the *eigenmodes*, of the form:

$$\underline{I}(z) = \underline{I}_n \exp(\pm\gamma_n z) \qquad\qquad \underline{V}(z) = \underline{V}_n \exp(\pm\gamma_n z) \tag{2.31}$$

where $\underline{I}_n$, $\underline{V}_n$ and γ_n are solutions of the eigenvalue problems:

$$\left[\underline{\underline{y}}\,\underline{\underline{z}}\right] \underline{I}_n = \gamma_n^2 \underline{I}_n \qquad\qquad \left[\underline{\underline{z}}\,\underline{\underline{y}}\right] \underline{V}_n = \gamma_n^2 \underline{V}_n \tag{2.32}$$

Building a diagonal matrix $\underline{\underline{\Gamma}} = \text{Diag}\left[\gamma_n^2\right]$ with the N_c eigenvalues and two modal matrices $\underline{\underline{J}}$ and $\underline{\underline{U}}$, the columns of which are the eigenvectors $\underline{I}_n$ and $\underline{V}_n$, respectively, the eigenvalue problems may be written:

$$\left[\underline{\underline{y}}\,\underline{\underline{z}}\right] \underline{\underline{J}} = \underline{\underline{J}}\,\underline{\underline{\Gamma}} \qquad\qquad \left[\underline{\underline{z}}\,\underline{\underline{y}}\right] \underline{\underline{U}} = \underline{\underline{U}}\,\underline{\underline{\Gamma}} \tag{2.33}$$

2.3.2 Normalization

The modal matrices $\underline{\underline{U}}$ and $\underline{\underline{J}}$ may not be chosen independently. Actually, using (2.29) and (2.31), they are linked by the following constraint :

$$\underline{\underline{J}}\,\underline{\underline{\Gamma}}\,\underline{\underline{U}}^{-1} = \underline{\underline{y}} \qquad\qquad \underline{\underline{U}}\,\underline{\underline{\Gamma}}\,\underline{\underline{J}}^{-1} = \underline{\underline{z}} \tag{2.34}$$

On the other hand, the eigenvectors $\underline{I}_n$ or $\underline{V}_n$ are not fully defined by the eigenvalues problems (2.33) : each eigenvector can be individually scaled, and the definition of a given basis in the subspace corresponding to a multiple eigenvalue is arbitrary. Additional constraints are necessary to make the solution unique.

Using (2.33) and (2.34), it can be shown that :

$$\underline{\underline{U}}^T \left(\underline{\underline{y}}\right) \underline{\underline{U}} = \left(\underline{\underline{U}}^T \underline{\underline{J}}\right) \underline{\underline{\Gamma}} = \underline{\underline{\Gamma}} \left(\underline{\underline{U}}^T \underline{\underline{J}}\right) = \underline{\underline{J}}^T \left(\underline{\underline{z}}\right) \underline{\underline{J}} \tag{2.35}$$

As $\underline{\underline{\Gamma}}$ is diagonal, (2.35) implies that the matrix product $\underline{\underline{U}}^T \underline{\underline{J}}$ is block-diagonal :

$$\underline{\underline{U}}^T \underline{\underline{J}} = \text{Diag}\left[\underline{\underline{X}}_m\right] \tag{2.36}$$

where each block $\underline{\underline{X}}_m$ is a symmetric matrix of size $\pi(m)$. From matrix theory, it is known (cf. [34], pp. 207) that for any symmetric matrix $\underline{\underline{X}}_m$, there exists a matrix $\underline{\underline{Y}}_m$ such that $\underline{\underline{X}}_m = \underline{\underline{Y}}_m^T \underline{\underline{Y}}_m$. We define the normalized modal matrices as follows :

$$\underline{\underline{U}}_0 = \underline{\underline{U}}\ \mathrm{Diag}\left[\underline{\underline{Y}}_m^{-1}\right] \qquad \underline{\underline{J}}_0 = \underline{\underline{J}}\ \mathrm{Diag}\left[\underline{\underline{Y}}_m^{-1}\right] \tag{2.37}$$

The normalized eigenvectors $\underline{I}_{0n}$ and $\underline{V}_{0n}$ are mutually orthonormal :

$$\underline{\underline{U}}_0^T \underline{\underline{J}}_0 = \underline{\underline{E}}_N \tag{2.38}$$

Another form of this normalization condition is given by :

$$\underline{\underline{U}}_0^T\, \underline{\underline{y}}\, \underline{\underline{U}}_0 = \underline{\underline{\Gamma}} = \underline{\underline{J}}_0^T\, \underline{\underline{z}}\, \underline{\underline{J}}_0 \tag{2.39}$$

2.3.3 Progressive and regressive waves

The general solution of the multiconductor line equations is finally given by :

$$\underline{V}(z) = \underline{\underline{U}}_0 \left[\underline{A}(z) + \underline{B}(z)\right] \qquad \underline{I}(z) = \underline{\underline{J}}_0 \left[\underline{A}(z) - \underline{B}(z)\right] \tag{2.40}$$

with

$$\underline{A}(z) = \mathrm{Diag}\left[\exp\left(-\gamma_n z\right)\right] \underline{A} \qquad \underline{B}(z) = \mathrm{Diag}\left[\exp\left(+\gamma_n z\right)\right] \underline{B} \tag{2.41}$$

where $\underline{A}$ and $\underline{B}$ are two column vectors of arbitrary constants to be determined by the boundary conditions. This very compact form of the solutions shows progressive and regressive eigenmodes with amplitudes $\underline{A}$ and $\underline{B}$.

Let us assume for instance that the boundary conditions are such that $A_n \neq 0$, all other elements of $\underline{A}$ and all elements of $\underline{B}$ being zero. Then the voltages and currents are given by

$$\underline{V}\,(z) = A_n\, \underline{V}_{0n}\, e^{-\gamma_n z} \qquad \underline{I}\,(z) = A_n\, \underline{I}_{0n}\, e^{-\gamma_n z}. \tag{2.42}$$

The normalized eigenvectors $\underline{I}_{0n}$ and $\underline{V}_{0n}$ give the distributions of voltages and currents for the n-th eigenmode and A_n is an amplitude factor. A given eigenmode is thus characterized by well defined distributions of voltages and currents, with a common propagation factor $e^{-\gamma_n z}$ for these voltages and currents. Thanks to the normalization condition (2.38), the scalars $A_n^2/2$ and $B_n^2/2$ give the complex power carried by the progressive and regressive waves, respectively, by the n-th eigenmode.

The concepts of characteristic impedance Z_c and admittance Y_c may be extended to the multidimensional case. Defining $(\underline{V}_+(z), \underline{I}_+(z))$ as the progressive waves, we get :

$$\begin{array}{rclcl} \underline{V}_+(z) & = & \left(\underline{\underline{UU}}^T\right) \underline{I}_+(z) & = & \underline{\underline{Z}}_C \underline{I}_+(z) \\ \underline{I}_+(z) & = & \left(\underline{\underline{JJ}}^T\right) \underline{V}_+(z) & = & \underline{\underline{Y}}_C \underline{V}_+(z) \end{array} \tag{2.43}$$

2.3.4 Line voltages

In Section 2.2.1, voltages were arbitrarily defined as the wire voltages with respect to the external screen, considered as a common reference. Currents were defined as the internal wire currents, whose sum gave rise to an equivalent current flowing in the opposite direction inside the external screen. These definitions correspond to a 'wire' formulation. Actually, there are alternative ways of defining voltages and currents in a multiconductor structure. A 'line' formulation may be more useful to describe the cable behavior. For instance, for a two-wire transmission line under a screen, one may prefer the use of the differential mode and common mode voltages and currents, rather than the individual wire voltages and currents.

The changes of variables between the 'wire' and the 'line' formulations is constrained to linear transformations of the type :

$$\underline{V}_L = \underline{\underline{N}}^{-1} \underline{V}_w \qquad\qquad \underline{I}_L = \underline{\underline{N}}^T \underline{I}_w \tag{2.44}$$

so as to maintain the power as given by $P = \frac{1}{2} I_L^* V_L = \frac{1}{2} I_w^* V_w$. It follows from (2.29) and (2.44) that the pair $(\underline{V}_L, \underline{I}_L)$ also obeys transmission lines equations. The corresponding change of variables for the lineic parameters is given by:

$$\underline{\underline{z}}_L = \underline{\underline{N}}^{-1} \underline{\underline{z}}_w \left(\underline{\underline{N}}^T\right)^{-1} \qquad\qquad \underline{\underline{y}}_L = \underline{\underline{N}}^T \underline{\underline{y}}_w \underline{\underline{N}} \tag{2.45}$$

There is an infinite number of ways to define a 'line' formulation, as this amounts to selecting an arbitrary matrix $\underline{\underline{N}}$. A pertinent choice leads to the diagonalization of the previously defined matrices. Let us select the columns of $\underline{\underline{N}}$ as a set of eigenvectors $\underline{V}_{0w}$:

$$\underline{\underline{N}} = \left[\begin{array}{ccc} V_{0w}^{(1)} & \cdots & V_{0w}^{(N_c)} \end{array} \right] \tag{2.46}$$

The amplitude of each eigenvector is here chosen to get a tractable expression of the resulting line voltages. Furthermore, as shown in last section, the eigenvectors corresponding to a multiple eigenvalue have to be chosen adequately. The resulting modal matrices $\underline{\underline{\mathrm{U}}}_{0L} = \underline{\underline{\mathrm{N}}}^{-1}\,\underline{\underline{\mathrm{U}}}_{0w}$ and $\underline{\underline{\mathrm{J}}}_{0L} = \underline{\underline{\mathrm{N}}}^{T}\,\underline{\underline{\mathrm{J}}}_{0w}$ are diagonal. This means that each line voltage and current propagates along the cable with its own propagation factor γ_n. From (2.39) and (2.43), it follows that the corresponding matrices $\underline{\underline{\mathrm{y}}}_L$, $\underline{\underline{\mathrm{z}}}_L$, $\underline{\underline{\mathrm{Z}}}_{CL}$ and $\underline{\underline{\mathrm{Y}}}_{CL}$ are also diagonal. In particular:

$$\underline{\underline{\mathrm{U}}}_{0L} = \mathrm{Diag}\left(\sqrt{Z_{C_n}}\right) \qquad \underline{\underline{\mathrm{J}}}_{0L} = \mathrm{Diag}\left(\sqrt{Y_{C_n}}\right) \tag{2.47}$$

with $Z_{C_n} = 1/Y_{C_n}$.

2.3.5 Application to powerline cables

In this section, the general results obtained in Sections 2.2 and 2.3 are applied to the case of low-voltage powerline cables used in the underground power distribution network. Figure 2.3 illustrates the cross-section of typical PLC cables with 3 or 4 inner conductors. The external conductor $\mathcal{C}_0$ is a circle of radius b. The internal conductors $\mathcal{C}_n$ are constrained inside a circle of radius a, and are surrounded by a dielectric sheath with a thickness $\Delta = b - a$.

Section 2.2 gives the expression of the lineic impedance and admittance matrices in the 'wire' formulation :

$$\begin{aligned} \underline{\underline{\mathrm{z}}}_w(f) &= (1+j)\,\underline{\underline{\mathrm{R}}}_w(f) + \frac{j\omega}{v^2}\,\underline{\underline{\mathrm{C}}}_w^{-1} && (2.48)\\ \underline{\underline{\mathrm{y}}}_w(f) &= (j+\delta_d)\,\omega\,\underline{\underline{\mathrm{C}}}_w && (2.49) \end{aligned}$$

where the lineic capacitance and resistance matrices are given by

$$\underline{\underline{\mathrm{C}}}_w = \varepsilon \begin{bmatrix} c_{11} & c_{12} & \cdots & c_{1N} \\ c_{12} & c_{22} & & \vdots \\ \vdots & & \ddots & \\ c_{1N} & \cdots & & c_{NN} \end{bmatrix} \tag{2.50}$$

$$\underline{\underline{\mathrm{R}}}_w = \sum_{k=0}^{N_c} \frac{R_{mk}(f)}{b} \begin{bmatrix} r_{11} & r_{12} & \cdots & r_{1N} \\ r_{12} & r_{22} & & \vdots \\ \vdots & & \ddots & \\ r_{1N} & \cdots & & r_{NN} \end{bmatrix}_k \tag{2.51}$$

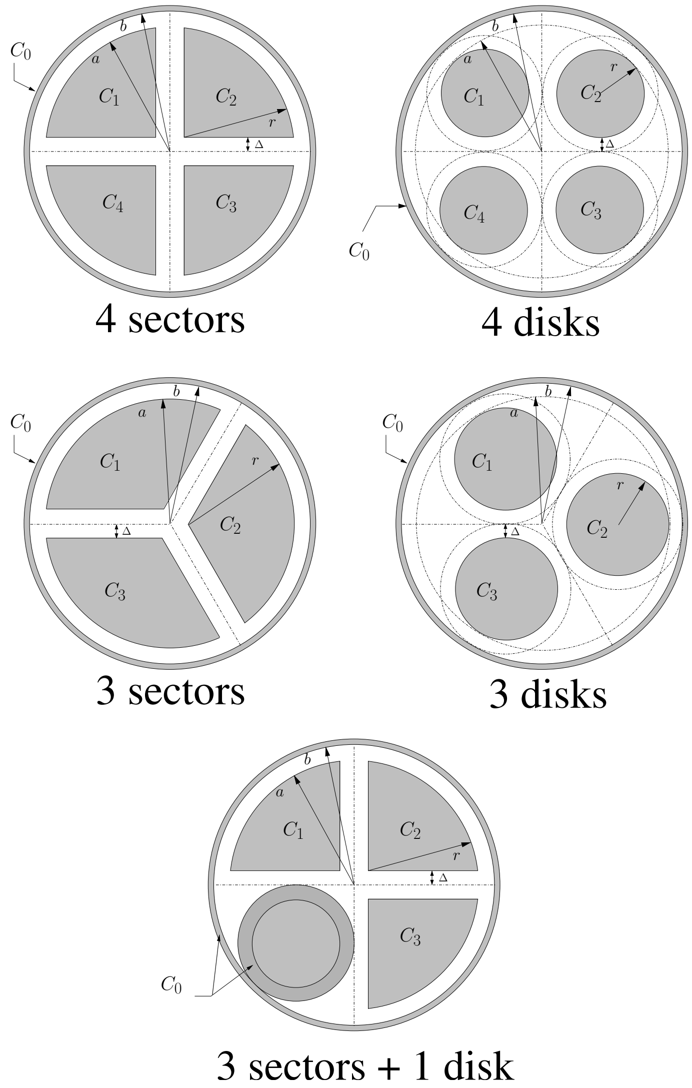

Figure 2.3: *Cross-section of 4-conductor and 3-conductor symmetric cables*

The computation of the adimensional entries c_{ij} and r_{ij} in the last expressions requires the resolution of the Laplace equation in the cable cross-section. For example, with the classical coax cable ($N_c = 1$) with dimensions a and b, the solution is given by [35]

$$c_{11} = \frac{2\pi}{\log(b/a)} \qquad\qquad r_{11} = \frac{1}{2\pi}\left(1 + \frac{b}{a}\right) \tag{2.52}$$

For a fixed cable structure (as given by one of the schemes in Figure 2.3), the parameters c_{ij} and r_{ij} only depend on the ratio $\rho = \frac{a}{b}$. The cable size b has no effect on the capacitance matrix, while the entries of the resistance matrix decrease as $1/b$ as suggested by equation (2.51). Taking into account the symmetry of matrices $\underline{\underline{\mathrm{C}}}_w$ and $\underline{\underline{\mathrm{R}}}_w$, i.e. $c_{ij} = c_{ji}$ and $r_{ij} = r_{ji}$, the solution of this geometrical problem finally provides $N_c^2 + N_c$ distinct real coefficients $\{c_{ij}\}$ and $\{r_{ij}\}$.

As explained in Section 2.3.4, the multiconductor transmission line analysis can also be performed in a 'line' formulation corresponding to the cable eigenmodes. The associated resistance and capacitance matrices are known to be diagonal. The diagonal entries can be written :

$$C_n = \varepsilon\, c_n(\rho) \qquad R_n = \sum_{k=0}^{N} \frac{R_{mk}(f)}{b} r_{nk}(\rho) = \frac{R_m(f)}{b}\, r_n(\rho) \tag{2.53}$$

where the last equality is only valid if all conductors have the same surface resistance R_m. The corresponding lineic inductances and admittances are

$$L_n = \frac{\mu}{c_n(\rho)} \qquad\qquad G_n = (2\pi f)\ \delta_d\, \varepsilon\, c_n(\rho) \tag{2.54}$$

In addition to the $2N_c$ geometrical parameters c_n and r_n, $N_c^2 - N_c$ parameters are actually needed to express the line voltages as a function of the wire voltages, according to equation (2.46), and considering that each eigenvector can be arbitrarily scaled. Both line and wire formulations of the solution thus require the same amount of $N_c^2 + N_c$ real parameters. As soon as there is some kind of geometrical symmetry in the cross-section, the number of relevant parameters generally decreases (examples will be given in Section 2.3.6).

Secondary parameters provide a meaningful description of the cable behavior. They are the lineic attenuation $\alpha_n(f)$, the phase velocity $v_n(f)$ and the complex characteristic impedance $Z_{C_n}(f)$ for each eigenmode :

$$\gamma_n(f) \triangleq \sqrt{(R_n + j\omega L_n)\,(G_n + j\omega C_n)} \tag{2.55}$$

$$= \alpha_n(f) + j\,\beta_n(f) = \alpha_n(f) + \frac{j\omega}{v_n(f)} \tag{2.56}$$

$$Z_{C_n}(f) \triangleq \sqrt{(R_n + j\omega L_n)\,/\,(G_n + j\omega C_n)} \tag{2.57}$$

Let us define the dielectric and conductor loss angles δ_d and $\delta_{c_n}(f)$ as follows:

$$\delta_d = \frac{G_n(f)}{\omega C_n} \qquad \delta_{c_n}(f) = \frac{R_n(f)}{\omega L_n} \tag{2.58}$$

The dielectric loss angle is a specific physical property depending on the dielectric type, while the conductor loss angle for the n-th mode is computed as follows:

$$\delta_{c_n}(f) = \frac{\sum_{k=0}^{N_c} \frac{R_{mk}(f)}{b} r_{nk}}{\omega\mu/c_n} = \frac{R_m(f)}{\omega\mu b}\, r_n\, c_n = \frac{\delta_{c_{n1}}}{\sqrt{f}} \tag{2.59}$$

where the unit-frequency conductor loss angle $\delta_{c_{n1}}$ is defined as :

$$\delta_{c_{n1}} \triangleq \frac{R_m(1)}{2\pi\mu b} r_n c_n. \tag{2.60}$$

Using these definitions, the propagation factor $\gamma_n(f)$ and the characteristic impedance $Z_{c_n}(f)$ can be expressed as :

$$\gamma_n(f) = \frac{\omega\sqrt{\kappa}}{c}\sqrt{(j+\delta_d)\,[(1+j)\,\delta_{c_n}(f)+j]} \tag{2.61}$$

$$Z_{C_n}(f) = \frac{Z_0}{\sqrt{\kappa}\,c_n}\sqrt{\frac{(1+j)\delta_{ci}(f)+j}{j+\delta_d}} \tag{2.62}$$

It can be shown that, when the losses are small, $(\delta_d, \delta_{c_n}(f)) \ll 1$, the lineic attenuation α_n, the phase velocity v_n and the characteristic impedance Z_{C_n} associated with the n-th mode are approximated by :

$$\alpha_n(f) \approx \frac{\omega\sqrt{\kappa}}{2c}\,[\delta_d + \delta_{c_n}(f)] \tag{2.63}$$

$$v_n(f) \approx \frac{c}{\sqrt{\kappa}}\left[\frac{1}{1+\frac{\delta_{c_n}(f)}{2}}\right] \tag{2.64}$$

$$Z_{C_n}(f) \approx \frac{Z_0}{\sqrt{\kappa}\,c_n}\left[\left(1+\frac{\delta_{c_n}(f)}{2}\right) + j\left(\frac{\delta_d - \delta_{c_n}(f)}{2}\right)\right] \tag{2.65}$$

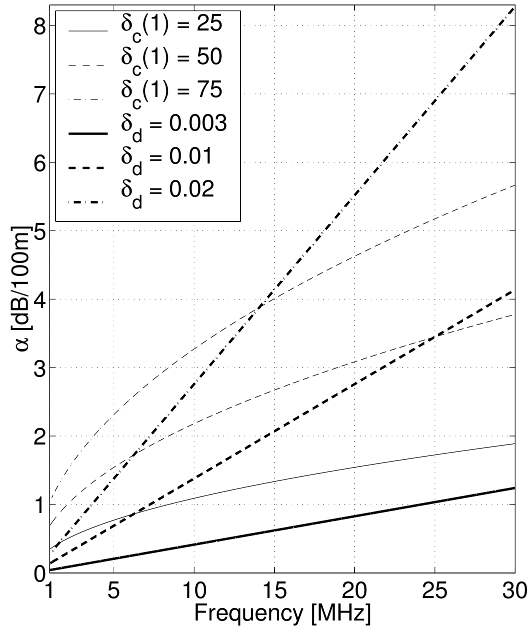

Figure 2.4: *Lineic attenuation α (in dB/100m) vs. frequency*

The phase velocity and characteristic impedance are approximately constant in the useful frequency range. The lineic attenuation α_n, however, varies quickly with the frequency. Figure 2.4 illustrates the evolution of $\alpha_n(f)$ in dB per 100 meter of cable, in the frequency range of 1 to 30 MHz. The bold curves give the contribution of dielectric losses for $\delta_d = \{0.003, 0.01, 0.02\}$, while the thin curves correspond to the conductor losses with $\delta_{c_1} = \{25, 50, 75\}$. As pointed out by equation (2.63), both contributions have to be added to obtain the global attenuation.

2.3.6 Examples

2.3.6.1 Symmetric 4-conductor cables

The first 2 schemes in Figure 2.3 give two kinds of highly symmetric cables with $N_c = 4$ internal conductors. Thanks to that symmetry, the derivation of the capacitance and resistance matrices (through the Laplace equation) involves 6 parameters $\{c_1, c_2, c_3\}$ and $\{r_1, r_2, r_3\}$ rather than $N_c^2 + N_c = 20$

parameters as in the general case :

$$\underline{\underline{C}}_w \propto \begin{bmatrix} c_1 & -c_2 & -c_3 & -c_2 \\ -c_2 & c_1 & -c_2 & -c_3 \\ -c_3 & -c_2 & c_1 & -c_2 \\ -c_2 & -c_3 & -c_2 & c_1 \end{bmatrix} \qquad \underline{\underline{R}}_w \propto \begin{bmatrix} r_1 & r_2 & r_3 & r_2 \\ r_2 & r_1 & r_2 & r_3 \\ r_3 & r_2 & r_1 & r_2 \\ r_2 & r_3 & r_2 & r_1 \end{bmatrix} \tag{2.66}$$

The eigenmodes are the same for both cable types (4 disks or 4 sectors as inner conductors). The line voltages are defined as follows:

$$\underline{V}_w = \begin{bmatrix} 1/2 & 0 & 1/2 & 1 \\ 0 & 1/2 & -1/2 & 1 \\ -1/2 & 0 & 1/2 & 1 \\ 0 & -1/2 & -1/2 & 1 \end{bmatrix} \underline{V}_L \tag{2.67}$$

$$\underline{V}_L = \begin{bmatrix} 1 & 0 & -1 & 0 \\ 0 & 1 & 0 & -1 \\ 1/2 & -1/2 & 1/2 & -1/2 \\ 1/4 & 1/4 & 1/4 & 1/4 \end{bmatrix} \underline{V}_w \tag{2.68}$$

The first two eigenmodes are the differential modes between opposite conductors, the third one is the phantom mode and the last one is the common mode. These eigenmodes are valid as long as the internal conductors are identical. Otherwise, the symmetry would be lost. The screen conductor, however, can be made from a different metal without modifying the definition of the eigenmodes. For the line voltages defined in equation (2.67), the capacitance and resistance coefficients are given by

$$\bar{c}_1 = \frac{1}{2}(c_1 + c_3) = \bar{c}_2 \qquad \bar{r}_1 = 2(r_1 + r_3) = \bar{r}_2 \tag{2.69}$$

$$\bar{c}_3 = c_1 - c_3 + 2c_2 \qquad \bar{r}_3 = r_1 - r_3 + 2r_2 \tag{2.70}$$

$$\bar{c}_4 = 4(c_1 - c_3 - 2c_2) \qquad \bar{r}_4 = \frac{1}{4}(r_1 - r_3 - 2r_2) \tag{2.71}$$

In Figure 2.2, the selected voltage configurations actually correspond to the 3 line voltages defined here. The figures illustrate the distribution of local currents/charges for a unit line voltage : by comparison, it can be observed that $\bar{c}_1 < \bar{c}_3 < \bar{c}_4$.

2.3.6.2 Symmetric 3-conductor cables

The third and fourth schemes in Figure 2.3 give two kinds of highly symmetric cables with $N_c = 3$ internal conductors. Here, 4 parameters $\{c_1, c_2\}$

and $\{r_1, r_2\}$ are required to obtain the resistance and capacitance matrices, rather than $N_c^2 + N_c = 12$ as in the general case :

$$\underline{\underline{C}}_w \propto \begin{bmatrix} c_1 & -c_2 & -c_2 \\ -c_2 & c_1 & -c_2 \\ -c_2 & -c_2 & c_1 \end{bmatrix} \qquad \underline{\underline{R}}_w \propto \begin{bmatrix} r_1 & r_2 & r_2 \\ r_2 & r_1 & r_2 \\ r_2 & r_2 & r_1 \end{bmatrix} \tag{2.72}$$

The line voltages corresponding to the eigenmodes can be defined as follows:

$$\underline{V}_w = \begin{bmatrix} 1/2 & 1/3 & 1 \\ 0 & -2/3 & 1 \\ -1/2 & 1/3 & 1 \end{bmatrix} \underline{V}_L \qquad \underline{V}_L = \begin{bmatrix} 1 & 0 & -1 \\ 1/2 & -1 & 1/2 \\ 1/3 & 1/3 & 1/3 \end{bmatrix} \underline{V}_w \tag{2.73}$$

The first two eigenmodes correspond to the same eigenvalue. The first one is defined as a 'phase-to-phase' mode between conductors 1 and 3, conductor 2 being hold at zero. The second one is defined as a 'symmetric mode' with equal voltages for conductors 1 and 3, conductor 2 getting the opposite polarity. The last one is the common mode. For the line voltages defined in equation (2.73), the capacitance and resistance coefficients are given by

$$\bar{c}_1 = \frac{1}{2}(c_1 + c_2) \qquad \bar{r}_1 = 2(r_1 - r_2) \tag{2.74}$$

$$\bar{c}_2 = \frac{2}{3}(c_1 + c_2) \qquad \bar{r}_2 = \frac{3}{2}(r_1 - r_2) \tag{2.75}$$

$$\bar{c}_3 = 3(c_1 - 2c_2) \qquad \bar{r}_3 = \frac{1}{3}(r_1 + 2r_2) \tag{2.76}$$

The coefficients associated with the first two eigenmodes are not independent.

2.3.6.3 Asymmetric 3-conductor cable

The last scheme of Figure 2.3 corresponds to a partly asymmetric cable. The external conductor is obtained by the concatenation of the circular screen and the neutral conductor in galvanic contact with the screen. The three internal conductors are no longer interchangeable. Here, the resolution of the Laplace equation finally provides 8 parameters $\{c_1, c_2, c_3, c_4\}$ and $\{r_1, r_2, r_3, r_4\}$:

$$\underline{\underline{C}}_w \propto \begin{bmatrix} c_1 & -c_2 & -c_3 \\ -c_2 & c_4 & -c_2 \\ -c_3 & -c_2 & c_1 \end{bmatrix} \qquad \underline{\underline{R}}_w \propto \begin{bmatrix} r_1 & r_2 & r_3 \\ r_2 & r_4 & r_2 \\ r_3 & r_2 & r_1 \end{bmatrix} \tag{2.77}$$

For this asymmetric configuration, the definition of the line voltages associated with the eigenmodes actually varies with the cable geometry. They can be expressed as follows :

$$\underline{\mathrm{V}}_w = \begin{bmatrix} 1/2 & \frac{\bar{v}_2}{3} & 1 \\ 0 & -\frac{1-\bar{v}_2}{3} & \bar{v}_3 \\ -1/2 & \frac{\bar{v}_2}{3} & 1 \end{bmatrix} \underline{\mathrm{V}}_L \tag{2.78}$$

$$\underline{\mathrm{V}}_L = \begin{bmatrix} 1 & 0 & -1 \\ \frac{\bar{v}_3}{2\bar{v}_{23}} & \frac{-1}{\bar{v}_{23}} & \frac{\bar{v}_3}{2\bar{v}_{23}} \\ \frac{1-\bar{v}_2/3}{2\bar{v}_{23}} & \frac{\bar{v}_2/3}{\bar{v}_{23}} & \frac{1-\bar{v}_2/3}{2\bar{v}_{23}} \end{bmatrix} \underline{\mathrm{V}}_w \tag{2.79}$$

with $\bar{v}_{23} \triangleq 1 + \frac{\bar{v}_2}{3}(\bar{v}_3 - 1)$. In the 'line voltage' formulation, the solution is then fully defined by the 8 parameters $\{\bar{c}_1, \bar{c}_2, \bar{c}_3\}$, $\{\bar{r}_1, \bar{r}_2, \bar{r}_3\}$ and $\{\bar{v}_2, \bar{v}_3\}$. For a given geometrical setup (as the last scheme of Figure 2.3 for instance), those 8 parameters only depend on the ratio a/b. The first mode is the phase-to-phase mode, the second one is a 'modified' symmetric mode parametrized by $\bar{v}_2$, and the last one is a 'modified' common mode parametrized by $\bar{v}_3$. The last two eigenmodes are the same as in the symmetric case for $\bar{v}_2 = 1$ and $\bar{v}_3 = 1$, respectively.

2.3.6.4 Computational results

Figures 2.5 and 2.6 give the evolution of the computed geometrical parameters with the ratio a/b, for each of the 5 types of cables proposed in Figure 2.3 and for each line voltage as given by equations (2.67), (2.73) and (2.79). The left part of the figures gives the product $\bar{c}_n \bar{r}_n$ for each eigenmode, which determines the conductor loss angle $\delta_{c_n}(f)$ as given by (2.59). The right part of the figures gives the ratio $Z_0/\bar{c}_n$ for each eigenmode, which determines the characteristic impedance $Z_{C_n}(f)$ as given by (2.62).

For the purpose of comparison, equivalent parameters are also represented for a standard coax cable with dimensions a and b. The geometrical parameters $\bar{c}_n$ and $\bar{r}_n$ are given by (2.52) for the coax cable ('line' voltages are equivalent to 'wire' voltages as $N_c = 1$).

Finally, Figure 2.7 gives the parameters $\bar{v}_2$ and $\bar{v}_3$, which determine the definition of the line voltages for the asymmetric cable as given by (2.79).

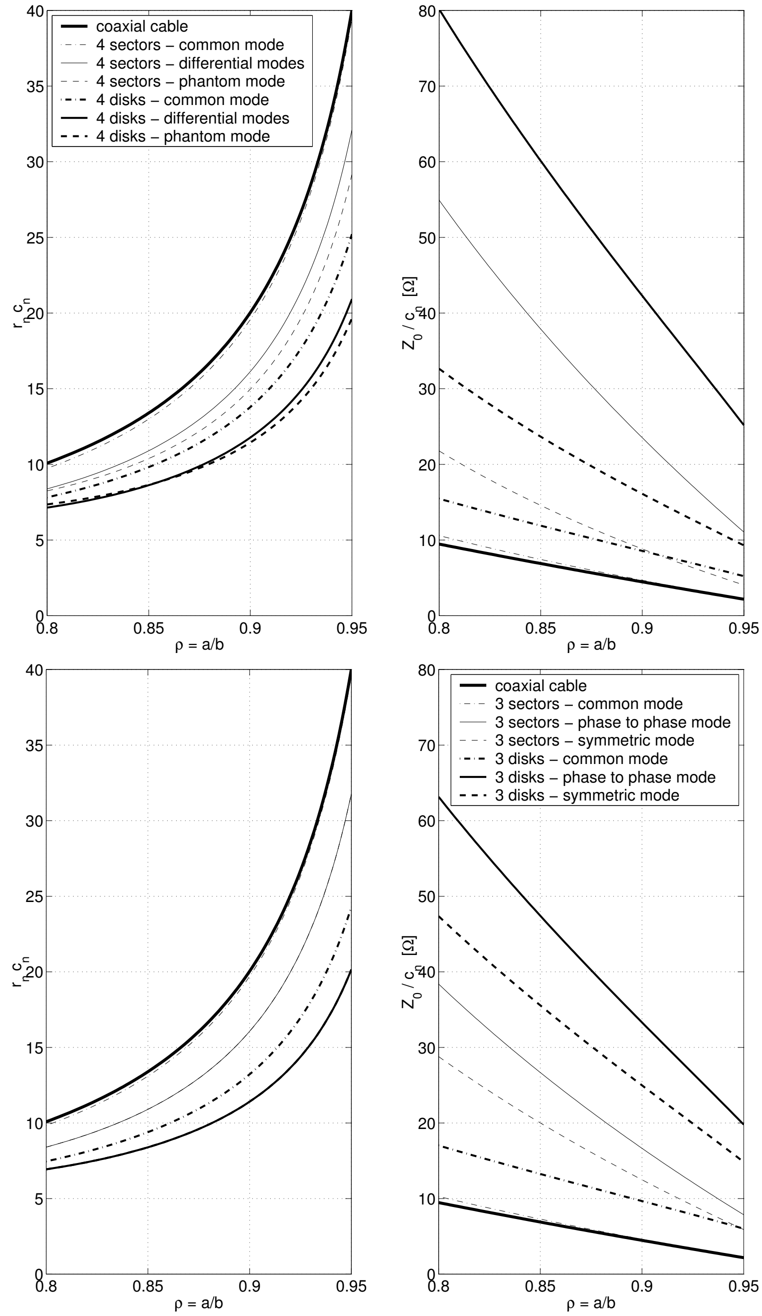

Figure 2.5: *$\bar{r}_n \bar{c}_n$ and $Z_0/\bar{c}_n$ computed for symmetric cables with 4 and 3 conductors*

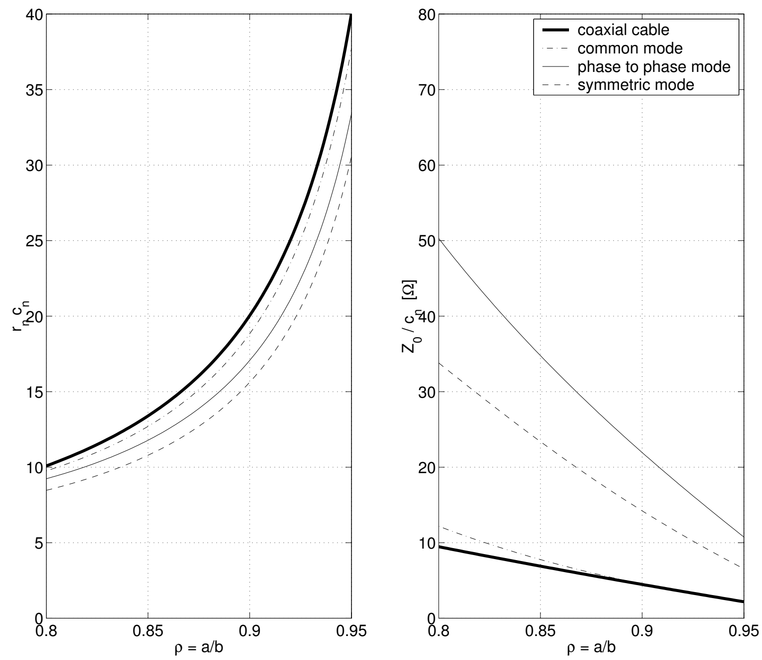

Figure 2.6: *$\bar{r}_n\bar{c}_n$ and $Z_0/\bar{c}_n$ computed for the 3 sector + 1 disk cable*

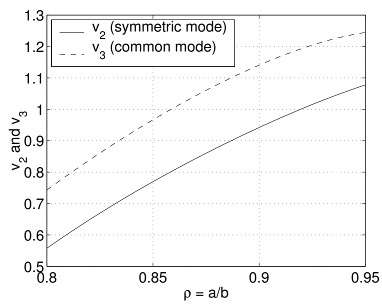

Figure 2.7: *Eigenmode parameters computed for the 3 sector + 1 disk cable*

2.3.7 Practical PLC cables

Table 2.1 gives the main characteristics of 5 PLC cables which are representative of the cables used in the underground power distribution network. The cable dimensions b and a/b are given in the table, and comparative drawings of the cable cross-sections are displayed above the table. Copper ($\sigma = 56.10^6 \mathrm{m}^{-1}\Omega^{-1}$) or aluminium ($\sigma = 35.10^6 \mathrm{m}^{-1}\Omega^{-1}$) is used for the conductors. In the case of the asymmetric cable, the composite external conductor is made of steel (screen) and lead (neutral conductor). Two types of dielectric material are currently used in the PLC cables : polyvinylchloride (PVC) with $\kappa \approx 3.3$ and $\delta_d \approx 0.03$, and polyethylene (PE) with $\kappa \approx 2.3$ and $\delta_d \approx 0.003$. The unit-frequency conductor loss angle $\delta_{c_{n1}}$ and the impedance characteristic $Z_{c_n} \approx \frac{Z_0}{\sqrt{\kappa \tilde{c}_n}}$ is given for each eigenmode. The first 3 types cables will be used in Section 2.5 for the simulation of a realistic PLC access network.

2.4 Impulse response associated with a cable segment

The object of this section is to analyze the channel impulse response $h(t, L)$ associated with a simple cable segment of length L.

Using the cable model developed in section 2.3.5, the cable impulse response can be expressed as the convolution of three components :

$$h(t, L) \approx \delta(t - \Delta) \otimes h_c(t, L) \otimes h_d(t, L) \tag{2.80}$$

where $\Delta \triangleq L/v$ is the propagation time corresponding to a cable length L and a wave velocity v. These components reflect specific physical mechanisms :

- $\delta(t - \Delta)$ represents a simple propagation delay, it gives the channel impulse response that would be associated with a perfect (lossless) cable
- $h_c(t, L) = \mathcal{F}^{-1}\{H_c(\omega, L)\}$ with $H_c(\omega, L) \triangleq e^{-\sqrt{j\omega}\,\sqrt{\pi}\,\delta_{c1}\Delta}$ represents the effect of conductor losses
- $h_d(t, L) = \mathcal{F}^{-1}\{H_d(\omega, L)\}$ with $H_d(\omega, L) \triangleq e^{-\omega\,\delta_d \Delta/2}$ represents the effect of dielectric losses

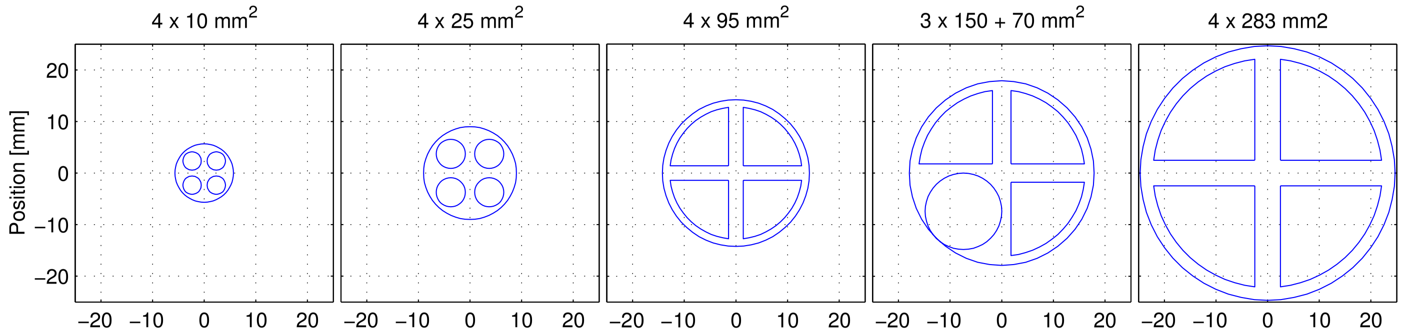

Name	Conductors (in/out)	b [mm]	$\frac{a}{b}$	Differential		Phantom		Common	
				δ_{c_1} [$\sqrt{\text{Hz}}$]	Z_c [Ω]	δ_{c_1} [$\sqrt{\text{Hz}}$]	Z_c [Ω]	δ_{c_1} [$\sqrt{\text{Hz}}$]	Z_c [Ω]
4×10	Cu	5.7	0.9	69.9	39.4	67.9	15.0	81.8	8.0
4×25	Cu	9	0.9	44.0	39.4	42.8	15.0	41.5	8.0
4×95	Alu	14	0.9	48.3	21.9	44.8	8.2	58.6	4.4
4×150	Alu	18	0.9	38.4	21.9	35.6	8.2	46.6	4.4
$3 \times 150 + 70$	Alu/Steel-Pb	18	0.9	45.9	21.9	40.9	14.2	51.6	4.6
4×283	Cu/Alu	25	0.9	24.0	21.9	21.9	8.2	30.0	4.4

Table 2.1: *Cross-section, conductors, geometrical dimensions and computed conductor losses and characteristic impedance of some powerline cables*

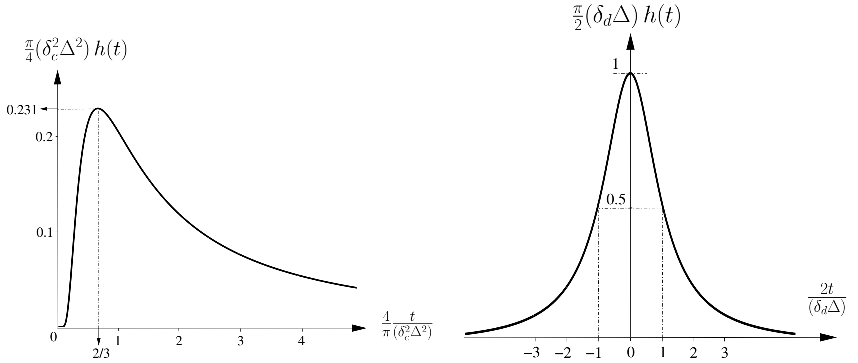

Figure 2.8: *Normalized pulses $K_c h_c(t,L)$ and $\pi K_d h_d(t,L)$*

Applying the inverse Fourier transform $\mathcal{F}^{-1}(.)$ to the partial frequency responses given above, explicit expressions of $h_c(t,L)$ and $h_d(t,L)$ can be obtained as follows [35][36] :

$$h_c(t,L) = \left(\frac{1}{K_c}\right)\frac{e^{\frac{-1}{\tau_c}}}{\sqrt{\pi\tau_c^3}} \tag{2.81}$$

$$h_d(t,L) = \left(\frac{1}{\pi K_d}\right)\frac{1}{\tau_d^2+1} \tag{2.82}$$

with the constant parameters $K_c \triangleq \frac{\pi}{4}(\delta_{c1}\Delta)^2$ and $K_d \triangleq \frac{\delta_d\Delta}{2}$, and the normalized time variables $\tau_c = t/K_c$ and $\tau_d = t/K_d$.

Figure 2.8 illustrates the normalized impulse responses $K_c h_c(t,L)$ and $\pi K_d h_d(t,L)$ in the ranges $\tau_c \in [0,5]$ and $\tau_d \in [-5,5]$, respectively. From the definitions given in (2.81)-(2.82), it appears that the length (resp. the maximum) of the partial impulse responses are proportional (resp. inversely proportional) to the squared product $(\delta_{c1}\Delta)^2$ for the conductor losses, and to the product $(\delta_d\Delta)$ for the dielectric losses. This gives an indication about how the shape of the cable impulse response varies with the cable length $L = \Delta v$.

An important remark should be made here concerning the validity of our dielectric model. The impulse response $h_d(t,L)$ derived above is obviously non-causal : it can not correspond to a physical process. The reason of this lies in the extreme simplicity of the dielectric model :

$$\varepsilon(\omega) = \varepsilon' - j\varepsilon" \qquad \forall\omega. \tag{2.83}$$

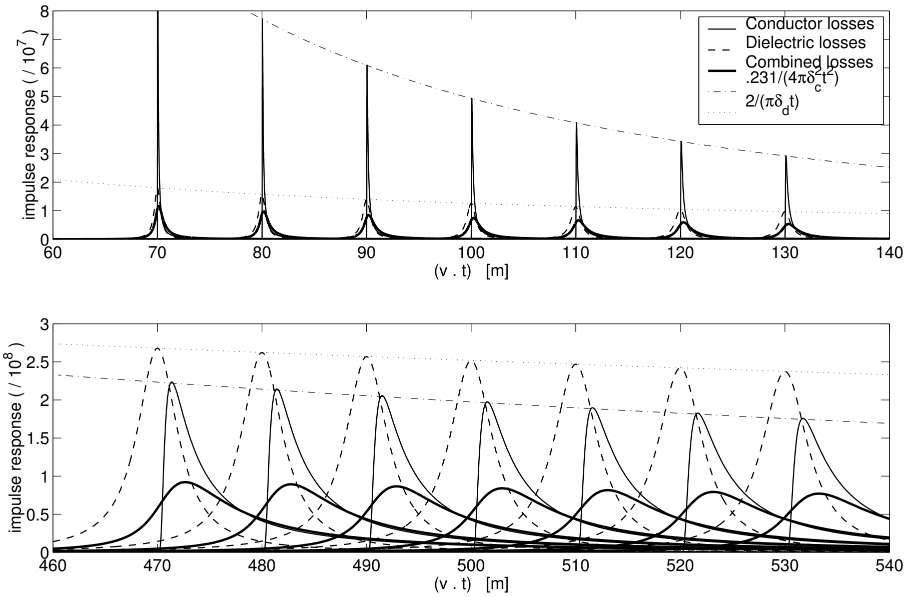

Figure 2.9: *Impulse responses for different cable lengths ($\delta_{c_1} = 48$, $\delta_d = 0.01$, $\kappa = 2.3$) around 100 m (up) and around 500 m (down)*

This is in contradiction with the Kronig and Kramers property [37] specifying that *"a dissipative material ($\varepsilon" \neq 0$) must be dispersive (ε varies with ω), and inversely"*. A valid dielectric model should include the variability of the dielectric properties in the useful frequency range, which is not the case here. However, the simple dielectric model proposed above offers a good approximation, even if the causality constraint is not satisfied. In particular, we have that $h_d(-\Delta)/h_d(0) \approx \delta_d^2/2 \ll 1$, which guarantees that the non-causal part of the impulse response is negligible if the propagation delay Δ is taken into account.

Figure 2.9 gives the (non-normalized) impulse responses $h_c(t-\Delta, L)$ (thin solid lines), $h_d(t-\Delta, L)$ (dashed lines) and $(h_c \otimes h_d)(t-\Delta, L)$ (bold solid lines) corresponding to various cable lengths around 100 meter (upper figure) and around 500 meter (lower figure). This allows the comparison of the respective influences of conductor and dielectric losses on the shape of the composite impulse response, as well as the evolution of this shape with the cable length.

The surface under the impulses $h_c(t, L)$ and $h_d(t, L)$ is independent of the cable length as

$$\int_{-\infty}^{+\infty} h_c(t,L)\ \mathrm{d}t = \int_{-\infty}^{+\infty} h_d(t,L)\ \mathrm{d}t = 1 \quad \forall L. \tag{2.84}$$

This unit value actually corresponds to the channel gain at a zero frequency $H_c(0)$ or $H_d(0)$. It should be reminded, however, that the propagation model derived here is only valid at high frequency (i.e. when the skin depth is small with respect to the conductor dimensions). The property considered here is then just a consequence of the propagation model extrapolation to the zero-frequency, and does not reflect a physical reality. But this approximation is acceptable in our context as the impulse responses studied here are going to be used in relation with passband signals only.

The energy of these impulses can be computed as :

$$\int_{-\infty}^{+\infty} h_c^2(t,L)\ \mathrm{d}t = \frac{1}{4\pi K_c} \tag{2.85}$$

$$\int_{-\infty}^{+\infty} h_d^2(t,L)\ \mathrm{d}t = \frac{1}{2\pi K_d} \tag{2.86}$$

These relations show that full-band signals transmitted on the cable would lose their energy proportionally to the cable length L (as far as the dielectric losses are concerned) or proportionally to the square of the cable length L^2 (as far as the conductor losses are concerned). The effective combined loss would be intermediate. Actually these conclusions are only valid asymptotically for large values of L as the real signals that will be transmitted on the cable have a limited bandwidth.

The effect of a cable segment of length L on a unit-energy band-limited pulse $p(t,T)$ of bandwidth $B = \frac{0.5}{T}$ would be more informative. That is what we propose to analyze now. Let $r(t,T,L)$ be the signal received after propagation over the cable segment, i.e. :

$$r(t,T,L) = p(t-\Delta,T) \otimes h_c(t,L) \otimes h_d(t,L) \tag{2.87}$$

The energy of the received signal is given by

$$\mathcal{E}_{cd}\,(T,L) \triangleq 2T \int_0^{\frac{0.5}{T}} |H_c(f)\,.H_d(f)|^2 \mathrm{d}f \tag{2.88}$$

Analytical results can be easily obtained by studying separately the dielectric and conductor effects :

$$\mathcal{E}_c\left(T,L\right) \triangleq 2T\int_0^{\frac{0.5}{T}} |H_c(f)|^2 \mathrm{d}f \qquad = \frac{2}{\rho_c^2}\left(1-e^{-\rho_c}\right) - \frac{2}{\rho_c}e^{-\rho_c} \tag{2.89}$$

$$\mathcal{E}_d\left(T,L\right) \triangleq 2T\int_0^{\frac{0.5}{T}} |H_d(f)|^2 \mathrm{d}f \qquad = \frac{1}{\rho_d}\left(1-e^{-\rho_d}\right) \tag{2.90}$$

with $\rho_c \triangleq \frac{\pi\delta_{c1}\Delta}{\sqrt{T/2}}$ and $\rho_d \triangleq \frac{\pi\delta_d\Delta}{T}$.

Figure 2.10 (left part) gives the logarithmic energy losses (in dB) for cable lengths in the range of 0 to 2000 meter and a baseband pulse of 10 MHz bandwidth. The solid curves represent the dielectric losses, the conductor losses and the combined losses as given by equations (2.90), (2.89) and (2.88), respectively. The dashed curves (straight lines) correspond to the asymptotic behavior for very short cables. Both types of losses are then cumulative :

$$\mathcal{E}_{cd}(T,L) \approx \mathcal{E}_c(T,L).\mathcal{E}_d(T,L) \approx 1 - \frac{2}{3}\rho_a - \frac{1}{2}\rho_b, \tag{2.91}$$

which corresponds to a global loss of

$$\frac{-10}{\log(10)}\frac{\pi}{v}\left(\frac{2}{3}\frac{\delta_{c1}}{\sqrt{T/2}} + \frac{1}{2}\frac{\delta_d}{T}\right) \qquad [\mathrm{dB/m}]$$

This approximation is valid for short distances (up to a few tens of meter). The dashed-dotted curves correspond to the asymptotic behavior for long cables. The respective losses increase then by 10 dB/decade ($\mathcal{E}_d$) and 20 dB/decade ($\mathcal{E}_c$), and the global loss is dominated by the contribution of conductor losses.

Finally, the effect of a cable segment on a passband pulse should be taken into consideration, as the lower part of the frequency spectrum is not available for the transmission of PLC signals. Assuming a unit-energy passband pulse $\sqrt{2}\,p(t,T)\,\cos(\omega_c t)$ with a useful bandwidth $[B_1, B_2] = [0.5/T_1, 0.5/T_2]$, the energy of the received signal can be obtained by

$$\bar{\mathcal{E}}_{cd}\left(T_1,T_2,L\right) = \frac{T_1}{T_1-T_2}\mathcal{E}_{cd}\left(T_2,L\right) - \frac{T_2}{T_1-T_2}\mathcal{E}_{cd}\left(T_1,L\right). \tag{2.92}$$

The right part of Figure 2.10 gives the logarithmic energy losses (in dB) for a passband pulse in the 1 Mhz - 10 MHz band and different combinations of cable properties ($\delta_d = 0.003$, 0.01 and 0.02, $\delta_{c1} = 25$, 50 and 75).

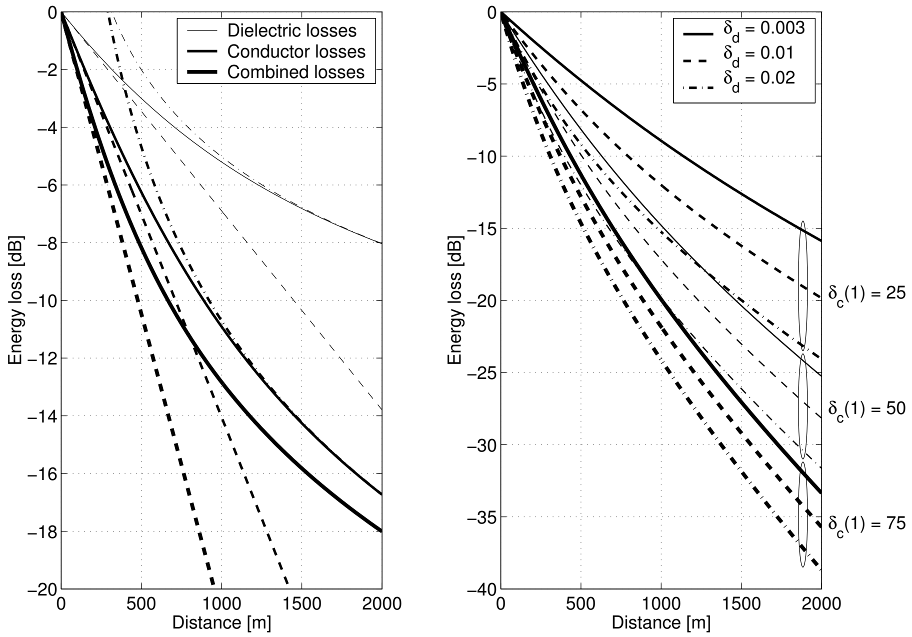

Figure 2.10: *Energy loss vs. distance. Left: relative effects of dielectric and conductor losses ($\delta_{c_1} = 50$, $\delta_d = 0.01$), and asymptotic behavior, with a baseband pulse. Right: energy loss for different combinations of δ_{c_1} and δ_d, with a passband pulse.*

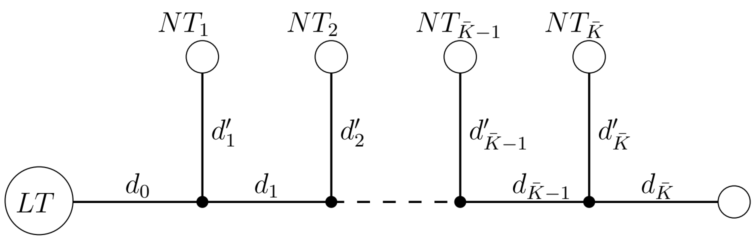

Figure 2.11: *Wireline multiaccess network*

2.5 Powerline access networks

Underground powerline access networks generally consist of a main *distribution cable* starting at the medium-voltage low-voltage transformer, and lying below the streets with *derivation cables* providing the final connection to the various subscriber buildings. Broadband modems (Network Terminations or NTs) may be connected on these termination points, just before the power meter, and tranmit and/or receive digital signals to/from the central office (Line Termination or LT). Evaluation of the communication link performance requires the knowledge of the end-to-end channel response. This global channel is the concatenation of several cable segments, and must take into account the presence of cable derivations and the various loads connected to the termination points.

Figure 2.11 illustrates the general access network topology, where d_k and d'_k denote the length of the different cable segments.
Many variations of the general prototype presented in Figure 2.11 could be investigated and analyzed, leading to different classes of powerline channel models. Many items have to be taken into consideration in the derivation of the channel model :

- The total number of derivations $\bar{K}$.
- The position of the $K \leq \bar{K}$ user modems along the distribution cable. The $\bar{K}-K$ remaining derivations correspond to simple power delivery points, without PLC access.
- The length of the different cable segments (d_k and d'_k).
- The nature of the different cables : number of conductors, definition of the eigenmodes, propagation parameters $(v, \delta_{c1}, \delta_d)$ and characteristic impedance Z_c for each mode.

- The structure of the derivation points (conductors interconnections).

- The nature of termination points (matched, open, other).

Our objective is not to give an exhaustive set of different PLC channel models, but rather to develop a detailed analysis of a representative example and to analyze the influence of some key parameters on the resulting channel responses.

The selected example is depicted in Figure 2.12. The proposed access network includes a 300 m distribution cable and $\bar{K} = 20$ derivations. A central office modem (LT) is located at the medium-voltage low-voltage transformer, and 5 user modems (NTs) are located at selected customer premises, as suggested on the figure. The distribution cable is supposed to be of aluminium with $4 \times 95\,\mathrm{mm}^2$ sectors, and the derivation cables are supposed to be of copper with $4 \times 25\,\mathrm{mm}^2$ or $4 \times 10\,\mathrm{mm}^2$ disks in the cross-section. The cable segments have a length in the set $\{5, 10, 15, 20, 25, 30, 35\}$ meter (the different values can be determined unambiguously from the figure). The main information relative to the position of the 5 NTs is summarized in the following table :

NT	Position k	$\sum_{l=0}^{k-1} d_l$ [m]	d'_k [m]	Total distance [m]
1	2	15	10	25
2	5	60	15	75
3	10	140	35	175
4	15	220	5	225
5	20	290	20	310

Table 2.2: *Position of the 5 NTs, and distance from the LT*

The three types of cables used here have identical eigenmodes (differential, phantom and common), but specific propagation parameters and characteristic impedances. Ideal connections between the respective cable conductors are assumed at the derivation points, which guarantees that the signals associated to each eigenmode do not mix to each other at these points. The termination points at modem locations (LT and 5 NTs) are assumed to be perfectly matched, simultaneously in the different eigenmodes. Finally the 16 remaining termination points are assumed to have an intermediate impedance, between open and matched.

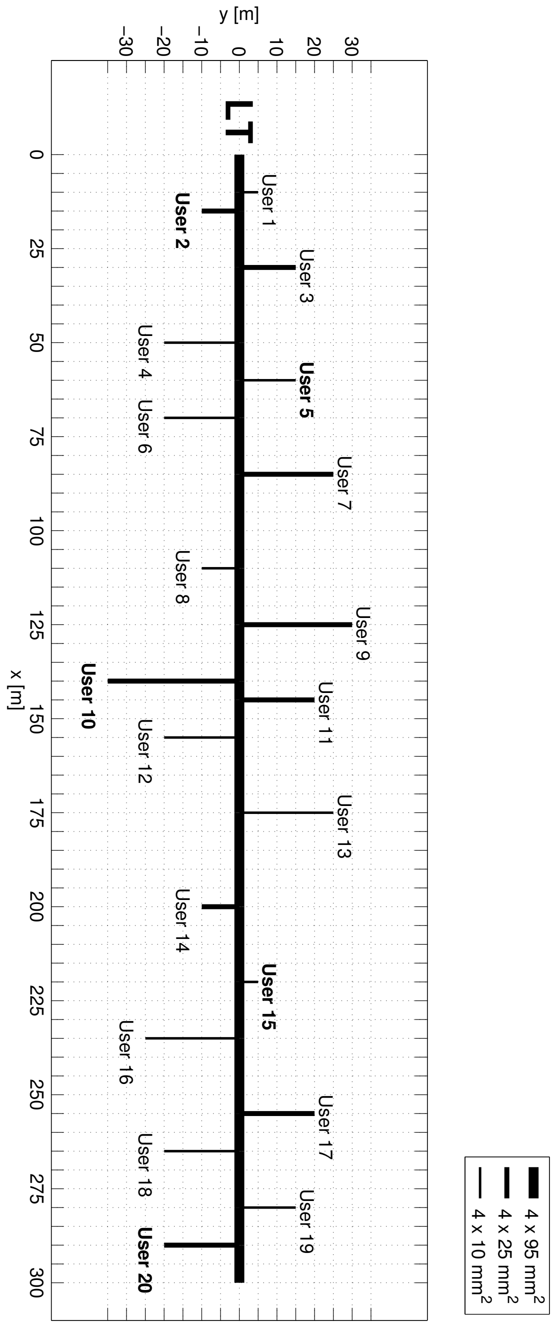

Figure 2.12: *A small powerline access network*

2.6 Network analysis based on the scattering matrix

2.6.1 The scattering matrix

The different elements constituting the low voltage access network may be modeled as 2N-port modules characterized by their multidimensional scattering matrix $\underline{\underline{\mathrm{S}}}$, that links the outgoing waves $(\underline{\mathrm{B}}_1, \underline{\mathrm{A}}_2)$ to the incoming waves $(\underline{\mathrm{A}}_1, \underline{\mathrm{B}}_2)$. Grouping together adjacent elements of the network leads to the cascading of the corresponding scattering matrices. A specific algebra for the combination of multidimensional scattering matrices has to be developed, taking into account the joint presence of cables with a different number of conductors. Assuming a given scattering matrix $\underline{\underline{\mathrm{S}}}_x$ with N_1-fold inputs and N_2-fold outputs, to be cascaded with a given scattering matrix $\underline{\underline{\mathrm{S}}}_y$ with N_2-fold inputs and N_3-fold outputs. The building blocks of the resulting scattering matrix $\underline{\underline{\mathrm{S}}}$ are given by :

$$\begin{aligned}
\underline{\underline{\mathrm{S}}}_{11} &= \underline{\underline{\mathrm{S}}}_{11}^T = \underline{\underline{\mathrm{S}}}_{x,11} + \underline{\underline{\mathrm{S}}}_{x,12} \left(\underline{\underline{\mathrm{E}}}_{N_2} - \underline{\underline{\mathrm{S}}}_{y,11} \underline{\underline{\mathrm{S}}}_{x,22} \right)^{-1} \underline{\underline{\mathrm{S}}}_{y,11} \underline{\underline{\mathrm{S}}}_{x,21} \\
\underline{\underline{\mathrm{S}}}_{12} &= \underline{\underline{\mathrm{S}}}_{21}^T = \underline{\underline{\mathrm{S}}}_{x,12} \left(\underline{\underline{\mathrm{E}}}_{N_2} - \underline{\underline{\mathrm{S}}}_{y,11} \underline{\underline{\mathrm{S}}}_{x,22} \right)^{-1} \underline{\underline{\mathrm{S}}}_{y,12} \\
\underline{\underline{\mathrm{S}}}_{22} &= \underline{\underline{\mathrm{S}}}_{22}^T = \underline{\underline{\mathrm{S}}}_{y,22} + \underline{\underline{\mathrm{S}}}_{y,21} \left(\underline{\underline{\mathrm{E}}}_{N_2} - \underline{\underline{\mathrm{S}}}_{x,22} \underline{\underline{\mathrm{S}}}_{y,11} \right)^{-1} \underline{\underline{\mathrm{S}}}_{x,22} \underline{\underline{\mathrm{S}}}_{y,12}
\end{aligned} \tag{2.93}$$

On the other hand, the transfer of a size-N_2 reflection matrix $\underline{\underline{\mathrm{K}}}_{\mathrm{out}}$ through a scattering matrix $\underline{\underline{\mathrm{S}}}$ with N_1-fold inputs and N_2-fold outputs provides a size-N_1 reflection matrix $\underline{\underline{\mathrm{K}}}_{\mathrm{in}}$ as follows :

$$\underline{\underline{\mathrm{K}}}_{\mathrm{in}} = \underline{\underline{\mathrm{S}}}_{11} + \underline{\underline{\mathrm{S}}}_{12} \left(\underline{\underline{\mathrm{E}}}_{N_2} - \underline{\underline{\mathrm{K}}}_{\mathrm{out}} \underline{\underline{\mathrm{S}}}_{22} \right)^{-1} \underline{\underline{\mathrm{K}}}_{\mathrm{out}} \underline{\underline{\mathrm{S}}}_{21}. \tag{2.94}$$

Figure 2.13 illustrates the various waves and submatrices involved in equations (2.93) and (2.94).

2.6.2 Reference basis and matrix base change

A given scattering matrix $\underline{\underline{\mathrm{S}}}$ depends on the definition of the waves $\underline{\mathrm{A}}$ and $\underline{\mathrm{B}}$ as a function of the line voltages and currents $\underline{\mathrm{V}}$ and $\underline{\mathrm{I}}$. Actually, any change of variables, from the pair $(\underline{\mathrm{V}}, \underline{\mathrm{I}})$ to the pair $(\underline{\mathrm{A}}, \underline{\mathrm{B}})$ may be investigated :

$$\underline{\mathrm{V}}(z) = \underline{\underline{\mathrm{U}}} \left[\underline{\mathrm{A}}(z) + \underline{\mathrm{B}}(z) \right] \qquad \underline{\mathrm{I}}(z) = \underline{\underline{\mathrm{J}}} \left[\underline{\mathrm{A}}(z) - \underline{\mathrm{B}}(z) \right] \tag{2.95}$$

where $\underline{\underline{\mathrm{U}}}$ has the dimensions of the square root of an impedance, and the normalization condition $\underline{\underline{\mathrm{U}}}^T \underline{\underline{\mathrm{J}}} = \underline{\underline{\mathrm{E}}}_N$ is satisfied. With these conditions, the

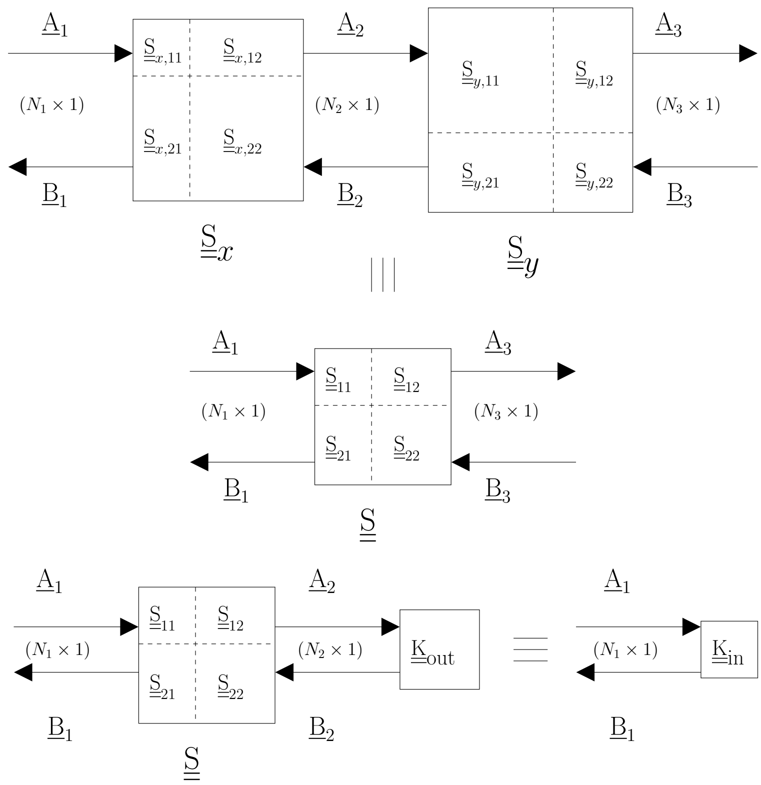

Figure 2.13: *Cascading scattering matrices*

dimension of the waves $\underline{A}$ and $\underline{B}$ in (2.95) is the square root of a power. The choice of modal matrices as in equation (2.40) results in the definition of eigenmodes, where the waves propagate with their own exponential propagation factor, but other choices are possible. A reference basis $(\underline{\underline{U}}_R, \underline{\underline{J}}_R)$ may be defined and used throughout the network. Different reference bases need to be defined for different parts of the network if the number of conductors varies from ones cable segment to another. It is then useful to develop equations for a base change, i.e. the relations between waves $(\underline{A}_x, \underline{B}_x)$ defined in a base $(\underline{\underline{U}}_x, \underline{\underline{J}}_x)$, and waves $(\underline{A}_y, \underline{B}_y)$ defined in another base $(\underline{\underline{U}}_y, \underline{\underline{J}}_y)$. The solution is expressed with a scattering matrix formalism as :

$$\begin{bmatrix} \underline{\underline{B}}_x \\ \underline{\underline{A}}_y \end{bmatrix} = \begin{bmatrix} (\underline{\underline{\Sigma}}_{xy})_{11} & (\underline{\underline{\Sigma}}_{xy})_{12} \\ (\underline{\underline{\Sigma}}_{xy})_{12}^T & (\underline{\underline{\Sigma}}_{xy})_{22} \end{bmatrix} \begin{bmatrix} \underline{\underline{A}}_x \\ \underline{\underline{B}}_y \end{bmatrix} \tag{2.96}$$

with the following submatrices :

$$\begin{aligned} (\underline{\underline{\Sigma}}_{xy})_{11} &= (\underline{\underline{z}}_{yx} + \underline{\underline{E}})^{-1}(\underline{\underline{z}}_{yx} - \underline{\underline{E}}) = (\underline{\underline{\Sigma}}_{yx})_{22} \\ (\underline{\underline{\Sigma}}_{xy})_{22} &= (\underline{\underline{z}}_{xy} + \underline{\underline{E}})^{-1}(\underline{\underline{z}}_{xy} - \underline{\underline{E}}) = (\underline{\underline{\Sigma}}_{yx})_{11} \\ (\underline{\underline{\Sigma}}_{xy})_{12} &= 2(\underline{\underline{z}}_{yx} + \underline{\underline{E}})^{-1}\underline{\underline{J}}_x^T\underline{\underline{U}}_y = (\underline{\underline{\Sigma}}_{yx})_{21} \end{aligned} \tag{2.97}$$

and $\underline{\underline{z}}_{yx} = \underline{\underline{J}}_x^T\underline{\underline{U}}_y\underline{\underline{U}}_y^T\underline{\underline{J}}_x = \underline{\underline{z}}_{yx}^T$, $\underline{\underline{z}}_{xy} = \underline{\underline{J}}_y^T\underline{\underline{U}}_x\underline{\underline{U}}_x^T\underline{\underline{J}}_y = \underline{\underline{z}}_{xy}^T$.

2.6.3 Cable segments

In the eigenbase $(\underline{\underline{U}}_0, \underline{\underline{J}}_0)$ of the cable, the scattering matrix representing a cable segment of length L is:

$$\underline{\underline{S}}_0 = \begin{bmatrix} \underline{\underline{0}}_N & \underline{\underline{T}} \\ \underline{\underline{T}} & \underline{\underline{0}}_N \end{bmatrix} \tag{2.98}$$

with $\underline{\underline{T}} = \mathrm{Diag}\,[\exp(-\gamma_n L)]$.

It is useful to express the scattering matrix $\underline{\underline{S}}_R$ of the cable segment in accordance with the chosen reference basis $\underline{\underline{U}}_R, \underline{\underline{J}}_R$. This is obtained by left- and right- cascading the initial matrix $\underline{\underline{S}}_0$ with the matrix base changes $\underline{\underline{\Sigma}}_{R0}$ and $\underline{\underline{\Sigma}}_{0R}$, respectively. The result is :

$$\begin{aligned} (\underline{\underline{S}}_R)_{11} = (\underline{\underline{S}}_R)_{22} = (\underline{\underline{\Sigma}}_{R0})_{11} + (\underline{\underline{\Sigma}}_{R0})_{12}\,\underline{\underline{T}} \\ \left[\underline{\underline{E}}_N - (\underline{\underline{\Sigma}}_{R0})_{22}\,\underline{\underline{T}}\,(\underline{\underline{\Sigma}}_{R0})_{22}\,\underline{\underline{T}}\right]^{-1} (\underline{\underline{\Sigma}}_{R0})_{22}\,\underline{\underline{T}}\,(\underline{\underline{\Sigma}}_{R0})_{21} \end{aligned} \tag{2.99}$$

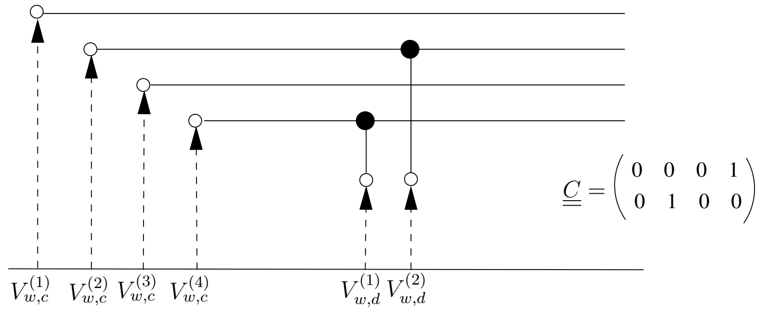

Figure 2.14: *Example of conductors interconnection and associated connection matrix*

$$(\underline{\underline{S}}_R)_{12} = (\underline{\underline{S}}_R)_{21}^T = (\underline{\underline{\Sigma}}_{R0})_{12}\,\underline{\underline{T}} \left[\underline{\underline{E}}_N - (\underline{\underline{\Sigma}}_{R0})_{22}\,\underline{\underline{T}}\,(\underline{\underline{\Sigma}}_{R0})_{22}\,\underline{\underline{T}}\right]^{-1} (\underline{\underline{\Sigma}}_{R0})_{21} \quad (2.100)$$

2.6.4 Cable derivations

Assume a main distribution cable with N wires, a reference basis $(\underline{\underline{U}}_c, \underline{\underline{J}}_c)$, and line voltages defined by $\underline{\underline{N}}_c$. At a given point, a derivation cable with n wires, a reference basis $(\underline{\underline{U}}_d, \underline{\underline{J}}_d)$, and line voltages defined by $\underline{\underline{N}}_d$, is connected to it. Let us define a $n \times N$ connection matrix $\underline{\underline{C}}$ giving the wire connections between the main cable and the derivation cable :

$$\underline{V}_{w,d} = \underline{\underline{C}}\,\underline{V}_{w,c} \quad (2.101)$$

where the entries of $\underline{\underline{C}}$ are 0's and 1's. Figure 2.14 gives an example of a matrix connection with $N = 4$ and $n = 2$. By its definition, the matrix connection satisfies the relation $\underline{\underline{C}}\,\underline{\underline{C}}^T = \underline{\underline{E}}_n$. We also define a modified connection matrix $\underline{\underline{D}}$ as follows :

$$\underline{\underline{D}} = \underline{\underline{J}}_d^T\,\underline{\underline{N}}_d^{-1}\,\underline{\underline{C}}\,\underline{\underline{N}}_c\,\underline{\underline{U}}_c \quad (2.102)$$

The derivation point actually corresponds to a 3-port network. We need to compute the scattering matrix obtained when one of the ports is connected to a known charge.
In figure 2.15, the charge is supposed to be connected on the derivation side. The transmission along the main cable is given by :

$$\begin{aligned} \underline{\underline{S}}_{11} &= \underline{\underline{S}}_{22} = \underline{\underline{T}} \\ \underline{\underline{S}}_{12} &= \underline{\underline{S}}_{21} = \underline{\underline{E}}_N + \underline{\underline{T}} \end{aligned} \quad (2.103)$$

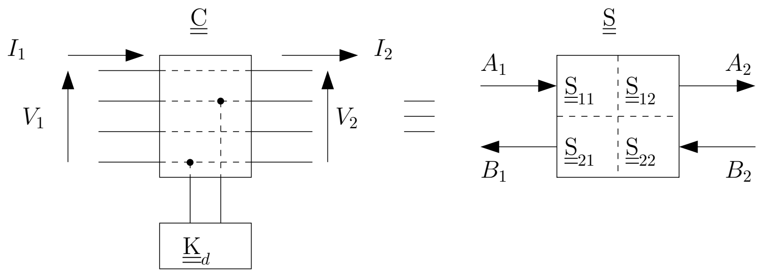

Figure 2.15: *Scattering matrix associated with a derivation (transmission along the distribution cable)*

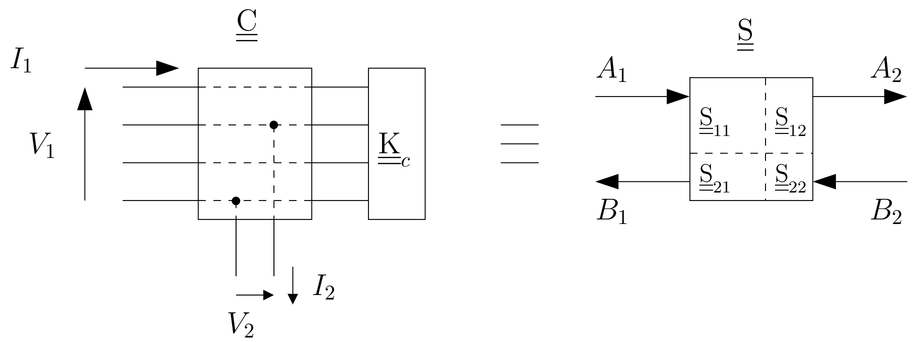

Figure 2.16: *Scattering matrix associated with a derivation (transmission from the distribution cable to the derivation cable)*

$$\underline{\underline{T}} = \underline{\underline{D}}^T \left(\underline{\underline{K}}_d - \underline{\underline{E}}_n\right) \left[\underline{\underline{D}}\,\underline{\underline{D}}^T \left(\underline{\underline{E}} - \underline{\underline{K}}_d\right) + 2\left(\underline{\underline{E}}_n + \underline{\underline{K}}_d\right)\right]^{-1} \underline{\underline{D}} \tag{2.104}$$

In figure 2.16, the charge is supposed to be connected on the main cable right side. The transmission from the main cable to the derivation cable is then given by :

$$\begin{aligned}\underline{\underline{S}}_{11} = \underline{\underline{S}}_{11}^T = \underline{\underline{K}}_c - \left(\underline{\underline{E}}_N + \underline{\underline{K}}_c\right) \underline{\underline{D}}^T & \\ \left[\underline{\underline{D}}\left(\underline{\underline{E}}_N + \underline{\underline{K}}_c\right) \underline{\underline{D}}^T + 2\,\underline{\underline{E}}_n\right]^{-1} \underline{\underline{D}}\left(\underline{\underline{E}}_N + \underline{\underline{K}}_c\right) &\end{aligned} \tag{2.105}$$

$$\underline{\underline{S}}_{12} = \underline{\underline{S}}_{21}^T = 2\left(\underline{\underline{E}}_N + \underline{\underline{K}}_c\right) \underline{\underline{D}}^T \left[\underline{\underline{D}}\left(\underline{\underline{E}}_N + \underline{\underline{K}}_c\right) \underline{\underline{D}}^T + 2\,\underline{\underline{E}}_n\right]^{-1} \tag{2.106}$$

$$\underline{\underline{S}}_{22} = \underline{\underline{S}}_{22}^{T} = \left[\underline{\underline{D}}\left(\underline{\underline{E}}_{N} + \underline{\underline{K}}_{c}\right)\underline{\underline{D}}^{T} + 2\,\underline{\underline{E}}_{n}\right]^{-1} \left[\underline{\underline{D}}\left(\underline{\underline{E}}_{N} + \underline{\underline{K}}_{c}\right)\underline{\underline{D}}^{T} - 2\,\underline{\underline{E}}_{n}\right] \quad (2.107)$$

2.6.5 Line terminations

Active and passive terminations are characterized by their multidimensional impedance and e.m.f. sources. The sources can be described by the equivalent Thevenin dipole representation:

$$\underline{V} = \underline{\mathcal{E}} - \underline{\underline{Z}}_{G}\underline{I} \quad (2.108)$$

where $\underline{\underline{Z}}_{G}$ is a diagonal matrix of the source impedances and $\underline{\mathcal{E}}$ is a column vector giving the e.m.f. of the sources. An equivalent representation for the waves in the reference basis $(\underline{\underline{U}}_{R}, \underline{\underline{J}}_{R})$ writes:

$$\underline{A} = \underline{G} - \underline{\underline{K}}_{G}\underline{B} \quad (2.109)$$

where

$$\underline{\underline{K}}_{G} = \left(\underline{\underline{z}}_{G} + \underline{\underline{E}}_{N}\right)^{-1}\left(\underline{\underline{z}}_{G} - \underline{\underline{E}}_{N}\right) \quad (2.110)$$

$$\underline{G} = \left(\underline{\underline{z}}_{G} + \underline{\underline{E}}_{N}\right)^{-1}\underline{\underline{U}}_{R}\underline{\mathcal{E}} = \frac{1}{2}\left(\underline{\underline{E}}_{N} - \underline{\underline{K}}_{G}\right)\underline{\underline{U}}_{R}\underline{\mathcal{E}} \quad (2.111)$$

and $\underline{\underline{z}}_{G} = \underline{\underline{J}}_{R}^{T}\underline{\underline{Z}}_{G}\underline{\underline{J}}_{R}$ can be seen as a reduced source impedance.

Similarly, a passive load at the end of the line will be described by:

$$\underline{V} = \underline{\underline{Z}}_{L}\underline{I} \quad (2.112)$$

The relation between the corresponding waves is given by a reflection matrix $\underline{\underline{K}}_{L}$:

$$\underline{B} = \underline{\underline{K}}_{L}\underline{A} \quad (2.113)$$

where

$$\underline{\underline{K}}_{L} = \left(\underline{\underline{z}}_{L} + \underline{\underline{E}}_{N}\right)^{-1}\left(\underline{\underline{z}}_{L} - \underline{\underline{E}}_{N}\right) = \left(\underline{\underline{z}}_{L} - \underline{\underline{E}}_{N}\right)\left(\underline{\underline{z}}_{L} + \underline{\underline{E}}_{N}\right)^{-1} \quad (2.114)$$

and $\underline{\underline{z}}_{L} = \underline{\underline{J}}_{R}^{T}\underline{\underline{Z}}_{L}\underline{\underline{J}}_{R}$ is again a reduced impedance matrix.

2.6.6 Network analysis

A generic multidimensional network analysis tool has been developed, that is able to handle an arbitrary network topology, with any type of cable in the different network segments. The eigenmodes associated with each type of cable present in the network are first computed, as well as their fundamental parameters (eigenbase ($\underline{\underline{U}}_0, \underline{\underline{J}}_0$), propagation factors $\{\gamma_n\}$). Simple reference bases ($\underline{\underline{U}}_R, \underline{\underline{J}}_R$) are defined for each number of conductors. The multidimensional scattering matrices associated with each cable segment are then generated and converted in the appropriate reference basis. Using the scattering matrix algebra developed in the previous sections, and considering the exact nature of the various derivation and termination points, K transfer matrices $\underline{\underline{T}}_k$ are finally obtained, that relate the incoming wave vector on the k-th NT $\underline{A}_k$ to the source $\underline{G}$ generated at the LT :

$$\underline{A}_k = \underline{\underline{T}}_k \, \underline{G}. \tag{2.115}$$

The size of each transfer matrix actually depends on the number of conductors at the LT and at the different NTs. The network analysis is performed sequentially for all frequencies in the useful frequency range from 1 to 10 MHz.

2.7 Multipath channel model

The global network analysis method proposed in the previous section is extremely powerful as it is able to predict the channel responses associated with very elaborate networks including various types of cables with any number of conductors, any type of interconnection at the derivation points, and any type of termination load. In particular, the problem of mode mixture can be put forward : signals produced at the transmitter on a given eigenmode can be transferred to the other eigenmodes at some points of the network (unbalanced derivations or terminations). However, the physical interpretation of the obtained end-to-end channel frequency responses $H_k(\omega)$ is not straightforward. The channel impulse responses $h_k(\omega)$ can only be obtained by application of the inverse Fourier transform, which is also rather restrictive.

In order to obtain a better intuition about the end-to-end channel responses and the respective effects due to cable losses, derivations and terminations, we propose to set up a simple multipath model.

Four fundamental assumptions are necessary to validate this simple model :

1. Cables with *identical eigenmodes* are used throughout the network. The derivation and termination points are perfectly balanced, which ensures that the different modes do not mix to each other. In this scenario, the multiconductor network analysis can be reduced to the parallel analysis of independent scalar-waves networks.

2. *Derivation points* act independently of the frequency : the 3×3 scattering matrices associated with each eigenmode do not vary with frequency. This assumption is valid if the ratio of the respective characteristic impedances remains constant in the useful frequency range. It is also valid, of course, if the derivation cables are identical to the distribution cable.

3. *Termination points* also act independently of the frequency : they are modeled by a simple reflection coefficient in the whole frequency range and for each eigenmode. Ideal matched or open terminations satisfy this hypothesis.

4. Finally, the *propagation parameters* $\alpha_i(f)$ *and* $v_i(f)$ associated with a given eigenmode are the same for all cable segments. With this assumption, the channel response corresponding to a given path through the network only depends on the total path distance, irrespectively of the specific cable segments that belong to the considered path.

The multipath model expresses the end-to-end channel frequency response from the LT to the k^{th} NT as the sum :

$$H_k^{(i)}(\omega) = \sum_{l=1}^{N_p} a_{lk}^{(i)} \, e^{-\gamma_i(\omega)\, L_{lk}} \tag{2.116}$$

where

- $\left\{a_{lk}^{(i)}, L_{lk}\right\}$ with $l \in [1, N_p]$ are the path weights and lengths. They only depend on the reflection and transmission coefficients related to the derivation and termination points. A given weight $a_{lk}^{(i)}$ generally results from the superposition of many distinct physical paths from the source to the destination, but all with the same total distance L_{lk}. The total number of paths N_p depends on the desired accuracy of the model. Mathematically, there is an infinite number of paths, but practically the number of significant paths is finite. The determination of N_p is a key parameter of the proposed multipath model.

- $\gamma_i(\omega) = f(\kappa, \delta_d, \delta_{c1}^{(i)})$ only depends on the propagation characteristics of the cables.

The resulting end-to-end channel impulse responses can be obtained as

$$h_k^{(i)}(t) = \sum_{l=1}^{N_p} a_{lk}^{(i)}\, h_{cd}^{(i)}(t, L_{lk}) \tag{2.117}$$

where the impulse response associated with a cable segment of length L_{lk} has been established in Section 2.4.

The computation of the path weights $\{a_{lk}\}$ and lengths $\{L_{lk}\}$ requires the analysis of a complex network including three types of elements ·

1. Two-acces ports representing the cable segments of length d_k or d'_k (see Figure 2.11). We assume that all cable segments have a length that is an integer multiple of a fundamental length L_0, i.e. $d_k = n_k L_0$ and $d'_k = n'_k L_0$ where n_k and n'_k are positive integers. In the example presented in Section 2.5, $L_0 = 5$ meter. The scattering matrix associated with a cable segment of length d_k is then given by

$$\underline{\underline{S}}_c(D) = \begin{pmatrix} 0 & D^{n_k} \\ D^{n_k} & 0 \end{pmatrix} \tag{2.118}$$

where the symbolic variable D represents the propagation through a basic cable segment of length L_0.

2. Three-access ports representing the derivation points. Balanced and lossless derivations result in a scattering matrix given by

$$\underline{\underline{S}}_d = \begin{pmatrix} r_c & t_c & t_d \\ t_c & r_c & t_d \\ t_d & t_d & r_d \end{pmatrix} \tag{2.119}$$

with $r_d^2 + 2t_d^2 = 1$ and $r_c^2 + t_c^2 + t_d^2 = 1$. The parameters r_c and r_d represent the reflection coefficients on the side of the distribution cable and on the side of the derivation cable, respectively. t_c gives the transmission coefficient along the distribution cable, and t_d gives the derivation coefficient. These parameters depend on the relative characteristic impedances of the cables. Let $\rho_{Z_c} = Z_{c2}/Z_{c1}$ be the ratio of the derivation cable impedance (Z_{c2}) and the distribution cable impedance (Z_{c1}). The different reflection and transmission coefficients in (2.119) are then given by

$$r_c = \frac{-1}{2\rho_{Z_c}+1} \qquad r_d = -\left(\frac{2\rho_{Z_c}-1}{2\rho_{Z_c}+1}\right) \tag{2.120}$$

$$t_c = \frac{2\rho_{Z_c}}{2\rho_{Z_c}+1} \qquad t_d = \frac{2\sqrt{\rho_{Z_c}}}{2\rho_{Z_c}+1} \tag{2.121}$$

In the special case where identical cables are used for the distribution and the derivation ($\rho_{Z_c} = 1$), these coefficients are $t_c = t_d = \frac{2}{3}$ and $r_c = r_d = -\frac{1}{3}$. This means that, on each derivation point, $\frac{1}{9}$ of the incoming energy is reflected, $\frac{4}{9}$ is derived and $\frac{4}{9}$ is transmitted along the distribution cable. A better transmission along the distribution cable (higher t_c, lower t_d, $|r_d|$ and $|r_c|$) is ensured for $\rho_{Z_c} > 1$.

3. Terminations that can be represented by a single reflection coefficient r_t.

The complex network is obtained by the interconnection of the elements depicted in the above list. By solving the network equations, the end-to-end transfer functions $T_k(D)$ can be obtained explicitly. They accept a Taylor expansion as follows :

$$T_k(D) = \sum_{j=0}^{\infty} \alpha_{jk}\, D^j \approx \sum_{l=1}^{N_p} a_{lk}\, D^{\frac{L_{lk}}{L_0}}. \tag{2.122}$$

The path weights $\{a_{lk}\}$ can be obtained by identification with the N_p first non-zero terms of the Taylor expansion.

Let us now analyze the network corresponding to the example given in Figure 2.12. All cable segments have a length that is an integer multiple of $L_0 = 5$ meter. The first path weight and length are given by (see also Table 2.2)

$$a_{1k} = t_c^{k-1}\, t_d \qquad L_{1k} = \sum_{j=0}^{k-1} d_j + d'_k. \tag{2.123}$$

For the type of cables used here ($\rho_{Z_c} = 1.8$, see Table 2.1), the transmission and derivation coefficients are $t_c = 0.78$ and $t_d = 0.58$ for the differential mode. Two successive paths are separated by a length of $2L_0 = 10$ meter. Figure 2.17 gives the normalized path weights obtained when all terminations are matched ($r_t(k) = 0 \quad \forall\ k$). The normalization is done with respect to the first path weight a_{1k}. In this scenario, the multipath effect can be exclusively attributed to the reflections on the derivation points. For example, the direct path from the LT to user 15 is 225 meter long and its weight is $a_{1,15} = t_c^{14} t_d = 0.019$. The second path is 235 meter long and corresponds to successive reflections on derivations $\{2, 1\}$ and $\{11, 10\}$. The corresponding weight is $a_{2,15} = 2r_c^2 a_{1,15} = 0.09a_{1,15}$. The third path is 245 meter long and corresponds to successive reflections on derivations $\{2, 1, 2, 1\}$, $\{2, 1, 11, 10\}$, $\{11, 10, 11, 10\}$, $\{5, 4\}$, $\{6, 5\}$ and $\{12, 11\}$. The corresponding weight is then $a_{3,15} = (3r_c^2 + 3r_c^4)a_{1,15} = 0.15a_{1,15}$. The next paths can be generated in the same way. Obviously, the relative weight of secondary paths increases with the user position k along the distribution cable.

For a unit energy wideband pulse transmitted at the LT, the received energy at each network termination is given by

$$\mathcal{E}_k^2 = \sum_{l=1}^{N_p} a_{lk}^2 \ < 1. \tag{2.124}$$

Considering both ends of the distribution cable as users 0 and $K + 1$, the global power budget gives $\sum_{l=0}^{K+1} \mathcal{E}_k^2 = 1$. The set of parameters $\left\{\mathcal{E}_k^2\right\}$ reflects the distribution of the transmitted energy from the network head-end towards the different users. The first part of Figure 2.18 gives the distribution of $\mathcal{E}_k^2$ in dB vs. the user index k for different values of the transmission factor t_c. The energy loss increases dramatically with the user position, especially for low values of t_c. The straight lines give the contribution of the first path weight, as given by (2.123). As expected, the relative strength of the secondary paths increases with k and with t_c (as can be observed by the divergence of the curves). The circles give the total received energy for a transmitted passband pulse in the range of 1 MHz to 10 MHz. The second part of Figure 2.18 gives the evolution of the received energy vs. the transmission factor t_c in the range of $\frac{2}{3}$ to 0.95, for users 2, 5, 10, 15 and 20. It can be observed that the inequality of the energy distribution can be moderated by increasing the transmission coefficient t_c. For lower values of t_c, the existence of the secondary paths also moderates the effect of energy dilution for remote users, but this gain is lost as soon as the passband pulse is taken into account in the power budget.

The observation made here is a crucial feature of the powerline access networks : the total energy transmitted by the LT is delivered in very unequal parts to the various users. The PLC network was not initially designed to

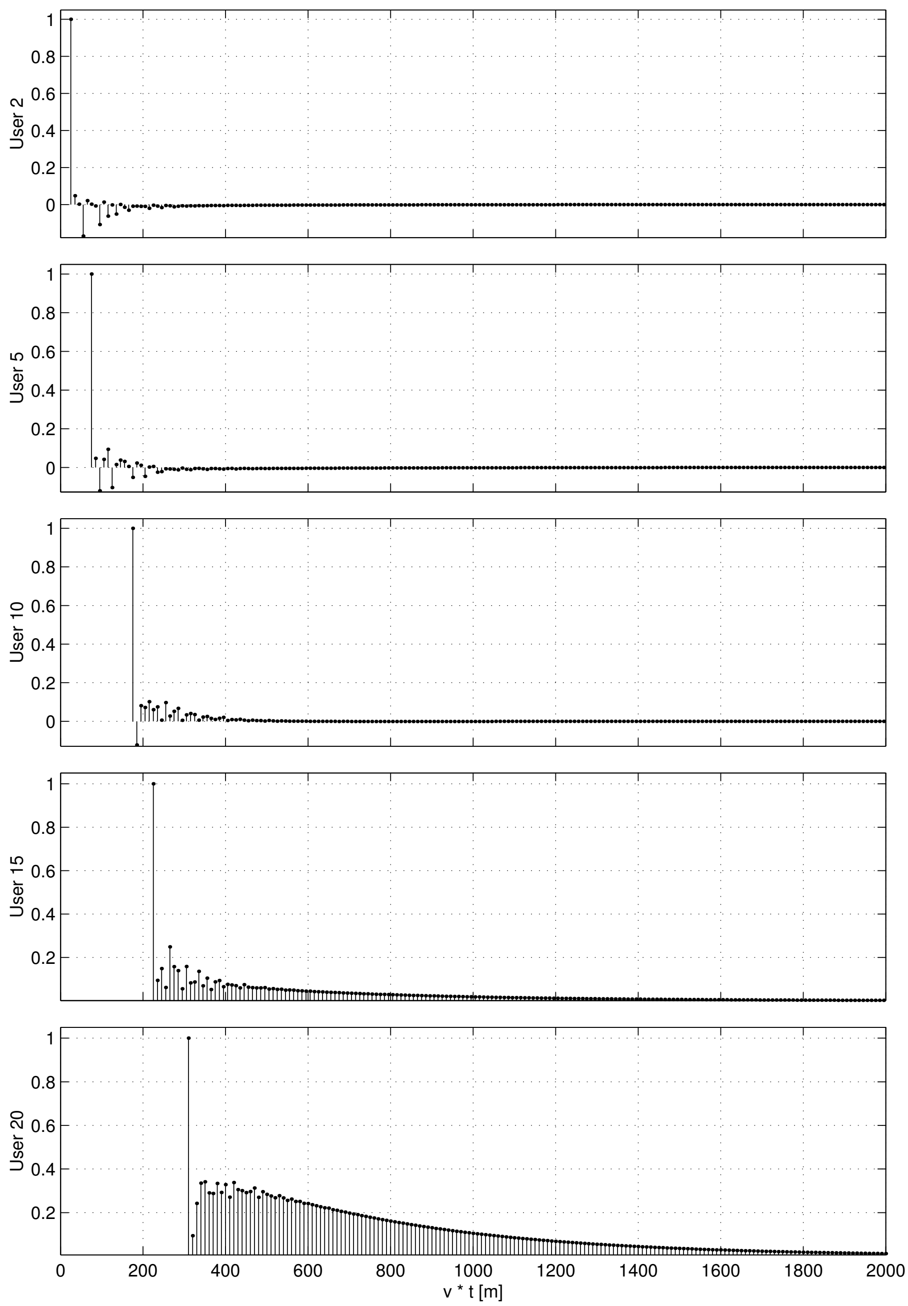

Figure 2.17: *Weights with matched terminations (normalized w.r.t. the first path weight)*

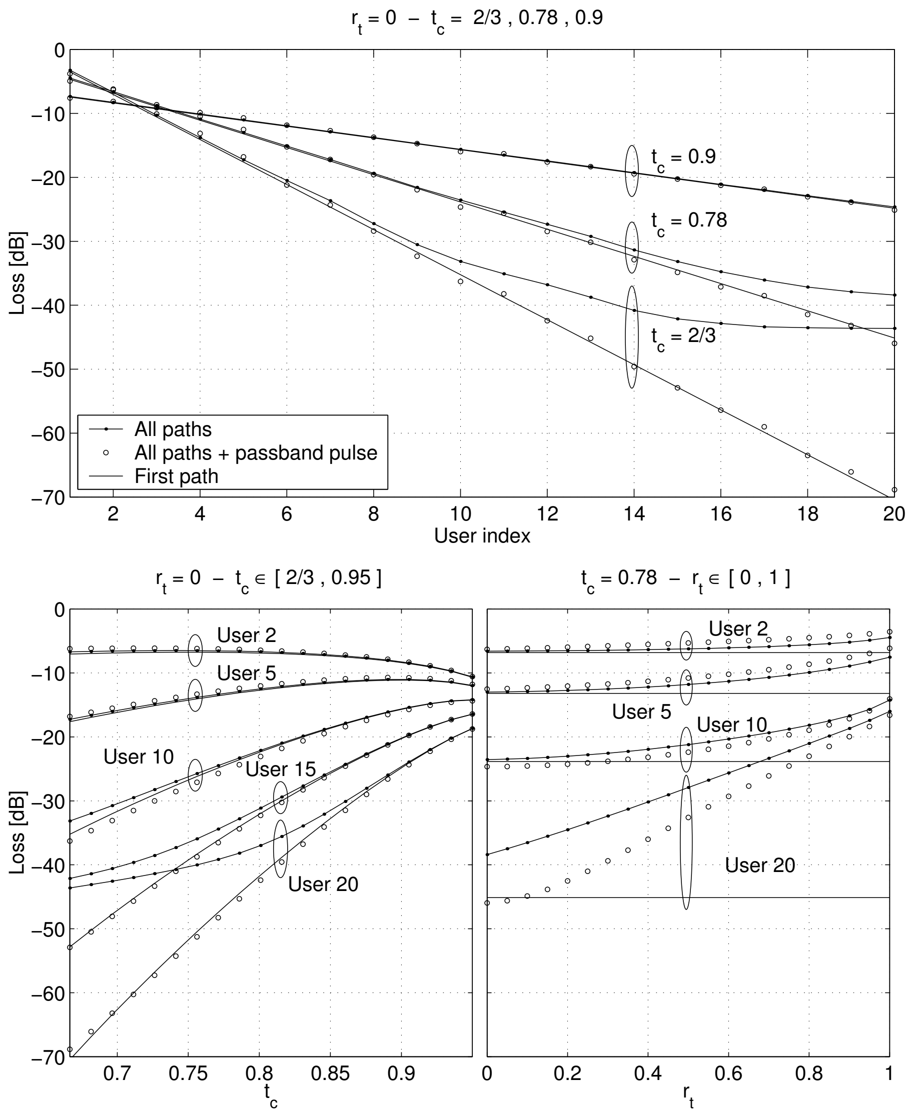

Figure 2.18: *Influence of network parameters on the total energy distributed to the different users : t_c (transmission factor along the main cable) and r_t (reflection factor at unused terminations)*

convey high-frequency signals to the subscribers. At very low frequency (e.g. the power frequency), what really matters is the sum of the path weights, which can be shown to be

$$H_k(f \approx 0) = \sum_{l=1}^{N_p} a_{lk} = \frac{2}{K+2} \quad \forall\, k \in (1, \cdots, K) \tag{2.125}$$

for identical loads at all network terminations. A balanced power distribution network can thus become very unbalanced at high frequency.

Figure 2.19 gives the normalized path weights obtained when all unused terminations are left open ($r_t(k) = 1 \quad \forall\, k \notin \{2, 5, 10, 15, 20\}$). In that scenario, a high number of additional physical paths have to be taken into account as the waves are also reflected on the open terminations. The relative importance of the secondary paths is considerably increased, especially for the remote users : for some of them, the first path is not even the strongest one any more. The energy distribution is less unbalanced than in the previous scenario : one reason for this is that the total energy delivered by the LT is now dissipated in 5 termination loads instead of $K+1$ as before. The last part of Figure 2.18 gives the evolution of the received energy vs. the reflection factor r_t at unused terminations in the range of 0 (matched) to 1 (open), for users 2, 5, 10 and 20.

2.8 PLC channel responses

This section is devoted to the derivation of the final end-to-end channel responses $H_k(\omega) = \mathcal{F}\{h_k(t)\}$ associated with the network example of Figure 2.12.

The channel impulse responses $h_k(t)$ actually result from the combined effect of :

- The multiple paths from the LT to the NTs through the multiple reflections on cable derivations and network terminations. The path weight distribution was analyzed in Section 2.7 in relation with the *network topology.*

- The *conductor and dielectric losses*, which increase with the distance. The impulse response associated with a cable segment was presented in Section 2.4.

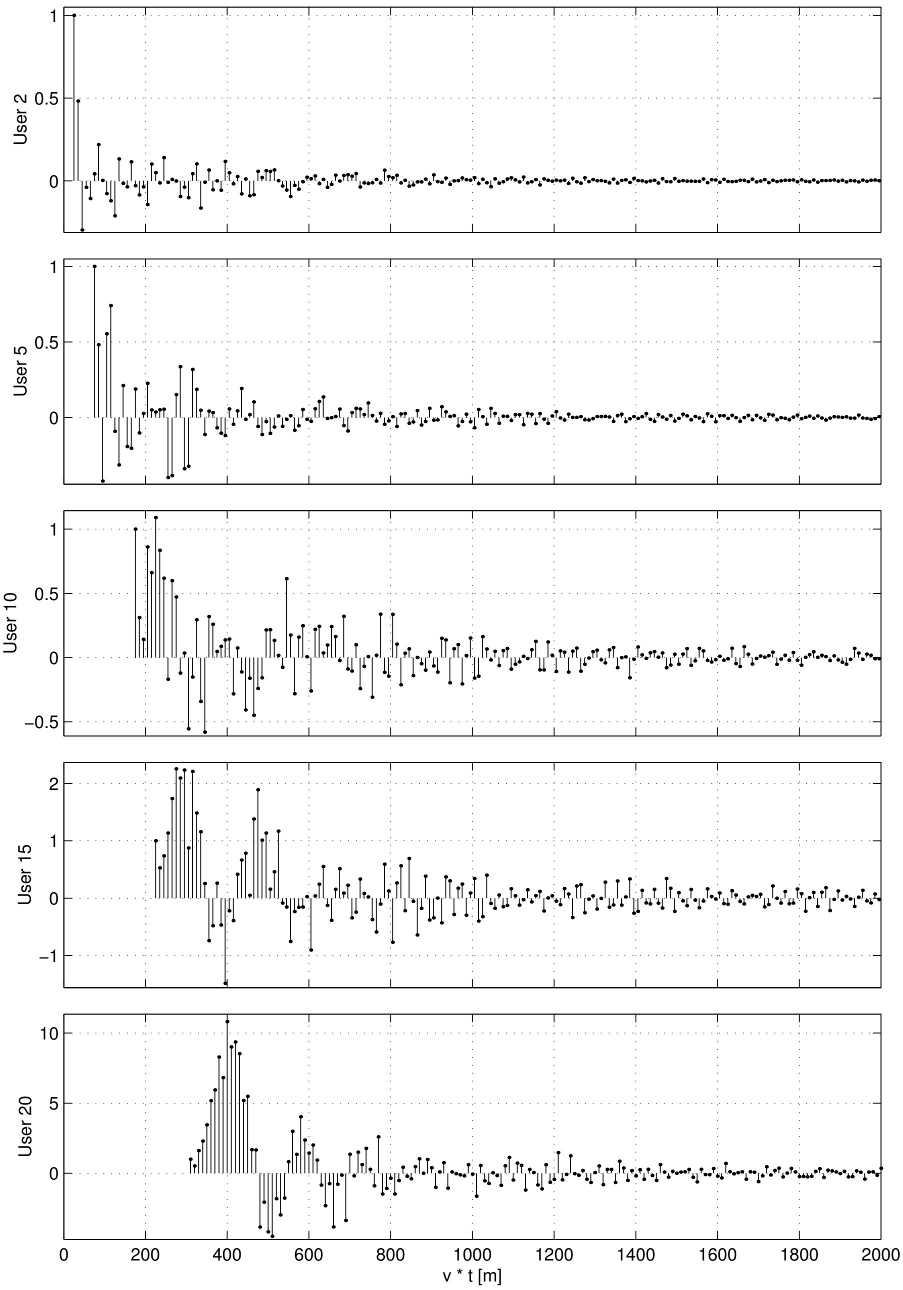

Figure 2.19: *Weights with open terminations (normalized w.r.t. the first path weight)*

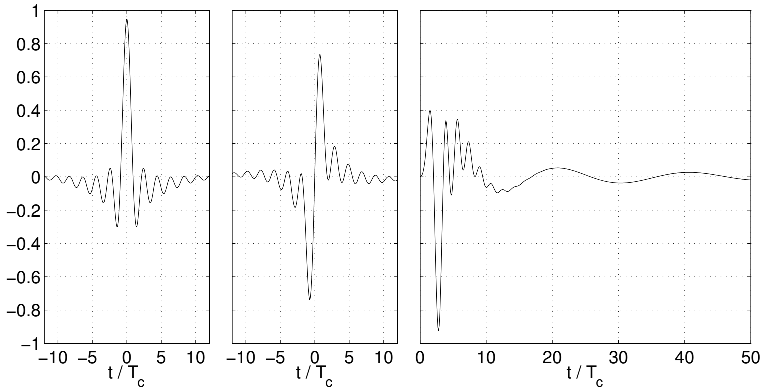

Figure 2.20: *Passband pulses : cosine modulated half-root Nyquist pulse (left, $\alpha = 0.15$), sine modulated half-root Nyquist pulse (middle, $\alpha = 0.15$) and analog filters impulse response (right)*

- The analog front end of the modems. One of their functions is to restrict the spectrum of the transmitted signals to the frequency band authorized for the high-speed PLC application, i.e. 1 MHz to 10 MHz. It is equivalent to consider the transmission of a passband pulse. Figure 2.20 gives three types of passband pulses (with $0.5/T_c =$ 10 MHz).

Figure 2.21 illustrates the combination of the path weights (vertical segments) with a baseband half-root Nyquist pulse, for users 2 and 20. The delay difference between two successive paths is here approximately 50 ns (for 10 meter difference and a phase velocity close to 2.10^8 m/s), which corresponds to the baseband pulse period : $T_c = 50$ ns. For the network topology chosen here, the successive paths are then only just resolvable. The bold curves include the additional effect of cable losses. The number of significant paths is then decreased as longer paths are more affected by the cable attenuation.
Figure 2.22 gives the final impulse responses $h_k(t)$ for users 2, 5, 10, 15 and 20, with a passband pulse. The thin curves include a cosine-modulated half-root Nyquist pulse while the bold curves include analog bandpass filters (elliptic filters). The passband pulses are illustrated in Figure 2.20.

Finally, the amplitude of the end-to-end channel frequency responses $|H_k(\omega)|^2$ (in dB) is given in Figure 2.23, in the frequency range of 0 to 25 MHz :

- The upper figure displays the 20 channel responses obtained with

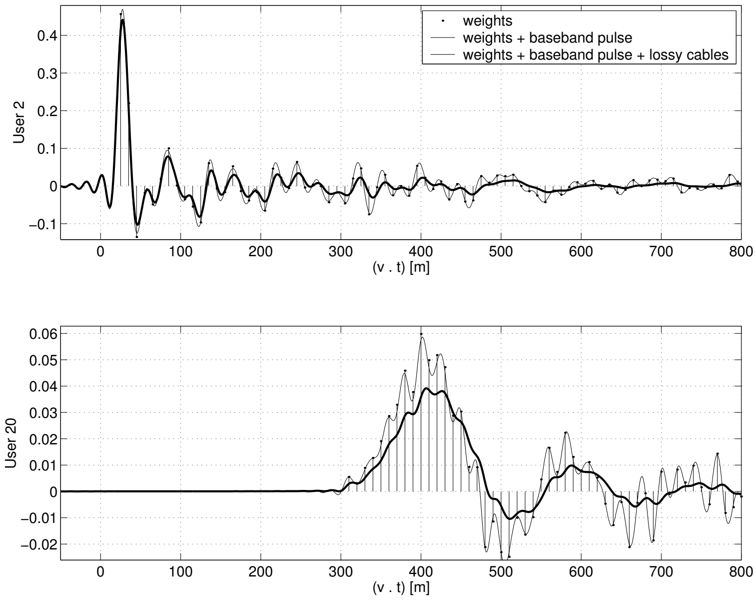

Figure 2.21: *Combination of path weights and a baseband pulse*

all-matched terminations, using the multipath model proposed in (2.116). Only the differential propagation mode is represented. The vertical ordering of the curves is in accordance with the channel index k : the higher curve corresponds to $H_1(\omega)$, the lower one corresponds to $H_{20}(\omega)$. Bold curves are used to highlight channels 2, 5, 10, 15 and 20. For these channels, the exact channel responses, as obtained by the scattering matrix formalism, are also given (dashed lines). Obviously, the multipath approximation is extremely accurate.

- The lower figure displays the 5 channel responses obtained when the unused terminations are left open. The scattering matrix formalism was used to derive exact channel responses. Here, the 3 modes of propagation (differential, phantom and common) are represented and can be compared.

2.9 Conclusion

It has been demonstrated that the channel transfer functions corresponding to practical outdoor PLC networks could be modeled analytically with the

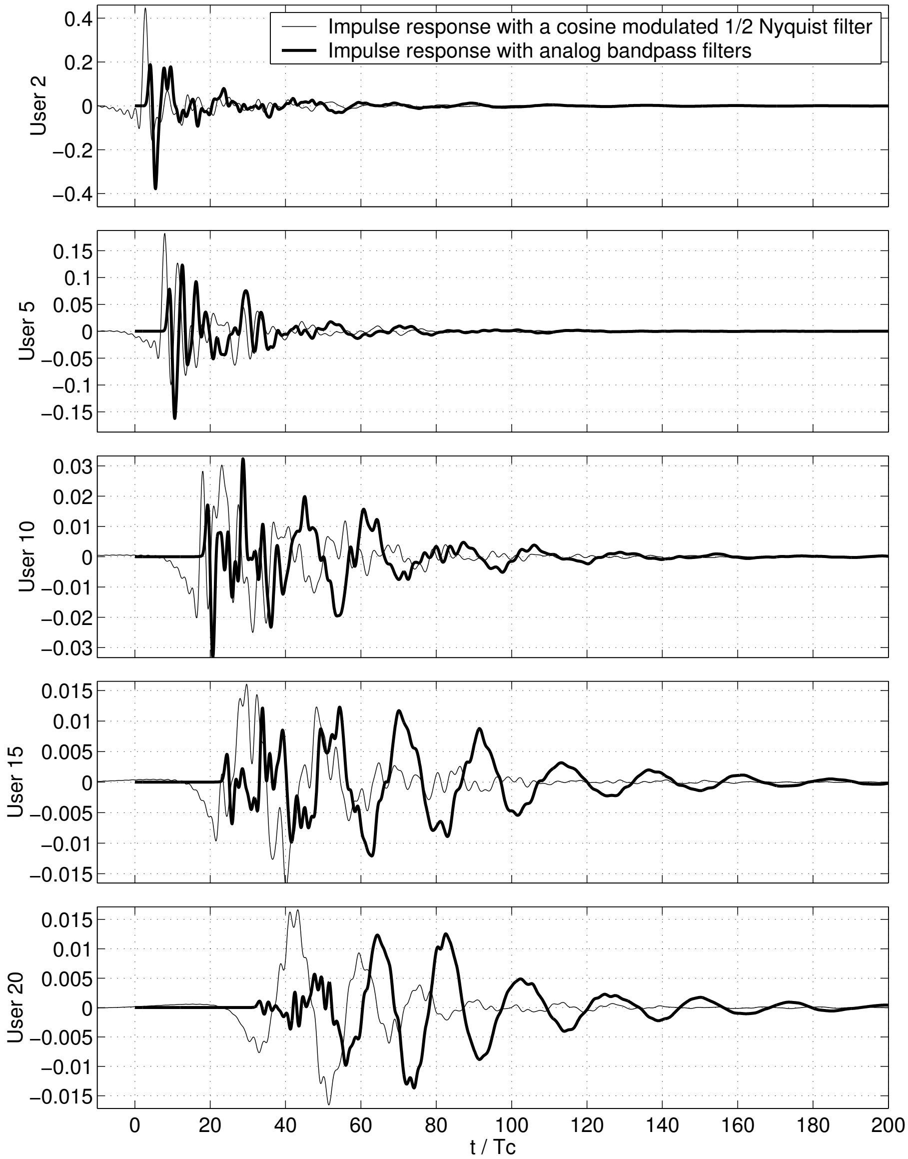

Figure 2.22: *Final impulse responses with open terminations (differential mode)*

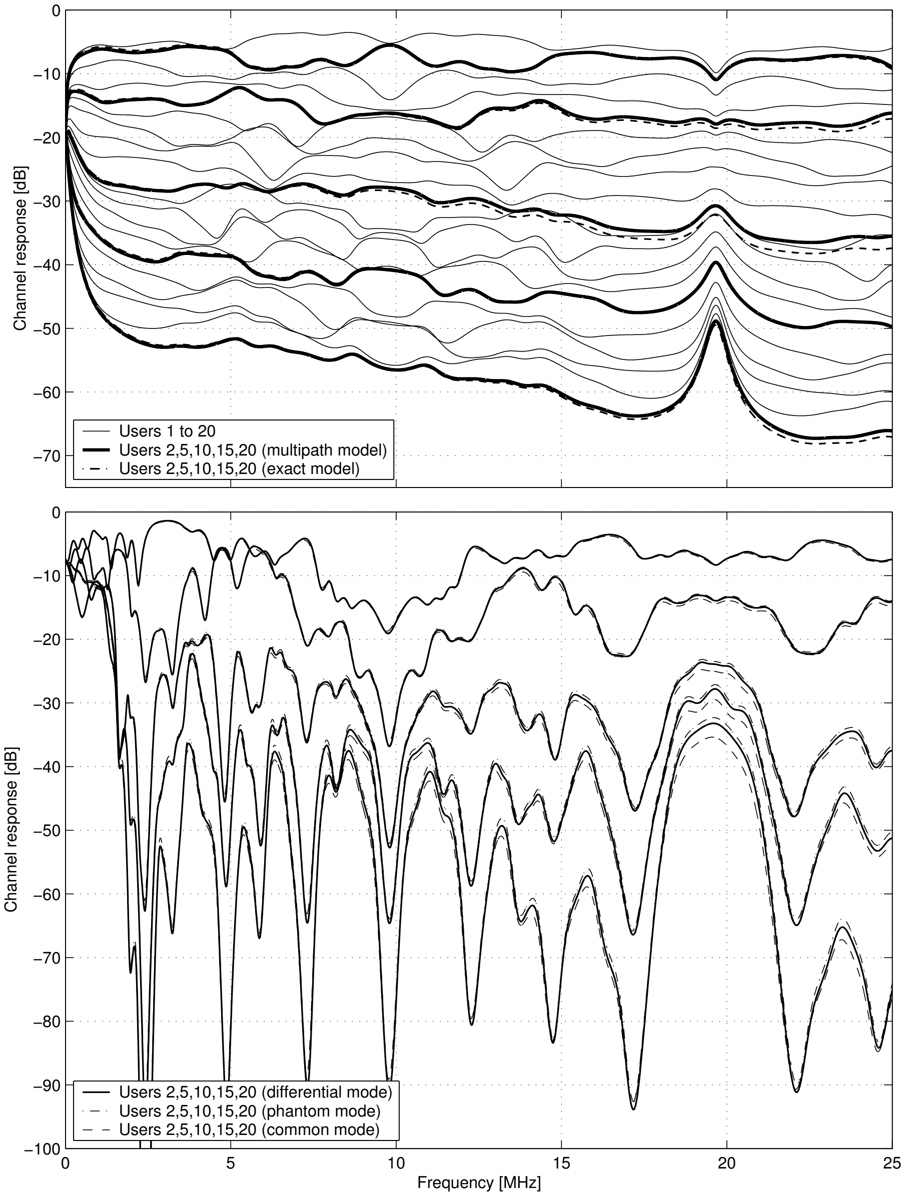

Figure 2.23: *Frequency responses with matched terminations (up) and open terminations (down)*

help of the multiconductor transmission line theory. The complete analysis combines two steps : the analysis of the multiconductor cables, and the analysis of the full network topology.

In the first step, the fundamental characteristics of the different types of multiconductor cables are derived. This analysis requires the resolution of an eigenvalue problem for each cable type, which leads to the definition of propagation eigenmodes, i.e. specific distributions of voltages and currents in the different conductors, that propagate with a unique propagation factor (including phase velocity and specific attenuation), and that are characterized by a well-defined characteristic impedance. Practical PLC cables have been analyzed, and the propagation eigenmodes (differential mode, common mode, phantom mode) have been derived as a function of the cable geometry and the used materials (conductors and dielectrics). A characteristic impedance of a few ohms (common mode) up to a few tens of ohms (differential mode) was found. The conductor losses (skin effect) were shown to be dependent on the propagation mode, due to the proximity effect. However, the difference was found to be rather small from one mode to another. The fundamental impulse response corresponding to the propagation over a given cable segment of a given length was analyzed in details. Three specific contributions were put forward : a propagation delay, an impulse due to conductor losses, and an impulse due to dielectric losses.

The second step combines the various cable segments (characterized by a given length and a given set of propagation modes with their own parameters) with the network discontinuities: derivations (cable interconnections) and terminations. Progressive and regressive multi-dimensional waves (one wave for each eigenmode) propagate along each cable segment. Multi-dimensional transmission and reflection happen on each network transition. This can be modeled accurately with the help of multi-dimensional scattering matrices.

The end-to-end channel transfer functions in the range of 1 to 50 MHz were derived for a practical PLC network including a main cable of 300 m, 20 derivations, and three types of 4-conductor cables. The channel responses associated with each eigenmode were found to be very close to each other. In the selected example, the 4 different propagations modes are well separated, which corresponds to 4 parallel and independent channels. In a more complex scenario, however, the different eigenmodes could be combined, depending on the cable interconnections and the diversity of the cables used in the network.

The channel losses were found to increase dramatically with the position of the user along the main cable. The fundamental reason for this is not the increased distance with respect to the cable headend, but rather the high number of derivations along the main cable, with important power losses at each derivation. The respective impacts of open and matched terminations were also compared.

Finally, the end-to-end channel impulse responses were derived. They were found to be a combination of a multipath channel (with a distribution of weights and distances that depends on the network topology and cable impedances) and the impulse responses resulting from conductor and dielectric losses. Between 50 and 100 significant paths were found for the selected example.

The PLC channel frequency responses derived in this Chapter will be used in Chapter 3 to obtain the capacity region of the powerline channel.

Chapter 3

Balanced capacity of wireline multiuser channels

3.1 Introduction

The wireline multiaccess channel is an example of multiuser channel with Inter-Symbol Interference (ISI). It provides simultaneous duplex connections between the cable head-end (access point to external services) and a number of subscribers spatially distributed along the common physical cable. Some practical applications are the outdoor powerline channel and the CATV network. Functionally, it can be modeled as a multiple access channel for the uplink and a broadcast channel for the downlink, and each user channel can be modeled as a linear time-invariant frequency-selective channel with Gaussian noise.

Some simple criteria are needed to characterize the performance of the multiaccess channel. The maximum error-free transmission rate for a given power budget is a commonly adopted criterion, although the minimum required power for a given target rate could also be investigated (see [38]). The list of single user Shannon capacities vs. the position of the remote modem along the cable gives thus a first idea of the channel potential. As pointed out in Chapter 2, the network topology (number of cable derivations before and after the modem under consideration) plays a major role in the determination of the multipath channel characteristics : the capacity profile does not only depend on the physical distance w.r.t. the cable head-end.

Single user capacities are sufficient to characterize the multiaccess channel when time domain multiplexing (TDM) is used in the downlink and time domain multiple access (TDMA) or random access methods are used in the uplink. If more elaborate multiuser signaling techniques are used (involving parallel transmission of the different user signals), the full characterization of the multiacces channel requires the determination of the capacity region. Each point of the capacity region is associated with a given power allocation, and successive decoding (with a specific decoding order) is generally necessary to obtain the corresponding data rates. The boundary of the capacity region can be traced out by maximizing a weighted sum of the individual data rates with variable priority coefficients α_k.

All points of the capacity region, however, are not desirable working points. For instance, many papers focus on the maximum sum-rate, but this solution does generally not guarantee a fair (or even a minimum) data rate to each subscriber. On the opposite, the common rate strategy (meaning that all users transmit or receive at the same rate) is not necessarily a good idea, especially when the attenuation levels associated with the various channels in competition are very different. As a trade-off, the idea of balanced capacity is introduced, and the set of maximum balanced user rates is proposed to characterize the performance of the multiaccess channel.

The **balanced capacity** of a multiuser system is defined as the distribution of maximum simultaneously achievable bit rates that are in proportion with the single-user rates. It is a specific point of the boundary of the capacity region for which the coexistence with the other users has the same relative cost for every user.

The computation of maximum balanced rates basically involves the computation of the right priority coefficients α_k associated with these balanced rates.

The objective of this chapter is to propose practical algorithms for the computation of the uplink/downlink balanced capacity of a multiaccess network with K users, where K may be much larger than two. Different types of power constraints are investigated, which will lead to distinct capacity regions. The problem of optimal duplexing is not considered here : the multiuser channel is supposed to be operated in uplink OR downlink at a given time.

The capacity of multiuser networks has been extensively studied in the past few years, but the issue of a fair rate distribution was generally ignored. In [39], a general expression for the capacity regions of multiaccess channels with memory was obtained. In [40], this result was used to derive the capacity region of a two-user Gaussian multiple access channel with ISI and the well-known single user water-filling algorithm (that provides the optimal power allocations) was extended to the two-user case. The authors of [41] extended these results to channels with an arbitrary number of users in the context of multiaccess fading channels. All these papers assume individual power constraints at the transmitters : the K user channels need to be scaled (concept of *equivalent channel*), so that the multiuser water-filling algorithm provides K power allocations that satisfy the K power constraints simultaneously. The K scaling coefficients have to be computed iteratively. A general algorithm is proposed in [41], while the authors of [42] and [43] propose practical algorithms well suited to specific situations (two-user channel and/or maximum sum rate solution). An alternative method for the computation of the maximum sum rate solution was proposed by [44] and basically involves the iterative application of the single user water-filling algorithm. A detailed analysis of this method is proposed in [45]. [46] addresses the problem of computing the FDMA capacity region (which is useful when successive decoding is undesired at the receiver) and proposes suboptimal algorithms for the two-user case in the context of optimal duplex in DSL. In the general case, the optimal user rates can be achieved through the use of multicarrier multiple access [47] [48] with appropriate coding on each carrier.

The multiuser water-filling process is highly simplified when the individual power constraint is relaxed and a single constraint is put on the transmission power sum. In that case, the uplink capacity region is known to be the same as the downlink one [49]-[50]. The capacity of Gaussian broadcast channels is analyzed in [51] and [52]. The issue of a fair rate allocation in the uplink was addressed in [53] with the same constraint relaxation.

This chapter is organized as follows. In Section 3.2, the wireline multiaccess channel model is revisited. Section 3.3 describes the notion of capacity region and introduces the concept of balanced capacity. In Section 3.4, the optimal power allocation associated with a given set of relative priorities α_k is analyzed in detail, for the K-user Gaussian memoryless broadcast and multiple access channels, respectively. A simple allocation algorithm is given, as well as explicit expressions for the optimal allocated powers and the associated user rates. An iterative method is derived to obtain balanced user rates. The problem of optimal spectrum allocation in multiuser frequency-selective channels is then addressed in Section 3.5. Different types of power constraints are introduced, and the spectrum allocation problem is analyzed in three specific situations. Practical algorithms for the computation of balanced user rates are finally proposed. Section 3.6 addresses the issue of FDMA balanced capacity. Finally, Section 3.7 presents detailed results obtained with a 20 user wireline access network.

3.2 Wireline multiaccess channels

The general multiaccess channel considered in this chapter (see Figure 2.11) is composed of a main cable (the *distribution cable*) and $\bar{K}$ derivations (the *connection cables*) whose terminations are connected to the $\bar{K}$ user modems. The end of the distribution cable is connected to the cable head-end which is supposed to provide a common access to the broadband services. Any subset of $K \leq \bar{K}$ user modems are about to establish a duplex connection with the cable head-end at a given time. Unlike the DSL access networks (where each user has its own twisted pair), the physical medium has to be shared by all the users who wish to establish a connection simultaneously.

The *uplink* (data transmission from the user modems to the cable head-end) corresponds to a *multiple access channel* (MA), while the *downlink* (data transmission from the cable head-end to the user modems) corresponds to a *broadcast channel* (BC). The schemes of these two types of multiuser channels are given in Figure 3.1. The additive noises at all receivers (n and $\{n_1, \cdots, n_K\}$) are supposed to be Gaussian and white, with a double-sided power spectral density $N_0/2$.

In a practical wireline communications system, constraints are put on the *bandwidth*, on the *powers*, and on the *power spectral densities* (PSD) of the transmitted signals. We assume in the sequel a transmission bandwidth $[0, B]$. The power constraint $\bar{P}$, and the PSD constraint $\bar{\gamma}$ will be analyzed separately. While in the downlink, the power constraint actually refers to the sum of all the user signals (located in the unique downlink transmitter), in the uplink, individual power constraints are generally associated with each transmitter. In the sequel, the individual power constraint is relaxed and a single power-sum constraint is considered both for the downlink and the uplink. The obtained results are then extended to the (more complex) individual power constraint scenario in the uplink.

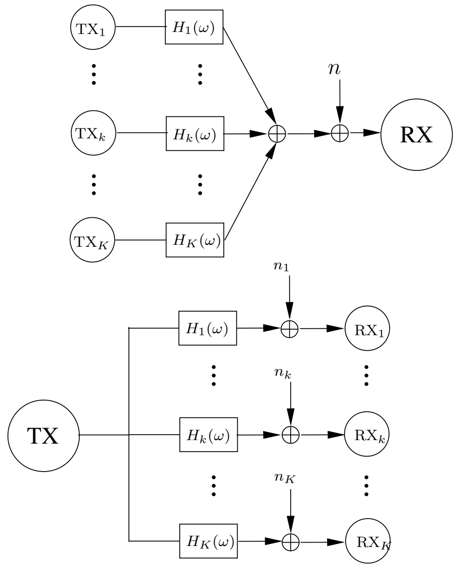

Figure 3.1: *Multiple access and broadcast channels*

3.3 Multiuser capacity region and balanced capacity

A multiuser capacity region is defined as the set of achievable rates $\{R_k\}$ at which the receiver(s) may decode information from the transmitter(s) without error for a given set of (power) constraints. For the Gaussian K-user channel, it is a convex region in the K-dimensional space. This region reflects the trade-off among the individual data rates of the different users competing for the limited resources. The boundary of the capacity region can be traced out by means of a set of relative priority coefficients α_k with $\sum_k \alpha_k = 1$. Each boundary point of the capacity region maximizes the linear combination of the user rates $R_\alpha = \sum_k \alpha_k R_k$.

Let $\mathbf{R}^* = [R_1^*, \cdots, R_k^*]^T$ be the vector of maximum user rates associated with a given vector of relative priorities $\boldsymbol{\alpha} = [\alpha_1, \cdots, \alpha_k]^T$. Actually, the coefficients α_k do not bring any information about the distribution of the maximum user rates R_k^*. Even with a higher relative priority $\alpha_k > 1/K$, a given user k with a poor channel quality could obtain a lower data rate R_k^* that the other users, or even a zero data rate. The only interpretation that can be associated with the relative priorities α_k is that $\mathbf{dR}^* \perp \boldsymbol{\alpha}$, which means that the boundary of the capacity region is normal to the vector $\boldsymbol{\alpha}$ in the neighbourhood of the point $\mathbf{R}^*$. In a two-user case, for example, the maximum rate distribution (R_1^*, R_2^*) associated with equal priorities $\alpha_1 = \alpha_2 = 1/2$ would have a local tangent with a slope of -45 degrees. The maximum rate distribution (R_1^*, R_2^*) associated with unequal priorities $\alpha_1 = 1/3$ and $\alpha_2 = 2/3$ would have a local tangent with a slope of $\arctan(-1/2) = -26.6$ degrees.

To obtain a practical characterization of the access network capacity, it is useful to put forward some specific points of the boundary :

- The *single user rates* R_k^1 are the maximum achievable rates in the single user communication scenario. They correspond to having only one alpha different from 0.

- The *maximum sum rate* corresponds to the setting $\alpha_k = 1/K$. It generally results in unfair situations where the users with the best channels have a much higher rate than the others, which is not desirable in practical applications. It may even happen that some subscribers do not have any bit rate at all.

- The *maximum common rate* [53] is such that $R_1 = \cdots = R_K$. When the single user rates are very different, the common rate constraint is generally a waste of resources as it forces the users with the best channels to lower their rate dramatically to reach the level of the weakest channels.

- The **maximum balanced rate** is such that $\frac{R_1}{R_1^1} = \cdots = \frac{R_K}{R_K^1}$. In other words, all users transmit at a rate R_k which is in the same proportion w.r.t. the potential rate R_k^1 offered by their own channel. The relative cost implied by the coexistence with the other users is the same for all the users.

Figure 3.2 gives an example of a convex capacity region and the corresponding boundary points for $K = 2$. A and F give the single user rates. E gives the maximum sum rate : it corresponds to the point where the tangent has a -45° slope. B gives the maximum common rate and D gives the maximum balanced rates.

As a lower bound on the balanced rates, time-domain multiplexing (TDM) or multiple access (TDMA) can be considered, with time slots of equal duration for each user. This strategy gives a set of rates $R_k = \frac{R_k^1}{K}$ (line AGF on Figure 3.2). Allowing simultaneous transmission of all the users, with

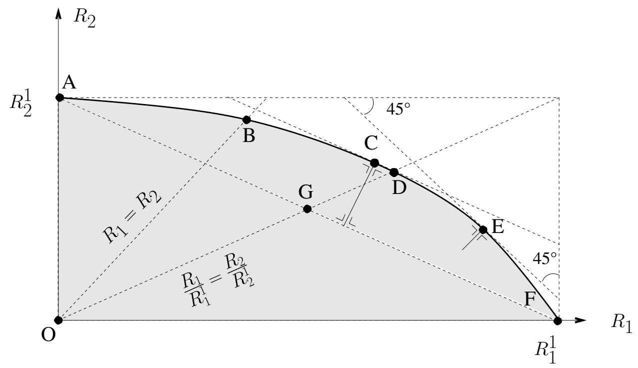

Figure 3.2: *Two-user capacity region and specific points of the boundary*

a smart power and spectrum management, offers higher balanced rates, of course. In any case, the maximum balanced rates can be written as :

$$R_k = g\,\frac{R_k^1}{K} \tag{3.1}$$

where g is the rate gain with respect to the TDM(A) strategy (OD/OG on Figure 3.2). Thanks to the convexity property of the capacity region, we know that $g \geq 1$. This gain will be referred to as the 'multiuser gain' in the sequel. The multiuser gain increases when the user channel frequency responses are very different. An equivalent concept in the context of multiuser fading channels is the concept of multiuser diversity (see [54] for example).

The aim of this chapter is to propose practical algorithms allowing the **computation of the maximum balanced rates for an arbitrary number of users**, and the corresponding (downlink and uplink) power allocations.

The derivation of these algorithms basically involves three steps :

- The computation of the maximum aggregate rate R_α for a fixed power allocation and a fixed sequence of priority coefficients $\{\alpha_k\}$.
- The computation of the optimal power allocation (i. e. maximizing R_α) for a fixed set of priority coefficients $\{\alpha_k\}$.
- The computation of the appropriate sequence $\{\alpha_k\}$ providing balanced user rates.

These three steps will firstly be analyzed in detail for the case of a multiuser memoryless channel (Section 3.4). Extensions will then be provided for a multiuser frequency selective channel with various kinds of power constraints (Section 3.5).

3.4 Memoryless channel

In the memoryless scenario, the channels are fully defined by the set of attenuation factors $\{h_k^2\}$ and the AWGN variance $\sigma^2 = N_0 B$. A total power $\bar{P}$ should be allocated among the different users. The maximum balanced rates $\{R_k^*\}$ are here associated with a specific power allocation $\{P_k\}$, and a specific decoding order.

3.4.1 Maximum aggregate rate for a given power allocation

This section provides explicit expressions for the MA and BC maximum aggregate rates R_α associated with a fixed power allocation $\{P_k\}$ and a fixed set $\{\alpha_k\}$. This allows to formulate the power allocation problem as a constrained optimization problem.

3.4.1.1 MA channel

The capacity region for the MA channel (uplink) is known to be [41] :

$$\left\{ \{R_k\} : \sum_{k \in \mathcal{S}} R_k \leq \mathcal{C}\left(\frac{\sum_{k \in \mathcal{S}} P_k h_k^2}{\sigma^2}\right) \ \forall \mathcal{S} \subset \{1, \cdots, K\} \right\} \tag{3.2}$$

where $\mathcal{C}(x) \triangleq B \log(1+x)$.[1] This region is defined by $2^K - 1$ constraints, each one corresponding to a nonempty subset $\mathcal{S}$ of users. It has $K!$ vertices in the positive quadrant. Each vertex is achievable by a successive decoding using one of the $K!$ possible orderings of the users. In the special case $K = 2$, the capacity region is a pentagon whose two useful vertices correspond to the decoding orders $(1,2)$ and $(2,1)$ respectively (see Figure 3.3). The 3-user capacity region is illustrated in Figure 3.4. The region is defined by 7 planes in the positive quadrant. It includes 6 useful vertices associated with the different decoding orders. Returning to the general case $K \geq 2$, and without loss of generality, we assume that *the users are ordered in ascending order of the priority coefficients* $\{\alpha_k\}$. For the choice of priority

[1] The logarithm used in the analytical derivations has a natural base, but a base of 2 is used in Section 3.6 in order to obtain numerical results expressed in Mbits/s.

coefficients $\{\alpha_k\}$, the maximum of R_α is then obtained at a single vertex that corresponds to the decoding order $\{1, \cdots, K\}$. In other words, the messages with the lower priorities are decoded first and subtracted from the received signal before decoding the messages with higher priorities. The maximum weighted rate is then given by:

$$R_{\alpha,\mathrm{MA}} = \sum_{k=1}^{K} \alpha_k \mathcal{C}\left(\frac{P_k h_k^2}{\sigma^2 + \sum_{l=k+1}^{K} P_l h_l^2}\right) \tag{3.3}$$

$$= \sum_{k=1}^{K} (\alpha_k - \alpha_{k-1}) \mathcal{C}\left(\frac{\sum_{l=k}^{K} P_l h_l^2}{\sigma^2}\right) \tag{3.4}$$

with $\alpha_0 \triangleq 0$.

3.4.1.2 BC channel

In the BC channel (downlink), the decoding strategy is different for each receiver. Here the decoding order is not dictated by the user relative priorities, but by the relative channel gains ([51]-[52]). A given receiver is able to decode the messages intended for the users with lower channel gains (and thus transmitted at a lower rate) before decoding its own message. The remaining messages are considered as noise. For a given set of transmission powers $\{P_k\}$, the capacity region has a single vertex that maximizes the weighted rate R_α for any set $\{\alpha_k\}$ [52] :

$$\left\{\{R_k\} : R_k \leq \mathcal{C}\left(\frac{P_k h_k^2}{\sigma^2 + \left(\sum_{h_k^2 < h_l^2} P_l\right) h_k^2}\right)\right\}. \tag{3.5}$$

Figure 3.3 gives the capacity region (a rectangle) for the two-user case, assuming $h_1^2 \geq h_2^2$. Let π be a permutation on the set $\{1, \cdots, K\}$ such that $h_{\pi(i)}^2 \geq h_{\pi(j)}^2$ for $i < j$. In other words, this permutation is used to sort the users in decreasing order of their channel gains. The maximum weighted rate is now:

$$R_{\alpha,\mathrm{BC}} = \sum_{k=1}^{K} \alpha_{\pi(k)} \mathcal{C}\left(\frac{P_{\pi(k)} h_{\pi(k)}^2}{\sigma^2 + \left[\sum_{l=1}^{k-1} P_{\pi(l)}\right] h_{\pi(k)}^2}\right). \tag{3.6}$$

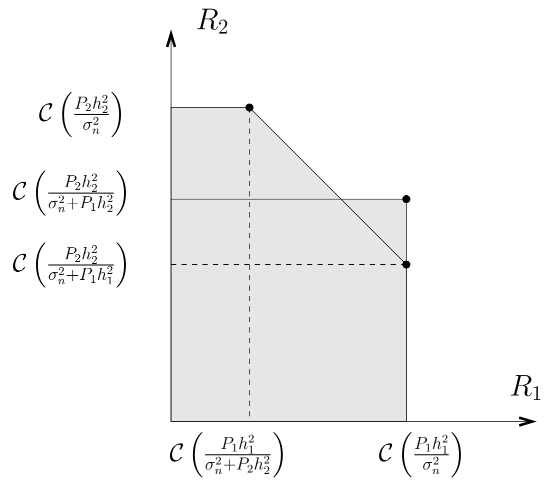

Figure 3.3: *Two-user capacity regions for a fixed power distribution : multiple access channel (pentagon) and broadcast channel (rectangle)*

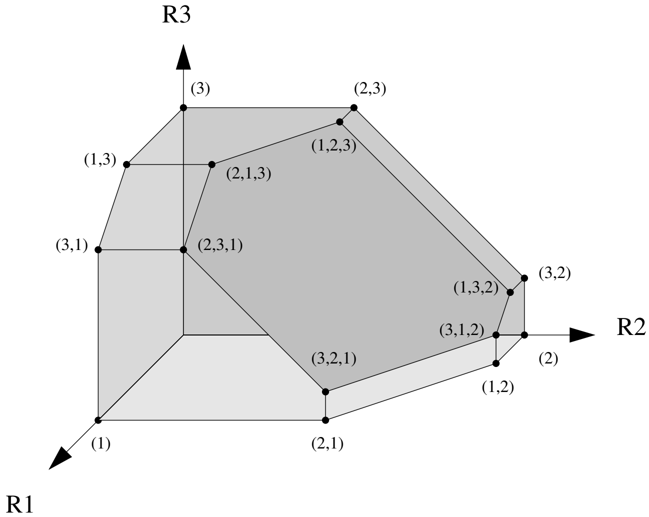

Figure 3.4: *Three-user capacity region for a fixed power distribution (multiple access channel)*

3.4.1.3 Formulation of the optimal power allocation problem

For a given constraint $\bar{P}$ on the total transmitted power, our objective is now to find the optimal power distributions $\{P_k^\circ\}$ and $\{P_k^*\}$ that maximize R_α for the MA and BC channels respectively:

$$\begin{aligned} \{P_k^\circ\} &= \arg\max \left[R_{\alpha,\mathrm{MA}}\left(\{P_k\}\right)\right] && (3.7) \\ \{P_k^*\} &= \arg\max \left[R_{\alpha,\mathrm{BC}}\left(\{P_k\}\right)\right] && (3.8) \end{aligned}$$

with constraints $\sum_k P_k \leq \bar{P}$ and $P_k \geq 0\ \forall k$. In each case, the solution satisfies the Kuhn-Tucker conditions:

$$\frac{1}{B}\frac{\partial R_\alpha}{\partial P_k}\begin{cases} = \mu & P_k > 0 \\ < \mu & P_k = 0 \end{cases} \tag{3.9}$$

where μ is a positive Lagrange multiplier.

3.4.2 Optimal power allocation for the BC memoryless channel

(Given $\{\alpha_k\}$)
The users are supposed to be sorted in decreasing order of their channel gains through the permutation π. Starting the allocation process with $P_{\pi(k)} = 0\ \forall k$, the marginal rate gain for each user is given by $\frac{1}{B}\frac{\partial R_\alpha}{\partial P_{\pi(k)}} = D_{\pi(k)}(0)$ where the functions $D_k(x)$ are defined by

$$D_k\left(x\right) \triangleq \frac{\alpha_k h_k^2/\sigma^2}{1 + x h_k^2/\sigma^2}. \tag{3.10}$$

Some power $P_{\pi(k_1)}$ is firstly allocated to the user $\pi(k_1)$ with the maximum $\alpha_{\pi(k)} h_{\pi(k)}^2$.

The users with a higher $h_{\pi(k)}^2$ but a lower $\alpha_{\pi(k)} h_{\pi(k)}^2$ can be discarded. Indeed, equation (3.6) ensures that, for $k < k_1$ (i.e. for users with a higher channel gain),

$$\begin{aligned} \frac{1}{B}\frac{\partial R_\alpha}{\partial P_{\pi(k)}} &= \frac{1}{B}\frac{\partial R_\alpha}{\partial P_{\pi(k_1)}} + \frac{1}{\sigma^2}\left(\alpha_{\pi(k)} h_{\pi(k)}^2 - \alpha_{\pi(k_1)} h_{\pi(k_1)}^2\right) \\ &< \frac{1}{B}\frac{\partial R_\alpha}{\partial P_{\pi(k_1)}}, \end{aligned} \tag{3.11}$$

if

$$P^*_{\pi(k)} = 0, \tag{3.12}$$

which is consistent with the Kuhn-Tucker conditions (3.9).

The marginal gain for the remaining users becomes $D_{\pi(k)}(P_{\pi(k_1)})$ with $k \in \{k_1, \cdots, K\}$. The power $P_{\pi(k_1)}$ is then increased until a second user $\pi(k_2)$ (with $k_2 > k_1$) reaches a marginal gain equal to that of user $\pi(k_1)$ (unless $\bar{P}$ is reached before). As $h^2_{\pi(k_2)} < h^2_{\pi(k_1)}$, this is only possible if $\alpha_{\pi(k_2)} > \alpha_{\pi(k_1)}$. When this happens, the common marginal gain can be shown to be:

$$\begin{aligned} D_{\pi(k_1)}\left(P^*_{\pi(k_1)}\right) &= D_{\pi(k_2)}\left(P^*_{\pi(k_1)}\right) \\ &= \left(\alpha_{\pi(k_2)} h^2_{\pi(k_2)}/\sigma^2\right) F_{\pi(k_1),\pi(k_2)} \end{aligned} \tag{3.13}$$

where the correction factor $F_{i,j} < 1$ is defined as

$$F_{i,j} = \frac{1 - \alpha_i/\alpha_j}{1 - h_i^{-2}/h_j^{-2}}. \tag{3.14}$$

User $\pi(k_2)$ is thus selected as the one with the largest $\left(\alpha_{\pi(k)} h^2_{\pi(k)}\right) F_{\pi(k_1),\pi(k)}$ on the set $k \in \{k_1 + 1, \cdots, K\}$. The power allocated to user $\pi(k_1)$ is then fixed to

$$P^*_{\pi(k_1)} = \sigma^2 G_{\pi(k_1),\pi(k_2)} \tag{3.15}$$

where

$$G_{i,j} \triangleq \frac{\alpha_i h_i^2 - \alpha_j h_j^2}{(\alpha_j - \alpha_i) h_i^2 h_j^2} = h_j^{-2}\left(F_{i,j}^{-1} - 1\right). \tag{3.16}$$

The users with a higher $h^2_{\pi(k)}$ but a lower $\left(\alpha_{\pi(k)} h^2_{\pi(k)}\right) F_{\pi(k_1),\pi(k)}$ can be discarded : from (3.6), it can be checked that

$$\begin{aligned} \frac{1}{B}\frac{\partial R_\alpha}{\partial P_{\pi(k)}} = \frac{1}{B}\frac{\partial R_\alpha}{\partial P_{\pi(k_2)}} + \frac{1}{\sigma^2}\Big(&\alpha_{\pi(k)} h^2_{\pi(k)} F_{\pi(k_1),\pi(k)} \\ &- \alpha_{\pi(k_2)} h^2_{\pi(k_2)} F_{\pi(k_1),\pi(k_2)}\Big) < \frac{1}{B}\frac{\partial R_\alpha}{\partial P_{\pi(k_2)}}, \end{aligned} \tag{3.17}$$

if

$$P^*_{\pi(k)} = 0 \qquad \forall k \in \{k_1 + 1, \cdots, k_2 - 1\}, \tag{3.18}$$

which is again consistent with the Kuhn-Tucker conditions (3.9).

The rate $R^*_{\pi(k_1)}$ for user $\pi(k_1)$ is given by

$$R^*_{\pi(k_1)} = B \log \left(\frac{\alpha_{\pi(k_1)} h^2_{\pi_{k_1}}}{\alpha_{\pi(k_2)} h^2_{\pi(k_2)} F_{\pi(k_1),\pi(k_2)}} \right). \tag{3.19}$$

This rate is left unaffected by the allocation of power to the other users (with $k > k_1$) as those users have a lower channel gain and their signals can be perfectly decoded and subtracted by receiver k_1. If there is still some power to allocate, then the allocation goes on with $P_{\pi(k_2)}$, which increases the rate $R_{\pi(k_2)}$ while leaving $R_{\pi(k_1)}$ unchanged, until a third user $\pi(k_3)$ (with a smaller $h^2_{\pi(k_3)}$ but a higher $\alpha_{\pi(k_3)}$) reaches the same marginal gain, and so on.

At the end of the allocation process, a subset $S_J = \{\pi(k_1), \cdots, \pi(k_J)\} \subset \{1, \cdots, K\}$ of $J \leq K$ users is obtained, who get a non-zero fraction of the total power $\bar{P}$. The users in this subset are sorted in *decreasing order of the channel gains* h^2_k and in *increasing order of the priority coefficients* α_k. As a consequence, the allocation algorithm can work indifferently on the user sequence $\{\pi(1), \cdots, \pi(K)\}$ or on the initial sequence $\{1, \cdots, K\}$. The allocation rule can be stated in very simple terms : *always add power to the user with the maximum* $D_k(P)$ where P is the power already allocated. Mathematically, we get:

$$\begin{aligned} R_\alpha &= B \sum_{i=1}^{J} \int_{P^*_{k_1}+\cdots+P^*_{k_{i-1}}}^{P^*_{k_1}+\cdots+P^*_{k_i}} D_{k_i}(x)dx \\ &= B \int_0^{\bar{P}} \max_{k\in\{1,\cdots,K\}} D_k(x)dx, \end{aligned} \tag{3.20}$$

which provides an intuitive graphical interpretation. Figure 3.5 illustrates the evolution of D_k and the individual powers as a function of the allocated power P for $K = 4$. In this example, $h^2_1 > h^2_2 > h^2_3 > h^2_4$ and $\alpha_1 < \alpha_2 < \alpha_3 < \alpha_4$. The optimal allocation gives $J = 3$ and $S_J = \{1, 2, 4\}$. For decreasing values of $\bar{P}$, the subset S_J can be reduced to $\{1, 2\}$ or $\{1\}$. Obviously, when the power to be allocated is large enough, the last user in the subset S_J is always the user with the highest priority α_k.

Once the subset S_J is known, the set of optimal powers $\left\{P^*_{k_i}\right\}$ can be

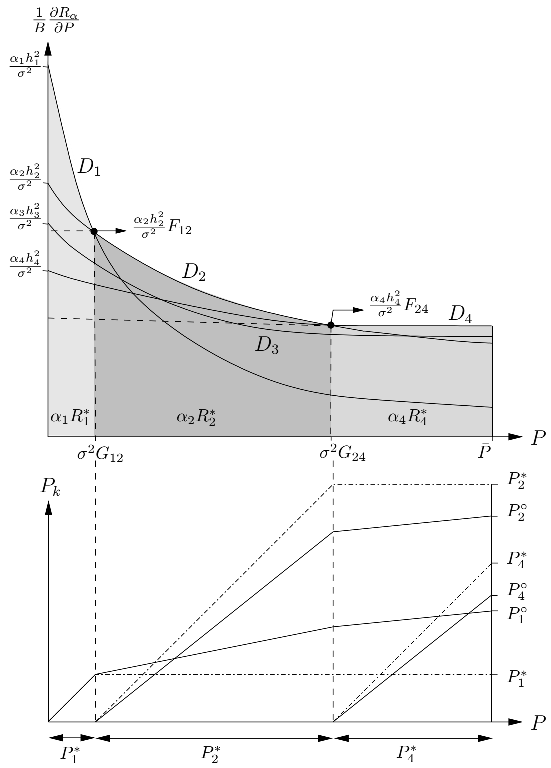

Figure 3.5: *Marginal gain and power distribution during the allocation process ($K = 4$)*

computed by solving the following system :

$$\begin{aligned} D_{k_i}\left(\sum_{l=1}^{i} P^*_{k_l}\right) &= D_{k_{i+1}}\left(\sum_{l=1}^{i} P^*_{k_l}\right), \quad i \leq J-1 \\ \sum_{i=1}^{J} P^*_{k_i} &= \bar{P} \end{aligned} \tag{3.21}$$

Finally, the complete allocation procedure and the corresponding user rates are explicitly given as follows :

Algorithm 3.1 *Algorithm for the selection of the user sequence receiving a fraction of the total power $\bar{P}$ (subset S_J) :*

- *Initialization* $(J = 1)$ *:*

$$k_1 = \arg\max_{k\in[1,K]} \left(\alpha_k h_k^2\right). \tag{3.22}$$

- *While $k_J < K$:*
  - *Compute the next candidate :*

$$k^* = \arg\max_{k\in[k_J+1,K]} \left(\alpha_k h_k^2\, F_{k_J,k}\right). \tag{3.23}$$

  - *If there is enough power :*

$$\bar{P} \geq \sigma^2\, G_{k_J,k^*} \tag{3.24}$$

    then: $J = J + 1,\ k_J = k^*$.
  - *Else: stop.*

Optimal BC allocated powers P^*_k (with $k \in S_J$) :

$$\begin{pmatrix} P^*_{k_1} \\ P^*_{k_2} \\ \cdots \\ P^*_{k_j} \\ \cdots \\ P^*_{k_{J-1}} \\ P^*_{k_J} \end{pmatrix} = \sigma^2 \begin{pmatrix} G_{k_1,k_2} \\ G_{k_2,k_3} - G_{k_1,k_2} \\ \cdots \\ G_{k_j,k_{j+1}} - G_{k_{j-1},k_j} \\ \cdots \\ G_{k_{J-1},k_J} - G_{k_{J-2},k_{J-1}} \\ -G_{k_{J-1},k_J} \end{pmatrix} + \begin{pmatrix} 0 \\ 0 \\ \cdots \\ 0 \\ \cdots \\ 0 \\ \bar{P} \end{pmatrix}. \tag{3.25}$$

Optimal user rates R_k^* (with $k \in S_J$) :

$$\begin{pmatrix} R_{k_1}^* \\ R_{k_2}^* \\ \cdots \\ R_{k_j}^* \\ \cdots \\ R_{k_{J-1}}^* \\ R_{k_J}^* \end{pmatrix} = B \log \begin{pmatrix} \frac{\alpha_{k_1} h_{k_1}^2}{\alpha_{k_2} h_{k_2}^2 F_{k_1,k_2}} \\ \frac{\alpha_{k_2} h_{k_2}^2 F_{k_1,k_2}}{\alpha_{k_3} h_{k_3}^2 F_{k_2,k_3}} \\ \cdots \\ \frac{\alpha_{k_j} h_{k_j}^2 F_{k_{j-1},k_j}}{\alpha_{k_{j+1}} h_{k_{j+1}}^2 F_{k_j,k_{j+1}}} \\ \cdots \\ \frac{\alpha_{k_{J-1}} h_{k_{J-1}}^2 F_{k_{J-2},k_{J-1}}}{\alpha_{k_J} h_{k_J}^2 F_{k_{J-1},k_J}} \\ \left[1 + \frac{\bar{P} h_{k_J}^2}{\sigma^2}\right] F_{k_{J-1},k_J} \end{pmatrix}. \tag{3.26}$$

Algorithm 3.1 ensures that the obtained powers and rates are positive.

3.4.3 Optimal power allocation for the MA memoryless channel

(Given $\{\alpha_k\}$*)*
The computation of the optimal allocation is very similar in the MA and the BC channels. These two channels are known to have the same capacity region when the constraint is put on the transmitted power sum [49]-[50]. However, the power distributions corresponding to a given boundary point of the capacity region are distinct. In this section, the expression of the optimal user rates (3.26) is derived again in the MA context, allowing the computation of an explicit expression for the optimal MA power allocation $\{P_k^\circ\}$.

The users are now sorted in increasing order of their priority coefficients α_k. For a given power allocation $\{P_k\}$, we define the sequence $\{x_k\} \leq 1$ as :

$$x_k = \left(1 + \sum_{i=k}^{K} P_i h_i^2 / \sigma^2\right)^{-1}. \tag{3.27}$$

From (3.3), the marginal rate gains can be obtained iteratively as follows :

$$\begin{aligned} \frac{1}{B}\frac{\partial R_\alpha}{\partial P_1} &= \frac{\alpha_1 h_1^2}{\sigma^2} x_1 \\ \frac{1}{B}\frac{\partial R_\alpha}{\partial P_{k+1}} &= \frac{h_{k+1}^2}{h_k^2}\left(\frac{1}{B}\frac{\partial R_\alpha}{\partial P_k}\right) + (\alpha_{k+1} - \alpha_k)\frac{h_{k+1}^2}{\sigma^2} x_{k+1}. \end{aligned} \tag{3.28}$$

The initial marginal rate gain for each user ($x_k = 1 \quad \forall k$) is again $\alpha_k h_k^2$. The power is thus firstly allocated to user k_1 with the maximum $\alpha_k h_k^2$.

The lower-indexed users (i.e. the users with a lower priority) are discarded: $P_k^\circ = 0$ for $k < k_1$. From (3.28), it follows that :

$$\begin{aligned} x_k &= x_{k_1} && (3.29) \\ \frac{\partial R_\alpha}{\partial P_k} &= \frac{\alpha_k h_k^2}{\alpha_{k_1} h_{k_1}^2} \frac{\partial R_\alpha}{\partial P_{k_1}} < \frac{\partial R_\alpha}{\partial P_{k_1}}, && (3.30) \end{aligned}$$

for $k < k_1$, which is consistent with the Kuhn-Tucker conditions (3.9).

The marginal gains for the remaining users is again $D_k\left(P_{k_1}\right)$. Power is thus allocated to user k_1 until $P_{k_1} = \sigma^2 G_{k_1,k_2}$ for a given user k_2 with

$$k_2 = \arg \max_{k \in \{k_1+1,\cdots,K\}} \left(\alpha_k h_k^2 F_{k_1,k}\right) \qquad (3.31)$$

and G_{k_1,k_2} is defined in (3.16). At that time, the power allocated to user k_1 is equal to $P_{k_1}^*$, that is to say the optimal power that would be allocated in a BC scenario (see Figure 3.5).

Now the allocation process becomes different. While in the BC channel, any power increase dP would be fully allocated to user k_2 (which increases R_{k_2} and leaves R_{k_1} unaffected), in the MA channel dP has to be shared by users k_1 and k_2. The fraction of power dP_{k_2} allocated to user k_2 directly increases the rate R_{k_2}. But this power is seen as noise by user k_1 (which is decoded *before* user k_2) : some power dP_{k_1} is then allocated to user k_1 to compensate for the noise enhancement and leave R_{k_1} unchanged. Some power is thus allocated simultaneously to users k_1 and k_2.

Users with an intermediate priority are discarded: $P_k^\circ = 0$ with $k_1 < k < k_2$. From (3.28), we obtain the system :

$$\begin{aligned} \frac{1}{B}\frac{\partial R_\alpha}{\partial P_{k_1}} &= \mu && (3.32) \\ \frac{1}{B}\frac{\partial R_\alpha}{\partial P_k} &= \frac{h_k^2}{h_{k_1}^2}\mu + (\alpha_k - \alpha_{k_1})\frac{h_k^2}{\sigma^2}x_{k_2} && (3.33) \\ \frac{1}{B}\frac{\partial R_\alpha}{\partial P_{k_2}} &= \frac{h_{k_2}^2}{h_{k_1}^2}\mu + (\alpha_{k_2} - \alpha_{k_1})\frac{h_{k_2}^2}{\sigma^2}x_{k_2} = \mu. && (3.34) \end{aligned}$$

Solving this system, we get :

$$\frac{\partial R_\alpha}{\partial P_k} = \frac{\partial R_\alpha}{\partial P_{k_1}} \Big(1 - h_k^2 \left(\alpha_k - \alpha_{k_1}\right) \Big[\left(\alpha_k h_k^2 F_{k_1,k}\right)^{-1} - \left(\alpha_{k_2} h_{k_2}^2 F_{k_1,k_2}\right)^{-1}\Big]\Big) < \frac{\partial R_\alpha}{\partial P_{k_1}}, \quad (3.35)$$

for $k_1 < k < k_2$, which is again consistent with the Kuhn-Tucker conditions (3.9).

The optimal rate $R^*_{k_1}$ for user k_1 is found to be the same as (3.19), and the common marginal gain can be shown to be :

$$\mu = D_{k_2}\left(P_{k_1} + P_{k_2}\right). \quad (3.36)$$

The two-user allocation continues until a third user $k_3 \in \{k_2 + 1, \cdots, K\}$ reaches the same marginal gain. When this happens, we have $P_{k_1} + P_{k_2} = P^*_{k_1} + P^*_{k_2}$, that is to say the total power allocated to users k_1 and k_2 is the same as the optimal power sum that would be allocated in a BC scenario (see Figure 3.5). Power is then allocated simultaneously to users (k_1, k_2, k_3), and so on.

The relation (3.20) given for the BC scenario remains valid for the MA channel. The allocation rule can be restated as : *always increase the rate of the user k_i with the maximum $D_k(P)$ while leaving the other rates unchanged*, where P is the power already allocated. This can be obtained by allocating power simultaneously to all the users in the set $\{k_1, \cdots, k_i\}$. The user subset S_J and the optimal user rates are found to be the same as in the BC channel (see algorithm 3.1 and equation (3.26)).

Once the subset S_J is known, the set of optimal powers $\left\{P^\circ_{k_i}\right\}$ can be computed from (3.28) and (3.9). The sequence x_{k_j} is first computed as

$$\begin{aligned} x_{k_1} &= \mu \left(\frac{\alpha_{k_1} h_{k_1}^2}{\sigma^2}\right)^{-1} \quad (3.37) \\ x_{k_{j+1}} &= \mu \left(\frac{\alpha_{k_{j+1}} h_{k_{j+1}}^2}{\sigma^2} F_{k_j,k_{j+1}}\right)^{-1}, \quad j \in \{1, \cdots, J-1\}. \end{aligned}$$

The optimal powers $P^\circ_{k_j}$ are then given by

$$\begin{aligned} P^\circ_{k_j} &= \sigma^2 h_{k_j}^{-2} \left(x_{k_j}^{-1} - x_{k_{j+1}}^{-1}\right), \quad j \in \{1, \cdots, J-1\} \\ P^\circ_{k_J} &= \sigma^2 h_{k_J}^{-2} \left(x_{k_J}^{-1} - 1\right) \quad (3.38) \end{aligned}$$

Using the power constraint, the marginal rate is computed as

$$\mu = \frac{\alpha_{k_J} h_{k_J}^2/\sigma^2}{1 + \bar{P} h_{k_J}^2/\sigma^2}. \tag{3.39}$$

Finally, the **optimal MA allocated powers** P_k° (with $k \in S_J$) are given explicitly as follows :

$$\begin{pmatrix} P_{k_1}^\circ \\ P_{k_2}^\circ \\ \cdots \\ P_{k_j}^\circ \\ \cdots \\ P_{k_{J-1}}^\circ \\ P_{k_J}^\circ \end{pmatrix} = \frac{1}{\alpha_{k_J}} \left(\bar{P} + \frac{\sigma^2}{h_{k_J}^2} \right) \mathbf{\Pi}\left(\alpha, \mathbf{h}\right) - \begin{bmatrix} 0 \\ 0 \\ \cdots \\ 0 \\ \cdots \\ 0 \\ \frac{\sigma^2}{h_{k_J}^2} \end{bmatrix} \tag{3.40}$$

with vector $\mathbf{\Pi}\left(\alpha, \mathbf{h}\right)$ defined as :

$$\mathbf{\Pi}\left(\alpha, \mathbf{h}\right) = \begin{bmatrix} h_{k_1}^{-2} \left(\alpha_{k_1} h_{k_1}^2 - \alpha_{k_2} h_{k_2}^2 F_{k_1,k_2} \right) \\ h_{k_2}^{-2} \left(\alpha_{k_2} h_{k_2}^2 F_{k_1,k_2} - \alpha_{k_3} h_{k_3}^2 F_{k_2,k_3} \right) \\ \cdots \\ h_{k_j}^{-2} \left(\alpha_{k_j} h_{k_j}^2 F_{k_{j-1},k_j} - \alpha_{k_{j+1}} h_{k_{j+1}}^2 F_{k_j,k_{j+1}} \right) \\ \cdots \\ h_{k_{J-1}}^{-2} \left(\alpha_{k_{J-1}} h_{k_{J-1}}^2 F_{k_{J-2},k_{J-1}} - \alpha_{k_J} h_{k_J}^2 F_{k_{J-1},k_J} \right) \\ h_{k_J}^{-2} \left(\alpha_{k_J} h_{k_J}^2 F_{k_{J-1},k_J} \right) \end{bmatrix} \tag{3.41}$$

Algorithm 3.1 also ensures that the obtained powers are positive.

3.4.4 Maximum balanced rates

The previous section explained how to compute the optimal power allocation $\{P_k\}$ for a given set of priority coefficients $\{\alpha_k\}$ and a total power $\bar{P}$.

To obtain a specific boundary point of the capacity region such that the corresponding user rates satisfy

$$\frac{R_1^*}{\beta_1} = \cdots = \frac{R_K^*}{\beta_k} = \bar{R} \tag{3.42}$$

for a predefined set of normalization coefficients $\{\beta_k\}$, the right set of priority coefficients $\{\alpha_k\}$ has to be found iteratively. Computation of the maximum balanced rates corresponds to $\beta_k = R_k^1$, but the idea is the same to get any other point of the capacity region. Equation (3.42) implies that every user gets a non-zero fraction of the power. Sorting the users in decreasing order of their channel gain h_k^2, the solution of our problem requires the computation of an appropriate set of priority coefficients $\alpha_1 < \cdots < \alpha_K$, such that algorithm 3.1 selects the whole set of users $(J = K$ and $S_K = \{1, \cdots, K\})$, and that the associated user rates in (3.26) satisfy the constraint in (3.42).

Introducing the expression of the optimal user rates (3.26) into the balanced rates constraints (3.42), we get :

$$\mathcal{A}_k = \frac{2^{\beta_k \bar{R}/B}}{\mathcal{H}_k} \tag{3.43}$$

with

$$\boldsymbol{\mathcal{H}} = \begin{pmatrix} \frac{h_2^{-2} - h_1^{-2}}{h_1^{-2}} \\ \frac{h_3^{-2} - h_2^{-2}}{h_2^{-2} - h_1^{-2}} \\ \vdots \\ \frac{h_{k+1}^{-2} - h_k^{-2}}{h_k^{-2} - h_{k-1}^{-2}} \\ \vdots \\ \frac{h_K^{-2} - h_{K-1}^{-2}}{h_{K-1}^{-2} - h_{K-2}^{-2}} \\ \frac{1 + \frac{\bar{P} h_K^{-2}}{\sigma^{-2}}}{1 - \frac{h_{K-1}^{-2}}{h_K^{-2}}} \end{pmatrix} \qquad \boldsymbol{\mathcal{A}} = \begin{pmatrix} \frac{\alpha_1}{\alpha_2 - \alpha_1} \\ \frac{\alpha_2 - \alpha_1}{\alpha_3 - \alpha_2} \\ \vdots \\ \frac{\alpha_k - \alpha_{k-1}}{\alpha_{k+1} - \alpha_k} \\ \vdots \\ \frac{\alpha_{K-1} - \alpha_{K-2}}{\alpha_K - \alpha_{K-1}} \\ \frac{\alpha_K - \alpha_{K-1}}{\alpha_K} \end{pmatrix} \tag{3.44}$$

The components of the vector $\boldsymbol{\mathcal{A}}$ have to satisfy the relation :

$$\sum_{j=1}^{K} \left(\prod_{i=j}^{K} \mathcal{A}_i \right) = 1. \tag{3.45}$$

There is a single target rate $\bar{R}$ producing a set of $\mathcal{A}_k$ that fulfills equation (3.45). The right value can be found by a simple binary search. The drawback of this simple algorithm is that it can not be extended to the case of multiuser frequency-selective channels.

Actually, the problem of maximum balanced rates computation can be modeled as a nonlinear system with K unknowns α_k as follows :

$$\mathbf{F}(\boldsymbol{\alpha}) = \begin{pmatrix} \frac{R_2^*}{\beta_2} - \frac{R_1^*}{\beta_1} \\ \vdots \\ \frac{R_K^*}{\beta_K} - \frac{R_1^*}{\beta_1} \\ \sum_k \alpha_k - 1 \end{pmatrix} = \begin{pmatrix} 0 \\ 0 \\ \vdots \\ 0 \end{pmatrix}. \tag{3.46}$$

A Newton-Raphson iterative search is proposed to find the solution:

Algorithm 3.2 *Maximum balanced rates for a Gaussian memoryless multiuser channel*

- *Start with* $\boldsymbol{\alpha}^{(0)} = [1/R_1^1, \cdots, 1/R_K^1]^T / \sum_k (1/R_k^1)$*, set* $i = 0$*.*
- *Compute the optimal power allocation with algorithm 3.1. Compute the corresponding user rates* $\{R_k^*\}$ *and the normalized rates* $\{R_k^*/\beta_k\}$*.*
- *Compute the average normalized rate* μ_{R_β} *and the standard deviation* σ_{R_β}*, defined by :*

$$\mu_{R_\beta} \triangleq \frac{1}{K} \sum_k (R_k^*/\beta_k) \tag{3.47}$$

$$\sigma_{R_\beta} \triangleq \sqrt{\frac{1}{K} \sum_k \left(R_k^*/\beta_k - \mu_{R_\beta}\right)^2} \tag{3.48}$$

- *While* $\sigma_{R_\beta}/\mu_{R_\beta} > \varepsilon$ *:*
  - *Update the set of priority coefficients as follows:*

$$\boldsymbol{\Delta}_\alpha^{(i)} = -\left(\frac{\partial \mathbf{F}}{\partial \boldsymbol{\alpha}}\right)^{-1}_{\boldsymbol{\alpha}=\boldsymbol{\alpha}^{(i)}} \mathbf{F}\left(\boldsymbol{\alpha}^{(i)}\right) \tag{3.49}$$

$$\boldsymbol{\alpha}^{(i+1)} = \boldsymbol{\alpha}^{(i)} + \lambda_i \, \boldsymbol{\Delta}_\alpha^{(i)}. \tag{3.50}$$

  - *Update* $\{R_k^*\}$*,* $\{R_k^*/\beta_k\}$*,* μ_{R_β} *and* σ_{R_β}*, set* $i = i + 1$*.*

where ε *is a tolerance parameter and the sequence* $\lambda_i \leq 1$ *is used to ensure convergence in the first few iterations.*

The computation of the update direction $\mathbf{\Delta}_\alpha^{(i)}$ requires the knowledge of the Jacobian matrix $\frac{1}{B}\frac{\partial \mathbf{R}}{\partial \boldsymbol{\alpha}}$. From (3.26), it is a symmetric tridiagonal matrix $\mathbf{T}(\boldsymbol{\alpha})$ with the following entries on the three main diagonals :

$$
\begin{aligned}
\mathbf{T}_{k_j,k_j} &= \frac{\alpha_{k_{j+1}} - \alpha_{k_{j-1}}}{(\alpha_{k_j} - \alpha_{k_{j-1}})(\alpha_{k_{j+1}} - \alpha_{k_j})} \\
\mathbf{T}_{k_j,k_{j+1}} &= \frac{-1}{\alpha_{k_{j+1}} - \alpha_{k_j}} = \mathbf{T}_{k_{j+1},k_j}
\end{aligned}
\tag{3.51}
$$

where $\alpha_{k_0} = \alpha_{k_{J+1}} \triangleq 0$. In particular, the Jacobian matrix is zero on the rows and columns corresponding to users who are not in the subset S_J. As this matrix should be invertible to allow the computation of the update direction, it is important to choose a convenient starting vector $\boldsymbol{\alpha}^{(0)}$, and to control the size of the updating step λ_i in order to keep $\boldsymbol{\alpha}^{(i+1)}$ close to the solution and keep the matrix inversion possible. The convexity property of the capacity region guarantees that every user is included in the allocation subset for the proposed $\boldsymbol{\alpha}^{(0)}$. Figure 3.2 illustrates the initial rates obtained with $\boldsymbol{\alpha}^{(0)}$ (point C) in a two-user problem. After some iterations, the solution converges to the maximum balanced rates (point D).

To conclude this section, it should be noted that the solution proposed here is probably not the most efficient one in the case of a multiuser memoryless channel : however, it can be easily extended to the case of a multiuser frequency selective channel, which is the purpose of the next section.

3.5 Frequency-selective channel

In the case of frequency-selective channels with frequency responses $H_k(\omega)$, the power allocation problem can be discretized by dividing the frequency spectrum into a large number N of frequency bins of width df. As N increases to infinity, a piece-wise constant channel model converges to the actual channels. Each frequency bin $n \in [1, N]$ corresponds to a multiuser memoryless Gaussian channel with channel gains $h_{kn}^2 \triangleq |H_k(\omega_n)|^2$ and a bandwidth B/N. The problem is now to find the K optimal power spectra P_{kn} corresponding to a given boundary point of the capacity region. The user rates R_k are computed by summing the partial rates R_{kn} corresponding to the N parallel subchannels.

3.5.1 Types of constraints

Talking about the capacity region of a multiuser channel may be confusing as this region actually depends on the nature of the power constraints. Various types of constraints can be considered, leading to distinct capacity regions. The next items should be taken in consideration in the definition of the capacity region :

- The constraints can be put on the transmitted powers or on the received powers. The latter scenario won't be investigated here.

- Considering a given user k, there can be one constraint on the total transmitted power $\sum_n (P_{kn})$ or N constraints on the power in each frequency bin P_{kn}. In a wired system, it is usual to impose a transmission mask on the power spectral density (PSD). This makes sense, for example, to solve the problem of electromagnetic compatibility with existing narrowband services (egress problem). Both constraints are also commonly combined : in that case, a total power $\bar{P}$ has to be distributed on the frequency axis, and the power in each frequency bin can not go beyond a given limit $\bar{\gamma}$ with $\bar{\gamma}\, df > \bar{P}/N$. The two types of constraints (power constraint and PSD constraint) will be analyzed separately in the sequel.

- In a multiuser setup, the constraint can be put on the power-sum or on the individual powers. In the uplink, the K different transmitters can be constrained separately or considered as a single 'distributed' entity, with a single constraint on the power-sum or PSD-sum. This makes sense again when the egress problem is considered, as an external receiver gets interference from the K transmitters simultaneously. For example, in a time-division duplex scheme, the signals are produced alternately by the single head-end (during the downstream time slots) and by the K user modems (during the upstream time slots). In the downlink, the sum of the signals intended to the different receivers will be considered as a unique power-constrained signal.

- An FDMA restriction is sometimes required to simplify the design of the communication system and avoid the use of successive decoding. In that case, each frequency bin n is exclusively allocated to a single user. The corresponding capacity region is then reduced as an additional constraint is added to the problem.

- A TDMA solution can also be investigated. This means that single user communications are established for each user in turn. The corresponding capacity region is a hyperplane defined by the K single user rates vectors. The TDMA solution provides a lower bound for the capacity region corresponding to the simultaneous transmission of signals by the different users.

- Even in the case of simultaneous transmission, timesharing can be used between different power allocations to reach specific points of the capacity region. These solutions can provide useful indications on the properties of the capacity region, but solutions corresponding to a fixed power distribution across the users will always be considered in the sequel.

- Finally, the upstream capacity region (MA channel) is not always the same as the downstream capacity region (BC channel). Both are identical in the following situations :

  - When the same power (or PSD) constraint is put on the LT transmitter (on one hand) and on the K NT transmitters considered as a single signal source (on the other hand). This was shown in section 3.4.
  - In the TDMA and FDMA scenarios, as the MA and BC channels are then reduced to K parallel single user channels.

Let us illustrate these considerations on a qualitative example with $K = 2$. Figure 3.6 gives the boundaries of various capacity regions. All these regions are valid for both the MA and BC channels, except when the opposite is explicitly mentioned.

PSD-constrained capacity regions :
Points A and B give the single user rates for a flat PSD : $\left(P_{1n} = 0, P_{2n} = \frac{\bar{P}}{N}\right)$ and $\left(P_{1n} = \frac{\bar{P}}{N}, P_{2n} = 0\right)$, respectively. The line ACB bounds the flat-PSD TDMA capacity region : every point on this line can be obtained by timesharing between the single-user solutions. The line OCE is the locus of balanced rates solutions. Pentagon AFGB bounds the MA capacity region for a flat PSD assigned to both users simultaneously : $\left(P_{1n} = \frac{\bar{P}}{N}, P_{2n} = \frac{\bar{P}}{N}\right)$. Every point on the segment FG is obtained by timesharing between the two possible decoding orders. The curve AEB gives the capacity region for a constraint on the PSD-sum : $P_{1n} + P_{2n} = \frac{\bar{P}}{N}$. Point S gives the maximum sum rate while point E gives the maximum balanced rate. The multiuser

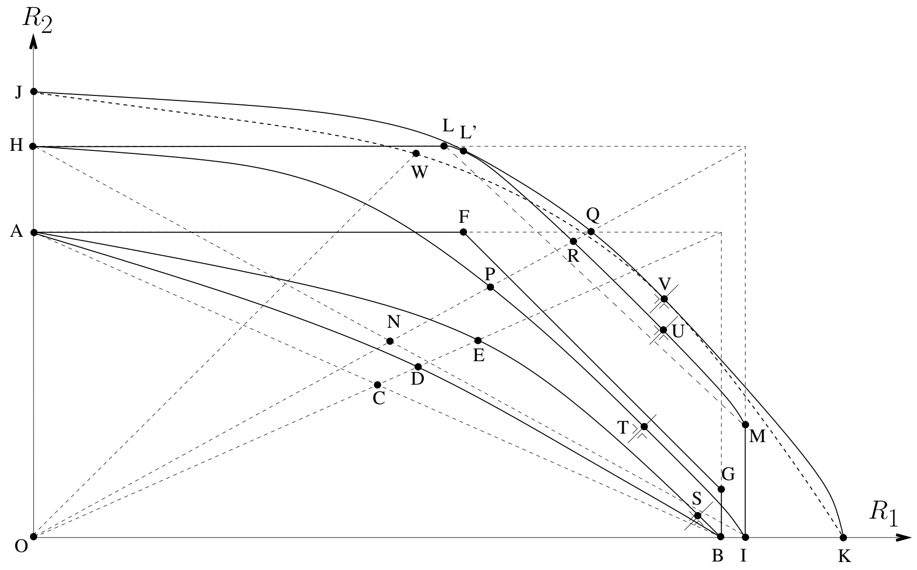

Figure 3.6: *Various capacity regions for ISI channels*

gain is obtained here by the ratio $\frac{\text{OE}}{\text{OC}}$. Finally, the curve ADB bounds the MA capacity region for a constraint on the PSD-sum and a flat PSD allocated to each user : $\left(P_{1n} = \gamma, P_{2n} = \frac{\bar{P}}{N} - \gamma\right)$. The ratio $\frac{\text{OD}}{\text{OC}}$ appears as a basic multiuser gain, which does not require channel knowledge at the transmitters. The ratio $\frac{\text{OE}}{\text{OD}}$ gives the additional gain obtained by a smart spectrum allocation, which requires knowledge of the channels at the transmitters.

Power-constrained capacity regions :
Points H and I give the single user rates for $\left(\sum_{n=1}^{N} P_{1n} = \bar{P}, P_{2n} = 0\right)$ and $\left(P_{1n} = 0, \sum_{n=1}^{N} P_{2n} = \bar{P}\right)$, respectively. These rates are of course higher than rates A and B as the flat PSD constraint is relaxed. The line HNI bounds the unconstrained-PSD TDMA capacity region. The locus of balanced rates solutions is here given by the line ONQ. The curve HPI gives the capacity region with a single constraint on the transmitted power sum : $\sum_n (P_{1n} + P_{2n}) = \bar{P}$. The multiuser gain is given here by $\frac{\text{OP}}{\text{ON}}$. The curve HLMI bounds the MA capacity region with constraints on the individual powers : $\left(\sum_{n=1}^{N} P_{1n} = \bar{P}, \sum_{n=1}^{N} P_{2n} = \bar{P}\right)$. Only the LM portion of the curve is useful. The multiuser gain is here $\frac{\text{OR}}{\text{ON}}$. JQVK gives the capacity

region obtained when the total power $2\bar{P}$ can be redistributed arbitrarily to the users : in other words, the constraint on the power sum is here $\sum_n (P_{1n} + P_{2n}) = 2\bar{P}$. This curve is tangent to the HLMI capacity curve at some point L' where the optimal power allocation happens to share the available power $2\bar{P}$ in two equal parts. On the JL' segment, the power allocated to user 1 is lower, while on the L'K segment it is higher. Finally, the dashed line JVK represents the same MA capacity region, but with an additional FDMA constraint (i.e. each frequency bin is exclusively allocated to one user). Both curves have a common point V with a tangent at 45 degrees : it is well known, indeed, that the maximum sum rate solution has the FDMA property [40]. The authors of [53] proposed a method to compute the maximum common rate of multiple access channels with that FDMA constraint, i.e. point W in the figure.

The object of the following sections is to provide efficient algorithms to compute the balanced rates solutions E, P (or Q) and R, as well as the associated power allocations, for an arbitrary number of users K. Note that these algorithms could be used to compute other boundary points of the capacity regions.

3.5.2 Multiuser diversity

If the constraint is put on the power-sum (or PSD-sum), the multiuser gain g defined in (3.1) is equal to 1 in the special case where all the users have identical channel responses ($H_k(\omega) = H_{k'}(\omega)\ \forall k, k'$). In other words, allowing simultaneous transmission by the different users does not increase the size of the capacity region if the channels of all users are identical. For this reason, g can be seen as a *multiuser diversity gain.*

If the constraint is put on the individual power, [40] showed that the capacity region is a polytope (a pentagon for $K = 2$) when the channels are identical. Some gain is thus available with respect to the balanced TDMA rates, as the users are not only allowed to transmit simultaneously, but also with the same power as in the single-user situation : the total power transmitted on the channel at a given time is K times higher than in the TDMA solution. However, the multiuser gain g increases when the channel responses are different. The origin of the multiuser gain is thus twofold :

- The gain brought by the transmission power increase. For K identical channels, this gain is given by $\frac{R_k^1(K\bar{P})}{R_k^1(\bar{P})} \leq 1 + \frac{B\log(K)}{R_k^1(\bar{P})}$ where $R_k^1(P)$ stands for the maximum single-user rate with a transmitted power P. The last inequality corresponds to the high-snr approximation.

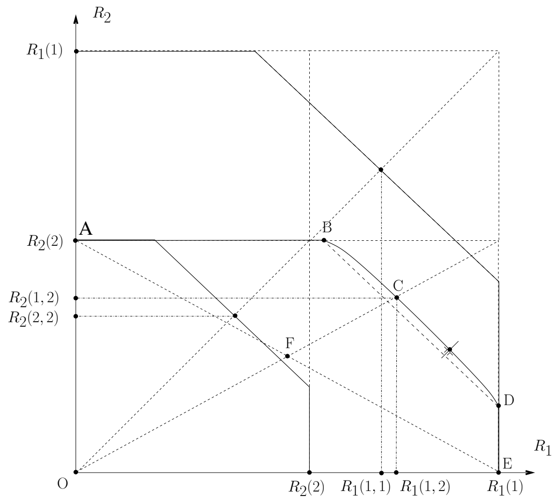

Figure 3.7: *Capacity regions for identical and different two-user channels*

- The multiuser diversity.

The maximum gain g is obtained when the user channels are sufficiently different to provide single-user optimal power allocations in K mutually exclusive sets of frequency bins. In that case, the users are not in competition for the best frequencies and they can all transmit at their SU maximum rate : $R_k = R_k^1 \; \forall k$. An upper bound for the multiuser gain is thus : $g \leq K$.

Figure 3.7 illustrates these ideas for $K = 2$. The bound of the capacity region for channels $(1, 2)$ is given by the curve ABCDE. The total multiuser gain is here $\frac{OC}{OF}$. The two pentagons give the capacity regions for identical channels (channels $(1, 1)$ or channels $(2, 2)$). The maximum balanced rates with different channels ($R_1(1, 2)$ and $R_2(1, 2)$) are higher than the corresponding balanced rates with identical channels ($R_1(1, 1)$ and $R_2(2, 2)$), which denotes the effect of multiuser diversity.

3.5.3 Maximum aggregate rate for a given power allocation

As the total rates are simply obtained by summing the partial rates in each frequency bin, the maximum aggregate rate R_α for a given power allocation

$\{P_{kn}\}$ is given by :

$$R_\alpha = \sum_{k=1}^{K} \alpha_k \left(\sum_{n=1}^{N} R_{kn} \right) \tag{3.52}$$

with

$$(R_{kn})_{\mathrm{MA}} = \frac{1}{N}\,\mathcal{C}\left(\frac{P_{kn}h_{kn}^2}{\sigma_n^2 + \sum_{l=k+1}^{K} P_{ln}h_{ln}^2} \right) \tag{3.53}$$

$$(R_{kn})_{\mathrm{BC}} = \frac{1}{N}\,\mathcal{C}\left(\frac{P_{kn}h_{kn}^2}{\sigma_n^2 + \left(\sum_{h_k^2<h_l^2} P_{ln}\right) h_{kn}^2} \right). \tag{3.54}$$

3.5.4 Optimal power allocation

(Given $\{\alpha_k\}$)
We wish now to compute the power allocations $\{P_{kn}^*\}$ and $\{P_{kn}^\circ\}$ maximizing the aggregate rate R_α for the MA and BC frequency selective channels, respectively. The general strategy used to solve this problem is made of two steps :

1. Find the solution along the frequency axis, i.e. compute the optimal spectral allocation of the power sum $\bar{P}_n = \sum_k P_{kn}$.

2. Find the solution along the multiuser axis, i.e. allocate the power $\bar{P}_n$ to the K users separately in each frequency bin n by using the results of Section 3.4.

Let us analyze in more details the three different scenarios.

3.5.4.1 PSD-sum constraint

The constraints are : $\sum_k \gamma_k(\omega) = \bar{\gamma}(\omega)$.

The spectrum allocation is trivially given by $\bar{P}_n = \sum_k P_{kn} = \bar{\gamma}(\omega_n)df$. The Kuhn-Tucker conditions are :

$$\frac{N}{B}\frac{\partial R_\alpha}{\partial P_{kn}} \begin{cases} = \mu_n & P_{kn} > 0 \\ < \mu_n & P_{kn} = 0 \end{cases} \tag{3.55}$$

The power allocation algorithm is then applied separately in the N frequency bins. A constraint on the PSD-sum actually generates independent constraints on the power-sum inside every frequency bin.

3.5.4.2 Power-sum constraint

The constraint is : $\sum_k \sum_n P_{kn} = \bar{P}$.

The Kuhn-Tucker conditions are now :

$$\frac{N}{B}\frac{\partial R_\alpha}{\partial P_{kn}} \begin{cases} = \mu & P_{kn} > 0 \\ < \mu & P_{kn} = 0 \end{cases} \tag{3.56}$$

Using (3.20), the partial derivative for each frequency bin is $\max_k \left\{ D_{kn}(\bar{P}_n) \right\}$ (the KN functions $D_{kn}(x)$ are defined in the same way as equation (3.10)), which provides the solution :

$$\mu \bar{P}_n = \max_{k \in [1,K]} \left(1 - \left[\frac{\mu}{h_{kn}^2/\sigma^2} + (1-\alpha_k) \right] \right)_+ \tag{3.57}$$

where $(x)_+$ denotes $\max(x, 0)$. The spectral allocation is the multiuser extension of the well-known water-filling algorithm ([52]-[40]). The solution can be represented in a single water-filling diagram with a common water level fixed to 1 and K containers $\mu\sigma^2/h_{kn}^2$ modified by the correction terms $(1-\alpha_k)$ reflecting the effect of the user relative priorities. The bottom of the resulting multiuser container is the minimum of the K modified individual containers. A simple binary search must be performed to find the right coefficient μ that satisfies the total power constraint. The power allocation algorithm is then applied separately for the N frequency bins.

3.5.4.3 Individual power constraint (MA channel only)

The K power constraints are : $\sum_n P_{kn} = \bar{P}_k$.

The Kuhn-Tucker conditions are :

$$\frac{N}{B}\frac{\partial R_\alpha}{\partial P_{kn}} \begin{cases} = \mu_k & P_{kn} > 0 \\ < \mu_k & P_{kn} = 0 \end{cases} \tag{3.58}$$

which is not directly compatible with (3.9) as the marginal gain for each user is now different. The solution lies in the observation that $R_\alpha = f\left(P_{kn}h_{kn}^2\right) = f\left(\mu_k P_{kn} \frac{h_{kn}^2}{\mu_k}\right)$, i.e. transmitting a signal with power P_{kn} in a channel with gain h_{kn}^2 is equivalent to transmitting a signal with power $\mu_k P_{kn}$ in a channel with gain $\frac{h_{kn}^2}{\mu_k}$ as far as the resulting capacity is concerned. The product $\mu_k P_{kn}$ appears as an 'equivalent power' allocated to user k for transmission on the 'equivalent channel' $\frac{h_{kn}^2}{\mu_k}$. If the equivalent power sum $\bar{P}_n^\mu \triangleq \sum_k \mu_k P_{kn}$ to be allocated on a given frequency bin n is known, then the optimal equivalent power allocation to the users $\{\mu_k P_{kn}\}$ verifies (3.9) with $\mu = 1$ and algorithm 3.1 can be used on the set of equivalent channels $\frac{h_{kn}^2}{\mu_k}$. Using equation (3.39), we get :

$$\frac{N}{B}\frac{\partial R_\alpha}{\partial\left(\mu_k P_{kn}\right)}\begin{cases} = 1 = \max_k\left(\frac{\frac{\alpha_k h_{kn}^2}{\mu_k\sigma^2}}{1+\bar{P}_n^{\mu}\frac{h_{kn}^2}{\mu_k\sigma^2}}\right) & P_{kn} > 0 \\ < 1 & P_{kn} = 0 \end{cases} \tag{3.59}$$

For a given set $\{\mu_k\}$, the distribution of the equivalent power sum $\bar{P}_n^{\mu}$ along the frequency axis is finally obtained as follows :

$$\bar{P}_n^{\mu} = \max_{k\in[1,K]}\left(1-\left[\frac{\mu_k}{h_{kn}^2/\sigma^2}+(1-\alpha_k)\right]\right)_+ . \tag{3.60}$$

The power allocation algorithm is then applied separately in the N frequency bins.

Equation (3.60) can be associated with a multiuser water-filling diagram as in [40]. Figure 3.8 is an example of a three-user water-filling diagram. The common water level is 1. The three containers (bold curves) are associated with the equivalent channels h_{kn}^2/μ_k, and are modified by $(1-\alpha_k)$ to reflect the different user relative priorities. The total area defined by the water level and the bottom of the composite container represents the equivalent power sum $\mu_1\bar{P}_1+\mu_2\bar{P}_2+\mu_3\bar{P}_3$. After the application of the power allocation algorithm in each equivalent subchannel, the water area can be subdivided in three parts (represented with three different patterns in Figure 3.8). The area of each part should be equivalent to the individual equivalent power $\mu\bar{P}_k$.

There is a single set of coefficients $\{\mu_k\}$ satisfying the K power constraints simultaneously. These coefficients have to be computed iteratively. [41] proposed a simple algorithm to compute the optimum μ_k : at iteration $i+1$, each $\mu_k^{(i+1)}$ is computed separately to satisfy the k^{th} power constraint while the $K-1$ other μ_k's remain fixed at $\mu_k^{(i)}$. We propose here an algorithm updating the K coefficients μ_k simultaneously, based on a careful analysis of the optimal power allocation in each frequency bin. Rewriting equation (3.40) with the equivalent powers $\mu_{k_j}P_{k_j n}$ and channels $h_{k_j n}^2/\mu_{k_j}$, and using (3.60), the vector of optimal powers allocated to the users in the subset $S_J(n)$ in the n^{th} frequency bin, and the corresponding optimal user rates

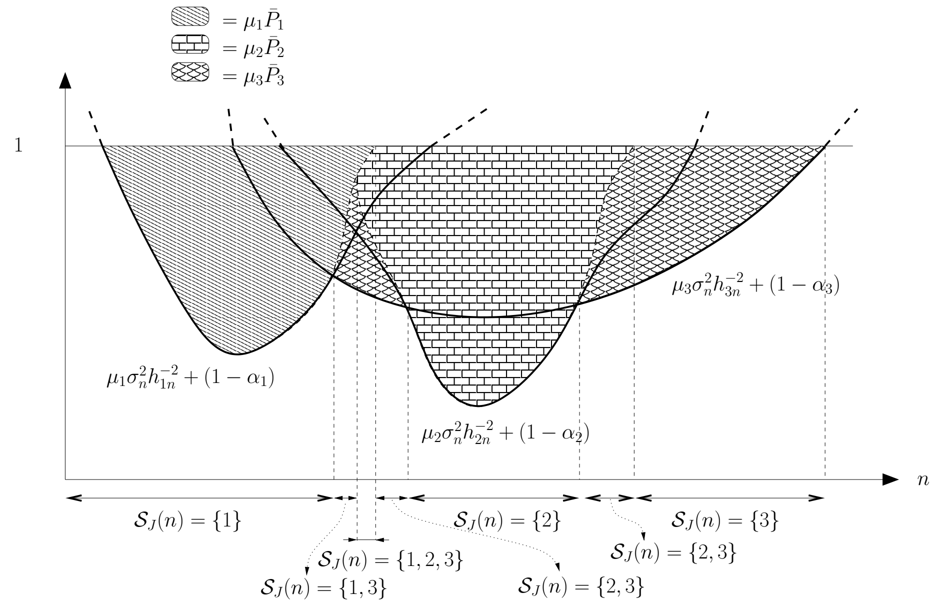

Figure 3.8: *Multiuser water-filling diagram*

are given explicitly as :

$$\begin{pmatrix} P^\circ_{k_1n} \\ P^\circ_{k_2n} \\ \vdots \\ P^\circ_{k_jn} \\ \vdots \\ P^\circ_{k_{J-1}n} \\ P^\circ_{k_Jn} \end{pmatrix} = \begin{bmatrix} h^{-2}_{k_1n}\left(\frac{\alpha_{k_1}}{\mu_{k_1}h^{-2}_{k_1n}} - \frac{\alpha_{k_2}-\alpha_{k_1}}{\mu_{k_2}h^{-2}_{k_2n}-\mu_{k_1}h^{-2}_{k_1n}}\right) \\ h^{-2}_{k_2n}\left(\frac{\alpha_{k_2}-\alpha_{k_1}}{\mu_{k_2}h^{-2}_{k_2n}-\mu_{k_1}h^{-2}_{k_1n}} - \frac{\alpha_{k_3}-\alpha_{k_2}}{\mu_{k_3}h^{-2}_{k_3n}-\mu_{k_2}h^{-2}_{k_2n}}\right) \\ \vdots \\ h^{-2}_{k_jn}\left(\frac{\alpha_{k_j}-\alpha_{k_{j-1}}}{\mu_{k_j}h^{-2}_{k_jn}-\mu_{k_{j-1}}h^{-2}_{k_{j-1}n}} - \frac{\alpha_{k_{j+1}}-\alpha_{k_j}}{\mu_{k_{j+1}}h^{-2}_{k_{j+1}n}-\mu_{k_j}h^{-2}_{k_jn}}\right) \\ \vdots \\ h^{-2}_{k_{J-1}n}\left(\frac{\alpha_{k_{J-1}}-\alpha_{k_J}}{\mu_{k_{J-1}}h^{-2}_{k_{J-1}n}-\mu_{k_J}h^{-2}_{k_Jn}} - \frac{\alpha_{k_J}-\alpha_{k_{J-1}}}{\mu_{k_J}h^{-2}_{k_Jn}-\mu_{k_{J-1}}h^{-2}_{k_{J-1}n}}\right) \\ h^{-2}_{k_Jn}\left(\frac{\alpha_{k_J}-\alpha_{k_{J-1}}}{\mu_{k_J}h^{-2}_{k_Jn}-\mu_{k_{J-1}}h^{-2}_{k_{J-1}n}} - \sigma_n^2\right) \end{bmatrix} \tag{3.61}$$

and

$$\begin{pmatrix} R^*_{k_1n} \\ R^*_{k_2n} \\ \vdots \\ R^*_{k_jn} \\ \vdots \\ R^*_{k_{J-1}n} \\ R^*_{k_Jn} \end{pmatrix} = \frac{B}{N}\log \begin{bmatrix} \frac{\alpha_{k_1}}{\mu_{k_1}h^{-2}_{k_1n}} \Big/ \frac{\alpha_{k_2}-\alpha_{k_1}}{\mu_{k_2}h^{-2}_{k_2n}-\mu_{k_1}h^{-2}_{k_1n}} \\ \frac{\alpha_{k_2}-\alpha_{k_1}}{\mu_{k_2}h^{-2}_{k_2n}-\mu_{k_1}h^{-2}_{k_1n}} \Big/ \frac{\alpha_{k_3}-\alpha_{k_2}}{\mu_{k_3}h^{-2}_{k_3n}-\mu_{k_2}h^{-2}_{k_2n}} \\ \vdots \\ \frac{\alpha_{k_j}-\alpha_{k_{j-1}}}{\mu_{k_j}h^{-2}_{k_jn}-\mu_{k_{j-1}}h^{-2}_{k_{j-1}n}} \Big/ \frac{\alpha_{k_{j+1}}-\alpha_{k_j}}{\mu_{k_{j+1}}h^{-2}_{k_{j+1}n}-\mu_{k_j}h^{-2}_{k_jn}} \\ \vdots \\ \frac{\alpha_{k_{J-1}}-\alpha_{k_J}}{\mu_{k_{J-1}}h^{-2}_{k_{J-1}n}-\mu_{k_J}h^{-2}_{k_Jn}} \Big/ \frac{\alpha_{k_J}-\alpha_{k_{J-1}}}{\mu_{k_J}h^{-2}_{k_Jn}-\mu_{k_{J-1}}h^{-2}_{k_{J-1}n}} \\ \frac{\alpha_{k_J}-\alpha_{k_{J-1}}}{\mu_{k_J}h^{-2}_{k_Jn}-\mu_{k_{J-1}}h^{-2}_{k_{J-1}n}} \Big/ \sigma_n^2 \end{bmatrix}. \tag{3.62}$$

Starting from an initial set of coefficients $\boldsymbol{\mu}^{(0)}$ the proposed updating strategy is given by :

$$\begin{aligned} \boldsymbol{\Delta}^{(i)}_{\mu} &= -\left[\sum_{n=1}^{N}\left(\frac{\partial \boldsymbol{P}^\circ_n}{\partial \boldsymbol{\mu}}\right)_{\boldsymbol{\mu}=\boldsymbol{\mu}^{(i)}}\right]^{-1}\left[\left(\sum_{n=1}^{N}\boldsymbol{P}^\circ_n\left(\boldsymbol{\mu}^{(i)}\right)\right) - \bar{\boldsymbol{P}}\right] && (3.63) \\ \boldsymbol{\mu}^{(i+1)} &= \boldsymbol{\mu}^{(i)} + \lambda_i \boldsymbol{\Delta}^{(i)}_{\mu}. && (3.64) \end{aligned}$$

From (3.61), each Jacobian matrix $\frac{\partial \boldsymbol{P}^\circ_n}{\partial \boldsymbol{\mu}}$ can be computed explicitly : the $J(n) \times J(n)$ submatrix corresponding to indexes in $S_J(n)$ is a tridiagonal matrix, and the remaining entries are all zero. The main difficulty with this algorithm is to find a starting point $\boldsymbol{\mu}^{(0)}$ such that the Jacobian matrix sum is invertible, and to keep this matrix invertible at each iteration. In particular, the total power allocated to each user has to be non-zero for each $\boldsymbol{\mu}^{(i)}$. The size of the updating step (coefficient λ_i) should be adapted accordingly.

3.5.5 Maximum balanced rates

Algorithm 3.2 can be extended to compute the maximum balanced rates of frequency selective multiuser channels. Let us analyze in more details the three different scenarios.

3.5.5.1 PSD-sum constraint

The Jacobian matrix $\frac{\partial \boldsymbol{R}}{\partial \boldsymbol{\alpha}}$ is now the sum of Jacobian matrices corresponding to each frequency bin. For each term, the $J(n) \times J(n)$ submatrix corresponding to the users active on the frequency bin n is a symmetric tridiagonal matrix $\mathbf{T}_n(\boldsymbol{\alpha})$ with non-zero entries defined in (3.51) :

$$\frac{N}{B}\frac{\partial \boldsymbol{R}}{\partial \boldsymbol{\alpha}} = \sum_{n=1}^{N} \mathbf{T}_n\left(\boldsymbol{\alpha}\right). \tag{3.65}$$

The resulting Jacobian matrix is generally not tridiagonal. The sum should be invertible to allow the computation of the update direction, which requires that each user gets some power in at least one frequency bin.

3.5.5.2 Power-sum constraint

The total power to be allocated in each frequency bin $\bar{P}_n$ is now dependent on the user relative priorities. From (3.26), it follows that a correction term $\mathbf{Q}_n(\boldsymbol{\alpha})$ should be included in the expression of $\frac{\partial \mathbf{R}_n}{\partial \boldsymbol{\alpha}}$:

$$\frac{N}{B}\frac{\partial \boldsymbol{R}}{\partial \boldsymbol{\alpha}} = \sum_{n=1}^{N} \left[\mathbf{T}_n\left(\boldsymbol{\alpha}\right) + \mathbf{Q}_n\left(\boldsymbol{\alpha}\right)\right]. \tag{3.66}$$

Let us define N_k as the number of frequency bins n such that $k_J(n) = k$ (i.e. the last user in the allocation process (algorithm 3.1) is user k), with $\sum_k N_k = N$. Combining the water-filling solution (3.57) with the power-sum constraint, the marginal rate μ and the total power allocation $\bar{P}_n$ can be expressed as :

$$\mu = \frac{\sum_{k=1}^{K} \alpha_k N_k}{\bar{P} + \sigma^2 \sum_{n=1}^{N} h_{k_J(n)}^{-2}} \tag{3.67}$$

$$\bar{P}_n = \frac{\alpha_{k_J(n)}}{\sum_{k=1}^{K} \alpha_k N_k} \left(\bar{P} + \sigma^2 \sum_{l=1}^{N} h_{k_J(l)}^{-2} \right) - \sigma^2 h_{k_J(n)}^{-2} \tag{3.68}$$

Using (3.26) and (3.68), the correction term $\mathbf{Q}_n(\boldsymbol{\alpha})$ has the following entries on its k_J^{th} row :

$$\begin{aligned} [\mathbf{Q}_n(\boldsymbol{\alpha})]_{k_J(n),k} &= \left(\frac{h_{k_J n}^2 / \sigma^2}{1 + P_n h_{k_J n}^2 / \sigma^2} \right) \frac{\partial P_n}{\partial \alpha_k} \\ &= \frac{1}{\alpha_{k_J(n)}} \left(\delta_{k_J(n),k} - \frac{\alpha_{k_J(n)} N_k}{\sum_{l=1}^{K} \alpha_l N_l} \right). \end{aligned} \tag{3.69}$$

The $K-1$ other rows of $\mathbf{Q}_n(\boldsymbol{\alpha})$ are all zero. The algorithm for the computation of the maximum balanced rates is then identical to the original algorithm, except that a new water level μ and a new spectral allocation $\{\bar{P}_n\}$ have to be computed by (3.57) for each new set of priority coefficients $\boldsymbol{\alpha}^{(i+1)}$.

3.5.5.3 Individual power constraint (MA channel only)

The computation of maximum balanced rates is much more complex in this case as the optimal vectors $\boldsymbol{\alpha}$ and $\boldsymbol{\mu}$ have to be found, that satisfy simultaneously the K balanced rates equations and the K individual power constraints :

$$\boldsymbol{R}^*(\boldsymbol{\alpha}, \boldsymbol{\mu}) = \sum_{n=1}^{N} \boldsymbol{R}_n^*(\boldsymbol{\alpha}, \boldsymbol{\mu}) = \left(\frac{g}{K} \right) \boldsymbol{R}^{\mathbf{1}} \tag{3.70}$$

$$\boldsymbol{P}^\circ(\boldsymbol{\alpha}, \boldsymbol{\mu}) = \sum_{n=1}^{N} \boldsymbol{P}_n^\circ(\boldsymbol{\alpha}, \boldsymbol{\mu}) = \bar{\boldsymbol{P}} \tag{3.71}$$

where the non-zero elements of $\boldsymbol{P}_n^\circ$ and $\boldsymbol{R}_n^*$ are given by equations (3.61) and (3.62).

We propose the following algorithm, that updates alternately the α_k's (to obtain balanced rates) and the μ_k's (to obtain balanced powers) until both sets of constraints are satisfied.

Algorithm 3.3 *Maximum balanced rates with individual power constraints (exact solution)*

- *Set* $i = 0$, $\boldsymbol{\mu}^{*(0)} = [1, \cdots, 1]^T$ *and* $\boldsymbol{\alpha}^{*(0)} = [1, \cdots, 1]^T / K$
- *While both sets of constraints (3.70) and (3.71) are not satisfied simultaneously :*
  - ***Rates balancing step***
    - *Consider the problem of allocating an equivalent power-sum* $\bar{P}^{\mu} = \sum_{k=1}^{K} \mu_k^{*(i)} \bar{P}_k$ *to the* K *users with equivalent channels* $h_{kn}^2 / \mu_k^{*(i)}$.
    - *Compute the set* $\left\{R_k^1\right\}$ *of SU rates for the current equivalent power* $\bar{P}^{\mu}$ *and the current equivalent channels.*
    - *Use algorithm 3.2 to compute* $\boldsymbol{\alpha}^{*(i+1)}$ *that satisfies the balanced rates constraints (3.70).*
    - *Start with* $\boldsymbol{\alpha}^{(0)} = [1/R_1^1, \cdots, 1/R_K^1]^T / \sum_k (1/R_k^1)$.
    - *Compute the scalar parameter* $\mu^{(i+1)}$ *from the multiuser water-filling equation (3.57) for the vector* $\boldsymbol{\alpha}^{*(i+1)}$ *obtained at convergence.*
    - *The pair* $\left[\boldsymbol{\alpha}^{*(i+1)}, \mu^{(i+1)} . \boldsymbol{\mu}^{*(i)}\right]$ *now satisfies the balanced rates constraints. But the individual power constraints are generally not satisfied : the power allocation is unbalanced.*
  - ***Powers balancing step***
    - *Compute the vector* $\boldsymbol{\mu}^{*(i+1)}$ *that satisfies the power constraints (3.71) with the updating equations (3.63) and (3.64).*
    - *Start with* $\boldsymbol{\mu}^{(0)} = \mu^{(i+1)} \boldsymbol{\mu}^{*(i)}$. *The corresponding optimal power allocation is known to provide balanced rates : each user gets some power and the sum of Jacobian matrices in (3.63) should be invertible.*
    - *The pair* $\left[\boldsymbol{\alpha}^{*(i+1)}, \boldsymbol{\mu}^{*(i+1)}\right]$ *now satisfies the individual power constraints, but the updated rates are generally unbalanced.*
  - *Set* $i = i + 1$

The complexity of the last algorithm is very high as two levels of iterations are involved. Its main utility lies in the fact that it provides the *exact solution*, which is helpful in the evaluation of alternative algorithms providing suboptimal solutions.

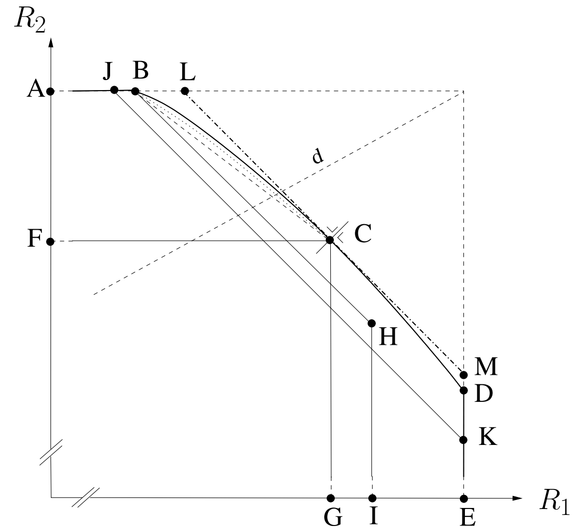

Figure 3.9: *Two-user capacity region and IMWF algorithm*

The alternative method we propose is based on the Iterative Multiuser Water-Filling algorithm (IMWF)[44]. The IMWF algorithm is used to compute the maximum sum-rate of a multiuser frequency selective channel, with individual power constraints. It is based on the observation that each power allocation $\boldsymbol{P}_k$ from the set of optimal power allocations $[\boldsymbol{P}_1, \cdots, \boldsymbol{P}_K]$ maximizing the rate-sum is obtained by single-user water-filling (SUWF) with an equivalent noise $\sigma_n'^2 = \sigma_n^2 + \sum_{k' \neq k} P_{k'n} h_{k'n}^2$. In other words, the set of K optimal power allocations should satisfy the *simultaneous water-filling* condition. The IMWF starts from arbitrary power allocations $\boldsymbol{P}_k$ and updates them successively by applying the SUWF algorithm with the $K-1$ other allocations fixed. The obtained solution can be shown to converge quickly to the simultaneous WF solution.

Figure 3.9 gives a two-user capacity region with individual power constraints (curve ABCDE). Line d is the locus of balanced rates pairs. The IMWF algorithm can be used to obtain the power allocation corresponding to point C ($\alpha_1 = \alpha_2 = \frac{1}{2}$). As this allocation is FDMA, the associated capacity region is the FCG rectangle. The rates obtained with this solution are unbalanced : a higher priority should be given to user 2 ($\alpha_2 > \alpha_1$), which involves that the decoding order would be $(1, 2)$. When the highest priority is given to user 2 ($\alpha_1 = 0, \alpha_2 = 1$), the solution consists of *successive water-filling* : $\boldsymbol{P}_1$ is first computed with the SUWF algorithm ignoring the presence of user 2, $\boldsymbol{P}_2$ is then computed with the same algorithm and an equivalent noise including the effect of user 1 signal. The capacity region associated with the successive WF algorithm is the ABHI pentagon, and B represents the useful rate pair. Obviously, the maximum balanced rates pair ($BC \cap d$) results from a compromise between the simultaneous WF solution and the successive WF solution. A lower bound for the BC curve can be found by considering the allocation $\boldsymbol{P}_1(x) = x\boldsymbol{P}_1^B + (1-x)\boldsymbol{P}_1^C$ for user 1, and the SUWF allocation $\boldsymbol{P}_2(x)$ for user 2, with noise including the effect of $\boldsymbol{P}_1(x)$. The rate pairs obtained with this allocation policy are given by the dotted line BC. For some x in the range $[0,1]$, balanced rates are obtained that are very close to the maximum balanced rates. A comparison with the rates obtained by algorithm 3.3 confirmed that the proposed solution is a tight lower bound for the optimal solution. Simple and useful lower and upper bounds (g_-, g_+) on the multiuser gain g can also be obtained as follows. The ALCME pentagon is obviously an upper bound for the convex capacity region. The corresponding balanced rates pair ($LC \cap d$) is $\frac{g_+}{2}(R_1^1, R_2^1)$. The AJKE pentagon is the capacity region obtained when the SUWF algorithm is applied separately for every user. This pentagon appears to be a lower bound for the true capacity region. The corresponding balanced rates pair ($JK \cap d$) is $\frac{g_-}{2}(R_1^1, R_2^1)$.

Generalizing these ideas to multiuser channels with an arbitrary number of users K is not easy as the optimal decoding order ($K!$ different combinations) is a priori unknown. The next algorithm is based on the idea that a higher priority should be given to the users to whom the IMWF algorithm is unfair.

Algorithm 3.4 *Maximum balanced rates with individual power constraints (approximate solution)*

- *Apply the SUWF and IMWF algorithms on the set* $\mathcal{S}_K = \{1, \cdots, K\}$. *Compute the corresponding power allocations, denoted by* $\left\{\boldsymbol{P}_k^1\right\}$ *and* $\left\{\boldsymbol{P}_k^{\mathcal{S}_K}\right\}$, *respectively. Compute the associated user rates, denoted by* $\left\{R_k^1\right\}$ *and* $\left\{R_k^{\mathcal{S}_K}\right\}$, *respectively.*
- *Compute initial bounds for the multiuser gain* g_- *and* g_+ *:*

$$\frac{g_-}{K} = \frac{\sum_n \mathcal{C}\left(\sum_k P_{kn}^1 h_{kn}^2/\sigma_n^2\right)}{\sum_k R_k^1} \tag{3.72}$$

$$\frac{g_+}{K} = \frac{\sum_k R_k^{\mathcal{S}_K}}{\sum_k R_k^1} \tag{3.73}$$

- *Set* $k_K = \arg\min_{k\in\mathcal{S}_K} R_k^{\mathcal{S}_K}/R_k^1$ *: the highest priority is given to the user whose normalized rate would be the lowest if the same priority was given to all users.*

- *While the balanced rates constraints are not satisfied :*

  – *Set* $i = K$ *and* $g^* = \frac{1}{2}(g_- + g_+)$.

  – *Set* $\boldsymbol{P}_{k_K}(x_K) = x_K \boldsymbol{P}_{k_K}^1 + (1 - x_K)\boldsymbol{P}_{k_K}^{\mathcal{S}_K}$. *Compute* x_K *such that :*

$$R_{k_K} = \sum_n \mathcal{C}\left(\frac{P_{k_K n}(x_K)h_{k_K n}^2}{\sigma_n^2}\right) = \frac{g^*}{K} R_{k_K}^1 \tag{3.74}$$

  x_K *can be found by a simple binary search in the interval* $[0,1]$.

  – *For* $i = K-1$ *down to* 2 *:*

    * *Set* $\mathcal{S}_i = \mathcal{S}_{i+1} \setminus \{k_{i+1}\}$
    * *Compute the equivalent noise* $\boldsymbol{I}_i$ *including the additive noise* $\boldsymbol{\sigma}^2$ *and the interference from higher-priority users :* $\boldsymbol{I}_i = \boldsymbol{\sigma}^2 + \sum_{j=i+1}^K \boldsymbol{P}_{k_j}^T \boldsymbol{h}_{k_j}^2$.
    * *Apply the IMWF algorithm on the set of remaining users* $\mathcal{S}_i$, *with an equivalent noise power* $\boldsymbol{I}_i$. *The obtained power allocations and the associated user rates are denoted* $\left\{\boldsymbol{P}_k^{\mathcal{S}_i}(\boldsymbol{I}_i)\right\}_{k\in\mathcal{S}_i}$ *and* $\left\{R_k^{\mathcal{S}_i}(\boldsymbol{I}_i)\right\}_{k\in\mathcal{S}_i}$. *The last IMWF allocation* $\left\{\boldsymbol{P}_k^{\mathcal{S}_{i+1}}(\boldsymbol{I}_{i+1})\right\}_{k\in\mathcal{S}_i}$ *can be updated to make the computation faster.*
    * *Set* $k_i = \arg\min_{k\in\mathcal{S}_i} R_k^{\mathcal{S}_i}(\boldsymbol{I}_i)/R_k^1$ *: the next higher priority is given to the user in* $\mathcal{S}_i$ *whose normalized rate would be the lowest if the same priority was given to all users in* $\mathcal{S}_i$.
    * *Apply the SUWF algorithm on user* k_i, *with an equivalent noise power* $\boldsymbol{I}_i$. *The obtained power allocation is* $\boldsymbol{P}_{k_i}^1(\boldsymbol{I}_i)$ *and the associated rate is* $R_{k_i}^1(\boldsymbol{I}_i)$.
    * *If* $R_{k_i}^{\mathcal{S}_i}(\boldsymbol{I}_i) > \frac{g^*}{K} R_{k_i}^1$, *set* $g_- = g^*$, *return to* $i = K$.
    * *Else, if* $R_{k_i}^1(\boldsymbol{I}_i) < \frac{g^*}{K} R_{k_i}^1$, *set* $g_+ = g^*$, *return to* $i = K$.
    * *Else, set* $\boldsymbol{P}_{k_i}(x_i) = x_i \boldsymbol{P}_{k_i}^1(\boldsymbol{I}_i) + (1-x_i)\boldsymbol{P}_{k_i}^{\mathcal{S}_i}(\boldsymbol{I}_i)$. *Compute* x_i *such that :*

$$R_{k_i} = \sum_n \mathcal{C}\left(\frac{P_{k_i n}(x_i)h_{k_i n}^2}{I_{in}}\right) = \frac{g^*}{K} R_{k_i}^1 \tag{3.75}$$

x_i can be found by a simple binary search in the interval $[0, 1]$.

- *Set* $k_1 = \mathcal{S}_2 \setminus \{k_2\}$.
- *Compute the equivalent noise* $\boldsymbol{I}_1 = \boldsymbol{\sigma}^2 + \sum_{j=2}^{K} \boldsymbol{P}_{k_j}^T \boldsymbol{h}_{k_j}^2$
- *Compute* $\boldsymbol{P}_{k_1}$ *by applying the SUWF algorithm on user* k_1*, with an equivalent noise power* $\boldsymbol{I}_1$*. The associated rate is* R_{k_1}.
- *If* $R_{k_1} > \frac{g^*}{K} R_{k_1}^1$ *: set* $g_- = g^*$*; else set* $g_+ = g^*$

In Section 3.7, the power allocation obtained with this suboptimal algorithm, and the corresponding balanced rates, are compared to the optimal solution provided by algorithm 3.3.

3.6 FDM(A) capacity

The purpose of this section is to investigate methods for the computation of maximum balanced rates with an FDM(A) constraint. The key to solving this class of problems is to find the optimal partition of the frequency spectrum among the different users. Once the frequency band assignment is fixed, the optimal spectra for each user are determined separately, depending on the type of power constraint. The three types of power constraints are considered again in the sequel. In the FDM(A) scenario, the uplink and downlink capacity regions are identical as successive decoding is not necessary any more. The results presented in this section are thus valid as well for the broadcast channel and for the multiple access channel.

3.6.1 PSD-sum constraint

With a constraint $\bar{\gamma}$ on the transmitted PSD, the powers P_{kn} assigned to the different users in every subchannel n can be written as :

$$P_{kn} = \rho_{kn} \cdot \bar{\gamma}\, \mathrm{d}f \qquad \text{with} \left\{ \begin{array}{ccc} \rho_{kn} & = & 0 \text{ or } 1 \\ \rho_{kn}\rho_{k'n} & = & 0 \quad \forall\, k \neq k' \end{array} \right. \tag{3.76}$$

The aggregate rate R_α is then given by

$$R_\alpha = \sum_{n=1}^{N} \sum_{k=1}^{K} \rho_{kn} \, (\alpha_k R_{kn}), \qquad \text{with } R_{kn} \triangleq \mathcal{C}\left(\frac{\bar{\gamma}\mathrm{d}f}{\sigma_n^2}\right). \tag{3.77}$$

The maximization of the aggregate rate R_α for a given set of relative priorities $\{\alpha_k\}$ is trivial :

$$\rho_{k^*n} = 1, \qquad k^* = \arg\max_k (\alpha_k R_{kn}) \tag{3.78}$$

$$\rho_{kn} = 0, \qquad \forall\, k \neq k^* \tag{3.79}$$

The balanced rate constraint requires the computation of allocation coefficients $\{\rho_{kn}\}$ providing identical normalized rates $\frac{1}{\beta_k}\sum_n \rho_{kn} R_{kn}$ for every user, with $\beta_k = \sum_n R_{kn}$. A balanced rate solution generally does not exist as it is highly probable that none of the K^N possible allocations strictly satisfies the balanced rate constraint. The balanced rate constraint can be relaxed, according to a given tolerance. The computation of maximum quasi-balanced rates, however, is quite complex. This problem actually belongs to the class of integer programming problems, which usually require an exhaustive search.

One possible simplification is to approximate the problem by its continuous relaxation. The difficulty in solving an integer programming problem lies in the fact that the constraint set is a set of isolated points ($\rho_{kn} = 0$ or 1). The idea of continuous relaxation is to enlarge the constraint set to include all convex combinations of the original points, thus generating a convex constraint set. Instead of forcing the assignment variables ρ_{kn} to be either 0 or 1, the constraint can be relaxed to :

$$0 \leq \rho_{kn} \leq 1, \qquad \sum_{k=1}^{K} \rho_{kn} = 1. \tag{3.80}$$

The interpretation of equation (3.80) is that each subchannel n of width $\mathrm{d}f$ can be subdivided arbitrarily into K narrower subchannels. For this reason, the continuous coefficients ρ_{kn} are called 'sharing coefficients' in the sequel. As the optimum frequency allocation usually involves only a few frequency bands, most of the sharing coefficients corresponding to the solution are 0 or 1. Only the few subchannels including the boundaries of those frequency bands have to be shared by two or more users. With the proposed relaxation, the subchannel allocation rule for a given set of relative priorities becomes :

Algorithm 3.5 *Subchannel allocation rule for a given set* $\{\alpha_k\}$

- $\forall\, n \in \{1, \cdots, N\}$, *do :*
  - *Compute the maximum weighted rate* $t_n \triangleq \max_k (\alpha_k R_{kn})$

– *Separate the users in two disjoint sets* $\mathcal{V}_n$ *and* $\bar{\mathcal{V}}_n$ *:*

$$\mathcal{V}_n = \{k \mid \alpha_k R_{kn} = t_n\} \qquad \bar{\mathcal{V}}_n = \{k \mid \alpha_k R_{kn} < t_n\}$$

– *Set the sharing coefficients* ρ_{kn} *as follows :*

$$\rho_{kn} = 0 \quad \forall\, k \in \bar{\mathcal{V}}_n, \qquad \sum_{k \in \mathcal{V}_n} \rho_{kn} = 1$$

- *If some of the subsets* $\mathcal{V}_n$ *contain more than one element, a number of positive coefficients* ρ_{kn} *are still undetermined. They are fixed by the introduction of the following additional relations :*

$$\frac{R_{k_1}}{\beta_{k_1}} = \frac{R_{k_2}}{\beta_{k_2}} \quad \forall\, k_1, k_2 \in \mathcal{U}^+, \qquad R_k = \sum_n \rho_{kn} R_{kn}$$

where $\mathcal{U}^+$ *is a well-chosen subset of users.*

The derivation of maximum balanced rates requires the computation of an appropriate set of coefficients $\{\alpha_k\}$ such that the allocation rule given by algorithm 3.5 provides only *positive sharing coefficients* ρ_{kn}, with $\mathcal{U}^+ = \{1, \cdots, K\}$. Let $\mathcal{U}^-$ and $\mathcal{U}^+$ be two user sets with low and high normalized rates $\frac{R_k}{\beta_k}$, respectively. Starting from initial priorities $\alpha_k^{(0)}$, the relative priorities of the users in $\mathcal{U}^-$ are progressively increased, allowing the transfer of selected subchannels from $\mathcal{U}^+$ to $\mathcal{U}^-$, until the balanced rates constraints are all satisfied. The next algorithm specifies how these transfers should be handled to reach the final solution after a finite number of steps.

Algorithm 3.6 *Optimal subchannel assignment with balanced rates constraints*

- *Set* $i = 0$*, start with an arbitrary set of priority coefficients* $\{\alpha_k^{(0)}\}$
- *Compute the initial sharing coefficients* $\left\{\rho_{kn}^{(0)}\right\}$ *according to algorithm 3.5, with* $\mathcal{U}^+ = \emptyset$*. The initial sharing coefficients are all 0 or 1. The maximum weighted rates for each subchannel are* $\left\{t_n^{(0)}\right\}$.
- *Compute the total user rates* $\left\{R_k^{(0)}\right\}$ *and the maximum normalized user rate* $\overline{R}_{max}^{(0)}$ *:*

$$\left\{R_k^{(0)}\right\} = \sum_n \rho_{kn}^{(0)} R_{kn} \qquad \overline{R}_{max}^{(0)} = \max_k \left(\frac{R_k^{(0)}}{\beta_k}\right)$$

- *Separate the users in two disjoint sets* $\mathcal{U}^+$ *and* $\mathcal{U}^-$ *:*

$$\mathcal{U}^+ = \left\{ k \mid \frac{R_k^{(0)}}{\beta_k} = \overline{R}_{max}^{(0)} \right\} \qquad \mathcal{U}^- = \left\{ k \mid \frac{R_k^{(0)}}{\beta_k} < \overline{R}_{max}^{(0)} \right\}$$

- *While* $\mathcal{U}^+ \neq \{1, \cdots, K\}$*, do :*
  - *Subdivide the user set* $\mathcal{U}^+$ *in two disjoint subsets* $\mathcal{U}_1^+$ *and* $\mathcal{U}_2^+$ *where :*
    * $\mathcal{U}_1^+$ *is the larger subset of* $\mathcal{U}^+$ *whose members share only subchannels with other members of* $\mathcal{U}_1^+$.
    * *The members of* $\mathcal{U}_2^+$ *share one or more subchannels with a member of* $\mathcal{U}^-$ *or with other members of* $\mathcal{U}_2^+$.
  - *Define* $\mathcal{U} = \mathcal{U}^- \bigcup \mathcal{U}_2^+$ *and* $\mathcal{S}$ *as the set of subchannels allocated to the users in* $\mathcal{U}_1^+$*, and compute* $\pi^{(i)}$ *as :*

$$\pi^{(i)} = \min_{(n \in \mathcal{S}),\, (k \in \mathcal{U})} \left(\frac{t_n^{(i)}}{\alpha_k^{(i)} R_{kn}} \right) > 1$$

    where the minimum is found for user k^* *and subchannel* n^*.
  - *Update the priority coefficients as follows :*

$$\alpha_k^{(i+1)} = \pi^{(i)}\, \alpha_k^{(i)}\, (k \in \mathcal{U}) \qquad \alpha_k^{(i+1)} = \alpha_k^{(i)}\, (k \in \mathcal{U}_1^+)$$

  - *Increase* $\rho_{k^*n^*}$ *as much as possible, while adapting the sharing coefficients* ρ_{kn} *of the other subchannels to maintain the equality of the normalized user rates in* $\mathcal{U}^+$*, until one of the following events happen :*

    case 1 $\rho_{k^*n^*} = 1$. *In that case, subchannel* n^* *can be fully transferred to user* k^*. *The remaining sharing coefficients just need to be updated to maintain equal normalized rates* $\frac{R_k}{\beta_k}$ *for the users in* $\mathcal{U}^+$.

    case 2 *One of the other non-zero sharing coefficients* ρ_{kn} *is decreased down to zero. A further increase of* $\rho_{k^*n^*}$ *would then break the equality of the normalized rates* $\frac{R_k}{\beta_k}$ *for the users in* $\mathcal{U}^+$. *The members of* $\mathcal{U}^+$ *sharing subchannel* n^* *with user* k^* *are placed in the subset* $\mathcal{U}_2^+$.

    case 3 *The normalized rate* $\frac{R_{k^*}}{\beta_k}$ *reaches the same value as that of the users in* $\mathcal{U}^+$. *User* k^* *is then incorporated into the set* $\mathcal{U}^+$.

– *Update* $\left\{\rho_{kn}^{(i+1)}\right\}$, $\left\{t_n^{(i+1)}\right\}$, $\left\{R_k^{(i+1)}\right\}$, $\overline{R}_{max}^{(i+1)}$, *and set* $i = i + 1$.

An example is illustrated in Figure 3.10 to clarify the mechanisms associated with algorithm 3.6. A set of $N = 8$ subchannels should be allocated to $K = 4$ users. The rates R_{kn} are given in the first matrix. The normalization coefficients β_k are all set to 1, which corresponds to a common rate constraint. The initial priority coefficients $\alpha_k^{(0)}$ are chosen arbitrarily. With these priority coefficients, the allocation rule (algorithm 3.5) assigns each subchannel to a single user : the sharing coefficients $\rho_{kn}^{(0)}$ are all 0 or 1. The total rates $R_k^{(0)}$ are all different, with a maximum for user 2. The user subsets are thus $\mathcal{U}^+ = \mathcal{U}_1^+ = \{2\}$ and $\mathcal{U}^- = \{1, 3, 4\}$. In step 1, the coefficients α_1, α_3 and α_4 are increased simultaneously until $\alpha_1^{(1)} R_{15} = \alpha_2^{(0)} R_{25}$. The allocation rule allows then the transfer of subchannel 5 from user 2 to user 1. The transfer is full here ('case 1' in algorithm 3.6), i.e. ρ_{25} goes from 1 to 0 and ρ_{15} goes from 0 to 1. The new total rates $R_k^{(1)}$ are again all different, with a maximum for user 2. The user subsets are unchanged. In step 2, the same coefficients α_1, α_3 and α_4 are increased together until $\alpha_1^{(2)} R_{17} = \alpha_2^{(1)} R_{27}$. Now the transfer of subchannel 7 from user 2 to user 1 is partial : with sharing coefficients $\rho_{17}^{(2)} = 0.13$ and $\rho_{27}^{(2)} = 0.87$, the updated total rates $R_1^{(2)}$ and $R_2^{(2)}$ are found to be equal ('case 3' in algorithm 3.6). The user subsets are now $\mathcal{U}^+ = \mathcal{U}_1^+ = \{1, 2\}$ and $\mathcal{U}^- = \{3, 4\}$. In step 3, coefficients α_3 and α_4 are increased until $\alpha_4^{(3)} R_{44} = \alpha_1^{(2)} R_{14}$. Subchannel 4 is then partially transferred from user 1 to user 4 while the sharing coefficients associated with subchannel 7 are updated to maintain equal total rates for users 1 and 2. The user subsets are then $\mathcal{U}^+ = \mathcal{U}_1^+ = \{1, 2, 4\}$ and $\mathcal{U}^- = \{3\}$. In step 4, the coefficient α_3 is increased until $\alpha_3^{(4)} R_{31} = \alpha_2^{(3)} R_{21}$. Subchannel 1 is then partially transferred from user 2 to user 3. The sharing coefficients associated with subchannels 4 and 7 are updated to maintain equal total rates for users 1, 2 and 4. For $\rho_{31} = 0.6$, the coefficient ρ_{17} is reduced to 0 and can not be reduced further ('case 2' in algorithm 3.6). Higher values of ρ_{31} would compromise the equality of the total rates R_k for users 1, 2 and 4. The user subsets become $\mathcal{U}_1^+ = \{1, 4\}$ and $\mathcal{U}_2^+ = \{2\}$. In step 5, coefficients α_2 and α_3 are increased until $\alpha_3^{(5)} R_{33} = \alpha_1^{(2)} R_{13}$. Subchannel 3 is then partially transferred from user 1 to user 3, until subchannel 4, that was previously shared by users 1 and 4, is fully transferred to user 1 in order to maintain the equality of the total rates for users 1, 2 and 4 ('case 2' again). The subsets become $\mathcal{U}_1^+ = \{4\}$ and $\mathcal{U}_2^+ = \{1, 2\}$. Finally, in step 6, coefficients

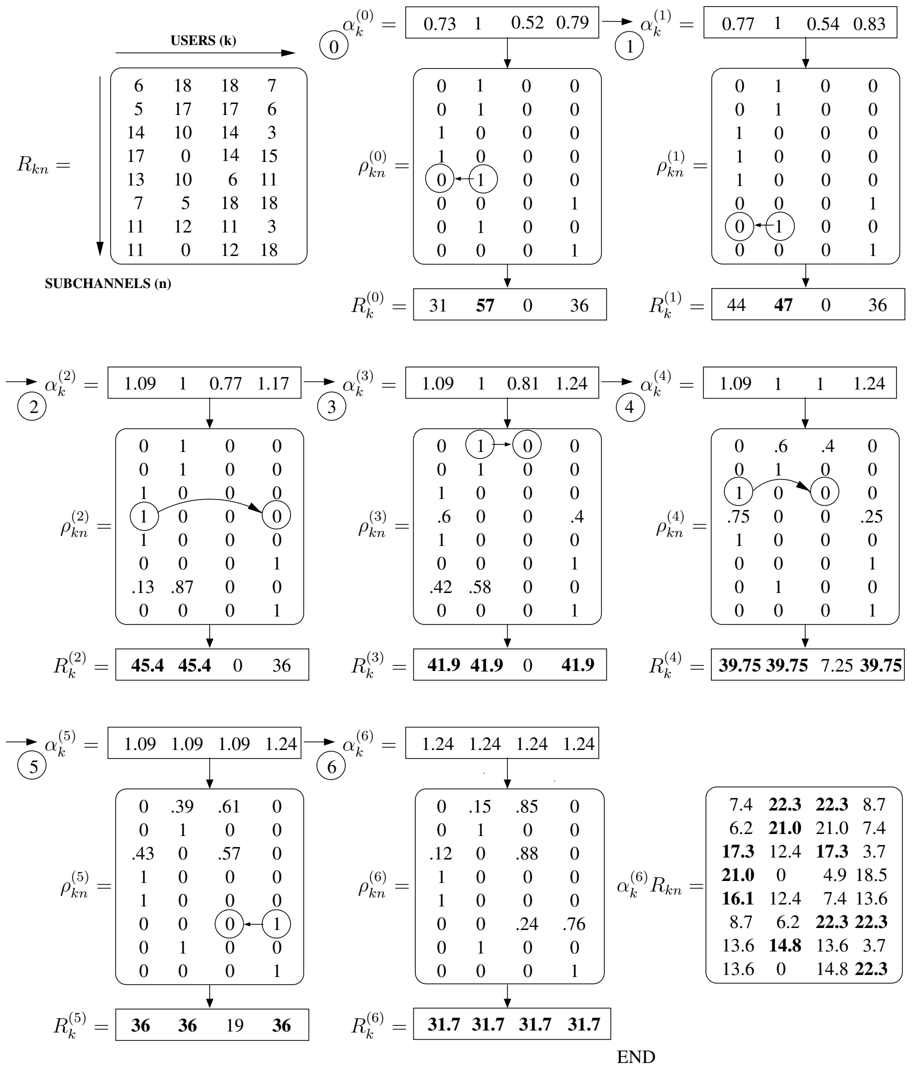

Figure 3.10: *Derivation of the optimal assignment of 8 subchannels to 4 users, with an equal rate constraint ($\beta_k = 1 \,\forall\, k$), using algorithm 3.6*

α_1, α_2 and α_3 are increased until $\alpha_3^{(6)} R_{36} = \alpha_4^{(2)} R_{46}$. Subchannel 6 is then partially transferred to user 3. With well-chosen sharing coefficients for subchannels 1, 3 and 6, all total rates $R_k^{(6)}$ are now equal ('case 3'). User 3 is added to the set $\mathcal{U}^+$ and the algorithm is terminated. The last matrix gives the weighted rates $\alpha_k^{(6)} R_{kn}$ associated with the final solution.

The algorithm proposed here is actually a special case of the well-known *simplex algorithm* used in linear optimization. Its convergence properties are thus identical to those of the simplex algorithm. The simplex algorithm moves along the edges of the polyhedron defined by the constraints, from one vertex to another, while decreasing the value of the objective function at each step. The exact solution is obtained after a finite number of steps. The implementation proposed here is much more efficient than a general-purpose simplex algorithm as the specific structure of the problem (objective function and constraints) has been taken into account.

The number of iterations required to reach the exact solution can be prohibitive, however, if the total number of subchannels is very high ($N \gg 1$) and if the initial priority coefficients $\boldsymbol{\alpha}^{(0)}$ are far from the solution. For this reason, it may be desirable to use an alternative method to obtain an approximate solution $\hat{\boldsymbol{\alpha}}$ that will serve as initial step for algorithm 3.6. Actually, for a large N, the total rates R_k can be considered on a large scale as approximately continuous functions of the priority coefficients α_k. For each vector $\boldsymbol{\alpha}^{(i)}$, a Jacobian matrix $\frac{\partial \boldsymbol{R}}{\partial \boldsymbol{\alpha}}$ can be computed, that approximates the behavior of the total rate functions R_k in the neighbourhood of $\boldsymbol{\alpha}^{(i)}$. A Newton-Raphson updating algorithm, similar to algorithm 3.2, can then be used to obtain a new vector $\boldsymbol{\alpha}^{(i+1)}$ that should be closer to the desired solution. After a few iterations of the Newton-Raphson updating strategy, the obtained priority coefficients $\boldsymbol{\alpha}^{(i)}$ are close to the solution, but can not get closer because of the discontinuity of the allocation rule. Further updates of the priority coefficients are then generated by algorithm 3.6, which provides the exact solution with a small number of iterations. The complete procedure for the computation of maximum balanced rates is finally given as follows :

1. Initialization : set $\boldsymbol{\alpha}^{(0)} = [1/R_1^1, \cdots, 1/R_K^1]^T / \sum_k (1/R_k^1)$.

2. Rough solution : update the relative priorities according to

$$\boldsymbol{\alpha}^{(i+1)} = \boldsymbol{\alpha}^{(i)} - \lambda_i \left(\frac{\partial \mathbf{F}}{\partial \boldsymbol{\alpha}} \right)^{-1}_{\boldsymbol{\alpha} = \boldsymbol{\alpha}^{(i)}} \mathbf{F}\left(\boldsymbol{\alpha}^{(i)}\right) \tag{3.81}$$

where the vector function $\mathbf{F}(\boldsymbol{\alpha})$ is defined in (3.46). Continue while convergence is observed. Set $\hat{\boldsymbol{\alpha}} = \boldsymbol{\alpha}^{(i+1)}$.

3. Final solution : apply algorithm 3.6 with $\boldsymbol{\alpha}^{(0)} = \hat{\boldsymbol{\alpha}}$.

The Jacobian matrix $\frac{\partial \boldsymbol{R}}{\partial \boldsymbol{\alpha}}$ can be obtained as follows. Let $\mathcal{S}_k$ be the set of subchannels allocated to user k by algorithm 3.5 and let $n_{k,k'}$ be the subchannel index defined by :

$$n_{k,k'} = \arg\min_{n \in \mathcal{S}_k} \frac{\alpha_k R_{kn}}{\alpha_{k'} R_{k'n}}. \tag{3.82}$$

In other words, increasing the relative priority of user k' with respect to that of user k will firstly prompt the transfer of subchannel $n_{k,k'}$ from user k to user k'. With this definition, the entries of the Jacobian matrix $\frac{\partial \boldsymbol{R}}{\partial \boldsymbol{\alpha}}$ can be shown to be :

$$\frac{\partial R_k}{\partial \alpha_k} \approx \frac{1}{2} \sum_{k \neq k'} \left[\frac{R_{kn_{k,k'}} + R_{kn_{k',k}}}{\alpha_{k'} \left(\frac{R_{k'n_{k,k'}}}{R_{kn_{k,k'}}} - \frac{R_{k'n_{k',k}}}{R_{kn_{k',k}}} \right)} \right] \tag{3.83}$$

$$\frac{\partial R_{k'}}{\partial \alpha_k} \approx -\frac{1}{2} \frac{R_{k'n_{k,k'}} + R_{k'n_{k',k}}}{\alpha_{k'} \left(\frac{R_{k'n_{k,k'}}}{R_{kn_{k,k'}}} - \frac{R_{k'n_{k',k}}}{R_{kn_{k',k}}} \right)} \quad \forall k' \neq k \tag{3.84}$$

3.6.2 Power-sum constraint

The authors of [53] propose an original method to compute the maximum common rate in multiple access channels with a constraint on the power sum $\bar{P}$. Individual power budgets $\{\bar{P}_k^{(0)}\}$ with $\sum_k \bar{P}_k = \bar{P}$ are fixed arbitrarily. The IMUWF algorithm [45] is then used to maximize the sum-rate $\sum_k R_k$ with the selected individual power constraints. The obtained power allocation is known to be of the FDMA type, i.e. power is allocated to the different users in separate frequency bands. The obtained user rates, however, can be very different. The total power $\bar{P}$ is then redistributed in parts $\{\bar{P}_k^{(i+1)}\}$ so as to enforce the same rate to all users, and the IMUWF algorithm is run again with the new set of individual power budgets. With an appropriate individual power updating strategy, the algorithm provides identical rates to all users after a few iterations. The extension of this method to the derivation of maximum balanced rates is trivial.

3.6.3 Individual power constraint

This problem can be solved easily once the optimal partition of the frequency spectrum among the different users is known : the optimal spectrum for each user is just the water-filling spectrum within the assigned band. Unfortunately, the derivation of the optimal frequency bands is extremely complex : K^N different partitions are possible and should be tested in turn. In [46], the maximization of the aggregate data rate R_α with both individual power constraints and an FDMA constraint is formulated as follows :

$$\{P_{kn}, \rho_{kn}\} = \arg \max_{P_{kn} \geq 0, \rho_{kn} \geq 0} \left[\sum_{k=1}^{K} \alpha_k \sum_{n=1}^{N} \rho_{kn} \log \left(1 + \frac{P_{kn} h_{kn}^2}{\rho_{kn} \sigma_n^2} \right) \right] \quad (3.85)$$

subject to

$$\sum_n P_{kn} = \bar{P}_k \quad \forall\, k \qquad \sum_k \rho_{kn} = 1 \quad \forall\, n \quad (3.86)$$

This formulation corresponds again to the continuous relaxation of the initial integer programming problem. As demonstrated in [46], the objective function in (3.85) is a concave function in (P_{kn}, ρ_{kn}). As the constraints in (3.86) are linear, this optimization problem is a standard convex programming problem and the global optimum can be obtained with a standard convex programming algorithm.

As usual, the derivation of maximum balanced rates requires the computation of relative priorities α_k such that the optimal power allocation in (3.85) offers balanced rates to the different users. This problem is extremely difficult and is not further developed in this work.

3.7 Applications to the powerline channel

3.7.1 Regular-pattern network with matched terminations

The case of a regular-pattern wireline access network with matched terminations is firstly considered. The basic network structure is given in Figure 2.11. The example considered here includes $\bar{K} = 20$ derivations, identical cable segments of length $d_k = d'_k = 15$ m, and ideal matched terminations. The lossy cables parameters are $\kappa = 2.3$, $\delta_d = 0.02$ and $\delta_{c1} = 85\sqrt{\text{Hz}}$ (see Chapter 2). The top of Figure 3.11 gives the channel frequency responses $|H_k(\omega)|^2$ in the bandwidth $[0, B]$ with $B = 10$ MHz. Through the combined effect of cable losses and multiple reflections on the cable derivations, the

Table 3.1: *Maximum balanced rates (in Mbits/s) for* $\mathcal{C}_4 = \{5, 10, 15, 20\}$

Constraint	User 5	User 10	User 15	User 20	%
Flat SU	127.41	59.82	13.12	4.05	100
PSD-sum	71.52	33.58	7.36	2.27	56
Flat FDMA	55.77	26.19	5.74	1.77	44
Flat TDMA	31.85	14.96	3.28	1.01	25
SU	127.41	59.85	16.04	7.06	100
Power-sum ($4\bar{P}$)	84.47	39.68	10.63	4.68	66
Individual power	77.94	36.61	9.81	4.32	61
Power-sum ($\bar{P}$)	65.99	31.00	8.31	3.66	52
TDMA	31.85	14.96	4.01	1.77	25

channel gains for the remote users can go below -100 dB at some frequencies. The noise level is chosen as -120 dBm/Hz.

Two kinds of power constraints are put on the SU transmission power : a maximum transmission PSD of $\overline{\gamma} = -60$ dBm/Hz ('flat PSD'), or a maximum transmission power of $\bar{P} = \overline{\gamma}\, B = 10$ mW ('water-filling PSD'). Figure 3.13 gives the evolution of the SU capacities R_k^1 for the two kinds of power constraints. The SU capacity decreases rapidly for the remote users. As expected, the water-filling solution provides a higher rate with respect to the flat PSD solution only for the users with a low received SNR, i.e. the most remote users. The SU water-filling PSD's (normalized with respect to $\overline{\gamma}$) are illustrated on the top of Figure 3.12 for users 5, 10, 15 and 20.

In a multiuser scenario, a subset $\mathcal{C}_K \subset \left\{1, \cdots, \bar{K}\right\}$ of $K \leq \bar{K}$ active users transmit their signals simultaneously. Table 3.1 gives the maximum balanced rates for $\mathcal{C}_4 = \{5, 10, 15, 20\}$ and different types of constraints, and compares them with the SU and TDMA rates. Figure 3.14 gives the multiuser gain g vs. K for various sets of active users $\mathcal{C}_K$. The main curves correspond to $\mathcal{C}_K = \{1, 2, \cdots, K\}$, i.e. the $K \leq \bar{K}$ closest modems are supposed to be active. The multiuser gain increases with K, and is much larger when the user channels in $\mathcal{C}_K$ are very different. Comparing these different curves, we get some insight in the respective gains that can be expected from :

- The simultaneous transmission by all users (with the same total power $\bar{P}$) instead of transmission in separate time slots.

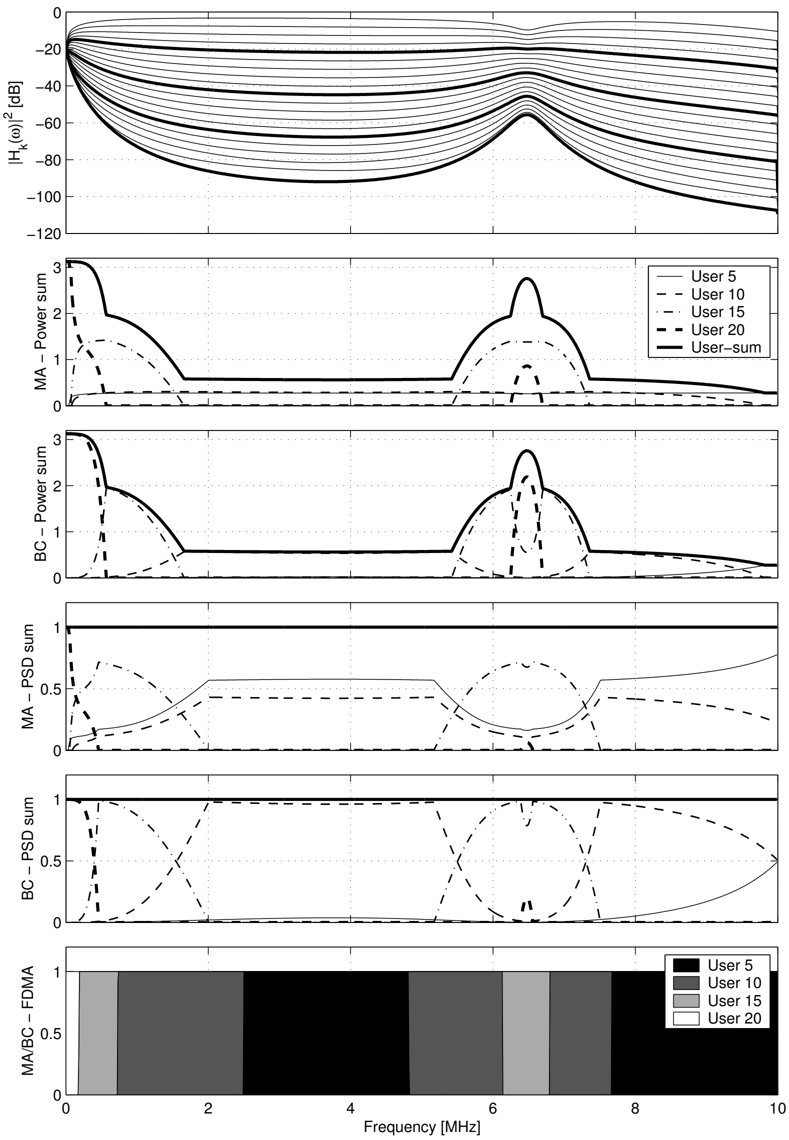

Figure 3.11: *Channel frequency responses (figure 1), MA and BC power allocations for $\mathcal{C}_4 = \{5, 10, 15, 20\}$: power-sum constraint (figures 2-3), PSD-sum constraint (figures 4-5), and flat-FDMA power allocation (figure 6).*

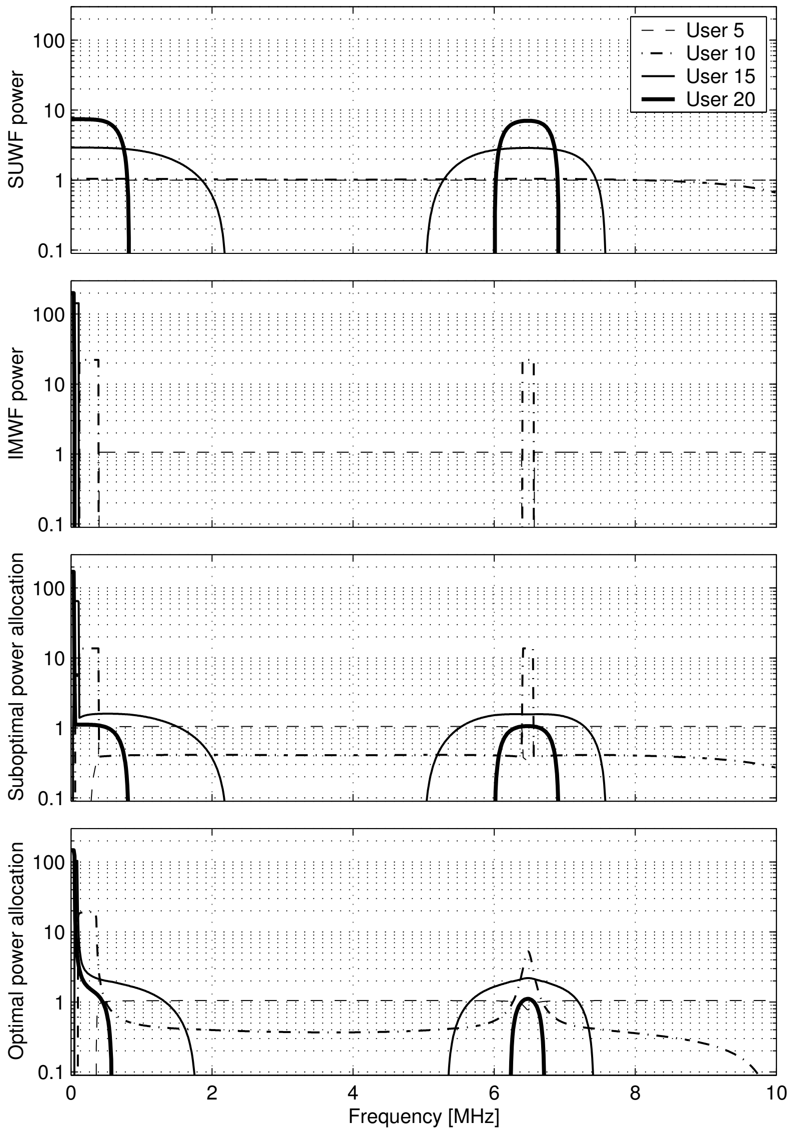

Figure 3.12: *Power allocations for $\mathcal{C}_4 = \{5, 10, 15, 20\}$ and individual power constraints*

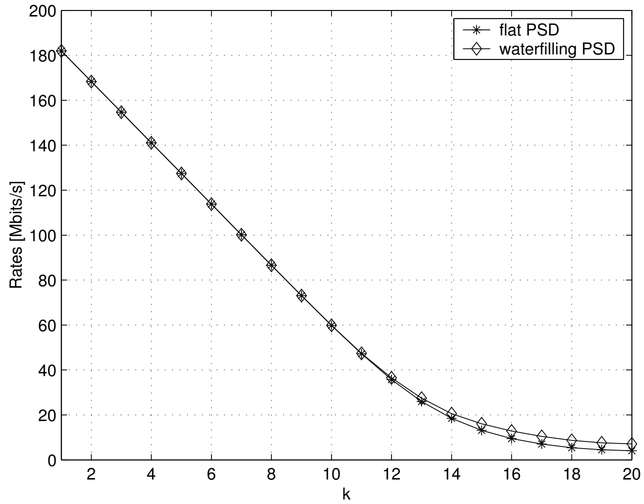

Figure 3.13: *Single user rates vs. user index k*

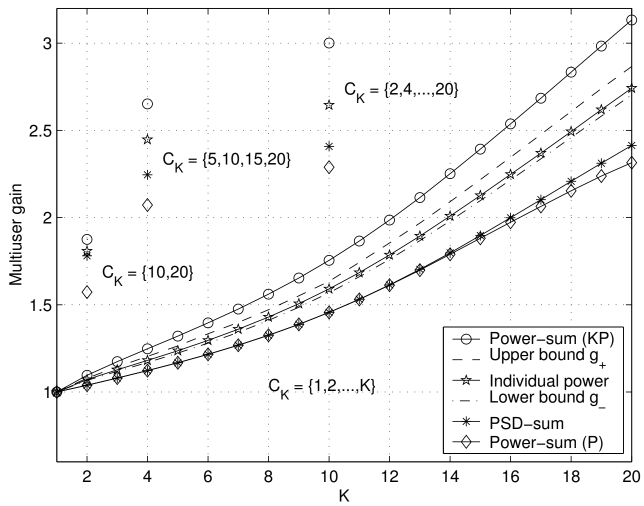

Figure 3.14: *Multiuser gain vs. number of active users K*

- The allocation of $K\bar{P}$ to the users ($\bar{P}$ for each) instead of $\bar{P}$.
- The redistribution of the total power $K\bar{P}$ in unequal parts.

The dashed lines give the lower and upper bounds g_- and g_+ obtained by equations (3.72) and (3.73).

Figure 3.11 also gives the results of the optimal MA and BC power allocations (normalized with respect to $\overline{\gamma}$) for $\mathcal{C}_4 = \{5, 10, 15, 20\}$, and three kinds of constraints (power-sum, PSD-sum, and flat-FDMA). The normalized optimal PSD-sum is also given (upper lines). As expected, the users with the weakest channels concentrate their transmission power in the best parts of the frequency spectrum while the users with the best channels (and lowest priorities) can make use of the remaining frequencies. The remote users require more power in the BC channel (where they are decoded first) than in the MA channel (where they are decoded last).

The lower part of Figure 3.12 gives the optimal MA power allocation for the same user set, but with constraints on the individual powers. As the remote users tend to concentrate their power $\bar{P}$ in a small fraction of the available bandwidth, a logarithmic scale was chosen for the vertical axis. This power allocation was obtained by algorithm 3.3. The suboptimal power allocation obtained by algorithm 3.4 is given in the third graph. It appears as a compromise between the SUWF power allocation (first graph) and the IMWF allocation (second graph). The rate loss associated with the suboptimal power allocation is negligible (less than 0.1 %). A smart redistribution of the total power $4\bar{P}$ between the 4 users would allocate less power and more bandwidth to the remote users (who benefit from the best frequencies), leading to improved balanced rates as illustrated in Table 3.1. Forcing each user to transmit with the same power $\bar{P}$ actually decreases the 'power price' associated with the remote users, and the excess power that needs to be allocated to these remote users is accumulated in a narrow frequency band, giving rise to very concentrated power allocations.

3.7.2 Complex network with open terminations

Similar results are now given for the case of the example powerline access network presented in Figure 2.12. This network has the same total length (300 meter) and the same number of derivations ($\bar{K} = 20$) as in the previous example, but the lengths of the different cable segments are not uniform, and the unused terminations are assumed to be open. The $K = 5$ active users are in positions $2, 5, 10, 15$ and 20. The 5 end-to-end channel transfer

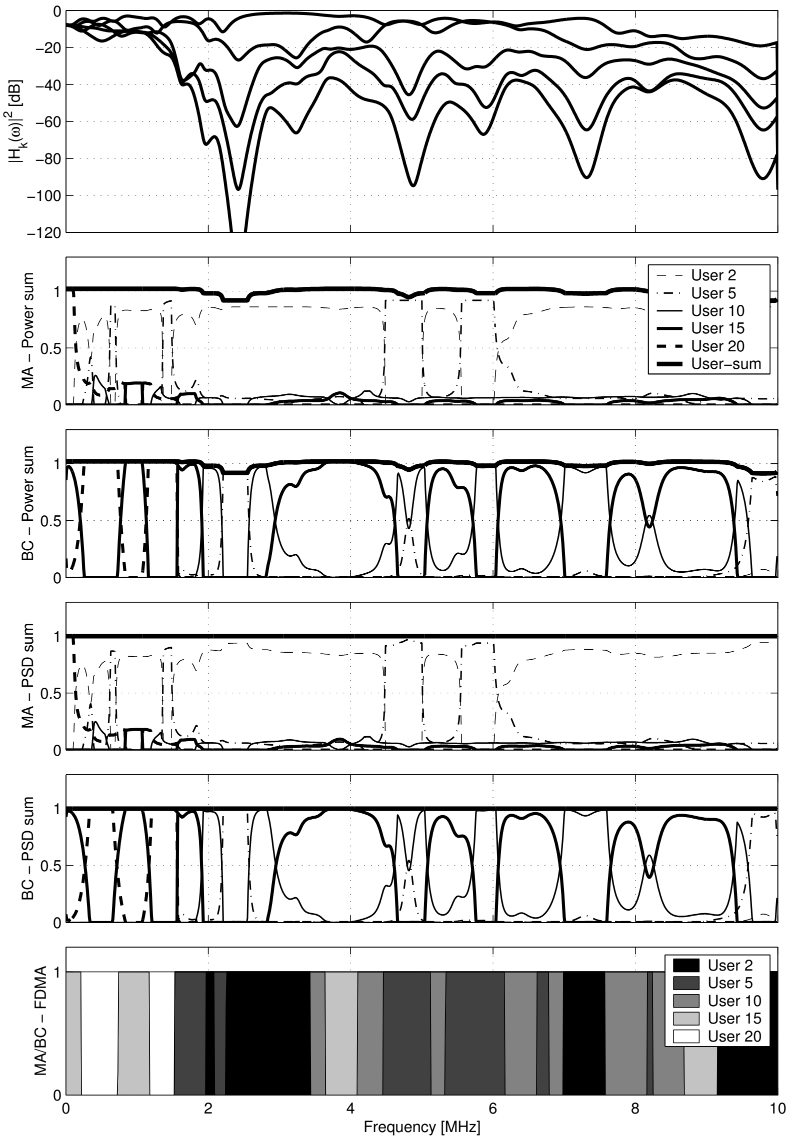

Figure 3.15: *Channel frequency responses (figure 1), MA and BC power allocations for $\mathcal{C}_4 = \{5, 10, 15, 20\}$: power-sum constraint (figures 2-3), PSD-sum constraint (figures 4-5), and flat-FDMA power allocation (figure 6).*

Table 3.2: *Maximum balanced rates (in Mbits/s) for* $\mathcal{C}_5 = \{2, 5, 10, 15, 20\}$

Constraint	User 2	User 5	User 10	User 15	User 20	%
Flat SU	175.09	149.36	107.03	73.33	49.63	100
PSD-sum	54.76	46.71	33.47	22.93	15.52	31
Flat FDMA	47.56	40.57	29.07	19.92	13.48	27
Flat TDMA	35.02	29.87	21.41	14.67	9.93	20
SU	175.09	149.36	107.13	74.29	52.64	100
Power-sum ($5\bar{P}$)	61.94	52.84	37.90	26.28	18.62	35
Individual power	58.77	50.14	35.96	24.94	17.67	34
Power-sum ($\bar{P}$)	54.33	46.34	33.24	23.05	16.33	31
TDMA	35.02	29.87	21.43	14.86	10.53	20

functions (see Figure 2.23) are reported on the top of Figure 3.15, in the bandwidth $[0, B]$ with $B = 10$ MHz. The noise level is again assumed to be -120 dBm/Hz in the whole bandwidth.

Table 3.2 gives the maximum balanced rates associated with the different types of power constraints. Figure 3.15 (to be compared with Figure 3.11) gives the optimal MA and BC power allocations (normalized with respect to $\overline{\gamma}$) for three kinds of constraints (power-sum, PSD-sum, and flat-FDMA). Finally, Figure 3.16 gives the optimal SUWF and IMWF power allocations, and the MA balanced power allocations with individual power constraints as given by Algorithms 3.3 and 3.4.

3.8 Conclusion

This chapter introduces the concept of *balanced capacity* to characterize the performance of multiuser channels. This concept appears as a smart compromise between the global system efficiency and fairness requirements among the users. The balanced capacity of a multiuser channel is actually a specific point on the boundary of the capacity region, corresponding to a specific (but a priori unknown) set of user relative priorities α_k. The uplink (multiple access channel) and downlink (broadcast channel) balanced capacities of wireline multiaccess networks are computed and compared *for an arbitrary number of users.*

A detailed analysis of the optimal power allocation (for a given set of relative priorities) in a *memoryless multiuser channel* is first given. The power

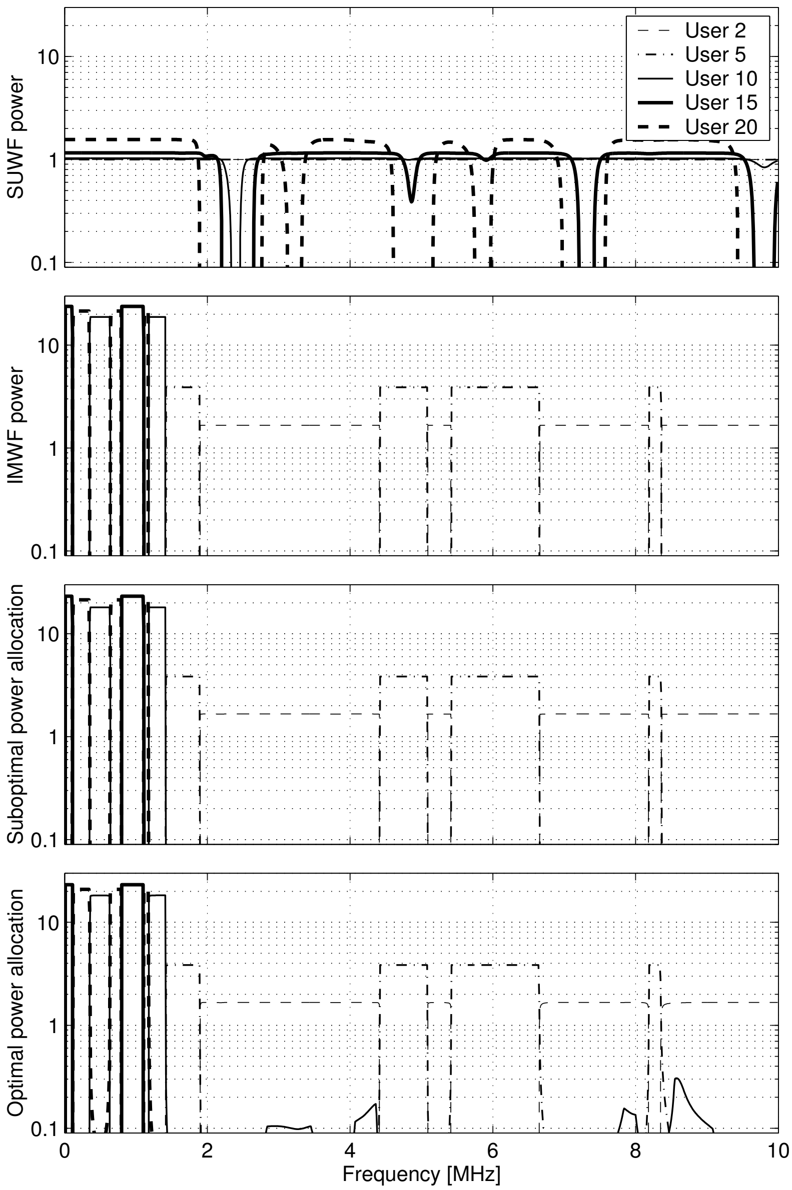

Figure 3.16: *Power allocations for* $\mathcal{C}_5 = \{2, 5, 10, 15, 20\}$ *and individual power constraints*

allocation algorithm is shown to be extremely simple, and an explicit expression of the corresponding powers and rates is available, as a function of the priorities α_k. These maximum rates are identical for the uplink and the downlink, but the respective power allocations are distinct. An iterative algorithm for the computation of the maximum balanced rates has been proposed : the user relative priorities α_k are updated at each iteration, which moves the rate distribution along the boundary of the capacity region until the balanced rate constraints are satisfied. The balanced capacity of the memoryless multiuser channel is found to be obtained within a few iterations.

This algorithm is then extended to the case of *frequency selective multiuser channels*. Three kinds of power constraints (with increasing complexity) are considered : a constraint on the total transmitted power spectral density, a constraint on the total transmitted power, and individual constraints on the transmitted powers. In the first scenario, the extension of the initial algorithm is trivial. The second scenario requires an additional step (*multiuser water-filling*) at each iteration, in order to specify the optimal distribution of the total allocated power along the frequency axis. In the third scenario, the extension of the initial algorithm is still possible by using the concept of *equivalent channel*, but the obtained method appeared to converge very slowly. An alternative algorithm, based on the iterative multiuser water-filling algorithm, has been proposed to compute a suboptimal power allocation, and the rate loss was found to be negligible.

Finally, the specific problem of FDMA balanced capacity computation with a PSD-sum constraint was analyzed separately and found to be equivalent to an optimal subchannel assignment problem. A fast (but tricky) algorithm was given, that is able to find the solution after a finite number of steps.

Results have been provided for a powerline access network with $K = 20$ users. A significant rate gain was found with respect to the trivial TDMA solution, which definitely proves the importance of a smart power allocation in a multiuser frequency selective channel.

Chapter 4

Multiple Access and Modulation Techniques

4.1 Introduction

Current powerline communication systems are characterized by a random multiple access method handled by the higher layer protocols. These techniques are more or less related to TDMA (Time Domain Multiple Access), in the sense that different users transmit their signals in separate time intervals. This method is quite simple to implement, but the obtained bit rates are suboptimal, as pointed out in Chapter 3. A better performance can be expected if all modems are allowed to transmit simultaneously.

In this chapter, a general transmission scheme is proposed for the multiuser uplink. Mutually orthogonal signatures are used by the subscriber modems to map the original binary data into spectrally shaped continuous waveforms and to allow the multiuser signal separation at the receiver. The effect of the frequency-selective channels and that of the receiver sampling unit are incorporated into the model. This provides a discrete equivalent model relating the initial data symbol streams produced by the different NTs to the received samples obtained at the LT.

The extension to downstream transmission is immediate : for a given downstream receiver, all signal components transmitted by the LT are just filtered by the same physical channel.

4.2 The multiple access model

The proposed multiple access model is depicted in Figure 4.1.

4.2.1 Bits, symbols and signatures

Binary data $d_k(n)$ are produced by the channel coder of each subscriber modem at a rate of R_k bits per second with $k \in \{1, \cdots, K\}$. The effect of error correcting codes is not analyzed in this work. The channel coder is assumed to include an ideal data scrambler, producing a sequence of mutually independent bits.

We assume that a set of N mutually orthogonal signature waveforms are available to ensure multiple access. Each user k is provided with the ability to modulate any subset $\mathcal{C}_k$ of these waveforms. A signature allocation algorithm, located in the central office, selects the appropriate subsets $\mathcal{C}_k$ with

$$\mathcal{C}_k \subseteq \{0, \cdots, N-1\} \text{ and } \mathcal{C}_k \cap \mathcal{C}_{k'} = \emptyset, \; k \neq k' \tag{4.1}$$

and transmits that information to the remote users through a dedicated downstream control channel. The number of signatures allocated to user k is denoted by N_k, with $\sum_k N_k = N$.

In each subscriber modem, the data sequence $d_k(n)$ is transformed into a number of parallel symbol streams $I_p(n)$ produced at a baud rate $1/T$. A given user produces as many parallel symbol streams as there are signatures in the subset $\mathcal{C}_k$. The symbols are obtained from a given PAM constellation according to a given bit coding scheme. The size 2^{b_p} of each constellation is adapted to the channel conditions and the required probability of error. The number of bits b_p associated with the different symbol sequences determines the total bit rate for each user :

$$R_k = \frac{1}{T} \sum_{p \in \mathcal{C}_k} b_p \tag{4.2}$$

Successive symbols of a given sequence are assumed to be mutually independent. The same assumption holds for symbols coming from distinct sequences. The symbol variance is denoted by σ_I^2.

4.2.2 Filter bank modulation

A filter bank (FB) including a set of N synthesis filters $s_p(n)$ defined at a chip rate $1/T_c = N/T$ is used to implement the modulation of multiple

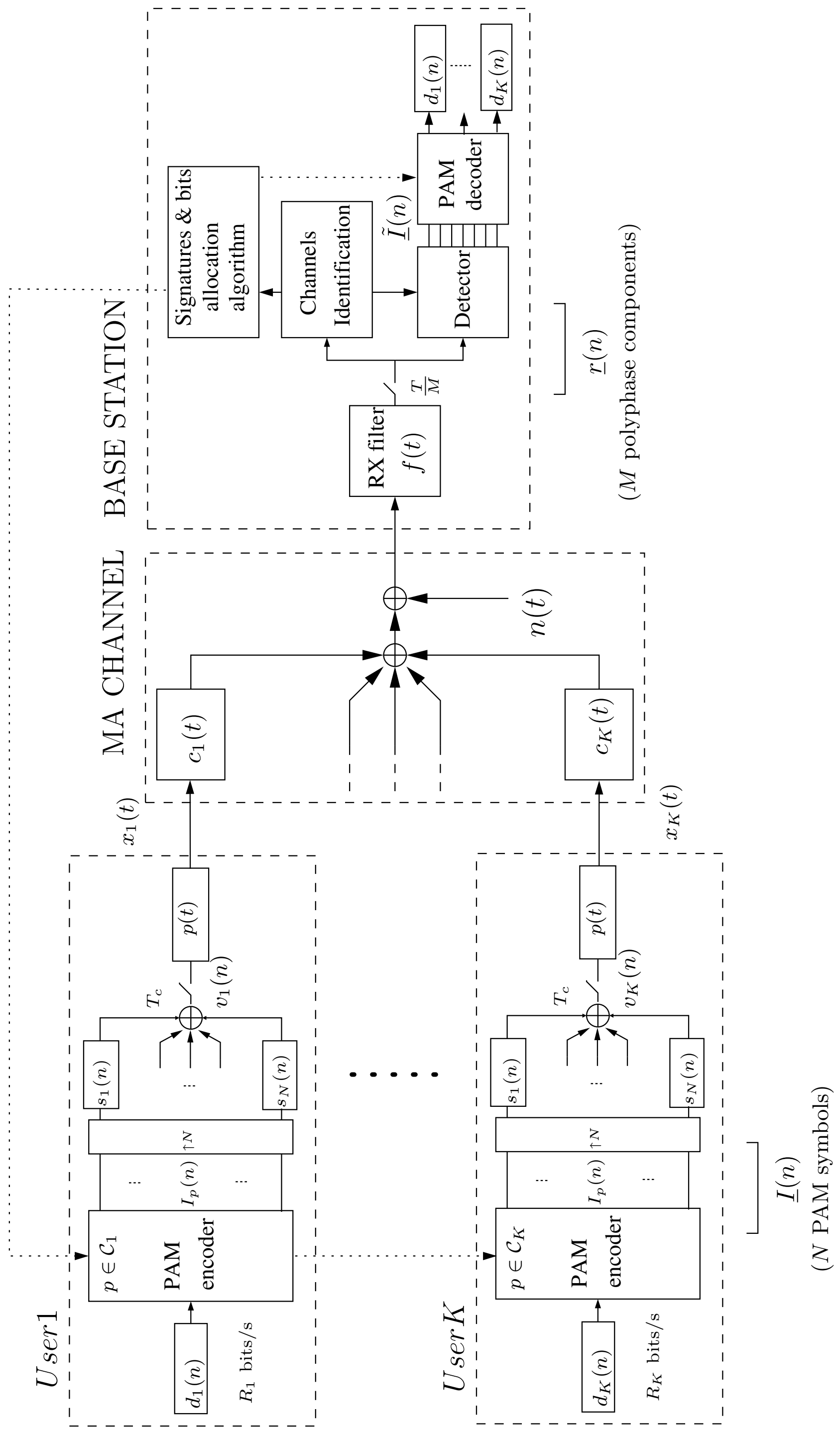

Figure 4.1: *Baseband FB multiple-access transmission scheme*

signatures efficiently in the digital domain. The synthesis filters $s_p(n)$ are considered here as signature codes. The samples produced by the synthesis operation are given by

$$v_k(n) = \sum_{p \in \mathcal{C}_k} \sum_{m=-\infty}^{+\infty} I_p(m)\, s_p(n - mN). \tag{4.3}$$

Splitting this sequence into its N type 1 polyphase components, we get

$$v_{\rho k}(n) = v_k(nN + \rho) = \sum_{p \in \mathcal{C}_k} \sum_{m=-\infty}^{+\infty} I_p(m)\, s_{\rho p}(n - m) \tag{4.4}$$

where $s_{\rho p}(m) = s_p(mN + \rho)$ and $\rho \in [0, N-1]$. Using z-transforms of the above quantities, we write :

$$V_{\rho k}(z) = \sum_{p \in \mathcal{C}_k} S_{\rho p}(z) I_p(z) \tag{4.5}$$

where $V_{\rho k}(z)$, $S_{\rho p}(z)$ and $I_p(z)$ are the z-transformed sequences $v_{\rho k}(n)$, $s_{\rho p}(n)$ and $I_p(n)$, respectively. Let $\underline{\underline{\mathrm{S}}}(z)$ be the $N \times N$ FB polyphase matrix obtained with the N polyphase sequences of the N synthesis filters, i.e.

$$\underline{\underline{\mathrm{S}}}(z) = \left[\ \underline{\mathrm{S}}_1(z) \quad \cdots \quad \underline{\mathrm{S}}_N(z)\ \right] \tag{4.6}$$

$$\underline{\mathrm{S}}_p(z) = \left[\ S_{1p}(z) \quad \cdots \quad S_{Np}(z)\ \right]^T \tag{4.7}$$

and let $\underline{\mathrm{I}}(z)$ be the $N \times 1$ vector obtained with the N symbol sequences, i.e.

$$\underline{\mathrm{I}}(z) \triangleq \left[I_1(z), \cdots, I_N(z)\right]^T . \tag{4.8}$$

The synthesis operation in (4.4) can be expressed shortly with a matrix notation as :

$$\underline{\mathrm{V}}_k(z) = \underline{\underline{\mathrm{S}}}_k(z)\, \underline{\mathrm{I}}_k(z) \tag{4.9}$$

where

$$\underline{\mathrm{V}}_k(z) \triangleq \left[V_{1k}(z), \cdots, V_{Nk}(z)\right]^T \tag{4.10}$$

$$\underline{\underline{\mathrm{S}}}_k(z) \triangleq \left[\underline{\underline{\mathrm{S}}}(z)\right]_{p \in \mathcal{C}_k} \tag{4.11}$$

$$\underline{\mathrm{I}}_k(z) \triangleq \left[\underline{\mathrm{I}}(z)\right]_{p \in \mathcal{C}_k} . \tag{4.12}$$

In the sequel, we focus on a specific type of synthesis filter banks that fulfill the paraunitary property :

$$\underline{\underline{\mathrm{S}}}(z)\, \underline{\underline{\mathrm{S}}}^H(1/z^*) = \underline{\underline{\mathrm{E}}}_N = \underline{\underline{\mathrm{S}}}^H(1/z^*)\, \underline{\underline{\mathrm{S}}}(z) \tag{4.13}$$

where $\underline{\underline{E}}_N$ stands for the unit matrix of size N. With this interesting property, a bank of N analysis filters matched to the synthesis bank provides the original symbol streams at its N outputs. All signatures in a paraunitary FB can be shown to have the same unit energy :

$$\sum_{n=-\infty}^{+\infty} s_p(n)^2 = \int_0^{2\pi} |S_p\left(e^{j\Omega}\right)|^2 \frac{\mathrm{d}\Omega}{2\pi} = 1 \tag{4.14}$$

where the signature Fourier transform is defined as :

$$S_p\left(e^{j\Omega}\right) = \sum_{n=-\infty}^{+\infty} s_p(n)\, e^{-jn\Omega}. \tag{4.15}$$

The transmitted power is thus unaffected by the FB modulation. Finally, paraunitary filter banks can be shown to preserve the total power spectral density as

$$\sum_{p=1}^{N} |S_p\left(e^{j\Omega}\right)|^2 = N \qquad \forall\ \Omega. \tag{4.16}$$

This implies that, for independent input data symbols with constant variance σ_I^2 on *all signatures*, the resulting transmitted power spectrum is flat.

4.2.3 Examples of filter banks

The choice of a specific set of signatures $s_p(n)$ to implement the multiple access scheme is widely arbitrary. Based on the knowledge of the user channels $c_k(t)$, the optimization of the transmitter could be investigated, leading to the choice of an optimal set of signatures according to some performance criterion in relation with a specific receiver structure (see [55]). This optimization is not considered in this work : the signatures are assumed to be fixed. The only degree of freedom considered here lies in the allocation of the predefined signature set to the different users. The only assumptions made here concerning the signatures is that the associated filter bank satisfies the paraunitary property and that the signatures are limited to a length of $N' \geq N$. For the purpose of illustration and comparison, four kinds of filter banks are considered, with increasing frequency selectivity :

- The **Single Carrier** modulation ($N' = N$) is obtained by letting $\underline{\underline{S}}(z) = \underline{\underline{E}}_N$, which is equivalent to a simple parallel-to-serial conversion. The N signatures correspond here to N successive time slots within a periodic frame of T seconds. The allocation of one or more time slots to each user is equivalent to Time-Division Multiple-Access (TDMA). Here the whole frequency spectrum is covered by all signatures. Nevertheless, the signature allocation has an impact on the system performance as it determines the interference structure of the received signal (relative origin of neighbouring symbols).

- The **Walsh-Hadamard codes** ($N' = N$) are binary : $s_p(n) = \pm\sqrt{\frac{1}{N}}$, and such an orthogonal set of codes exists for N being a power of 2. The synthesis operation is extremely fast for these binary signatures. Figure 4.2 illustrates the Hadamard signatures $s_5(n)$, $s_6(n)$, $s_{21}(n)$ and $s_{22}(n)$ for $N = 64$. The corresponding signature frequency responses $S_p(e^{j\Omega})$ are given in Figure 4.4. The implementation of multiple-access through binary signature codes is actually equivalent to Code-Division Multiple-Access (CDMA).

- The **Discrete Multi Tone (DMT)** modulation ($N' = N$) is based on the (Inverse) Discrete Fourier Transform or (I)DFT. For baseband transmission, the equivalent signatures are given by

$$s_0(n) = \sqrt{\frac{1}{N}} \qquad s_{N-1}(n) = \sqrt{\frac{1}{N}}(-1)^n \tag{4.17}$$

$$s_{2p-1}(n) = \sqrt{\frac{2}{N}}\cos\left(\frac{2\pi np}{N}\right) \qquad s_{2p}(n) = -\sqrt{\frac{2}{N}}\sin\left(\frac{2\pi np}{N}\right) \tag{4.18}$$

with $n \in [1 \cdots N]$ and $p \in [1 \cdots N/2 - 1]$. The synthesis operation is implemented efficiently by means of the Inverse Fast Fourier Transform (IFFT) whose basis functions are

$$s_{p,DMT}(n) = \frac{1}{\sqrt{N}} e^{\frac{2\pi jnp}{N}}, \tag{4.19}$$

with the following complex sequences $J_p(m)$ at the N inputs of the IFFT operator :

$$J_0(m) = I_0(m) \qquad J_{N/2}(m) = I_{N-1}(m) \tag{4.20}$$

$$J_p(m) = \frac{1}{\sqrt{2}}\left(I_{2p-1}(m) + jI_{2p}(m)\right) \qquad J_{N-p}(m) = J_p^*(m). \tag{4.21}$$

Figure 4.3 illustrates the DMT signatures $s_5(n)$, $s_6(n)$, $s_{21}(n)$ and $s_{22}(n)$ for $N = 64$. The corresponding signature frequency responses

$S_p(e^{j\Omega})$ are given in Figure 4.5. The implementation of multiple-access through IDFT basis functions is equivalent to Orthogonal Frequency-Division Multiple-Access (OFDMA).

- The **Perfect Reconstruction Modulated Filter Bank (PRMF)** ($N' = 2N$) is based on a single prototype $p_0(n)$, that is modulated around different frequencies. The prototype can be optimized to provide good spectral properties, e.g. a very high frequency selectivity. The basis functions are given by

$$s_p(n) = p_0(n)\,\cos\left[\frac{\pi}{N}(p+\frac{1}{2})(n-N-\frac{1}{2}) - (-1)^p\frac{\pi}{4}\right] \tag{4.22}$$

with $n \in [1 \cdots 2N]$. Unlike the first three examples, the signatures given by (4.22) have a length of 2 symbol periods. This means that successive modulated symbols overlap in time. This is the price to pay to obtain an increased frequency selectivity. The polyphase matrix associated with this set of signatures can be written as $\underline{\underline{S}}(z) = \underline{\underline{S}}_0 + \underline{\underline{S}}_1 z^{-1}$, while for the first three examples the matrix expansion is limited to the zero-order term $\underline{\underline{S}}_0$. The multiple access scheme associated with PRMF is more or less equivalent to Frequency-Division Multiple-Access (FDMA).

4.2.4 Transmitted signals

The signal $x_k(t)$ transmitted by user k is obtained after digital-to-analog conversion (DAC) through a chip shaping filter $p(t)$:

$$x_k(t) = \sum_{n=-\infty}^{+\infty} v_k(n)\,p(t - nT_c). \tag{4.23}$$

A realistic shaping filter $p(t)$ should include the effect of the analog front end circuitry of the transmitter. A convenient model used for theoretical investigations is the square-root raised cosine Nyquist filter with a roll-off α and a bandwidth given by $B = 0.5\,(1+\alpha)/T_c$. Continuous-time signature waveforms $g_p(t)$ are obtained by combining the signature codes $s_p(n)$ with the shaping filter $p(t)$:

$$g_p(t) = \sum_{n=-\infty}^{+\infty} s_p(n)p(t - nT_c). \tag{4.24}$$

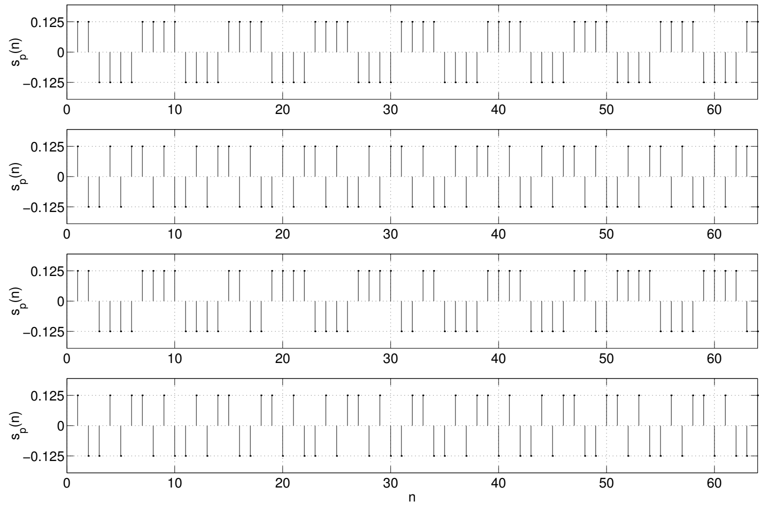

Figure 4.2: *Examples of signatures for the Hadamard filter bank ($N = 64$)*

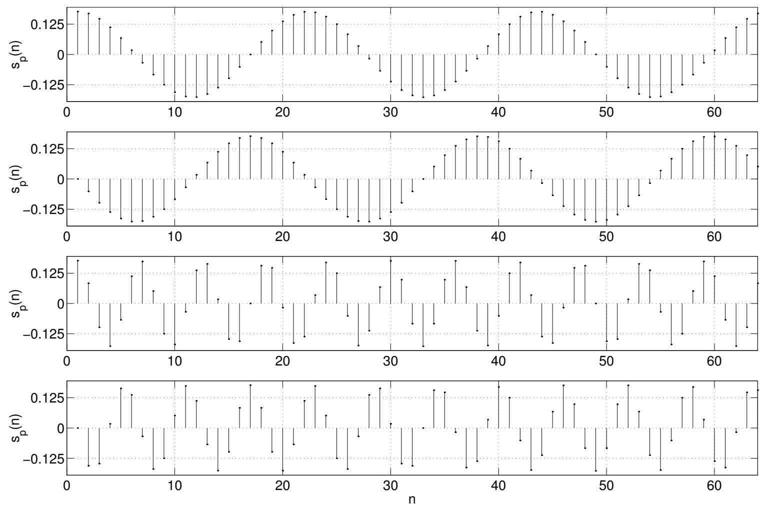

Figure 4.3: *Examples of signatures for the DMT filter bank ($N = 64$)*

The transmitted signals can be expressed as sums of modulated signature waveforms :

$$x_k(t) = \sum_{m=-\infty}^{+\infty} \sum_{p \in \mathcal{C}_k} I_p(m) g_p(t - mT). \tag{4.25}$$

The power spectral density of the transmitted signal is given by

$$\gamma_{x_k}(f) = \frac{\sigma_I^2}{T} \sum_{p \in \mathcal{C}_k} |G_p(f)|^2 \tag{4.26}$$

with $G_p(f) = \mathcal{F}\{g_p(t)\}$ and $\mathcal{F}\{.\}$ denotes the Fourier transform. Thanks to property (4.16) of the paraunitary filter banks, the power spectral density of $x_k(t)$ can be shown to be upper bounded as follows :

$$\gamma_{x_k}(f) \leq \frac{\sigma_I^2}{T_c} |P(f)|^2 \tag{4.27}$$

where $P(f) = \mathcal{F}\{p(t)\}$ and equality holds if all signatures are allocated to user k, with symbol sequences of equal variance σ_I^2 at the N inputs. This property allows to control the transmitted power spectral density when a limitation (power mask) $\gamma_{x_k}(f) \leq \overline{\gamma}(f)$ is imposed.

4.2.5 Multiuser channel and receiver front-end

At the output of the multiple access channel, the transmitted signals are filtered by the user-specific channels $c_k(t)$ and corrupted by additive noise $n(t)$:

$$\begin{aligned} r(t) &= \sum_{k=1}^{K} [x_k(t) \otimes c_k(t)] + n(t) && (4.28) \\ &= \sum_{n=-\infty}^{+\infty} \sum_{k=1}^{K} v_k(n) \tilde{c}_k(t - nT_c) + n(t) && (4.29) \\ &= \sum_{m=-\infty}^{+\infty} \sum_{k=1}^{K} \sum_{p \in \mathcal{C}_k} I_p(m) h_{pk}(t - mT) + n(t) && (4.30) \end{aligned}$$

with $\tilde{c}_k(t) = p(t) \otimes c_k(t)$, $h_{pk}(t) = g_p(t) \otimes c_k(t)$ and $\otimes$ denotes convolution. The channel impulse responses $c_k(t)$ include the effect of multipath propagation and that of cable losses. The derivation of the impulse responses from the cable characteristics and the network topology was discussed in

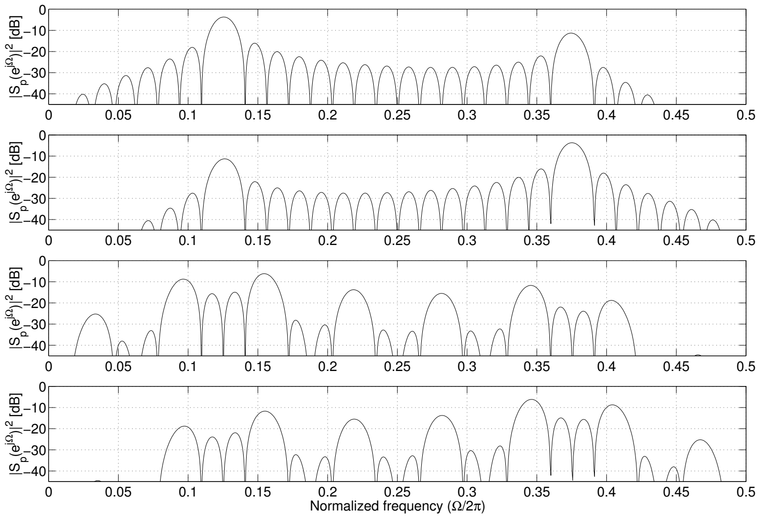

Figure 4.4: *Examples of signature frequency responses for the Hadamard filter bank ($N = 64$)*

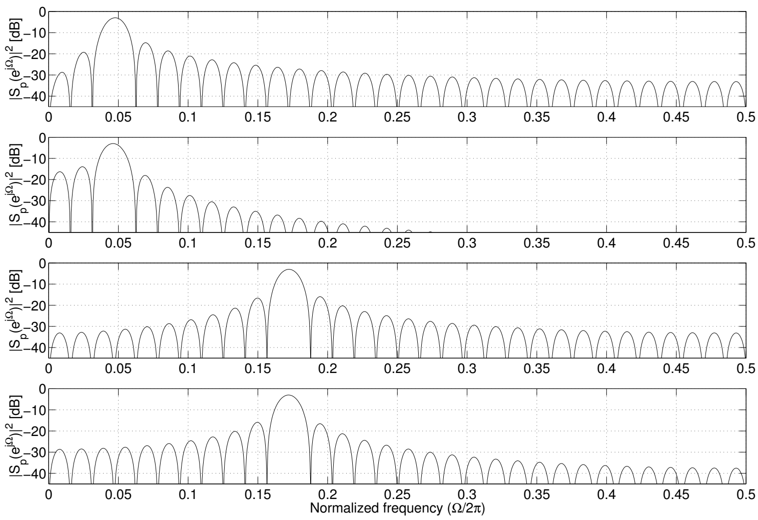

Figure 4.5: *Examples of signature frequency responses for the DMT filter bank ($N = 64$)*

Chapter 2. The additive noise $n(t)$ is assumed to be a white Gaussian noise (AWGN) with double-sided power spectral density $N_0/2$.

The equivalent channel equations for the downlink are

$$r_k(t) = \left[\sum_{l=1}^{K} x_l(t)\right] \otimes c_k(t) + n_k(t) \qquad (k \in \{1, \cdots, K\}) \tag{4.31}$$

where $r_k(t)$ and $n_k(t)$ denote the received signal and the additive noise in the k-th receiver.

The *energy* and the *mean square bandwidth* of the received symbols $I_p(m)$ associated with the signature waveform $g_p(n)$ and the user channel $c_k(t)$ are given by:

$$\mathcal{E}_{pk} = \sigma_I^2 \int_{-\infty}^{+\infty} |h_{pk}(t)|^2 \, dt = \sigma_I^2 \int_{-\infty}^{+\infty} |H_{pk}(f)|^2 \, df \tag{4.32}$$

$$W_{pk}^2 = \frac{\int_{-\infty}^{\infty} (2\pi f)^2 |H_{pk}(f)|^2 \, df}{\int_{-\infty}^{\infty} |H_{pk}(f)|^2 \, df} \tag{4.33}$$

These quantities depend both on the spectral characteristics of the signature and on the effect of the considered channel on that signature.

The received signal is filtered by means of a presampling filter $f(t)$ with cutoff $M/2T$ and sampled at the fractional rate $1/T_s = M/T$ where $M \geq N(1+\alpha)$ is an integer chosen large enough in order to cover the whole bandwidth of the signal spectrum. The filtered received signal and the filtered noise are denoted by $\overline{r}(t) = r(t) \otimes f(t)$ and $\overline{n}(t) = n(t) \otimes f(t)$, respectively. The filtered channel impulse responses are $\overline{c}_k(t) = p(t) \otimes c_k(t) \otimes f(t)$.

We define M polyphase components $r_\rho(m)$ (resp. $n_\rho(m)$) of the received signal (resp. the filtered noise), with $\rho \in [0, M-1]$, as follows :

$$r_\rho(m) = \overline{r}\left(mT + \rho T_s\right). \tag{4.34}$$

The M received polyphase sequences $r_\rho(m)$ can be related to the KN transmitted polyphase sequences $v_{\rho' k}(n)$ as follows :

$$\begin{aligned} r_\rho(m) &= \sum_{n=-\infty}^{+\infty} \sum_{k=1}^{K} v_k(n) \overline{c}_k(mT + \rho T_s - nT_c) + \overline{n}\left(mT + \rho T_s\right) \\ &= \sum_{n=-\infty}^{+\infty} \sum_{k=1}^{K} \sum_{\rho'=0}^{N-1} c_{\rho\rho' k}(n-m) v_{\rho' k}(n) + n_\rho(m) \end{aligned} \tag{4.35}$$

where the MN polyphase channel sequences $c_{\rho\rho'\,k}(m)$ are

$$c_{\rho\rho'\,k}(m) = \overline{c}_k\left(mT + \rho T_s - \rho' T_c\right). \tag{4.36}$$

The received sequences can also be related to the N initial symbol sequences $I_p(m)$ by

$$\begin{aligned} r_\rho(m) &= \sum_{n=-\infty}^{+\infty}\sum_{k=1}^{K}\sum_{p\in\mathcal{C}_k} I_p(n)\overline{h}_{pk}(mT + \rho T_s - nT) + \overline{n}\left(mT + \rho T_s\right) \\ &= \sum_{n=-\infty}^{+\infty}\sum_{k=1}^{K}\sum_{p\in\mathcal{C}_k} h_{\rho\, pk}(m-n)I_p(n) + n_\rho(m) \end{aligned} \tag{4.37}$$

The $h_{\rho\, pk}(m)$ polyphase component represents the cumulative effect of the signature waveform $g_p(t)$, the channel $c_k(t)$ and the filter $f(t)$, sampled at the symbol rate T with a phase ρT_s :

$$\begin{aligned} h_{\rho\, pk}(m) &= \overline{h}_{pk}\left(mT + \rho T_s\right) \\ &= \sum_{n=\infty}^{+\infty} s_p(n)\overline{c}_k(mT + \rho T_s - nT_c) \\ &= \sum_{n=\infty}^{+\infty}\sum_{\rho'=0}^{N-1} s_{\rho' p}(n)c_{\rho\rho',k}(m-n). \end{aligned} \tag{4.38}$$

The noise variance after sampling at M/T is $\sigma_n^2 = N_0 M/2T$.

4.2.6 IIR observation model

Taking the z-transform of equation (4.35), we write

$$R_\rho(z) = \sum_{\rho'=0}^{N-1}\sum_{k=1}^{K} V_{\rho' k}(z)C_{\rho\rho',k}(z) + N_\rho(z) \tag{4.39}$$

where $R_\rho(z)$, $C_{\rho\rho',k}(z)$ and $V_{\rho',k}(z)$ are the z-transformed sequences $r_\rho(m)$, $c_{\rho\rho',k}(m)$ and $v_{\rho',k}(n)$, respectively. Let $\underline{\underline{C}}(z)$ be the $M\times N$ channel polyphase matrix obtained with the MN polyphase channel sequences, i.e.

$$\underline{\underline{C}}(z) = \begin{bmatrix} C_{11}(z) & \cdots & C_{1N}(z) \\ \vdots & \ddots & \vdots \\ C_{M1}(z) & \cdots & C_{MN}(z) \end{bmatrix} \tag{4.40}$$

and let $\underline{\mathrm{R}}(z)$ (resp. $\underline{\mathrm{N}}(z)$) be the $M \times 1$ vector obtained with the M received (resp. noise) polyphase sequences, i.e.

$$\begin{aligned} \underline{\mathrm{R}}(z) &\triangleq [R_1(z), \cdots, R_M(z)]^T \\ \underline{\mathrm{N}}(z) &\triangleq [N_1(z), \cdots, N_M(z)]^T . \end{aligned} \tag{4.41}$$

The multiuser channel equations (4.35) and (4.37) can be expressed shortly with a matrix notation as :

$$\begin{aligned} \underline{\mathrm{R}}(z) &= \sum_{k=1}^{K} \underline{\underline{\mathrm{C}}}_k(z)\, \underline{\mathrm{V}}_k(z) + \underline{\mathrm{N}}(z) \\ &= \sum_{k=1}^{K} \underline{\underline{\mathrm{H}}}_k(z)\, \underline{\mathrm{I}}_k(z) + \underline{\mathrm{N}}(z) \end{aligned} \tag{4.42}$$

where the IIR equivalent channel matrix $\underline{\underline{\mathrm{H}}}_k(z) = \underline{\underline{\mathrm{C}}}_k(z)\, \underline{\underline{\mathrm{S}}}_k(z)$ can be obtained with the adequate z-transformed sequences $h_{\rho pk}(m)$. The IIR channel matrix $\underline{\underline{\mathrm{C}}}_k(z)$ is Toeplitz in the special case where $T_s = T_c$. In the general case, however, i.e. when the receiver operates at a fractional rate, this property is not satisfied. Equation (4.42) provides an IIR observation model for the general multiple access channel depicted in Figure 4.1. This model is associated with a continuous mode of transmission, with symbol sequences $I_p(m)$ transmitted continuously at a rate $1/T$.

4.2.7 FIR observation model

Even in the case of a continuous mode of transmission, it is often desirable to build an FIR observation model that relates a finite-length observation window of the received signal to a finite set of transmitted symbols. This is possible if the channel impulse responses $\bar{c}_k(t)$ and the signature codes $s_p(n)$ have a finite size.

Let $N_f T = (n_1 + n_2 + 1)T$ be the length of the observation window, i.e. the received signal is observed in the time interval $[(n - n_2)T, (n + n_1 + 1)T]$. With the sampling rate $1/T_s = M/T$, a vector of $N_f M$ samples is sufficient to represent the received signal in the selected time interval. Grouping together the M polyphase components of the received signal (resp. the additive noise), we define received signal vectors $\underline{\mathrm{r}}(n)$ (resp. noise vectors $\underline{\mathrm{n}}(n)$) as follows :

$$\underline{\mathrm{r}}(n) = \begin{bmatrix} r_{M-1}(n) \\ \vdots \\ r_0(n) \end{bmatrix} \qquad \underline{\mathrm{n}}(n) = \begin{bmatrix} n_{M-1}(n) \\ \vdots \\ n_0(n) \end{bmatrix} \tag{4.43}$$

The signal observed in a time interval of length $N_f T$ is obtained by stacking N_f received signal vectors as defined in equation (4.43).

The user channel impulse responses $c_k(t)$ are assumed to be causal and to have a length of $L_c T_c$ with $L_c \geq 0$. The length of the composite channels $h_{pk}(t) = \sum_n s_p(n)\bar{c}_k(t - nT_c)$ is then upper-bounded by $(L+1)T$ with

$$L = \lceil \frac{L_c + N'}{N} \rceil - 1 \geq 0. \tag{4.44}$$

The minimum length of T corresponds to ideal Dirac channels $\bar{c}_k(t) = \delta(t)$ associated with signatures $s_p(n)$ of length N.

Grouping the M equivalent channel polyphase sequences associated with the N signature waveforms in a $M \times N$ rectangular matrix, we define channel blocks $\underline{\underline{\mathrm{h}}}(n)$ and $\underline{\underline{\mathrm{h}}}_k(n)$ as follows :

$$\underline{\underline{\mathrm{h}}}(n) = \begin{bmatrix} h_{M-1,1}(n) & \cdots & h_{M-1,N}(n) \\ \vdots & \ddots & \vdots \\ h_{0,1}(n) & \cdots & h_{0,N}(n) \end{bmatrix} \qquad \underline{\underline{\mathrm{h}}}_k(n) = \left[\underline{\underline{\mathrm{h}}}(n)\right]_{\{p \in \mathcal{C}_k\}}. \tag{4.45}$$

With FIR channels, $L+1$ channel blocks are non-zero. Channel matrices $\underline{\underline{\mathrm{H}}}$ and $\underline{\underline{\mathrm{H}}}_k$ are defined by stacking the $L+1$ non-zero channel blocks as follows :

$$\underline{\underline{\mathrm{H}}} = \begin{bmatrix} \underline{\underline{\mathrm{h}}}(L) \\ \vdots \\ \underline{\underline{\mathrm{h}}}(0) \end{bmatrix} \qquad \underline{\underline{\mathrm{H}}}_k = \left[\underline{\underline{\mathrm{H}}}\right]_{\{p \in \mathcal{C}_k\}}. \tag{4.46}$$

The N columns of $\underline{\underline{\mathrm{H}}}$ actually contain the N composite impulse responses $h_{pk}(t)$ sampled at a rate M/T and stored in reverse order. User-specific channel matrices $\underline{\underline{\mathrm{H}}}_k$ are just obtained by selecting the columns corresponding to the signatures allocated to user k.

Finally, the global channel equation relating received samples to transmitted symbols can be written as follows :

$$\begin{bmatrix} \underline{\mathrm{r}}(n+n_1) \\ \vdots \\ \underline{\mathrm{r}}(n) \\ \vdots \\ \underline{\mathrm{r}}(n-n_2) \end{bmatrix} = \begin{bmatrix} \underline{\underline{\mathrm{h}}}(0) & \underline{\underline{\mathrm{h}}}(1) & \cdots & \underline{\underline{\mathrm{h}}}(L) & & & & \\ & \underline{\underline{\mathrm{h}}}(0) & \cdots & \underline{\underline{\mathrm{h}}}(L-1) & \underline{\underline{\mathrm{h}}}(L) & & & \\ & & \ddots & \ddots & \ddots & \ddots & & \\ & & & \underline{\underline{\mathrm{h}}}(0) & \underline{\underline{\mathrm{h}}}(1) & \cdots & \underline{\underline{\mathrm{h}}}(L) & \\ & & & & \underline{\underline{\mathrm{h}}}(0) & \cdots & \underline{\underline{\mathrm{h}}}(L-1) & \underline{\underline{\mathrm{h}}}(L) \end{bmatrix}$$

$$\cdot \begin{bmatrix} \underline{\mathrm{I}}(n+n_1) \\ \vdots \\ \underline{\mathrm{I}}(n) \\ \vdots \\ \underline{\mathrm{I}}(n-n_2-L) \end{bmatrix} + \begin{bmatrix} \underline{\mathrm{n}}(n+n_1) \\ \vdots \\ \underline{\mathrm{n}}(n) \\ \vdots \\ \underline{\mathrm{n}}(n-n_2) \end{bmatrix}. \tag{4.47}$$

Using the following notation to denote the concatenation of successive vectors coming from an arbitrary sequence $\underline{\mathrm{x}}(n)$:

$$\underline{\mathrm{x}}_{n_2}^{n_1}(n) \triangleq \begin{bmatrix} \underline{\mathrm{x}}(n+n_1)^T & \cdots & \underline{\mathrm{x}}(n-n_2)^T \end{bmatrix}^T, \tag{4.48}$$

the channel equation (4.47) can be rewritten shortly as

$$\underline{\mathrm{r}}_{n_2}^{n_1}(n) = \underline{\underline{\mathcal{H}}}_{N_f}\, \underline{\mathrm{I}}_{n_2+L}^{n_1}(n) + \underline{\mathrm{n}}_{n_2}^{n_1}(n). \tag{4.49}$$

The global channel matrix $\underline{\underline{\mathcal{H}}}_{N_f}$, defined by identification with equation (4.47), is a *block-Toeplitz* matrix of size $N_f M \times (N_f + L)N$, generated with the $L+1$ channel blocks $\underline{\underline{\mathrm{h}}}(n)$ defined in (4.45). It can be obtained by stacking N_f cyclic shifts of the first row of $M \times N$ channel blocks. The relative contribution of the different users can be put forward by writing the global channel equation as the sum of user-specific contributions :

$$\underline{\mathrm{r}}_{n_2}^{n_1}(n) = \sum_{k=1}^{K} \underline{\underline{\mathcal{H}}}_{N_f,k}\, (\underline{\mathrm{I}}_k)_{n_2+L}^{n_1}(n) + \underline{\mathrm{n}}_{n_2}^{n_1}(n) \tag{4.50}$$

where the block-Toeplitz matrices $\underline{\underline{\mathcal{H}}}_{N_f,k}$ are generated with the user channel blocks $\underline{\underline{\mathrm{h}}}_k(n)$ defined in (4.45).

4.3 Bit rates computation

As shown in Figure 4.1, a joint detector (JD) located in the receiver has the task to build estimates $\hat{I}_p(n)$ of the N symbol sequences transmitted by the K users. Different kinds of joint detectors are analyzed and compared in Chapter 5. Whatever the detector implemented in the receiver, the obtained symbol estimates can be expressed as

$$\hat{I}_p(n) = \sum_{m=-\infty}^{+\infty} \sum_{k=1}^{K} \sum_{p' \in \mathcal{C}_k} x_{pp'}(m)\, I_{p'}(n-m) + \nu_p(n). \tag{4.51}$$

Expression (4.51) includes five types of terms :

- A contribution of the useful symbol $x_{pp}(0)I_p(n)$.
- A weighted sum of past and future symbols associated with the same signature waveform $g_p(t)$. This is the residual ISI (Inter-Symbol-Interference).
- A weighted sum of symbols associated with other signature waveforms $g_{p'}(t)$ with $p' \neq p$ that are allocated to user k. This is the residual ICI (Inter-Code-Interference).
- A weighted sum of symbols transmitted by the other users $k' \neq k$. This is the residual MAI (Multiple-Access-Interference).
- The contribution of the additive Gaussian noise $\nu_p(n)$.

The performance index for the p-th detector output is the Signal-to-Interference-plus-Noise Ratio (SINR) denoted by ρ_p and given by

$$\rho_p = \frac{x_{pp}^2(0)\, \sigma_I^2}{\left(\sum_{(m,p') \neq (0,p)} x_{pp'}^2(m)\right)\, \sigma_I^2 + \sigma_{\nu_p}^2}. \tag{4.52}$$

For a PAM constellation of size $N_p = 2^{b_p}$, the symbol error probability p_s is known to be

$$p_s = \frac{N_p - 1}{N_p} \text{erfc}\left(\sqrt{\frac{3\,\rho_p}{2(N_p^2 - 1)}}\right). \tag{4.53}$$

This expression is valid only if all sources of noise (including ISI, ICI and MAI) are Gaussian. It remains approximately valid, however, if a high number of independent PAM symbols contribute to the expression of the composite interference. It is also assumed that Gray mapping is used for the PAM constellations, which implies that an error on one symbol generates an error on one single bit. The bit error probability is then $p_b = p_s/b_p$.

For a given target bit-error-rate p_b, the maximum constellation size can be derived from equation (4.53) as

$$b_p = \frac{1}{2}\log_2\left(1 + \frac{\rho_p}{\Gamma\left(p_b\right)}\right) \tag{4.54}$$

where Γ is called the 'SNR gap' and can be approximated by

$$\Gamma\left(p_b\right) \approx \frac{2}{3}\left[\mathrm{erfc}^{-1}\left(p_b\right)\right]^2. \tag{4.55}$$

The effective SNR gap should be modified to take into account the effect of error correcting codes. Actually, equation (4.53) does not guarantee that an integer number of bits is obtained for the PAM constellation. In a practical system, the effective bit error rate associated with the different user signatures can be slightly higher or lower than the reference probability p_b, as long as the average bit error rate over all signatures allocated to a given user is equal to p_b. The selected constellation size is then rounded to the upper or lower nearest integer value, depending on the signature under consideration. For the bit rate computations presented in this work, the number of bits are given by (4.54) and are not rounded, which has a negligible impact on the accuracy of the presented results. Finally, the global bit rate for a given user is given by

$$R_k = \frac{1}{T}\sum_{p\in\mathcal{C}_k} b_p = \frac{1}{T}\log_2\left[\prod_{p\in\mathcal{C}_k}\left(1+\frac{\rho_p}{\Gamma}\right)\right] \approx \frac{N_k}{T}\left[\log_2\left(\overline{\rho}_k\right) - \log_2\left(\Gamma\right)\right] \tag{4.56}$$

where the geometrical SINR for user k is defined by

$$\overline{\rho}_k = \sqrt[N_k]{\prod_{p\in\mathcal{C}_k}\rho_p} \tag{4.57}$$

and the last approximation in (4.56) is valid for high values of the SINR's.

4.4 CAP-FB transmission

A common constraint in high-speed communications over wired channels (like DSL and PLC) is that the lower part of the frequency spectrum (from 0 to F_0 MHz) should remain unaffected by the broadband signals. As a consequence, the broadband signals must be of the passband type, but with a carrier frequency f_c of the same order as the available bandwidth $B - F_0$.

In these conditions, it is desirable to make use of a carrierless modulation technique. This is obtained by directly producing a digital passband signal at the input of the DAC. Two options are available to build a passband signal in the digital domain : either the signatures corresponding to the forbidden frequencies are not loaded, or all signatures are loaded but the obtained baseband signal is filtered by means of a well-chosen passband digital filter.

The first option assumes the use of a *frequency-selective filter bank*. With the DFT or PRMF filters, for example, the different signatures can be associated with specific subbands. The signatures located in the lower subbands are not modulated. The total number of signatures to be allocated to the K users is then $\overline{N} < N$. Figure 4.6 (upper figure) gives the power spectral density $\gamma_{x_k}(f)$ of the transmitted signal obtained with an ideal frequency-selective FB with $N = 16$ subbands, a raised-cosine filter with roll-off α, and signatures 3 to 16 allocated to the same user k. With a practical FB, of course, sidelobes have to be taken into account and an analog highpass filter should be used to attenuate the signal spectrum in the forbidden frequency band.

The second option uses the *Carrierless Amplitude-Phase modulation (CAP)*. Basically, the CAP modulation is equivalent to a single carrier QAM modulation at low frequency, which implies that the modulation operation can be obtained directly by the use of sine- and cosine-modulated shaping filters $p_a(t)$ and $p_b(t)$ operating on two distinct symbol sequences $I_a(n)$ and $I_b(n)$, at a rate $1/T_c' = B - F_0$. The shaping filters form a Hilbert pair :

$$\begin{aligned} p_a(t) &= \sqrt{2}\,p'(t)\,\cos(\omega_c t) = \tilde{p}_b(t) \qquad (4.58)\\ p_b(t) &= \sqrt{2}\,p'(t)\,\sin(\omega_c t) = \tilde{p}_a(t) \qquad (4.59)\end{aligned}$$

where f_c is an arbitrary carrier frequency with the constraint $f_c \geq \frac{1+\alpha'}{2T_c'}$, and $p'(t)$ is a baseband half root Nyquist filter with roll-off α'. Practically, the CAP modulation can be performed with two digital filters $p_a(\frac{nT_c'}{3})$ and $p_b(\frac{nT_c'}{3})$ followed by the digital to analog conversion. The oversampling factor of 3 is generally sufficient when $F_0 \ll B$.

The CAP technique can be extended to filter bank modulation. In the CAP-FB scheme, two baseband digital signals $v_{ka}(n)$ and $v_{kb}(n)$ are produced by each user, with an arbitrary FB, at a rate $1/T_c'$. Let $\underline{\mathrm{V}}_{ka}(z)$ and $\underline{\mathrm{V}}_{kb}(z)$ be the respective polyphase sequences obtained at the output of a filter bank $\underline{\underline{\mathrm{S}}}(z)$ with inputs $\underline{\mathrm{I}}_{ka}(z)$ and $\underline{\mathrm{I}}_{kb}(z)$:

$$\left[\ \underline{\mathrm{V}}_{ka}(z) \quad \underline{\mathrm{V}}_{kb}(z)\ \right] = \underline{\underline{\mathrm{S}}}_k(z)\ \left[\ \underline{\mathrm{I}}_{ka}(z) \quad \underline{\mathrm{I}}_{kb}(z)\ \right] \qquad (4.60)$$

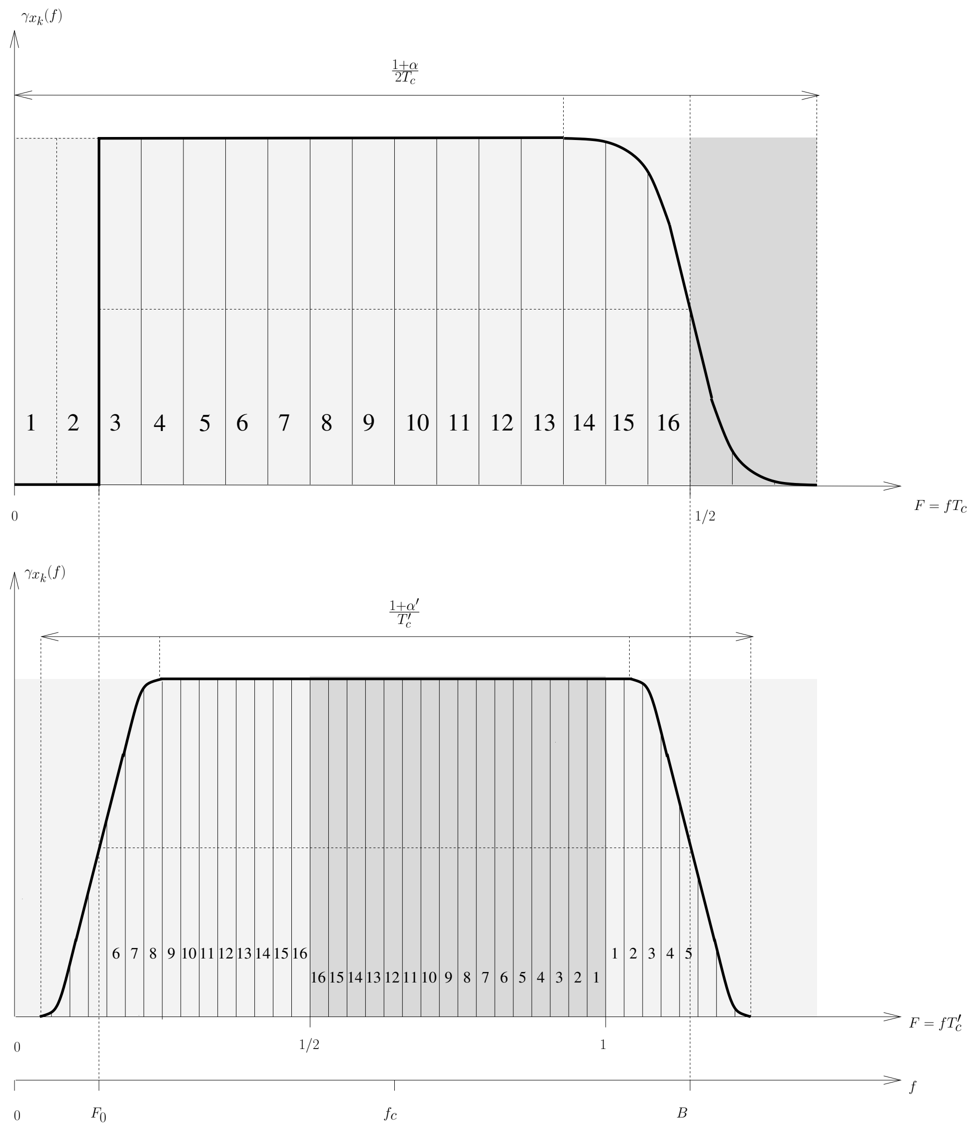

Figure 4.6: *Power spectrum of baseband-FB and CAP-FB modulated signals*

These sequences are used to modulate the two quadrature shaping filters.

The received signal becomes :

$$\begin{aligned} r(t) &= \sum_{n=-\infty}^{+\infty} \sum_{k=1}^{K} \left[v_{ka}(n)\, c_{ka}(t - nT'_c) + v_b(n)\, c_{kb}(t - nT'_c) \right] + n(t) && (4.61) \\ &= \sum_{m=-\infty}^{+\infty} \sum_{k=1}^{K} \sum_{p \in \mathcal{C}_k} \left[I_{p,a}(m) h_{pk,a}(t - mT') + I_{p,b}(m) h_{pk,b}(t - mT') \right] \\ &+ n(t) && (4.62) \end{aligned}$$

with $c_{ka}(t) = p_a(t) \otimes c_k(t)$ and $c_{kb}(t) = p_b(t) \otimes c_k(t) = \tilde{c}_{ka}(t)$ and two series of equivalent channels :

$$h_{pk,a}(t) = \sum_{n=-\infty}^{+\infty} s_p(n) c_{ka}(t - nT'_c) \qquad (4.63)$$

$$h_{pk,b}(t) = \sum_{n=-\infty}^{+\infty} s_p(n) c_{kb}(t - nT'_c) = \tilde{h}_{pk,a}(t). \qquad (4.64)$$

The received signal is sampled at a fractional rate M/T'. The constraint on the oversampling factor M is now :

$$M \geq 2 f_c T' + N(1 + \alpha'). \qquad (4.65)$$

The IIR observation model (4.42) relating the M received polyphase sequences to the $2N$ sequences of transmitted symbols becomes :

$$\begin{aligned} \underline{\mathrm{R}}(z) &= \sum_{k=1}^{K} \left[\underline{\underline{\mathrm{C}}}_{ka}(z)\, \underline{\mathrm{V}}_{ka}(z) + \underline{\underline{\mathrm{C}}}_{kb}(z)\, \underline{\mathrm{V}}_{kb}(z) \right] + \underline{\mathrm{N}}(z) && (4.66) \\ &= \sum_{k=1}^{K} \left[\underline{\underline{\mathrm{H}}}_{ka}(z)\, \underline{\mathrm{I}}_{ka}(z) + \underline{\underline{\mathrm{H}}}_{kb}(z)\, \underline{\mathrm{I}}_{kb}(z) \right] + \underline{\mathrm{N}}(z) && (4.67) \end{aligned}$$

with $\underline{\underline{\mathrm{H}}}_{ka}(z) = \underline{\underline{\mathrm{C}}}_{ka}(z)\underline{\underline{\mathrm{S}}}_k(z)$ and $\underline{\underline{\mathrm{H}}}_{kb}(z) = \underline{\underline{\mathrm{C}}}_{kb}(z)\underline{\underline{\mathrm{S}}}_k(z)$. The extension of the FIR observation model (4.49) is straightforward.

Figure 4.6 (lower figure) gives the power spectral density $\gamma_{x_k}(f)$ of the CAP-FB signal obtained with an ideal frequency-selective FB with $N = 16$ subbands. Actually, the CAP-FB scheme can be used with an arbitrary set of signatures. The difference between QAM and CAP is also visible in

Figure 4.6. The spectrum of the different signatures is not moved by f_c as in the classical QAM modulation. With CAP, the periodic spectrum of the signatures $|S_p(e^{2\pi j F'})|^2$ with $F' = fT'_c$ is fixed, and the pulse shaping filters select the frequencies in the range $F' \in \left[f_c T'_c - \frac{1}{2}, f_c T'_c + \frac{1}{2}\right]$.

The complex envelope of the transmitted signals $x_k(t)$ is given by

$$\begin{aligned} e_{x_k}(t) &= \sum_{p \in \mathcal{C}_k} \sum_{n=-\infty}^{+\infty} \sum_{m=-\infty}^{+\infty} \overline{I}_p(m) \,.\, s_p(n - mN) \,.\, e^{-2\pi j n f_c T'_c} \, p'(t - nT'_c) \\ &= \sum_{p \in \mathcal{C}_k} \sum_{n=-\infty}^{+\infty} \sum_{m=-\infty}^{+\infty} \left[\overline{I}_p(m) \, e^{-2\pi j m f_c T'}\right] \,.\, \overline{s}_p(n - mN) \\ &\qquad .\, p'(t - nT'_c) \end{aligned} \tag{4.68}$$

where the complex QAM symbols $\overline{I}_p(m)$ and the complex modulated signatures $\overline{s}_p(n)$ are defined by

$$\overline{I}_p(m) = I_{p,a}(m) + jI_{p,b}(m) \tag{4.69}$$

$$\overline{s}_p(n) = s_p(n) \, e^{-2\pi j n f_c T'_c}. \tag{4.70}$$

From (4.68), it appears that the analysis of the CAP-FB transmission scheme could be achieved with a lowpass equivalent model including complex symbol sequences $\overline{I}_p(m)$ and a set of complex modulated signatures $\overline{s}_p(n)$, by rotating the complex symbols $\overline{I}_p(m)$ with an angle $-2\pi m f_c T'$ that varies according to the symbol index m. In the sequel, however, the bandpass formalism will be used.

Finally, it should be noted that the total bit rates offered by the two passband schemes displayed in Figure 4.6 are roughly the same. In the first scheme (baseband FB transmission), $\overline{N}$ signatures are modulated at a baud rate $1/T$. In the second scheme (CAP-FB transmission), $2N$ signatures are modulated at a baud rate $1/T'$. As $\frac{\overline{N}}{N} = \frac{2T}{T'} = \frac{B - F_0}{B}$, the potential bit rates are roughly equivalent.

4.5 CAP-CDMA with long codes

In the case of *binary signature codes of length* N, the CAP-FB multiple access technique described in the last section is referred to as CAP-CDMA. The basic CAP-CDMA system uses short codes, that is to say codes which have a length equal to the symbol period. The code used for all the symbols of a given user is then the same. It may happen that the amount of interference experienced by this code is high and it will stay so. A careful code allocation algorithm must be implemented in order to obtain the best matching between the allocated codes and the user channel responses. Moreover, several signature codes should be allocated to the weakest users to offer them a fair level of performance.

Many CDMA-based communications standards utilize aperiodic or longer period sequences instead of short codes. In WCDMA [56], for example, a long scrambling code truncated to the 10 msec frame length is used. The long scrambling code $a(n)$ is superimposed on the short spreading code $s_k(n)$, by modulo-2 addition. This means that successive symbols of a given user are spread by different code segments, and a certain code segment only repeats after, say, P symbols or PN chips where the spreading factor is denoted by N and P is the code period measured in symbol periods. The long code is split in P segments $a_p(n)$ of length N. One period of the long code can be obtained from the concatenation of the P sequences $a_p(n)$ with $p \in [0, P-1]$. The resulting signature associated with the p-th segment is given by

$$s_{k,p}(n) = s_k(n) \,.\, a_p(n) \tag{4.71}$$

where the product is equivalent to modulo-2 addition with antipodal sequences. In the long code scenario, the interference experienced by successive symbols changes, and on average all users will experience similar levels of interference. The signature allocation algorithm is not needed anymore. Whatever the initial signature code $s_k(n)$ selected for user k, the average level of performance is roughly constant thanks to the effect of the long code. The relative performance of the different users can be controlled in two ways : either by varying the number of parallel signatures allocated to each user (i.e. by using multicode CDMA), or by varying the transmission power of the different user signals $x_k(t)$. To simplify notations, we assume in the sequel that a single signature code $s_k(n)$ is allocated to each user.

The discrete time chip-rate signals $v_{k,q}(n)$ with $q \in \{a, b\}$ produced by user k are given by

$$v_{k,q}(n) = \sum_{m=-\infty}^{\infty} \sum_{p=0}^{P-1} I_{k,q}(mP + p)\, s_{k,p}(n - mPN - pN). \tag{4.72}$$

The received signal can be written as

$$r(t) = \sum_{k=1}^{K} \sum_{m=-\infty}^{\infty} \sum_{p=0}^{P-1} \sum_{q \in \{a,b\}} I_{k,p,q}(m)\, h_{k,p,q}(t - mPT') + n(t) \tag{4.73}$$

where $I_{k,p,q}(m) = I_{k,q}(mP + p)$ and

$$h_{k,p,q}(t) = \sum_{n=1}^{N} s_{k,p}(n)\, c_{k,q}(t - pT' - nT'_c) \tag{4.74}$$

is the composite impulse response resulting from the cascade of the p-th code segment and the channel impulse response $c_{kq}(t) = p_q(t) \otimes c_k(t)$. The advantage of this representation of each user signal by means of P parallel streams is that the code used in each stream is time-invariant.

An important parameter to compare performance is the received energy per symbol. Obviously not all symbols will be received with the same energy if the transmission power is constant. As a matter of fact, each code segment has a specific frequency response and hence the energy left after propagation over the channel will be segment dependent. The received symbol energy for a symbol transmitted with phase p in a packet of P symbols is given by

$$\mathcal{E}_{k,p,q} = \sigma_I^2 \int_{-\infty}^{\infty} |h_{k,p,q}(t)|^2 \, \mathrm{d}t \tag{4.75}$$

where σ_I^2 is the symbol variance. The averaged received symbol energy for a given user is

$$\mathcal{E}_k = \frac{1}{2P} \sum_{p=0}^{P-1} \sum_{q \in \{a,b\}} \mathcal{E}_{k,p,q}. \tag{4.76}$$

The received signal is sampled at a fractional rate $1/T_s = M/T'$ where M has to satisfy the constraint in (4.65). As the symbol sequences in (4.73) are now defined at a baud rate of $1/PT'$, the total number of polyphase sequences needed to represent the received signal is MP :

$$\begin{aligned} r_\rho(n) &= \overline{r}[(nMP + \rho)T_s] && (4.77) \\ &= \sum_{k=1}^{K} \sum_{m=-\infty}^{\infty} \sum_{p=0}^{P-1} \sum_{q \in \{a,b\}} I_{k,p,q}(m) h_{k,p,\rho,q}(n-m) + n_\rho(n) && (4.78) \end{aligned}$$

with $h_{k,p,\rho,q}(n-m) = h_{k,p,q}[((n-m)MP + \rho)T_s]$ and $\rho \in [0, MP-1]$. The IIR observation model relating the MP received polyphase sequences to the $2KP$ transmitted symbol sequences is

$$\underline{\mathrm{R}}(z) = \underline{\underline{\mathrm{H}}}(z)\, \underline{\mathrm{I}}(z) + \underline{\mathrm{N}}(z) \tag{4.79}$$

where $\underline{\mathrm{R}}(z)$ and $\underline{\mathrm{N}}(z)$ are of size MP, $\underline{\mathrm{I}}(z)$ of size $2KP$ and $\underline{\underline{\mathrm{H}}}(z)$ of size $MP \times 2KP$.

With finite-length channel impulse responses $c_{k,q}(t)$, the composite channels $h_{k,p,q}(t)$ are non-zero in a time interval of length $(L+1)T'$. A *segment-dependent* FIR observation model can be obtained as follows. Let $\underline{\mathrm{I}}_p(n)$ be the block of $2K$ real symbols transmitted by the users on the p-th code segments and $\underline{\mathrm{r}}_p(n)$ (resp. $\underline{\mathrm{n}}_p(n)$) be the block of M signal (resp. noise) samples received during the p-th segment of duration T' :

$$\underline{\mathrm{I}}_p(n) = \begin{bmatrix} I_{1,p,a}(n) \\ I_{1,p,b}(n) \\ \vdots \\ I_{K,p,a}(n) \\ I_{K,p,b}(n) \end{bmatrix} \qquad \underline{\mathrm{r}}_p(n) = \begin{bmatrix} r_{pM+M-1}(n) \\ \vdots \\ r_{pM}(n) \end{bmatrix} \tag{4.80}$$

Grouping M adjacent polyphase components of the $2K$ composite impulse responses $h_{k,p,q}(t)$ associated with the p-th code segments in a $M \times 2K$ matrix, we define segment-dependent channel blocks $\underline{\underline{\mathrm{h}}}_p(n)$ as follows :

$$\underline{\underline{\mathrm{h}}}_p(n) = \begin{bmatrix} h_{M-1,p,1}(n) & \tilde{h}_{M-1,p,1}(n) & \cdots & h_{M-1,p,K}(n) & \tilde{h}_{M-1,p,K}(n) \\ \vdots & \vdots & \ddots & \vdots & \vdots \\ h_{0,p,1}(n) & \tilde{h}_{0,p,1}(n) & \cdots & h_{0,p,K}(n) & \tilde{h}_{0,p,K}(n) \end{bmatrix}. \tag{4.81}$$

With FIR channels, $L+1$ channel blocks are non-zero. Segment-specific channel matrices $\underline{\underline{\mathrm{H}}}_p$ are defined by stacking the $L+1$ non-zero channel blocks as follows :

$$\underline{\underline{\mathrm{H}}}_p = \begin{bmatrix} \underline{\underline{\mathrm{h}}}_p(L) \\ \vdots \\ \underline{\underline{\mathrm{h}}}_p(0) \end{bmatrix}. \tag{4.82}$$

The MP samples received during the n-th period of length PT' are given by

$$\underline{\mathrm{r}}_0^{P-1}(n) = \overline{\underline{\underline{\mathcal{H}}}} \begin{bmatrix} \underline{\mathrm{I}}_0^{P-1}(n) \\ \underline{\mathrm{I}}_{P-L}^{P-1}(n-1) \end{bmatrix} + \underline{\mathrm{n}}_0^{P-1}(n) \tag{4.83}$$

where the global channel matrix $\overline{\underline{\underline{\mathcal{H}}}}$ is of size $MP \times 2K(P+L)$. This matrix is built with the $2KP$ composite channels as shown in Figure 4.7. Because of the long code, it is not a block-Toeplitz matrix any more. For very long codes, i.e. $P \gg L$, this matrix is sparse as only a few blocks around the

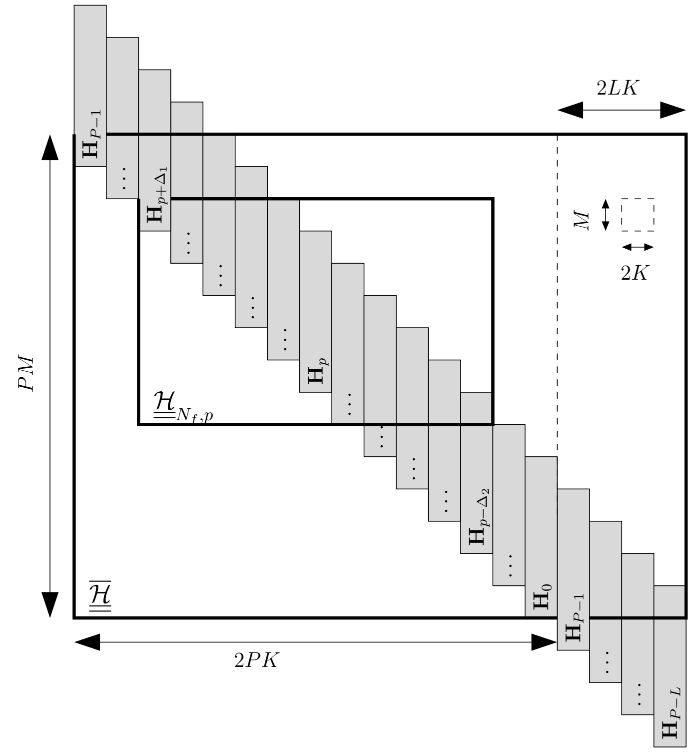

Figure 4.7: *Structure of the global channel matrix*

main diagonal are nonzero. This reflects the fact that only a few symbols $I_{p,k,q}(n)$ have a contribution to a given received block $\underline{\mathrm{r}}_p(n)$. It is useful to propose a shorter-window observation model :

$$\underline{\mathrm{r}}_{p-n_2}^{p+n_1}(n) = \underline{\underline{\mathcal{H}}}_{N_f,p}\, \underline{\mathrm{I}}_{p-n_2-L}^{p+n_1}(n) + \underline{\mathrm{n}}_{p-n_2}^{p+n_1}(n) \tag{4.84}$$

where the segment-dependent channel matrix $\underline{\underline{\mathcal{H}}}_{N_f,p}$ is the size $MN_f \times 2K(N_f + L)$ submatrix of $\overline{\underline{\underline{\mathcal{H}}}}$ centered around $\underline{\underline{\mathrm{H}}}_p$, as illustrated in Figure 4.7. Actually, the segment indices in Equation (4.84) should be defined modulo P. To keep the notation simple, the border effect, corresponding to a case where samples or symbols in blocks $n \pm 1$ would have to be used, has not been considered.

4.6 Cyclic-prefixed block transmission

An alternative to the continuous transmission schemes developed in the previous sections is the block-based multiple access. For a *baseband block transmission* associated with a given FB of size N, the chip-rate sequence transmitted by each user (see Equation (4.3)) becomes :

$$v_k(n) = \sum_{p \in \mathcal{C}_k} I_p\, s_p(n) \quad \leftrightarrow \quad \underline{\mathrm{v}}_k = \underline{\underline{\mathrm{S}}}_k\, \underline{\mathrm{I}}_k, \tag{4.85}$$

where the signature matrix $\underline{\underline{\mathrm{S}}}_k$ is of size $N' \times N_k$ and contains the length-N' signature codes allocated to user k as its N_k columns. Everything happens as if a single block of N_k symbols was transmitted by each user. The next block of symbols can be transmitted after a short idle time of duration νT_c, with the condition that successive blocks do not interfere with each other in the receiver. As the channel impulse responses $\overline{c}_k(t)$ have a length of $L_c T_c$, the duration of the inter-block interval must satisfy :

$$\nu \geq L_c. \tag{4.86}$$

The baud rate associated with the N sequences of symbols $I_p(n)$ is now $1/T_b = \frac{N}{N+\nu} 1/T$. A systematic penalty of $\frac{N}{N+\nu}$ is thus associated with the bit rate obtained with block-based transmission. That is the price to pay in order to suppress the inter-block interference in the receiver.

Rather than transmitting nothing during the inter-block interval, the cyclic prefix (CP) technique can be used to cyclically extend the transmitted sequence $\underline{\mathrm{v}}_k$:

$$\underline{\mathrm{v}}_k^{\nu} = \left(\begin{array}{c|c} \underline{\underline{0}}_{\nu \times N'} & \underline{\underline{\mathrm{E}}}_{\nu} \\ \hline \multicolumn{2}{c}{\underline{\underline{\mathrm{E}}}_{N'}} \end{array} \right) \underline{\mathrm{v}}_k \tag{4.87}$$

where $\underline{\underline{\mathrm{E}}}_x$ denotes a unit matrix of size x. After propagation over the frequency-selective channels, the received signal is sampled at the chip rate $1/T_c$. The received sequence is obtained by linear convolution of the transmitted sequences $v_k^{\nu}(n)$ and the channel response $c_k(n) = \overline{c}_k(nT_c)$:

$$r(n) = \sum_{k=1}^{K} c_k(n) \otimes v_k^{\nu}(n) + n_(n). \tag{4.88}$$

This can be expressed in matrix form as follows :

$$\underline{\mathrm{r}}^{\nu} = \sum_{k=1}^{K} \underline{\underline{\mathcal{C}}}_k^{\nu} \underline{\mathrm{v}}_k^{\nu} + \underline{\mathrm{n}}^{\nu} \tag{4.89}$$

where the $(N' + 2\nu) \times (N' + \nu)$ matrix $\underline{\underline{\mathcal{C}}}_k^{\nu}$ is a *Toeplitz matrix* generated with the samples $[c_k(\nu), \cdots, c_k(0)]$, appended by zeros. After removal of the cyclic prefix, the $N' \times 1$ received vectors are finally :

$$\begin{aligned}
\underline{\mathrm{r}} &= \left(\underline{\underline{0}}_{N'\times\nu} \;\middle|\; \underline{\underline{\mathrm{E}}}_{N'} \;\middle|\; \underline{\underline{0}}_{N'\times\nu} \right) \underline{\mathrm{r}}^{\nu} && (4.90)\\
&= \sum_{k=1}^{K} \underline{\underline{\mathcal{C}}}_k \underline{\mathrm{v}}_k + \underline{\mathrm{n}} && (4.91)\\
&= \sum_{k=1}^{K} \underline{\underline{\mathrm{H}}}_k \underline{\mathrm{I}}_k + \underline{\mathrm{n}} && (4.92)
\end{aligned}$$

where $\underline{\underline{\mathrm{H}}}_k = \underline{\underline{\mathcal{C}}}_k \underline{\underline{\mathrm{S}}}_k$ and the $N' \times N'$ matrix $\underline{\underline{\mathcal{C}}}_k$ is now a *circulant matrix.* The effect of the cyclic prefix is thus to turn the linear convolutions associated with time dispersive channels into circular convolutions. This principle is already exploited in the well-known multicarrier modulation technique based on the DFT filter bank. Actually, it can be extended to any type of FB, including single carrier modulation [20]. The circulant matrices $\underline{\underline{\mathcal{C}}}_k$ are known to have the following eigenvalue decomposition :

$$\underline{\underline{\mathcal{C}}}_k = \underline{\underline{\mathrm{W}}}_{N'} \underline{\underline{\Lambda}}_k \underline{\underline{\mathrm{W}}}_{N'}^{H} \qquad (4.93)$$

where $\underline{\underline{\mathrm{W}}}_{N'}$ is the orthonormal DFT matrix of size N' and $\underline{\underline{\Lambda}}_k$ is a diagonal matrix formed with the values of the DFT of the channel impulse responses $c_k(n)$.

4.7 Conclusion

A general framework for the uplink of a PLC system was introduced in this Chapter. A large number of parallel subchannels are implemented through the modulation of N mutually orthogonal signatures by independent sequences of multilevel information symbols. The signature set can be represented by a filter bank. Classical multiple access methods (OFDMA, CDMA, TDMA) can be obtained by selecting the appropriate FB. Actually, any kind of FB can be investigated, leading to an infinity of multiple access systems. In this work, we restrict our attention to the class of paraunitary FBs.

For a given FB, the number of signatures is assumed to be much larger than the number of users. Each user gets a subset of signatures, according to a subchannel allocation algorithm. The allocation algorithm allows the spectral shaping of the transmitted signals as a function of the user-specific channel responses, with a maximum of flexibility. The amount of information in each subchannel is adapted to the signal to noise ratio measured at the output of the receiver.

IIR and FIR observation models have been established, relating the received signal at the output of the noisy multiuser channel, to the different sequences of information symbols. Practical joint detectors will be derived in Chapter 5 on the basis of these observation models.

Finally, three variants of the initial scheme have been proposed. The first one, CAP-FB transmission, provides a passband multiple access system (which is required for PLC), but without the need for a carrier. The second one, CAP-CDMA with long codes, represents an alternative to the signature allocation algorithm : the signature corresponding to a given subchannel changes from one symbol to another, which provides an identical level of performance for all signatures. Finally, cyclic-prefixed block transmission, which is classically restricted to OFDM, has been extended to the general FB transmission scheme.

Chapter 5

Joint Detection

5.1 Introduction

This chapter is dedicated to the derivation of practical joint detection structures. The matched filter receiver is firstly described in Section 5.2. In Section 5.3, the effect of the selected modulation scheme on the multiuser capacity region is investigated. The matched filter bound (MFB) is derived as an alternative upper bound on the optimal performance that can be expected from real detectors. Infinite linear and decision-feedback (DF) minimum mean square error (MMSE) joint detectors are presented in Section 5.4. Their performance is computed and compared to the multiuser capacity. Their FIR counterparts are derived in Section 5.5, and the computational complexity associated with the coefficient computation is analyzed in detail. The scenario of CAP-CDMA with long codes is analyzed separately in Section 5.6, and reduced-complexity algorithms for the computation of MMSE joint detectors suited to long-code CDMA are proposed. Finally, cyclic-prefixed equalization structures are analyzed in Section 5.7 and performance is compared for different FBs.

5.2 The matched filter receiver

Let us consider a baseband FB-based multiple access system with K users and N signature codes. The continuous-time signal received at the output of the multiple access channel is

$$r(t) = \sum_{m=-\infty}^{+\infty} \sum_{k=1}^{K} \sum_{p \in \mathcal{C}_k} I_p(m) h_{pk}(t - mT) + n(t) \tag{5.1}$$

where the $h_{pk}(t)$'s denote the equivalent channels including the p-th signature code $s_p(n)$, the pulse shaping filter $p(t)$, the k-th user channel $c_k(t)$, and the receiver filter $f(t)$ (see Chapter 4).

A sufficient statistic of the received signal is obtained by the use of a matched filter bank at the receiver. The outputs of the N matched filters $h_{pk}(-t)$ are sampled at the symbol rate $1/T$, which provides the N sequences :

$$y_p(m) = \int_{-\infty}^{+\infty} r(t)\, h_{pk}(t - mT). \tag{5.2}$$

This operation can be done by first filtering the received signal with $c_k(-t)$ in the analog domain and sampling the result at the chip rate $1/T_c$:

$$\begin{aligned} q_k(n) &= [r(t) \otimes c_k(-t)]\ (nT_c) && (5.3) \\ &= \sum_{k'=1}^{K} \sum_{n=-\infty}^{+\infty} v_{k'}(n)\, g_{kk'}((m-n)T_c) + \nu_k(n) && (5.4) \end{aligned}$$

where $g_{kk'}(t) = \int_{-\infty}^{+\infty} c_{k'}(\tau)\, c_k(\tau - t)\, d\tau$ are the user channel cross-correlation functions and $\nu_k(t) = n(t) \otimes c_k(-t)$ are the filtered noises with covariance $\Gamma_{\nu_k \nu_{k'}}(\tau) = \frac{N_0}{2}\, g_{kk'}(\tau)$. The N polyphase components of the K filter outputs $q_{\rho k}(n) = q_k(nN + \rho)$ are expressed, with z transforms, as :

$$\begin{pmatrix} \underline{\mathrm{Q}}_1(z) \\ \vdots \\ \underline{\mathrm{Q}}_K(z) \end{pmatrix} = \begin{pmatrix} \underline{\underline{\mathrm{G}}}_{11}(z) & \cdots & \underline{\underline{\mathrm{G}}}_{1K}(z) \\ \vdots & \ddots & \vdots \\ \underline{\underline{\mathrm{G}}}_{1K}^H(1/z^*) & \cdots & \underline{\underline{\mathrm{G}}}_{KK}(z) \end{pmatrix} \begin{pmatrix} \underline{\mathrm{V}}_1(z) \\ \vdots \\ \underline{\mathrm{V}}_K(z) \end{pmatrix} + \begin{pmatrix} \underline{\mathrm{U}}_1(z) \\ \vdots \\ \underline{\mathrm{U}}_K(z) \end{pmatrix} \tag{5.5}$$

The channel correlation polyphase matrices $\underline{\underline{\mathrm{G}}}_{kk'}(z)$ are Toeplitz of size $N \times N$ with element (i,j) given by the z transform of $g(nT + (i-j)T_c)$. They are related to the channel polyphase matrices $\underline{\underline{\mathrm{C}}}_k(z)$ as follows :

$$\underline{\underline{\mathrm{G}}}_{kk}(z) = \frac{T}{M}\, \underline{\underline{\mathrm{C}}}_k^H(1/z^*)\, \underline{\underline{\mathrm{C}}}_k(z). \tag{5.6}$$

As $g_{kk}(t)$ are even and real autocorrelation functions, we have the property:

$$\underline{\underline{\mathrm{G}}}_{kk}(z) = \underline{\underline{\mathrm{G}}}_{kk}^H(1/z^*) \qquad \forall k \tag{5.7}$$

The noise vector cross-spectra are $\underline{\underline{\gamma}}_{\nu_k,\nu_{k'}}(z) = \frac{N_0}{2}\, \underline{\underline{\mathrm{G}}}_{kk'}(z)$.

The matched filter outputs $y_p(m)$ are finally computed by passing the K sequences $q_k(n)$ through a bank of analysis filters matched to the synthesis bank :

$$
\begin{aligned}
y_p(m) &= \sum_{n=-\infty}^{+\infty} q_k(n - mN)\, s_p(n), \qquad p \in \mathcal{C}_k && (5.8) \\
&= \sum_{m=-\infty}^{+\infty} \sum_{k=1}^{K} \sum_{p' \in \mathcal{C}_k} x_{pp'}(m)\, I'_p(n-m) + w_p(n). && (5.9)
\end{aligned}
$$

The N^2 sequences of interference coefficients $x_{pp'}(n)$ are given by

$$x_{pp'}(n) = \int_{-\infty}^{+\infty} h_{pk}(t)\, h_{p'k'}(t - nT)\, \mathrm{d}t, \qquad p \in \mathcal{C}_k, p' \in \mathcal{C}_{k'}. \tag{5.10}$$

The global IIR observation model including the matched filters is given by

$$\begin{pmatrix} \underline{\mathrm{Y}}_1(z) \\ \vdots \\ \underline{\mathrm{Y}}_K(z) \end{pmatrix} = \begin{pmatrix} \underline{\underline{\mathrm{X}}}_{11}(z) & \cdots & \underline{\underline{\mathrm{X}}}_{1K}(z) \\ \vdots & \ddots & \vdots \\ \underline{\underline{\mathrm{X}}}_{1K}^H(1/z^*) & \cdots & \underline{\underline{\mathrm{X}}}_{KK}(z) \end{pmatrix} \begin{pmatrix} \underline{\mathrm{I}}_1(z) \\ \vdots \\ \underline{\mathrm{I}}_K(z) \end{pmatrix} + \begin{pmatrix} \underline{\mathrm{W}}_1(z) \\ \vdots \\ \underline{\mathrm{W}}_K(z) \end{pmatrix} \tag{5.11}$$

or, more compactly,

$$\underline{\mathrm{Y}}(z) = \underline{\underline{\mathrm{X}}}(z)\, \underline{\mathrm{I}}(z) + \underline{\mathrm{W}}(z). \tag{5.12}$$

The size $N_k \times N_{k'}$ interference matrices $\underline{\underline{\mathrm{X}}}_{kk'}(z)$ are given by

$$\underline{\underline{\mathrm{X}}}_{kk'}(z) = \underline{\underline{\mathrm{S}}}_k^H(1/z^*)\, \underline{\underline{\mathrm{G}}}_{kk'}(z)\, \underline{\underline{\mathrm{S}}}_{k'}(z). \tag{5.13}$$

The noise vector cross-spectrum is $\underline{\underline{\gamma}}_{w,w}(z) = \frac{N_0}{2}\, \underline{\underline{\mathrm{X}}}(z)$.

Let us now derive a first bound on the joint detector performance, called the *matched filter bound*. This bound is based on the principle that the joint detector cannot do better than removing ISI, ICI and MAI without enhancing the additive noise. These ideal symbol estimates are given by

$$\hat{I}_p(n) = x_{pp}(0) I_p(n) + w_p(n). \tag{5.14}$$

The corresponding signal to noise ratio is

$$\rho_p = \frac{x_{pp}^2(0)\sigma_I^2}{\sigma_{w_p}^2} = \frac{x_{pp}^2(0)\sigma_I^2}{x_{pp}(0)\, N_0/2} = \frac{2\mathcal{E}_{pk}}{N_0}. \tag{5.15}$$

5.3 Capacity of FB-based multiple access

In this Section, we compute the multiuser capacity of the FB-based multiple access system. This capacity region is smaller than the true capacity region computed in Chapter 3, as additional constraints are introduced : the signals $x_k(t)$ produced by the transmitters are now the outputs of a finite-size FB modulated by mutually independent sequences of information symbols. The power spectral density of the transmitted signals is not arbitrary any more, and the available degrees of freedom depend on both the nature and the size of the selected FB.

5.3.1 Mutual information and capacity region

In order to derive a practical expression of the multiuser capacity region, we firstly propose a slightly modified version of the FB-based multiple-access observation model. The modifications are :

- All K users are assumed to transmit symbols on all N signatures simultaneously. The symbol variance for the k-th user and the n-th signature becomes $\lambda_{pk}^2 \sigma_I^2$. The allocation of a given signature n to a single user k translates into the constraint : $\lambda_{pk} = 1$ and $\lambda_{k'n} = 0$, $\forall k' \neq k$.

- A limited number of N_b symbols per signature are transmitted by the users. This block transmission model actually converges to the initial continuous transmission model for $N_b \to \infty$.

- The information symbols $I_{pk}(n)$ are assumed to have a Gaussian distribution. This distribution is known to maximize the mutual information between power-constrained transmitted and received signals [52].

Let $\mathcal{S}$ be an arbitrary subset of K_1 users. We denote by $\overline{\mathcal{S}}$ the complementary subset, including $K_2 = K - K_1$ users. The observation model is now

$$
\begin{aligned}
\underline{\mathrm{r}}^{N_b} &= \sum_{k \in \mathcal{S}} \underline{\underline{\mathcal{H}}}_k^{N_b} \, \underline{\mathrm{I}}_k^{N_b} + \sum_{k' \in \overline{\mathcal{S}}} \underline{\underline{\mathcal{H}}}_{k'}^{N_b} \, \underline{\mathrm{I}}_{k'}^{N_b} + \underline{\mathrm{n}}^{N_b} && (5.16) \\
&= \underline{\underline{\mathcal{H}}}_{\mathcal{S}}^{N_b} \, \underline{\mathrm{I}}_{\mathcal{S}}^{N_b} + \underline{\underline{\mathcal{H}}}_{\overline{\mathcal{S}}}^{N_b} \, \underline{\mathrm{I}}_{\overline{\mathcal{S}}}^{N_b} + \underline{\mathrm{n}}^{N_b} && (5.17) \\
&= \underline{\mathrm{r}}_1^{N_b} + \underline{\mathrm{r}}_2^{N_b} + \underline{\mathrm{n}}^{N_b} && (5.18)
\end{aligned}
$$

where $\underline{\mathrm{I}}_k^{N_b}$ is the vector of N_bN symbols transmitted by user k, $\underline{\mathrm{r}}^{N_b}$ and $\underline{\mathrm{n}}^{N_b}$ are of size $(N_b+L)M$, and $\underline{\underline{\mathcal{H}}}_k^{N_b}$ is a size $(N_b+L)M \times N_bN$ block-Toeplitz matrix. The continuous transmission model, obtained by letting N_b go to infinity, is given by

$$\underline{\mathrm{R}}(z) = \underline{\underline{\mathrm{H}}}_{\mathcal{S}}(z)\,\underline{\mathrm{I}}_{\mathcal{S}}(z) + \underline{\underline{\mathrm{H}}}_{\overline{\mathcal{S}}}(z)\,\underline{\mathrm{I}}_{\overline{\mathcal{S}}}(z) + \underline{\mathrm{N}}(z) \tag{5.19}$$

where $\underline{\underline{\mathrm{H}}}_{\mathcal{S}}(z)$ and $\underline{\underline{\mathrm{H}}}_{\overline{\mathcal{S}}}(z)$ are the $M \times K_1N$ and $M \times K_2N$ polyphase matrices associated with the composite channels $h_{pk}(t)$.

For a fixed block size N_b and a fixed power allocation defined by the set of coefficients $\left\{\lambda_{pk}^2\right\}$, the set of achievable data rates is known to be :

$$\mathcal{C}_{N_b}\left(\lambda_{pk}^2\right) = \left\{\{R_k\} : 0 \leq \sum_{k\in\mathcal{S}} R_k \leq \frac{1}{N_b}\mathcal{I}\left(\underline{\mathrm{r}}^{N_b};\underline{\mathrm{I}}_{\mathcal{S}}^{N_b}|\underline{\mathrm{I}}_{\overline{\mathcal{S}}}^{N_b}\right)\ \forall\mathcal{S}\subset\{1,\cdots,K\}\right\} \tag{5.20}$$

where $\mathcal{I}\left(\underline{\mathrm{x}};\underline{\mathrm{y}}|\underline{\mathrm{z}}\right)$ denotes the conditional mutual information between the vectors $\underline{\mathrm{x}}$ and $\underline{\mathrm{y}}$, for a given vector $\underline{\mathrm{z}}$. This region is a K-dimensional polyhedron defined by 2^K-1 constraints, and including $K!$ vertices in the positive quadrant. The global capacity region is then obtained by

$$\mathcal{C} = \text{closure}\left(\lim_{N_b\to\infty}\left[\bigcup_{\lambda_{pk}^2}\mathcal{C}_{N_b}\left(\lambda_{pk}^2\right)\right]\right). \tag{5.21}$$

The union is taken over all admissible input-power distributions, i.e. all admissible sets of coefficients λ_{pk}^2.

Let us firstly derive the expression of the mutual information $\mathcal{I}\left(\underline{\mathrm{r}}^{N_b};\underline{\mathrm{I}}_{\mathcal{S}}^{N_b}|\underline{\mathrm{I}}_{\overline{\mathcal{S}}}^{N_b}\right)$ from the observation model given by (5.16) :

$$\begin{aligned}\mathcal{I}\left(\underline{\mathrm{r}}^{N_b};\underline{\mathrm{I}}_{\mathcal{S}}^{N_b}|\underline{\mathrm{I}}_{\overline{\mathcal{S}}}^{N_b}\right) &= \mathbf{h}\left(\underline{\mathrm{r}}^{N_b}|\underline{\mathrm{I}}_{\overline{\mathcal{S}}}^{N_b}\right) - \mathbf{h}\left(\underline{\mathrm{r}}^{N_b}|\underline{\mathrm{I}}_{\mathcal{S}}^{N_b},\underline{\mathrm{I}}_{\overline{\mathcal{S}}}^{N_b}\right) && (5.22)\\ &= \mathbf{h}\left(\underline{\mathrm{r}}_1^{N_b}+\underline{\mathrm{n}}^{N_b}\right) - \mathbf{h}\left(\underline{\mathrm{n}}^{N_b}\right) && (5.23)\end{aligned}$$

where $\mathbf{h}\left(\underline{\mathrm{x}}\right)$ denotes the differential entropy of the continuous random vector $\underline{\mathrm{x}}$ and $\mathbf{h}\left(\underline{\mathrm{x}}|\underline{\mathrm{y}}\right)$ denotes the average conditional entropy of $\underline{\mathrm{x}}$ given $\underline{\mathrm{y}}$. The differential entropy of a size-N zero-mean Gaussian vector $\underline{\mathrm{x}} \sim \mathcal{N}\left(\underline{0},\underline{\underline{\mathrm{R}}}_{xx}\right)$ is known to be

$$\mathbf{h}\left(\underline{\mathrm{x}}\right) = \log\left[(\pi e)^N\ \det\left(\underline{\underline{\mathrm{R}}}_{xx}\right)\right]. \tag{5.24}$$

Introducing this result into (5.22), we get

$$\mathcal{I}\left(\underline{\mathrm{r}};\underline{\mathrm{I}}_{\mathcal{S}}|\underline{\mathrm{I}}_{\overline{\mathcal{S}}}\right) = \log\left[\frac{\det\left(\underline{\underline{\mathrm{R}}}_{r_1r_1}+\underline{\underline{\mathrm{R}}}_{nn}\right)}{\det\left(\underline{\underline{\mathrm{R}}}_{nn}\right)}\right] \tag{5.25}$$

$$= \log\left[\det\left(\underline{\underline{\mathrm{E}}}_{M(N_b+L)}+\frac{\sigma_I^2}{\sigma_n^2}\underline{\underline{\mathcal{H}}}_{\mathcal{S}}^{N_b}\left(\underline{\underline{\Lambda}}_{\mathcal{S}}^{N_b}\right)^2(\underline{\underline{\mathcal{H}}}_{\mathcal{S}}^{N_b})^T\right)\right]$$

$$= \log\left[\det\left(\underline{\underline{\mathrm{E}}}_{N_bK_1N}+\frac{\sigma_I^2}{\sigma_n^2}\underline{\underline{\Lambda}}_{\mathcal{S}}^{N_b}(\underline{\underline{\mathcal{H}}}_{\mathcal{S}}^{N_b})^T\underline{\underline{\mathcal{H}}}_{\mathcal{S}}^{N_b}\underline{\underline{\Lambda}}_{\mathcal{S}}^{N_b}\right)\right] \tag{5.26}$$

where the diagonal matrix $\underline{\underline{\Lambda}}_{\mathcal{S}}^{N_b}$ is defined by

$$E\left\{\underline{\mathrm{I}}_{\mathcal{S}}^{N_b}\ (\underline{\mathrm{I}}_{\mathcal{S}}^{N_b})^T\right\} = \sigma_I^2\ \left(\underline{\underline{\Lambda}}_{\mathcal{S}}^{N_b}\right)^2. \tag{5.27}$$

Using the asymptotic properties of Toeplitz matrices, it can be demonstrated [57] that the average mutual information in (5.26) becomes

$$\overline{\mathcal{I}}_{\mathcal{S}} = \lim_{N_b\to\infty}\frac{1}{N_b}\mathcal{I}\left(\underline{\mathrm{r}};\underline{\mathrm{I}}_{\mathcal{S}}|\underline{\mathrm{I}}_{\overline{\mathcal{S}}}\right) \tag{5.28}$$

$$= \frac{1}{2\pi}\int_{-\pi}^{\pi}\log\left[\det\left(\underline{\underline{\mathrm{E}}}_{K_1N}+\frac{\sigma_I^2}{\sigma_n^2}\underline{\underline{\Lambda}}_{\mathcal{S}}\underline{\underline{\mathrm{H}}}_{\mathcal{S}}^H\left(e^{j\Omega}\right)\underline{\underline{\mathrm{H}}}_{\mathcal{S}}\left(e^{j\Omega}\right)\underline{\underline{\Lambda}}_{\mathcal{S}}\right)\right]\mathrm{d}\Omega$$

$$= \frac{1}{2\pi}\int_{-\pi}^{\pi}\log\left[\det\left(\underline{\underline{\mathrm{E}}}_{K_1N}+\frac{\sigma_I^2}{N_0/2}\underline{\underline{\Lambda}}_{\mathcal{S}}\underline{\underline{\mathrm{X}}}_{\mathcal{S}}\left(e^{j\Omega}\right)\underline{\underline{\Lambda}}_{\mathcal{S}}\right)\right]\mathrm{d}\Omega \tag{5.29}$$

when the burst size goes to infinity. The demonstration is not given here, but can be found in [55]. It is based on the observation that the determinant of the matrix in (5.26) is equal to the product of the N_bK_1N eigenvalues $(1+\frac{\sigma_I^2}{\sigma_n^2}\rho_i)$ of this matrix. When N_b goes to infinity, the eigenvalues ρ_i converge to those of an equivalent circulant matrix.

The result in (5.28) can be further developed to underline the role of the signature allocation coefficients λ_{pk}^2 :

$$\overline{\mathcal{I}}_{\mathcal{S}} = \frac{1}{2\pi}\int_{-\pi}^{\pi}\log\left[\det\left(\underline{\underline{\mathrm{E}}}_M+\frac{\sigma_I^2}{\sigma_n^2}\underline{\underline{\mathrm{H}}}_{\mathcal{S}}\left(e^{j\Omega}\right)\underline{\underline{\Lambda}}_{\mathcal{S}}^2\underline{\underline{\mathrm{H}}}_{\mathcal{S}}^H\left(e^{j\Omega}\right)\right)\right]\mathrm{d}\Omega \tag{5.30}$$

$$= \frac{1}{2\pi}\int_{-\pi}^{\pi}\log\left[\det\left(\underline{\underline{\mathrm{E}}}_M+\frac{1}{\sigma_n^2}\sum_{k\in\mathcal{S}}\underline{\underline{\mathrm{C}}}_k\left(e^{j\Omega}\right)\underline{\underline{\gamma}}_{v_kv_k}\left(e^{j\Omega}\right)\underline{\underline{\mathrm{C}}}_k^H\left(e^{j\Omega}\right)\right)\right]\mathrm{d}\Omega$$

where the polyphase spectrum $\underline{\underline{\gamma}}_{v_k v_k}(z)$ associated with the chip-rate sequence $v_k(n)$ produced by user k is

$$\begin{aligned} \underline{\underline{\gamma}}_{v_k v_k}\left(e^{j\Omega}\right) &= \sigma_I^2 \, \underline{\underline{\mathrm{S}}}\left(e^{j\Omega}\right) \underline{\underline{\Lambda}}_k^2 \, \underline{\underline{\mathrm{S}}}^H\left(e^{j\Omega}\right) \\ &= \sigma_I^2 \sum_{p=1}^{N} \lambda_{pk}^2 \, \underline{\mathrm{S}}_p\left(e^{j\Omega}\right) \underline{\mathrm{S}}_p^H\left(e^{j\Omega}\right). \end{aligned} \tag{5.31}$$

For a fixed signature allocation $\{\lambda_{pk}^2\}$, the capacity region is a polyhedron defined by the $2^K - 1$ constraints $\overline{\mathcal{I}}_{\mathcal{S}}$. With K users and N signatures, there are K^N possible polyhedrons, corresponding to the K^N distinct signature allocations. Considering the restrictive two-user scenario, the polyhedron is a pentagon defined by

$$\mathcal{C}_\infty\left(\lambda_{pk}^2\right) = (R_1, R_2) : \begin{cases} 0 \le R_1 \le \overline{\mathcal{I}}_{\{1\}} \\ 0 \le R_2 \le \overline{\mathcal{I}}_{\{2\}} \\ 0 \le R_1 + R_2 \le \overline{\mathcal{I}}_{\{1,2\}} \end{cases} \tag{5.32}$$

Figure 5.1 illustrates the $2^4 = 16$ regions obtained with $N = 4$ Hadamard signature codes of length 4. Only 14 of these regions are really pentagons. The two remaining ones are degenerated to vertical or horizontal segments : they correspond to the allocation of all signatures to the same user. As given by equation (5.21), the global capacity region is obtained by taking the convex closure of the union of the pentagons. The boundary of the resulting capacity region is given by the dashed line in Figure 5.1. A given rate pair (R_1, R_2) of the boundary is generally achieved by timesharing between two distinct signature allocations.

5.3.2 Optimal signature allocation

The computation of an optimal signature allocation scheme in terms of achievable data rates belongs to the class of integer programming problems. The problem can be considerably simplified by considering its continuous relaxation. A similar strategy was adopted in Chapter 3 to compute the FDMA capacity of frequency selective multiuser channels. The idea, here, is to allow all users to use all signatures simultaneously. The constraint on the power allocation coefficients λ_{pk}^2 becomes

$$0 \le \lambda_{pk}^2 \le 1 \qquad\qquad \sum_{k=1}^{K} \lambda_{pk}^2 = 1. \tag{5.33}$$

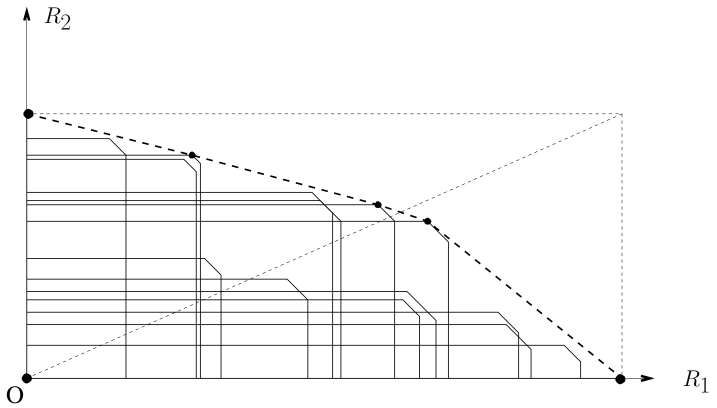

Figure 5.1: *Two-user capacity region for a size-4 FB-based transmitter (Hadamard signature codes)*

With the relaxed constraints, the new capacity region is generated by the union of an infinite number of polyhedrons. Moreover, as every convex combination of feasible signature allocations is also a feasible signature allocation, *the convex closure operation is not needed any more* to generate the global capacity region. This implies that every point of the global capacity region can be achieved with a fixed signature allocation.

The constraints in (5.33) implicitly assume that the same total power is transmitted on each signature code. The consequence for the polyphase spectra $\underline{\underline{\gamma}}_{v_k v_k}(z)$ is

$$\sum_{k=1}^{K} \underline{\underline{\gamma}}_{v_k v_k}(z) = \sigma_I^2 \, \underline{\underline{S}}(z) \left(\sum_{k=1}^{K} \underline{\underline{\Lambda}}_k \right) \underline{\underline{S}}^H(1/z^*) \tag{5.34}$$

$$\leq \sigma_I^2 \, \underline{\underline{S}}(z) \, \underline{\underline{S}}^H(1/z^*) = \sigma_I^2 \, \underline{\underline{E}}_N \tag{5.35}$$

where the inequality of matrices in (5.34) means that the matrix difference is non-negative definite. This is equivalent to the *PSD-sum constraint* introduced in Chapter 3. Alternative constraints could be investigated like the power sum constraint (obtained with $\sigma_I^2 \sum_k \sum_p \lambda_{pk}^2 \leq \overline{P}$) or the individual power constraint (obtained with $\sigma_I^2 \sum_p \lambda_{pk}^2 \leq \overline{P}_k \ \ \forall k$), but are beyond the scope of this work.

Like for the true capacity region, the boundary of the FB-based capacity region can be traced out by maximizing the aggregate rate $R_\alpha = \sum_k \alpha_k R_k$

for a given set of relative priorities $\{\alpha_k\}$. The maximum aggregate rate is known to be obtained with successive decoding at the receiver, and a decoding order in accordance with the user relative priorities. Assuming that the users are ordered in ascending order of the relative priorities, the individual data rates are given by

$$R_k = \overline{\mathcal{I}}_{\{k,\cdots,K\}} - \overline{\mathcal{I}}_{\{k+1,\cdots,K\}} \qquad \forall k < K \tag{5.36}$$

$$R_K = \overline{\mathcal{I}}_{\{K\}}. \tag{5.37}$$

The aggregate rate is thus

$$R_\alpha = \sum_{k=1}^{K} \alpha_k R_k = \sum_{k=1}^{K} (\alpha_k - \alpha_{k-1})\ \overline{\mathcal{I}}_{\{k,\cdots,K\}}. \tag{5.38}$$

The quantities $\overline{\mathcal{I}}_{\mathcal{S}}$ in last equation are given by equation (5.30) and depend on the signature allocation. The computation of the optimal signature allocation scheme λ_{pk}^2 is then formulated as follows :

$$\left\{\lambda_{pk}^2\right\} = \arg\max_{\lambda_{pk}^2} \left[R_\alpha\left(\left\{\lambda_{pk}^2\right\}\right)\right]. \tag{5.39}$$

It can be demonstrated that the objective function (5.38) is a concave function in the parameters λ_{pk}^2. This property, associated with the linear constraints in (5.33), guarantees that the optimization problem in (5.39) is a standard convex programming problem : a local maximum is also a global maximum, and standard numerical search algorithms can be used to find the solution efficiently.

5.3.3 Maximum balanced rates

One may be interested in a specific point of the capacity region, like the balanced rate solution defined in Chapter 3. In that case, the optimization problem in (5.39) has to be solved iteratively for different sets of relative priorities $\left\{\alpha_k^{(i)}\right\}$, until the solution satisfies the balanced rate constraint. Actually, two major difficulties have to be taken into account in the computation of the maximum balanced rates associated with a FB-based system.

Firstly, there is no closed form solution to the problem of optimal signature allocation for a given set of relative priorities. At each iteration i, a new convex programming problem has to be solved.

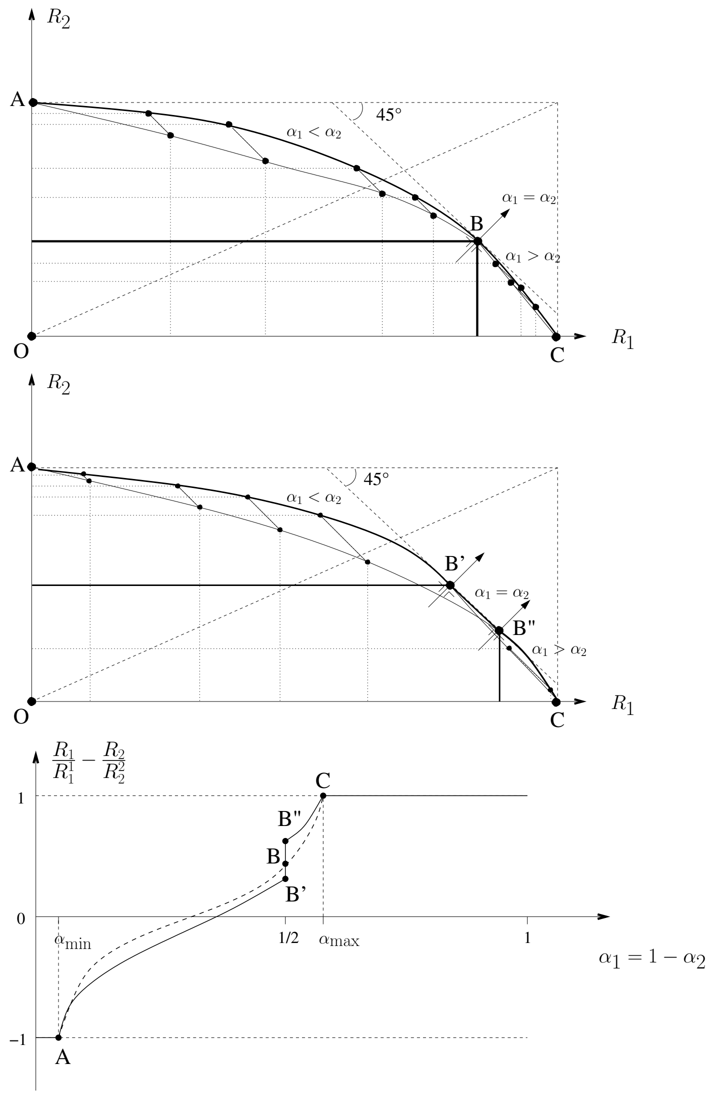

Figure 5.2: *Generation of the true capacity region and the FB-constrained capacity region by the union of pentagons*

Secondly, the solution proposed in (5.36) is restricted to be a vertex of the K-dimensional polyhedron corresponding to the selected signature allocation. The vertex is chosen in accordance with the ordering of the relative priorities α_k. The boundary of the true capacity region is effectively generated by the union of such vertices. In the case of a FB-constrained capacity region, however, some parts of the boundary are not covered by the union of these vertices. Figure 5.2 illustrates this difference in a two-user case. The first graph gives the true capacity region (as considered in Chapter 3). It is a convex region generated by the union of pentagons. Each pentagon has a lower and an upper vertex. The boundary of the capacity region is the curve ABC. The segment AB of the curve is generated by upper vertices, which means that the decoding order is $(1, 2)$. All points of this segment can be obtained by maximizing the aggregate rate R_α with $\alpha_1 < \alpha_2$. The segment BC of the curve is generated by lower vertices, which means that the decoding order is $(2, 1)$. All points of this segment can be obtained by maximizing the aggregate rate R_α with $\alpha_1 > \alpha_2$. Finally, point B corresponds to the maximum sum rate : it is obtained by maximizing the aggregate rate R_α with $\alpha_1 = \alpha_2$. As the maximum sum rate solution is of the FDMA type, the associated pentagon is degenerated into a rectangle. Indeed, the power is allocated to the users in separate frequency bands, and successive decoding is not needed any more. The second graph gives the corresponding FB-based capacity region. It is also a convex region generated by the union of pentagons. But now the maximum sum rate solution ($\alpha_1 = \alpha_2$) is also a pentagon, with distinct vertices B' and B". Indeed, under the FB constraint, an FDMA power allocation is not feasible any more (because of the spectral overlapping among the different signatures). As a consequence, the whole segment BB' belongs to the boundary of the capacity region, but only points B' and B" are pentagon vertices. The intermediate solutions are obtained by timesharing between the two possible decoding orders, and the corresponding rate pairs (R_1, R_2) are not given by the general solution in (5.36). The third graph gives the weighted rate imbalance $R_1/R_1^1 - R_2/R_2^1$ as a function of $\alpha_1 = 1 - \alpha_2$. The dashed line corresponds to the true capacity region, while the continuous line corresponds to the FB-based capacity region. The maximum balanced rates solution corresponds to the root of this function. If the balanced rate solution is located in one of the intervals AB' or B"C, then the root can be found by searching through the intervals $\alpha_{\text{min}} < \alpha_1 < 1/2$ and $1/2 < \alpha_1 < \alpha_{\text{max}}$, respectively. This case corresponds to the displayed figure. It could happen, however, that the balanced rate solution be located in the interval

B'B" : then the search algorithm would fail to find the root of the function. This problem can be handled easily in the restrictive two-user case, but it is not tractable in the general K-user scenario.

5.3.4 Influence of the FB

We firstly investigate the effect of the FB choice on the SU capacity. In a SU scenario, all signatures can be fully allocated to the same user, i.e. $\lambda_{1p}^2 = 1 \; \forall p$. With a paraunitary FB, this implies that the transmitted polyphase spectrum $\underline{\underline{\gamma}}_{v_1 v_1}(z)$ is

$$\underline{\underline{\gamma}}_{v_1 v_1}(z) \;=\; \sigma_I^2 \, \underline{\underline{\mathrm{S}}}(z) \, \underline{\underline{\Lambda}}_1^2 \, \underline{\underline{\mathrm{S}}}^H(z) = \sigma_I^2 \, \underline{\underline{\mathrm{E}}}_N. \tag{5.40}$$

The SU capacity is then given by

$$\begin{aligned} \overline{\mathcal{I}}_1 &= \frac{1}{2\pi} \int_{-\pi}^{\pi} \log \left[\det \left(\underline{\underline{\mathrm{E}}}_M + \frac{\sigma_I^2}{\sigma_n^2} \underline{\underline{\mathrm{C}}}_1 \left(e^{j\Omega}\right) \underline{\underline{\mathrm{C}}}_1^H \left(e^{j\Omega}\right) \right) \right] \mathrm{d}\Omega \\ &= \int_{-\infty}^{\infty} \log \left(1 + \frac{\sigma_I^2}{N_0/2} |C_1(f)|^2 \right) \mathrm{d}f, \end{aligned} \tag{5.41}$$

irrespectively of the selected FB. In particular, the SU FB-based capacity is identical to that of the single carrier modulation obtained by letting $\underline{\underline{\mathrm{S}}}(z) = \underline{\underline{\mathrm{E}}}_N$. As a consequence, it is also independent of N, as the SU single carrier modulation can obviously be represented with a unit-matrix FB of arbitrary size. The single-user FB-based capacity is thus independent of the *choice of signatures* and of the *number of signatures*, provided that the associated FB is paraunitary. The fundamental reason for this is that any paraunitary FB of any size produces the same flat power spectral density at its output when it is modulated by independent sequences of equal variance.

The boundary of the TDMA capacity region, i.e. the hyperplane joining the SU rate solutions, is then also independent of the FB. Consequently, the relative performance of different FBs can be compared adequately through the *multiuser gain* defined in Chapter 3 as the ratio of the maximum balanced rates to the TDMA balanced rates. The multiuser gain is different for every FB. Actually, it depends on the ability of the FB to model the power spectral density of the transmitted signals with as much flexibility as possible. This flexibility is limited by the N degrees of freedom corresponding to the N different signatures.

An upper bound on the FB-constrained capacity region is the (PSD-sum constrained) true capacity region presented in Chapter 3. In the two-user case, its boundary is represented by the line AEB in Figure 3.6. This upper bound can be approached with a frequency-selective FB of size $N \gg 1$, i.e. with a FB able to shape the transmission PSD of each user with an arbitrary flexibility.

On the opposite, a lower bound on the FB-constrained capacity region is obtained by forcing, for each user, the allocation of a uniform power to all signatures :

$$\lambda_{pk}^2 = \lambda_k^2 \ \ \forall p \qquad\qquad \sum_{k=1}^{K} \lambda_k^2 = 1. \tag{5.42}$$

With this signature allocation, all users are forced to transmit a flat-PSD signal. The corresponding capacity region is independent of the FB as (5.30) becomes

$$\begin{aligned} \overline{\mathcal{I}}_{\mathcal{S}} &= \frac{1}{2\pi}\int_{-\pi}^{\pi} \log\left[\det\left(\underline{\underline{\mathrm{E}}}_M + \frac{\sigma_I^2}{\sigma_n^2}\sum_{k\in\mathcal{S}} \lambda_k^2\, \underline{\underline{\mathrm{C}}}_k\left(e^{j\Omega}\right)\underline{\underline{\mathrm{C}}}_k^H\left(e^{j\Omega}\right)\right)\right]\mathrm{d}\Omega \\ &= \int_{-\infty}^{\infty} \log\left(1 + \frac{\sigma_I^2}{N_0/2}\sum_{k=\in\mathcal{S}} \lambda_k^2\,|C_k(f)|^2\right)\mathrm{d}f. \end{aligned} \tag{5.43}$$

This is also the capacity region corresponding to a degenerated FB with $N = 1$ signature, i.e. a FB with the lowest flexibility as possible. In the two-user case, the boundary of this region is represented by the line ADB in Figure 3.6. The same capacity region can be expected from the long-code multiple access system introduced in Section 4.5, as the variability of the signature codes used by each user makes the PSD of the transmitted signals almost uniform.

5.3.5 Capacity vs. MFB

In this section, we show how the SINR bound provided by the MFB can be used to provide a simple upper bound on the multiuser capacity. Equation

(5.28) can be rewritten as

$$\begin{aligned}
\overline{\mathcal{I}}_{\mathcal{S}} &= \frac{1}{2\pi}\int_{-\pi}^{\pi} \log\left[\det\left(\underline{\underline{\mathrm{E}}}_{K_1N} + \frac{\sigma_I^2}{N_0/2}\underline{\underline{\Lambda}}_{\mathcal{S}}\underline{\underline{\mathrm{X}}}_{\mathcal{S}}\left(e^{j\Omega}\right)\underline{\underline{\Lambda}}_{\mathcal{S}}\right)\right]\mathrm{d}\Omega \\
&\leq \frac{1}{2\pi}\int_{-\pi}^{\pi} \log\left[\prod_{i=1}^{K_1N}\left(\underline{\underline{\mathrm{E}}}_{K_1N} + \frac{\sigma_I^2}{N_0/2}\underline{\underline{\Lambda}}_{\mathcal{S}}\underline{\underline{\mathrm{X}}}_{\mathcal{S}}\left(e^{j\Omega}\right)\underline{\underline{\Lambda}}_{\mathcal{S}}\right)_{ii}\right]\mathrm{d}\Omega \\
&= \frac{1}{2\pi}\sum_{k\in\mathcal{S}}\sum_{p=1}^{N}\int_{-\pi}^{\pi} \log\left[1 + \frac{\sigma_I^2}{N_0/2}\lambda_{pk}^2\left(\underline{\underline{\mathrm{X}}}_k\right)_{pp}\right]\mathrm{d}\Omega \\
&\leq \sum_{k\in\mathcal{S}}\sum_{p=1}^{N} \log\left[1 + \frac{\sigma_I^2}{N_0/2}\lambda_{pk}^2\frac{1}{2\pi}\int_{-\pi}^{\pi}\left(\underline{\underline{\mathrm{X}}}_k\right)_{pp}\mathrm{d}\Omega\right] \\
&= \sum_{k\in\mathcal{S}}\sum_{p=1}^{N} \log\left[1 + \frac{2\mathcal{E}_{pk}}{N_0}\right].
\end{aligned} \tag{5.44}$$

The first inequality follows from the property that the determinant of a symmetric positive definite matrix is always smaller than the product of its diagonal values. For the second one, it is known that for any positive function $f(x)$,

$$\frac{1}{2\pi}\int_{-\pi}^{\pi}\log\left[f(x)\right]dx \leq \log\left[\frac{1}{2\pi}\int_{-\pi}^{\pi}f(x)dx\right] \tag{5.45}$$

with equality if and only if $f(x)$ is constant. This result shows that, under some very restrictive conditions, the multiuser capacity is simply the sum of the single channel capacities associated with every signature p and every user k, which only depend on the ratios $\mathcal{E}_{pk}/N_0$. Actually, the proposed bound is really valuable if all the following conditions are satisfied :

- Every signature is allocated to a single user.
- The inter-signature orthogonality is not destroyed by the multiuser channel selectivity. This should be valid for any multiuser channel. This condition implies that all signatures should be located in separate frequency bands. A frequency selective FB with non-overlapping subbands should be used for that purpose.
- Each subchannel is sufficiently flat, so that the SINR in every subchannel is roughly equal to the channel SNR at the corresponding frequency. As a consequence, the size N of the frequency-selective FB must be very large.

- The SNR gap Γ is equal to 1, i.e. perfect coding is assumed in every separate subchannel.

A simple signature allocation algorithm can be implemented on the basis of the MFB. The MFB-based aggregate rate $\overline{R}_\alpha$ can be written as

$$\overline{R}_\alpha = \sum_{p=1}^{N} \sum_{k=1}^{K} \lambda_{pk}^2 \left(\alpha_k \overline{R}_{pk}\right), \qquad \text{with } \overline{R}_{pk} \triangleq \mathcal{C}\left(\frac{2\mathcal{E}_{pk}}{N_0}\right) \tag{5.46}$$

with a single $\lambda_{pk}^2 = 1$ and the others equal to 0, for every p. Let us define the following continuous relaxation of the signature allocation constraint :

$$0 \leq \lambda_{pk}^2 \leq 1, \qquad \sum_{k=1}^{K} \lambda_{pk}^2 = 1. \tag{5.47}$$

For equation (5.46) to remain valid, the coefficients λ_{pk}^2 must be re-interpreted as time-sharing coefficients, and not as power allocation coefficients as in the previous Sections. The maximization of the aggregate rate R_α in (5.46) under the relaxed constraints (5.47) is identical to the FDMA subchannel allocation problem analyzed in Section 3.6.1. The solution is given by Algorithm 3.5. The computation of maximum balanced rates, that requires the iterative computation of adequate relative priorities α_k, is obtained by Algorithm 3.6. Linear optimization theory tells us that at least one solution exists that comprises at most $N + (K - 1)$ non-zero components λ_{pk}^2. This implies that a maximum of $K - 1$ signatures will be shared between couples of users, or alternatively a single signature could be shared between all of the K users, all other signatures being allocated to a single user. Assuming that $N \gg K$, we can see that time-sharing only concerns a small fraction of the available signatures. If time-sharing is not allowed, we have to approximate the continuous solution given by Algorithm 3.6 and force the allocation of each signature to a single user. It results that the balanced rates constraints are not exactly satisfied any more. A measure of the deviation from these conditions is given through the 'user imbalance index' defined as follows, together with a practical upper bound :

$$\Delta_{\text{users}} = \frac{\sigma_k\left(\frac{R_k}{\beta_k}\right)}{\overline{m}_k\left(\frac{R_k}{\beta_k}\right)} \leq \frac{K}{2\,N}\sqrt{\frac{1}{K^3}\sum_k (\frac{1}{\alpha_k})^2} \tag{5.48}$$

where $\sigma_k(.)$ and $\overline{m}_k(.)$ stand for standard deviation and mean across the users respectively. Equation (5.48) shows that the rounding effect associated with a discrete signature allocation is negligible if the ratio N/K

is large. With a large number of signatures, indeed, the boundary of the capacity region can be covered with a better granularity.

The MFB-based signature allocation is suboptimal in the sense that the inter-signature interference is ignored. However, it provides a useful initial allocation for more advanced allocation algorithms as it ensures the best matching as possible between the set of available signatures and the user channel attenuations and noises. The method can be generalized to all situations where a K-user channel can be modeled as a parallel transmission of information in N separate and independent subchannels.

5.4 IIR joint detectors

In the case of a frequency-selective channel, the symbol estimates obtained at the output of the matched filter bank are severely corrupted by interference. A popular solution consists in the use of a MIMO equalizer that intends to compute more reliable estimates of the symbols on the basis of a minimum mean square error criterion (MMSE).

In this section we investigate the structure of IIR linear or decision-feedback (DF) joint detectors designed for the MMSE criterion. These structures are the best possible linear and DF joint detectors, and their corresponding performance provides an upper bound of the performance which can be achieved by their FIR counterparts. This is the main motivation to investigate these IIR detectors. Their FIR counterparts will be investigated in the following section.

For all continuous transmission schemes presented in Chapter 4, a generic IIR observation model was defined as follows (See (4.42), (4.67) and (4.79)) :

$$\underline{\mathrm{R}}(z) = \underline{\underline{\mathrm{H}}}(z)\,\underline{\mathrm{I}}(z) + \underline{\mathrm{N}}(z). \tag{5.49}$$

The IIR joint detectors derived in this Section rely on this generic observation model. The baseband FB transmission scheme is assumed in the next derivations, but the application to CAP-FB transmission or CAP-CDMA with long codes is straightforward.

5.4.1 MMSE linear joint detection

A fractionally spaced linear joint detector (JD) builds estimates of the N transmitted symbol sequences $I_p(n)$ as follows :

$$\hat{\underline{\mathrm{I}}}(z) = \underline{\underline{\mathrm{W}}}(z)\,\underline{\mathrm{R}}(z) \tag{5.50}$$

where $\underline{\underline{W}}(z)$ is a bank of $N \times M$ infinite length filters. The vector of z-transformed estimation errors is defined by :

$$\underline{\epsilon}(z) = \underline{I}(z) - \hat{\underline{I}}(z). \tag{5.51}$$

This IIR linear JD can be designed for an MMSE criterion : the coefficients of the filters $\underline{\underline{W}}(z)$ are then computed in order to minimize the variance of the estimation errors. The orthogonality principle can be used to derive the optimal estimator. It states that the error associated with the optimal estimator is orthogonal to the data samples used to build the estimate. This property can be written as follows :

$$\underline{\underline{\gamma}}_{\underline{\epsilon}\underline{R}}(z) = \underline{0}_{K \times M} \tag{5.52}$$

where $\underline{\underline{\gamma}}_{\underline{x}\underline{y}}$ stands for the cross-spectrum between $\underline{x}(z)$ and $\underline{y}(z)$. Using the orthogonality principle (5.52), the observation model (5.49), the estimation model (5.50) and the error definition (5.51), we get

$$\begin{aligned}
\underline{\underline{W}}(z) &= \underline{\underline{\gamma}}_{\underline{I}\underline{R}}(z)\, \underline{\underline{\gamma}}^{-1}_{\underline{R}\underline{R}}(z) && (5.53)\\
&= \sigma_I^2\, \underline{\underline{H}}^H(1/z^*) \left[\sigma_n^2\, \underline{\underline{E}}_M + \sigma_I^2\, \underline{\underline{H}}(z)\, \underline{\underline{H}}^H(1/z^*)\right]^{-1} && (5.54)\\
&= \left[\sigma_I^{-2}\, \underline{\underline{E}}_N + \sigma_n^{-2}\, \underline{\underline{H}}^H(1/z^*)\underline{\underline{H}}(z)\right]^{-1} \underline{\underline{H}}^H(1/z^*)\, \sigma_n^{-2}. && (5.55)
\end{aligned}$$

The last expression is obtained thanks to the matrix inversion lemma.[1] Equation (5.55) shows that the first operation performed by the equalizer is to apply a bank of matched filters whose outputs are down-sampled to the symbol rate $1/T$. This operation is achieved by $\underline{\underline{H}}^H(1/z^*)$. Then the symbol MIMO (multi-input/multi-output) equalization is applied. It has a MIMO transfer function given by the inverse of the key power spectrum:

$$\underline{\underline{S}}_c(z) = \left[\sigma_I^{-2}\, \underline{\underline{E}}_N + \sigma_n^{-2}\, \underline{\underline{H}}^H(1/z^*)\underline{\underline{H}}(z)\right]. \tag{5.56}$$

[1] Let $\underline{\underline{A}}$ and $\underline{\underline{B}}$ be square positive definite matrices of size $n_1 \times n_1$, $\underline{\underline{D}}$ be a square positive definite matrix of size $n_2 \times n_2$ and $\underline{\underline{C}}$, $\underline{\underline{F}}$ be arbitrary rectangular matrices of size $n_1 \times n_2$, with

$$\underline{\underline{A}} = \underline{\underline{B}}^{-1} + \underline{\underline{C}}\,\underline{\underline{D}}^{-1}\,\underline{\underline{F}}^H.$$

The matrix inversion lemma states that

$$\underline{\underline{A}}^{-1} = \underline{\underline{B}} - \underline{\underline{B}}\,\underline{\underline{C}}\,(\underline{\underline{D}} + \underline{\underline{F}}^H\,\underline{\underline{B}}\,\underline{\underline{C}})^{-1}\,\underline{\underline{F}}^H\,\underline{\underline{B}}$$

.

With the detector obtained in (5.55), the symbol estimates (5.50) become

$$\hat{\underline{\mathrm{I}}}(z) = \left(\underline{\underline{\mathrm{E}}}_N - \underline{\underline{\mathrm{S}}}_c^{-1}(z)\,\sigma_I^{-2}\right)\,\underline{\mathrm{I}}(z) + \left(\underline{\underline{\mathrm{S}}}_c^{-1}(z)\,\sigma_n^{-2}\,\underline{\underline{\mathrm{H}}}^H(1/z^*)\right)\,\underline{\mathrm{N}}(z). \quad (5.57)$$

For the estimation errors after optimal linear joint detection we have

$$\underline{\underline{\gamma}}_{\epsilon\epsilon}(z) = \underline{\underline{\mathrm{S}}}_c^{-1}(z) = \sigma^2\,\underline{\underline{\mathrm{E}}}_N - \underline{\underline{\mathrm{W}}}(z)\,\underline{\underline{\gamma}}_{\mathrm{RR}}(z)\,\underline{\underline{\mathrm{W}}}^H(\frac{1}{z^*}). \quad (5.58)$$

The mean square estimation errors are provided by the diagonal elements of the order 0 matrix in the expansion of $\underline{\underline{\gamma}}_{\epsilon\epsilon}(z)$ as a z polynomial :

$$\underline{\underline{\Gamma}}_{\epsilon\epsilon}(0) = \frac{1}{2\pi}\int_{-\pi}^{\pi}\underline{\underline{\gamma}}_{\epsilon\epsilon}\left(e^{j\Omega}\right)\,\mathrm{d}\Omega. \quad (5.59)$$

5.4.2 MMSE decision-feedback joint detection

The DF joint detector is made of a $(N\times M)$ bank of forward filters, denoted by $\underline{\underline{\mathrm{W}}}(z)$, and of a causal feedback bank of $N\times N$ filters, denoted by $\underline{\underline{\mathrm{B}}}(z) - \underline{\underline{\mathrm{E}}}_N$, and builds an estimate $\hat{\underline{\mathrm{I}}}(z)$ in the following way:

$$\hat{\underline{\mathrm{I}}}(z) = \underline{\underline{\mathrm{W}}}(z)\,\underline{\mathrm{R}}(z) - \left[\underline{\underline{\mathrm{B}}}(z) - \underline{\underline{\mathrm{E}}}_N\right]\,\tilde{\underline{\mathrm{I}}}(z). \quad (5.60)$$

The feedback section processes previous decisions $\tilde{\underline{\mathrm{I}}}(z)$. However we assume that they are correct and hence use the original symbols $\underline{\mathrm{I}}(z)$ in the next derivations. The filter bank $\underline{\underline{\mathrm{B}}}(z)$ is stable, causal and monic. It means that

$$\underline{\underline{\mathrm{B}}}(z) = \sum_{n\geq 0}\underline{\underline{\mathrm{B}}}(n)\,z^{-n} \quad (5.61)$$

where $\underline{\underline{\mathrm{B}}}(0) - \underline{\underline{\mathrm{E}}}_N$ is a lower triangular matrix with zeros on the main diagonal. The triangular nature of the order 0 feedback matrix means that each time a new decision is available, it is used for the next estimate to be computed.

If this IIR JD with a causal IIR feedback section is designed for an MMSE criterion, we can again use the orthogonality principle (5.52). With the observation model (5.49), the estimation model (5.60) and the error definition (5.51), it gives

$$\begin{aligned}
\underline{\underline{\mathrm{W}}}(z) &= \underline{\underline{\mathrm{B}}}(z)\,\underline{\underline{\gamma}}_{\mathrm{IR}}(z)\,\underline{\underline{\gamma}}_{\mathrm{RR}}^{-1}(z) && (5.62)\\
&= \underline{\underline{\mathrm{B}}}(z)\,\sigma_I^2\,\underline{\underline{\mathrm{H}}}^H(1/z^*)\,\left[\sigma_n^2\,\underline{\underline{\mathrm{E}}}_M + \sigma_I^2\,\underline{\underline{\mathrm{H}}}(z)\,\underline{\underline{\mathrm{H}}}^H(1/z^*)\right]^{-1} && (5.63)\\
&= \underline{\underline{\mathrm{B}}}(z)\,\underline{\underline{\mathrm{S}}}_c^{-1}(z)\,\underline{\underline{\mathrm{H}}}^H(1/z^*)\,\sigma_n^{-2} && (5.64)
\end{aligned}$$

where the last equality comes from the matrix inversion lemma. The power spectrum of the estimation error is now

$$\underline{\underline{\gamma}}_{\epsilon\epsilon}(z) = \underline{\underline{B}}(z)\,\underline{\underline{S}}_c^{-1}(z)\,\underline{\underline{B}}^H(1/z^*). \tag{5.65}$$

Let us now compute the optimal feedback filters $\underline{\underline{B}}(z)$. The key power spectrum can be factored in the following way [58]:

$$\underline{\underline{S}}_c(z) = \underline{\underline{D}}^H(1/z^*)\,\underline{\underline{\Lambda}}\,\underline{\underline{D}}(z), \tag{5.66}$$

where matrix $\underline{\underline{\Lambda}}$ is diagonal and $\underline{\underline{D}}(z)$ is a causal, monic and stable matrix transfer function with causal and stable inverse. Hence the power spectrum of the estimation error (5.65) becomes

$$\underline{\underline{\gamma}}_{\epsilon\epsilon}(z) = \underline{\underline{B}}(z)\,\underline{\underline{D}}^{-1}(z)\,\underline{\underline{\Lambda}}^{-1}\,\underline{\underline{D}}^{-H}(1/z^*)\,\underline{\underline{B}}^H(1/z^*). \tag{5.67}$$

The geometrical mean of the error variances is given by the product of the diagonal elements of the estimation error covariance matrix given by Equation (5.59). For the positive definite error covariance matrix, it is known that

$$\prod_{p=1}^{N}\left[\underline{\underline{\Gamma}}_{\epsilon\epsilon}(0)\right]_{pp} \geq \det\left[\underline{\underline{\Gamma}}_{\epsilon\epsilon}(0)\right] \tag{5.68}$$

where equality is only obtained if the error covariance matrix is diagonal. Furthermore, we know from [59] that

$$\begin{aligned} \log\left[\det\left(\underline{\underline{\Gamma}}_{\epsilon\epsilon}(0)\right)\right] &\geq \frac{1}{2\pi}\int_{-\pi}^{\pi}\log\left[\det\left(\underline{\underline{\gamma}}_{\epsilon\epsilon}\left(e^{j\Omega}\right)\right)\right]\,\mathrm{d}\Omega && (5.69)\\ &= \log\left(\underline{\underline{\Lambda}}\right) && (5.70)\end{aligned}$$

where the last equality results from the Szegö formula [58]. If the feedback section $\underline{\underline{B}}(z)$ is chosen as the spectral factor $\underline{\underline{D}}(z)$ defined in (5.66), the power spectrum of the estimation error (5.67) and the associated covariance matrix (5.59) reduce to

$$\underline{\underline{\gamma}}_{\epsilon\epsilon}(z) = \underline{\underline{\Gamma}}_{\epsilon\epsilon}(0) = \underline{\underline{\Lambda}}^{-1}. \tag{5.71}$$

As the error power spectrum $\underline{\underline{\gamma}}_{\epsilon\epsilon}\left(e^{j\Omega}\right)$ does no longer depend on Ω, (5.69) is an equality and the determinant of the error covariance matrix is minimized. Furthermore, as the error covariance matrix is a diagonal matrix, (5.68) is also an equality and the product of the estimation error variances is minimized. The selected feedback matrix $\underline{\underline{B}}(z)$ is thus optimal regarding the MMSE criterion.

The optimal feedback and feedforward filters are finally :

$$\begin{aligned}\underline{\underline{B}}(z) &= \underline{\underline{D}}(z) \\ \underline{\underline{W}}(z) &= \underline{\underline{\Lambda}}^{-1}\left[\underline{\underline{D}}^H(1/z^*)\right]^{-1}\underline{\underline{H}}^H(1/z^*)\,\sigma_n^{-2}.\end{aligned} \tag{5.72}$$

The feedforward filter appears to be made first of a bank of matched filters. Then it is cascaded with an anticausal bank.

The obtained estimation error is white as shown by (5.71). The product of error variances can also be computed by using the Szegö formula [58] as follows :

$$\log\left[\det\left(\underline{\underline{\Lambda}}^{-1}\right)\right] = \frac{1}{2\pi}\int_{-\pi}^{\pi}\log\left[\det\left(\sigma_I^{-2}\,\underline{\underline{E}}_N + \sigma_n^{-2}\,\underline{\underline{H}}^H(1/z^*)\underline{\underline{H}}(z)\right)^{-1}\right]\mathrm{d}\Omega. \tag{5.73}$$

Regarding the symbol detection order, the product of the error variances is constant.

5.4.3 Influence of the FB

Invariance properties relative to the choice of the paraunitary FB can be put forward in the single-user configuration ($K = 1$). In that configuration, the global channel matrix can be written as $\underline{\underline{H}}(z) = \underline{\underline{C}}_1(z)\,\underline{\underline{S}}(z)$ where $\underline{\underline{S}}(z)$ is the full $N \times N$ FB polyphase matrix.

With a paraunitary FB, the key matrix $\underline{\underline{S}}_c(z)$ defined in (5.56) can be written as

$$\underline{\underline{S}}_c(z) = \left[\sigma_I^{-2}\underline{\underline{E}}_N + \frac{2}{N_0}\underline{\underline{S}}^H(1/z^*)\,\underline{\underline{G}}_{11}(z)\,\underline{\underline{S}}(z)\right] \tag{5.74}$$

$$= \underline{\underline{S}}^H(1/z^*)\,\underline{\underline{S}}_{c0}(z)\,\underline{\underline{S}}(z) \tag{5.75}$$

where $\underline{\underline{S}}_{c0}(z) = \sigma_I^{-2}\underline{\underline{E}}_N + \frac{2}{N_0}\underline{\underline{G}}_{11}(z)$ and the paraunitary property was used.

We first investigate the performance of the linear MMSE JD. From (5.58) and (5.74), the arithmetic mean of the error variances is given by :

$$\frac{1}{N}\sum_{p=1}^{N}\sigma_{\epsilon_p}^2 = \frac{1}{2\pi N}\int_{-\pi}^{\pi}\mathrm{tr}\left[\underline{\underline{S}}^H(e^{j\Omega})\,\underline{\underline{S}}_{c0}^{-1}(e^{j\Omega})\,\underline{\underline{S}}(e^{j\Omega})\right]d\Omega \tag{5.76}$$

An important conclusion may be drawn from the last expression: *at the output of a paraunitary FB transmission scheme with linear MMSE receiver, the arithmetic mean of the error variances does not depend on the filter bank.* In particular, the size of the FB has no impact on this arithmetic mean, which is equal to the unique error variance obtained with a single carrier system. The proof relies on the following matrix properties :

1. Two matrices $\underline{\underline{A}}$ and $\underline{\underline{B}}$ are similar (i.e. they have the same eigenvalues) if there exists an invertible matrix $\underline{\underline{C}}$ such that $\underline{\underline{A}} = \underline{\underline{C}}^{-1}\underline{\underline{BC}}$.

2. The trace of a matrix is equal to the eigenvalue sum.

The first property can be applied to (5.76) thanks to the paraunitary property of the FB polyphase matrix $\underline{\underline{S}}(z)$.

The arithmetic mean of the error variances is not preserved in the case of a DF-JD, because of the (non-paraunitary) feedback matrix in (5.65). It can be shown, however, that *the geometrical mean of the error variances is independent of the selected FB* :

$$\sqrt[N]{\prod_{p=1}^{N} \sigma_{\epsilon_p}^2} = \sqrt[N]{\det(\underline{\underline{\Lambda}})^{-1}}. \tag{5.77}$$

The determinant in (5.77) can be evaluated by means of Equation (5.73) as follows :

$$\log\left[\det\left(\underline{\underline{\Lambda}}^{-1}\right)\right] = \frac{1}{2\pi}\int_{-\pi}^{\pi} \log\left[\det\left(\underline{\underline{S}}^H(1/z^*)\,\underline{\underline{S}}_{c_0}(z)\,\underline{\underline{S}}(z)\right)^{-1}\right] d\Omega. \tag{5.78}$$

The result does not depend on the FB as long as it satisfies the paraunitary property.

These invariance properties are no longer satisfied in a multiuser configuration. The distribution of error variances depends on the selected signature allocation.

5.4.4 Multiuser capacity and DF joint detection

Decisions about the transmitted symbols can be taken separately in the N subchannels, on the basis of the MMSE estimates $\hat{I}_p(n)$ obtained at the output of the DF-JD. In every subchannel, the MMSE estimate can be written, according to (4.51), as

$$\begin{aligned}
\hat{I}_p(n) &= x_{pp}(0)\, I_p(n) + J_p(n) + \nu_p(n) && (5.79)\\
&= I_p(n) + (x_{pp}(0) - 1)\ I_p(n) + J_p(n) + \nu_p(n) && (5.80)\\
&= I_p(n) - \epsilon_p(n) && (5.81)
\end{aligned}$$

where $J_p(n)$ represents the total interference (ISI-ICI-MAI). The fundamental role of the IIR DF joint detector is to transform the initial frequency-selective multiuser (and multi-signature) channel into a set of N parallel and independent AWGN subchannels. The capacity associated with every subchannel, assuming Gaussian-distributed symbols, is given by

$$R_p = \log(1 + \rho_p) \qquad \text{with } \rho_p = \frac{x_{pp}^2(0)\sigma_I^2}{\sigma_{J_p}^2 + \sigma_{\nu_p}^2}. \tag{5.82}$$

Error-free transmission is possible at a rate R_p in every subchannel, assuming the use of an ideal AWGN decoder in each separate receiver. The MMSE estimator is known to be biased, i.e. $x_{pp}(0) < 1$. From the MMSE criterion, it can be shown that

$$\sigma_I^2\,(1 - x_{pp}(0)) = \sigma_{\epsilon_p}^2. \tag{5.83}$$

for any type of MMSE estimator. The bias of the MMSE estimator is directly proportional to the estimation error variance. As a consequence, the SINR associated with an MMSE estimate can be shown to be

$$\rho_p = \frac{\sigma_I^2}{\sigma_{\epsilon_p}^2} - 1. \tag{5.84}$$

Combining the MMSE-SINR definition (5.84) with the Szegö formula (5.73), the error covariance definition (5.71) and the mutual information definition (5.28), we get

$$\begin{aligned}
\overline{\mathcal{I}}_{\{1,\cdots,K\}} &= \log\left[\det\left(\sigma_I^2\,\underline{\underline{\Lambda}}\right)\right] && (5.85)\\
&= \log\left[\prod_{p=1}^{N}\left(\frac{\sigma_I^2}{\sigma_{\epsilon_p}^2}\right)\right] && (5.86)\\
&= \sum_{p=1}^{N}\log(1+\rho_p) = \sum_{p=1}^{N} R_p. && (5.87)
\end{aligned}$$

The very important conclusion of last equation is that *the sum-capacity of the frequency-selective multiuser channel can be achieved by means of an IIR DF-JD followed by ideal AWGN decoders.*

All points of the FB-constrained multiuser capacity region cannot be achieved with the IIR DF-JD, however. Indeed, the boundary of the capacity region is generated by the union of polyhedron vertices as given by Equation (5.36) and illustrated in Figure 5.2. Successive decoding is needed to obtain the set of rates R_k associated with these vertices. With the IIR DF-JD, the only degrees of freedom are the ordering of the decisions for the current block of symbols. The best we can do for a given user with the highest priority α_k is to suppress the causal interference from the $K-1$ other users, including the contribution of the symbols in the current block. But the anticausal interference cannot be suppressed. Figure 5.3 illustrates this in a two-user scenario. The capacity region for a given signature allocation is a pentagon, with useful vertices A and D. All points of the segment AD are not achievable with the IIR DF-JD. Point B represents the rate pair (R_1, R_2) obtained by ordering the decisions as follows : firstly all subchannels allocated to user 1 (in any order), secondly all subchannels allocated to user 2 (in any order). Point C represents the rate pair obtained with the opposite ordering. A few intermediate points between B and C can be obtained by interleaving the subchannels of both users in the decision ordering. Finally, the whole segment BC is covered by using time-sharing between two or more decision orderings. Even though the available sum rate $R_1 + R_2$ is the same as for the initial pentagon, the useful vertices are now B and C rather than A and D. As a consequence, the multiuser FB-constrained capacity region associated with the IIR DF-JD is strictly smaller than the general FB-constrained capacity region defined in Section 5.2. Only the maximum sum-rate and the single-user rates are equivalent.

While the computation of the sum-capacity in (5.85) is made easy by the Szegö formula (5.73), the derivation of individual data rates R_k requires the computation of the diagonal matrix $\underline{\underline{\Lambda}}$, which requires in turn the effective spectral factorization of (5.66).

5.5 FIR joint detectors

In the previous section we have obtained the structure and the associated MMSE performance of IIR joint detectors. With continuous transmission, the number of coefficients associated with these optimal detectors is generally infinite. Practically, a finite-length JD is implemented in the receiver.

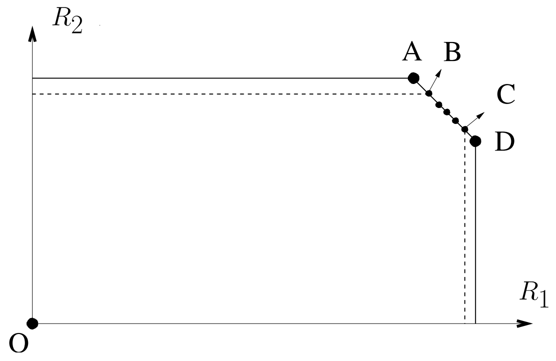

Figure 5.3: *Reduced pentagon associated with the IIR DF-JD*

The received signal is observed within a finite-length window and an estimation of the transmitted symbols is built on the basis of the observed segment. The size and the position of the observation window must be chosen carefully. A feedback section of appropriate length can also be implemented to subtract the causal interference. Both the linear and DF FIR JDs can be designed with an MMSE criterion.

The following parameters are defined :

- $L+1$ is the *length of the composite channel impulse responses* $h_{pk}(t)$ expressed as a multiple of the symbol duration T. It depends on the length of both the channel impulse responses $c_k(t)$ and the signature codes $s_p(n)$, as given by (4.44).

- $N_f \geq 1$ is the *length of the observation window*, expressed as a multiple of the symbol duration T. This parameter determines the performance of the FIR JD. It should be chosen large enough to provide a performance comparable to that of the optimal (IIR) JD, but not too large in order to limit the computational complexity to a reasonable level.

- Δ is the *decision delay*, expressed as a multiple of the symbol duration T. This parameter determines the position of the observation window, which corresponds to the time interval $[(n - N_f + \Delta)T, (n + \Delta)T]$ for the estimation of the n-th block of symbols. For a given N_f, there is an optimal decision delay that can be found by an exhaustive search. For causal impulse responses of length $L+1$, the decision delay is restricted to the interval : $0 \leq \Delta \leq N_f + L - 1$. Outside this interval, the received segment would contain no contribution from the symbols that have to be estimated. For short observation windows, the optimal decision delay is generally the one that allows the capture of the maximum energy from the useful symbols. When a decision-feedback section is implemented, the interference from past symbols is assumed to be perfectly removed : in that case, the decision delay Δ is restricted to the (shorter) interval $N_f - 1 \leq \Delta \leq N_f + L - 1$.

- N_b is the *length of the feedback section.* It gives the number of past blocks of symbols whose contribution is subtracted from the output of the feedforward section to build the DF estimates, in addition to the decisions already taken in the current block. For a given pair (N_f, Δ), the number of past blocks affecting the output of the feedforward section is $\overline{N}_b = N_f + L - 1 - \Delta$. The feedback parameter should be selected in the interval $0 \leq N_b \leq \overline{N}_b$. In the sequel, a maximum-length feedback section is assumed, i.e. $N_b = \overline{N}_b$.

The following generic FIR observation model is used for the derivation of the MMSE FIR JD coefficients :

$$\underline{\mathrm{r}}^{\Delta}_{N_b-L}(n) = \left[\underline{\underline{\mathcal{H}}}_{N_f}\right] \underline{\mathrm{I}}^{\Delta}_{N_b}(n) + \underline{\mathrm{n}}^{\Delta}_{N_b-L}(n). \tag{5.88}$$

This model combines the initial FIR observation model (4.49), developed in the context of baseband FB transmission, with the newly defined parameters N_f, Δ and N_b. The extension to CAP-FB transmission is immediate. The case of CAP-CDMA with long codes deserves a specific treatment and is discussed in detail in Section 5.5.

5.5.1 MMSE linear joint detection

The FIR linear JD computes estimates of the transmitted symbols as follows :

$$\underline{\hat{\mathrm{I}}}(n) = \underline{\underline{\mathrm{W}}} \cdot \underline{\mathrm{r}}^{\Delta}_{N_b-L}(n) \tag{5.89}$$

where $\underline{\underline{\mathrm{W}}}$ is a matrix of size $N \times N_f M$. The estimation error is given by

$$\underline{\epsilon}(n) = \underline{\mathrm{I}}(n) - \underline{\hat{\mathrm{I}}}(n) = \left(\underline{\underline{\mathrm{F}}}_{\Delta} - \underline{\underline{\mathrm{W}}}\,\underline{\underline{\mathcal{H}}}_{N_f}\right) \cdot \underline{\mathrm{I}}^{\Delta}_{N_b}(n) - \underline{\underline{\mathrm{W}}} \cdot \underline{\mathrm{n}}^{\Delta}_{N_b-L}(n) \tag{5.90}$$

where the extraction matrix $\underline{\underline{\mathrm{F}}}_{\Delta}$ is defined by

$$\underline{\underline{\mathrm{F}}}_{\Delta} = \left(\underline{\underline{0}}_{N \times \Delta N} \;\middle|\; \underline{\underline{\mathrm{E}}}_{N} \;\middle|\; \underline{\underline{0}}_{N \times N_b N} \right). \tag{5.91}$$

The orthogonality principle states that the error variance is minimal when the error is orthogonal to each data sample. Hence the cross-correlation between the error and received vectors is

$$\underline{\underline{\mathrm{R}}}_{\underline{\epsilon}\underline{\mathrm{r}}} = \underline{\underline{0}}_{N \times N_f M}. \tag{5.92}$$

The expression of the MMSE linear JD becomes

$$\begin{aligned}
\underline{\underline{\mathrm{W}}} &= \underline{\underline{\mathrm{R}}}_{\underline{\mathrm{I}}\underline{\mathrm{r}}}\, \underline{\underline{\mathrm{R}}}_{\underline{\mathrm{r}}\underline{\mathrm{r}}}^{-1} \\
&= \underline{\underline{\mathrm{F}}}_{\Delta}\, \sigma_I^2\, \underline{\underline{\mathcal{H}}}_{N_f}^T \left(\sigma_n^2\, \underline{\underline{\mathrm{E}}}_{N_f M} + \sigma_I^2\, \underline{\underline{\mathcal{H}}}_{N_f}\, \underline{\underline{\mathcal{H}}}_{N_f}^T \right)^{-1} && (5.93)\\
&= \underline{\underline{\mathrm{F}}}_{\Delta} \left(\sigma_I^{-2}\, \underline{\underline{\mathrm{E}}}_{(N_f+L)N} + \sigma_n^{-2}\, \underline{\underline{\mathcal{H}}}_{N_f}^T\, \underline{\underline{\mathcal{H}}}_{N_f} \right)^{-1} \underline{\underline{\mathcal{H}}}_{N_f}^T\, \sigma_n^{-2} && (5.94)
\end{aligned}$$

where the last equality results from the matrix inversion lemma. The first stage $\underline{\underline{\mathcal{H}}}_{N_f}^T\, \sigma_n^{-2}$ of the FIR MMSE linear JD is equivalent to a bank of N matched filters, each one providing $N_f + L$ outputs corresponding to the $N_f + L$ symbols contributing to the received signal segment. Some of these filters are truncated, due to the limited size of the observation window. The second stage is a square matrix of size $(N_f + L)N$ whose purpose is to minimize the interference. It is given by the inverse of the key matrix

$$\overline{\underline{\underline{\mathrm{R}}}}_{N_f} = \left(\sigma_I^{-2}\, \underline{\underline{\mathrm{E}}}_{(N_f+L)N} + \sigma_n^{-2}\, \underline{\underline{\mathcal{H}}}_{N_f}^T\, \underline{\underline{\mathcal{H}}}_{N_f} \right). \tag{5.95}$$

The last stage $\underline{\underline{\mathrm{F}}}_{\Delta}$ selects the appropriate block of N symbols according to the chosen decision delay. A modification of the decision delay Δ for a fixed detector length N_f just requires the modification of the extraction matrix $\underline{\underline{\mathrm{F}}}_{\Delta}$ in the JD expression (5.94). The symbol estimates (5.89) are

$$\hat{\underline{\mathrm{I}}}(n) = \underline{\underline{\mathrm{F}}}_{\Delta} \left[\left(\underline{\underline{\mathrm{E}}}_{(N_f+L)N} - \overline{\underline{\underline{\mathrm{R}}}}_{N_f}^{-1}\, \sigma_I^{-2} \right) \underline{\mathrm{I}}_{N_b}^{\Delta}(n) + \left(\overline{\underline{\underline{\mathrm{R}}}}_{N_f}^{-1}\, \sigma_n^{-2}\, \underline{\underline{\mathcal{H}}}_{N_f}^T \right) \underline{\mathrm{n}}_{N_b - L}^{\Delta}(n) \right] \tag{5.96}$$

and the corresponding error covariance matrix becomes

$$\underline{\underline{\mathrm{R}}}_{\underline{\epsilon}\underline{\epsilon}} = \underline{\underline{\mathrm{F}}}_{\Delta}\, \overline{\underline{\underline{\mathrm{R}}}}_{N_f}^{-1}\, \underline{\underline{\mathrm{F}}}_{\Delta}^T. \tag{5.97}$$

5.5.2 MMSE decision-feedback joint detection

The FIR DF-JD also uses a number of previous decisions to build improved symbol estimates. As in the case of the IIR DF-JD, it is assumed that each time a new symbol is detected, it is used for the next estimation to be performed. Hence, the estimation is computed as follows :

$$\hat{\underline{\mathrm{I}}}(n) = \underline{\underline{\mathrm{W}}} \cdot \underline{\mathrm{r}}^{\Delta}_{N_b-L}(n) - \left(\underline{\underline{\mathrm{B}}} - \underline{\underline{\mathrm{F}}}_{\Delta}\right) \tilde{\underline{\mathrm{I}}}^{\Delta}_{N_b}(n) \tag{5.98}$$

where the causal feedback matrix $\underline{\underline{\mathrm{B}}}$ has the following structure :

$$\underline{\underline{\mathrm{B}}} = \left(\begin{array}{c|c|c|c|c} \underline{\underline{0}}_{N \times \Delta N} & \underline{\underline{\mathrm{B}}}_0 & \underline{\underline{\mathrm{B}}}_1 & \cdots & \underline{\underline{\mathrm{B}}}_{N_b} \end{array} \right). \tag{5.99}$$

The first block $\underline{\underline{\mathrm{B}}}_0$ is constrained to be a $N \times N$ upper triangular matrix with '1's on the main diagonal. In the next derivations, the decisions are assumed to be correct.

We can use again the orthogonality principle. It comes

$$\begin{aligned} \underline{\underline{\mathrm{W}}} &= \underline{\underline{\mathrm{R}}}_{\mathrm{Ir}} \, \underline{\underline{\mathrm{R}}}_{\mathrm{rr}}^{-1} \\ &= \sigma_I^2 \, \underline{\underline{\mathrm{B}}} \, \underline{\underline{\mathcal{H}}}_{N_f}^T \left(\sigma_n^2 \, \underline{\underline{\mathrm{E}}}_{N_f M} + \sigma_I^2 \, \underline{\underline{\mathcal{H}}}_{N_f} \, \underline{\underline{\mathcal{H}}}_{N_f}^T \right)^{-1} && (5.100) \\ &= \underline{\underline{\mathrm{B}}} \, \overline{\underline{\underline{\mathrm{R}}}}_{N_f}^{-1} \, \underline{\underline{\mathcal{H}}}_{N_f}^T \, \sigma_n^{-2}. && (5.101) \end{aligned}$$

The error covariance matrix becomes

$$\underline{\underline{\mathrm{R}}}_{\epsilon\epsilon} = \underline{\underline{\mathrm{B}}} \, \overline{\underline{\underline{\mathrm{R}}}}_{N_f}^{-1} \, \underline{\underline{\mathrm{B}}}^T. \tag{5.102}$$

Let us now derive the optimal feedback matrix $\underline{\underline{\mathrm{B}}}$. First of all, we note that the Cholesky factorization can be applied on the symmetric positive definite matrix $\underline{\underline{\mathrm{R}}}_{N_f}$ defined in (5.95) :

$$\overline{\underline{\underline{\mathrm{R}}}}_{N_f} = \underline{\underline{\mathrm{L}}}_{N_f} \, \underline{\underline{\mathrm{D}}}_{N_f} \underline{\underline{\mathrm{L}}}_{N_f}^T \tag{5.103}$$

where $\underline{\underline{\mathrm{L}}}_{N_f}$ is a lower triangular matrix and $\underline{\underline{\mathrm{D}}}_{N_f}$ is diagonal. Using (5.103), the error covariance matrix in (5.102) can be written as follows :

$$\underline{\underline{\mathrm{R}}}_{\epsilon\epsilon} = \left(\underline{\underline{\mathrm{B}}} \, \underline{\underline{\mathrm{L}}}_{N_f}^{-T} \right) \underline{\underline{\mathrm{D}}}_{N_f}^{-1} \left(\underline{\underline{\mathrm{B}}} \, \underline{\underline{\mathrm{L}}}_{N_f}^{-T} \right)^T. \tag{5.104}$$

The product $\underline{\underline{\mathrm{B}}} \, \underline{\underline{\mathrm{L}}}_{N_f}^{-T}$ has the same structure as the feedback matrix $\underline{\underline{\mathrm{B}}}$ itself, i.e. the structure given by Equation (5.99). As a consequence, the estimation error variances are lower bounded as follows :

$$\begin{aligned}
\operatorname{diag}\left(\underline{\underline{\mathrm{R}}}_{\epsilon\epsilon}\right) &= \operatorname{diag}\left(\left[\underline{\underline{\mathrm{F}}}_{\Delta} + \left(\underline{\underline{\mathrm{B}}}\,\underline{\underline{\mathrm{L}}}_{N_f}^{-T} - \underline{\underline{\mathrm{F}}}_{\Delta}\right)\right] \underline{\underline{\mathrm{D}}}_{N_f}^{-1} \left[\underline{\underline{\mathrm{F}}}_{\Delta} + \left(\underline{\underline{\mathrm{B}}}\,\underline{\underline{\mathrm{L}}}_{N_f}^{-T} - \underline{\underline{\mathrm{F}}}_{\Delta}\right)\right]^T\right) \\
&= \operatorname{diag}\left(\underline{\underline{\mathrm{F}}}_{\Delta}\,\underline{\underline{\mathrm{D}}}_{N_f}^{-1}\,\underline{\underline{\mathrm{F}}}_{\Delta}^T + \left[\underline{\underline{\mathrm{B}}}\,\underline{\underline{\mathrm{L}}}_{N_f}^{-T} - \underline{\underline{\mathrm{F}}}_{\Delta}\right] \underline{\underline{\mathrm{D}}}_{N_f}^{-1} \left[\underline{\underline{\mathrm{B}}}\,\underline{\underline{\mathrm{L}}}_{N_f}^{-T} - \underline{\underline{\mathrm{F}}}_{\Delta}\right]^T\right) \\
&\geq \operatorname{diag}\left(\underline{\underline{\mathrm{F}}}_{\Delta}\,\underline{\underline{\mathrm{D}}}_{N_f}^{-1}\,\underline{\underline{\mathrm{F}}}_{\Delta}^T\right) \qquad (5.105)
\end{aligned}$$

with equality if and only if $\underline{\underline{\mathrm{B}}}\,\underline{\underline{\mathrm{L}}}_{N_f}^{-T} = \underline{\underline{\mathrm{F}}}_{\Delta}^T$. The optimal feedback matrix and the associated error covariance matrix are

$$\underline{\underline{\mathrm{B}}} = \underline{\underline{\mathrm{F}}}_{\Delta}\,\underline{\underline{\mathrm{L}}}_{N_f}^T \qquad\qquad \underline{\underline{\mathrm{R}}}_{\epsilon\epsilon} = \underline{\underline{\mathrm{F}}}_{\Delta}\,\underline{\underline{\mathrm{D}}}_{N_f}^{-1}\,\underline{\underline{\mathrm{F}}}_{\Delta}^T. \qquad (5.106)$$

The estimation error is white, and the error variances are given by a subset of the inverse eigenvalues of the key matrix $\overline{\underline{\underline{\mathrm{R}}}}_{N_f}$. The subset depends on the selected decision delay Δ. The optimal feedforward matrix (5.101) becomes

$$\underline{\underline{\mathrm{W}}} = \underline{\underline{\mathrm{F}}}_{\Delta}\,\underline{\underline{\mathrm{D}}}_{N_f}^{-1}\,\underline{\underline{\mathrm{L}}}_{N_f}^{-1}\,\underline{\underline{\mathcal{H}}}_{N_f}^T\,\sigma_n^{-2}. \qquad (5.107)$$

Finally, it can be demonstrated that, as in the IIR scenario, the product of error variances does not depend on the decision ordering. Let $\underline{\underline{\mathrm{Q}}}$ be the permutation matrix associated with an arbitrary permutation of the decision order. This matrix, obtained by permuting the columns of the size-N unit matrix, is unitary, i.e. $\underline{\underline{\mathrm{Q}}}\,\underline{\underline{\mathrm{Q}}}^T = \underline{\underline{\mathrm{E}}}_N$. The key matrix $\overline{\underline{\underline{\mathrm{R}}}}^{(q)}$ associated with the new decision order is given by

$$\overline{\underline{\underline{\mathrm{R}}}}_{N_f}^{(q)} = \underline{\underline{\mathcal{Q}}}\,\overline{\underline{\underline{\mathrm{R}}}}_{N_f}\,\underline{\underline{\mathcal{Q}}}^T \qquad \text{with } \underline{\underline{\mathcal{Q}}} = \begin{pmatrix} \underline{\underline{\mathrm{E}}}_{\Delta N} & & \\ & \underline{\underline{\mathrm{Q}}} & \\ & & \underline{\underline{\mathrm{E}}}_{N_b N} \end{pmatrix}. \qquad (5.108)$$

Let $\underline{\underline{\mathrm{D}}}_{N_f}^{(q)}$ be the diagonal eigenvalue matrix associated with $\overline{\underline{\underline{\mathrm{R}}}}_{N_f}^{(q)}$. The product of estimation error variances obtained with the permuted decision order is given by

$$\begin{aligned}
\prod_{p=1}^{N}\left(\underline{\underline{\mathrm{R}}}_{\epsilon\epsilon}^{(q)}\right)_{pp} &= \det\left(\underline{\underline{\mathrm{F}}}_{\Delta}\left(\underline{\underline{\mathrm{D}}}_{N_f}^{(q)}\right)^{-1}\underline{\underline{\mathrm{F}}}_{\Delta}^T\right) &(5.109)\\
&= \det\left(\underline{\underline{\mathrm{Q}}}\left[\underline{\underline{\mathrm{F}}}_{\Delta}\,\underline{\underline{\mathrm{D}}}_{N_f}^{-1}\,\underline{\underline{\mathrm{F}}}_{\Delta}^T\right]\underline{\underline{\mathrm{Q}}}^T\right) &(5.110)\\
&= \det\left(\underline{\underline{\mathrm{F}}}_{\Delta}\,\underline{\underline{\mathrm{D}}}_{N_f}^{-1}\,\underline{\underline{\mathrm{F}}}_{\Delta}^T\right) = \prod_{p=1}^{N}\left(\underline{\underline{\mathrm{R}}}_{\epsilon\epsilon}\right)_{pp}. &(5.111)
\end{aligned}$$

The second equality can be demonstrated by using the *nesting property* of the Cholesky factorization. This property states that the lower triangular and diagonal Cholesky factors of the $k \times k$ submatrix of $\overline{\underline{\underline{\mathrm{R}}}}_{N_f}^{(q)}$ formed from its first k rows and columns are equal to the first k rows and columns of $\underline{\underline{\mathrm{L}}}_{N_f}^{(q)}$ and $\underline{\underline{\mathrm{D}}}_{N_f}^{(q)}$, respectively.

5.5.3 Complexity analysis

In this Section, we analyze in more details the complexity associated with the computation of the filter coefficients.

The FIR linear JD is given by Equations (5.93) and (5.94). Both the direct and indirect expressions can be used to compute the filter coefficients. The best choice depends on the respective size parameters N, M, L, N_f and Δ. As the indirect method (5.94) must be implemented for the derivation of the DF-JD filters, we propose here the analysis of the direct method (5.93) for the computation of the linear JD.

Algorithm 5.1 *Computation of the FIR linear JD coefficients :*

$$\left(\underline{\underline{\mathcal{H}}}_{N_f}, \sigma_I^2, \sigma_n^2\right) \rightarrow \underline{\underline{W}}$$

with the direct method. The algorithm proceeds in three steps:

1. *Computation of the channel output correlation matrix:*

$$\underline{\underline{R}}_{rr} = \sigma_n^2 \, \underline{\underline{E}}_{N_f M} + \sigma_I^2 \, \underline{\underline{\mathcal{H}}}_{N_f} \, \underline{\underline{\mathcal{H}}}_{N_f}^T.$$

   The result is a Hermitian block banded matrix with N_f blocks of size $M \times M$ and a bandwidth of L blocks.

2. *Cholesky factorization of the channel output correlation matrix:*

$$\underline{\underline{R}}_{rr} = \underline{\underline{L}}_r \underline{\underline{L}}_r^T.$$

   The Cholesky factor $\underline{\underline{L}}_r$ is lower triangular and has the same size, block-size and bandwidth as $\underline{\underline{R}}_{rr}$.

3. *Resolution of the Wiener-Hopf equation:*

$$\left(\underline{\underline{L}}_r \, \underline{\underline{L}}_r^T\right) \underline{\underline{W}}^T = \underline{\underline{R}}_{Ir}^T.$$

   This implies N resolutions of two banded triangular systems.

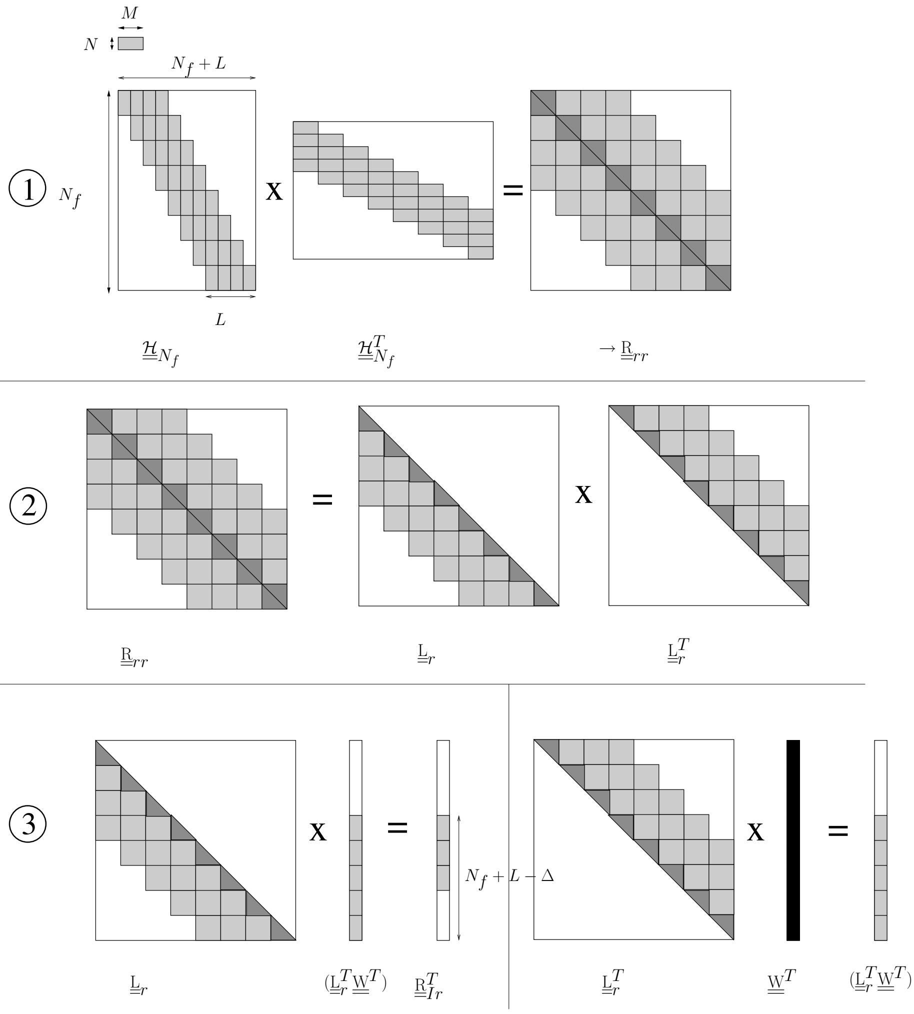

Figure 5.4: *Matrix manipulations for the FIR linear JD computation*

Figure 5.4 illustrates the matrix manipulations associated with the three steps of Algorithm 5.1.

The FIR DF-JD is given by Equations (5.106) and (5.107). The computation of the feedworward and feedback filters requires the factorization of the key matrix $\underline{\underline{\overline{\mathrm{R}}}}_{N_f}$.

Algorithm 5.2 *Computation of the FIR DF-JD coefficients ·*

$$\left(\underline{\underline{\mathcal{H}}}_{N_f}, \sigma_I^2, \sigma_n^2\right) \rightarrow \left(\underline{\underline{W}}, \underline{\underline{B}}\right)$$

The algorithm is made up of three steps:

1. *Computation of the MMSE matrix:*

$$\underline{\underline{\overline{R}}}_{N_f} = \left(\sigma_I^{-2} \underline{\underline{E}}_{(N_f+L)N} + \sigma_n^{-2} \underline{\underline{\mathcal{H}}}_{N_f}^T \underline{\underline{\mathcal{H}}}_{N_f}\right). \tag{5.112}$$

The result is a Hermitian block banded matrix with $N_f + L$ blocks of size $N \times N$ and a bandwidth of L blocks. The computation may be restricted to the first $N(\Delta + 1)$ columns.

2. *Cholesky factorization of the MMSE matrix:*

$$\underline{\underline{\overline{R}}}_{N_f} = \underline{\underline{\overline{L}}}_{N_f} \underline{\underline{\overline{L}}}_{N_f}^T.$$

The Cholesky factor $\underline{\underline{L}}_{n_2}$ is lower triangular and has the same size, block-size and bandwidth as $\underline{\underline{\overline{R}}}_{N_f}$. The feedback filters are then immediately obtained with elementary matrix manipulations:

$$\underline{\underline{D}}_{N_f}^{1/2} = diag\left(\underline{\underline{\overline{L}}}_{N_f}\right) \tag{5.113}$$

$$\underline{\underline{B}} = \underline{\underline{F}}_{\Delta} \underline{\underline{D}}_{N_f}^{-1/2} \underline{\underline{\overline{L}}}_{N_f}. \tag{5.114}$$

3. *Computation of the feedforward filters:*

$$\underline{\underline{\overline{L}}}_{N_f} \underline{\underline{\overline{W}}}_{N_f} = \sigma_n^{-2} \underline{\underline{\mathcal{H}}}_{N_f}^T. \tag{5.115}$$

Only the first $(\Delta + 1)N$ rows of $\underline{\underline{\overline{W}}}_{N_f}$ need to be computed. This equation represents N_f times M triangular systems of decreasing size from $(\Delta + 1)N$ down to $(\Delta + 2 - N_f)N$. The feedforward filters are then obtained by:

$$\underline{\underline{W}} = \underline{\underline{F}}_{\Delta} \underline{\underline{D}}_{N_f}^{-1/2} \underline{\underline{\overline{W}}}_{N_f}. \tag{5.116}$$

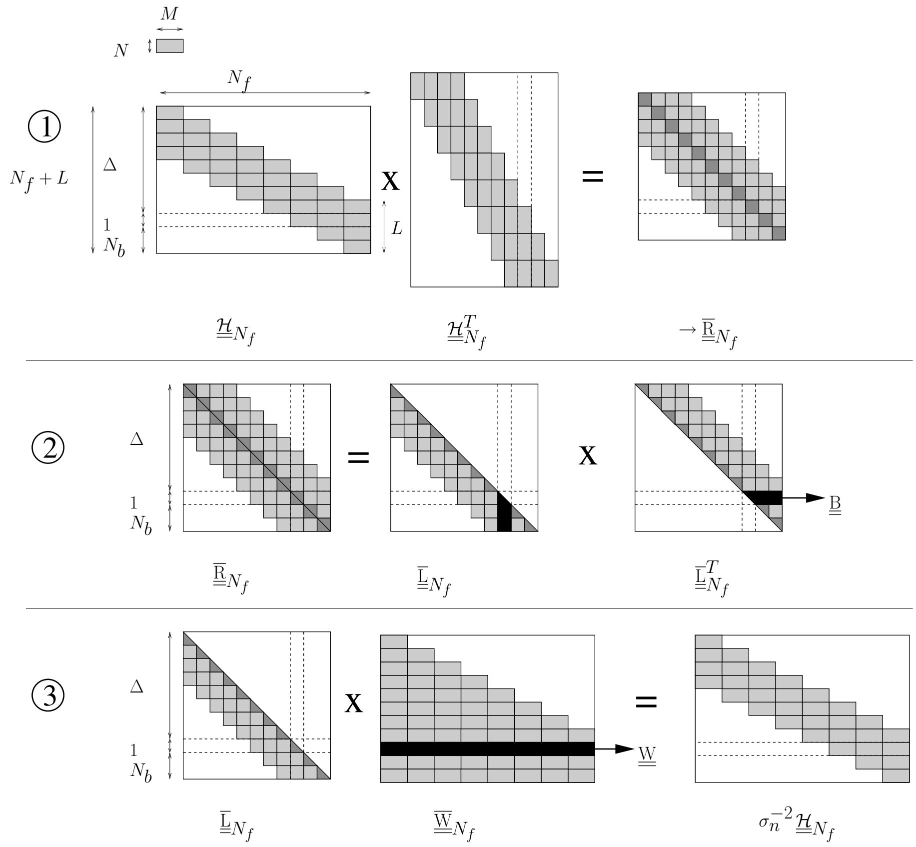

Figure 5.5: *Matrix manipulations for the FIR DF-JD computation*

Table 5.1: *Approximate complexity (in scalar operations) associated with the full computation of FIR-JD coefficients*

	Full Linear JD	Full DF-JD
1	$NM^2 \quad \frac{1}{2}N_f L^2$	$N^2M \quad \frac{1}{2}N_f L^2$
2	$M^3 \quad \left(\frac{1}{2}N_f L^2 - \frac{1}{3}L^3\right)$	$N^3(\frac{1}{2}N_f L^2 - \frac{1}{3}L^3)$
3	$NM^2 \quad 2(N_f L - \frac{1}{2}L^2)$	$N^2M \quad \frac{1}{2}N_f^2 L$

Figure 5.5 illustrates the matrix manipulations associated with the three steps of Algorithm 5.2.

Table 5.1 gives a rough order-of-magnitude estimate of the computational complexity associated with each of the three steps of the presented algorithms, assuming $N_f \gg L \gg 1$. The values given here correspond to the approximate number of scalar operations required for each matrix manipulation, taking the banded structure of the matrices into account [60].

Faster algorithms can be investigated when the channel matrix $\underline{\underline{\mathcal{H}}}_{N_f}$ has a *periodic structure* :

- Concerning the FIR linear JD computation with the direct method, the channel output correlation matrix $\underline{\underline{\mathrm{R}}}_{rr}$ is then block-Toeplitz. Its computation (Step 1 in Algorithm 5.1) requires only $\mathcal{O}\left(NM^2\,\frac{1}{2}L^2\right)$ scalar operations. The resolution of the Wiener-Hopf equation (Steps 2 and 3 in Algorithm 5.1) can be performed by N successive applications of the Levinson algorithm [60], which requires $\mathcal{O}\left(NM^2\,N_f L\right)$ scalar operations.

- Concerning the FIR DF-JD computation, the key matrix $\overline{\underline{\underline{\mathrm{R}}}}_{N_f}$ is then also block-Toeplitz. The computation of the key Cholesky factor $\overline{\underline{\underline{\mathrm{L}}}}$ (Steps 1 and 2 in Algorithm 5.2) can be performed very efficiently by using the so-called generalized Schur algorithm. This method is based on the observation by [61] that the block-symmetric matrix

$$\underline{\underline{\mathcal{M}}}_{N_f} \triangleq \begin{bmatrix} \sigma_n^2\,\underline{\underline{\mathrm{E}}}_{N_f M} & \underline{\underline{\mathcal{H}}}_{N_f} \\ \underline{\underline{\mathcal{H}}}_{N_f}^T & -\sigma_I^2\,\underline{\underline{\mathrm{E}}}_{(N_f+L)N} \end{bmatrix} \tag{5.117}$$

admits a triangular factorization of the following form :

$$\underline{\underline{\mathcal{M}}}_{N_f} = \begin{bmatrix} \underline{\underline{\mathcal{L}}}_1 & \\ \underline{\underline{\mathcal{L}}}_2 & \underline{\underline{\mathcal{L}}}_3 \end{bmatrix} \begin{bmatrix} \underline{\underline{\mathrm{E}}}_{N_f M} & \\ & -\underline{\underline{\mathrm{E}}}_{(N_f+L)N} \end{bmatrix} \begin{bmatrix} \underline{\underline{\mathcal{L}}}_1 & \\ \underline{\underline{\mathcal{L}}}_2 & \underline{\underline{\mathcal{L}}}_3 \end{bmatrix}^T \tag{5.118}$$

where the lower triangular matrix $\underline{\underline{\mathcal{L}}}_3$ satisfies the relation

$$\underline{\underline{\overline{\mathrm{R}}}}_{N_f} = \underline{\underline{\mathcal{L}}}_3 \underline{\underline{\mathcal{L}}}_3^T, \tag{5.119}$$

so that the desired Cholesky factor $\underline{\underline{\overline{\mathrm{L}}}}_{N_f}$ is given by

$$\underline{\underline{\overline{\mathrm{L}}}}_{N_f} = \underline{\underline{\mathcal{L}}}_3. \tag{5.120}$$

The triangular factorization (5.118) can be performed with simple operations (Givens rotations and hyperbolic rotations) on the matrix $\underline{\underline{\mathcal{M}}}_{N_f}$, which requires $\mathcal{O}\left(N^2 \left(N_f + L\right)^2\right)$ scalar operations.

5.6 Joint detection for CAP-CDMA with long codes

The linear and DF IIR MMSE JDs designed for a CAP-CDMA transmission system with long codes are also given by Equations (5.55) and (5.72), respectively, where the channel matrix $\underline{\underline{\mathrm{H}}}(z)$ is now of size $MP \times 2KP$, and corresponds to the observation model proposed in Equation (4.79). Their interpretation deserves some comments. The matched filter receiver $\underline{\underline{\mathrm{H}}}^H(1/z^*)$ is made here of a bank of $2KP$ branches, each one matched to a particular code segment of a particular user. In fact, the $2P$ parallel matched filters associated with a particular user are nothing but a parallel description (with P time invariant branches) of two periodically time varying matched filters. The outputs of these matched filters are downsampled to the symbol rate $(1/PT')$. Then a MIMO equalizer $\underline{\underline{\mathrm{S}}}_c^{-1}(z)$ takes care of both multiple access interference and the possible interference between the different code segments of the different users. In this MIMO filter, $2P$ outputs are associated with each user. Each one of these outputs is obtained by processing the $2KP$ matched filter outputs by means of a specific set of $2KP$ filters. This again appears to be a parallel version of a time varying process. For a given user the P sets of $2KP$ time invariant filters are in fact equivalent to a single set of $2KP$ time varying filters, with period P. Finally, the feedback section $\underline{\underline{\mathrm{B}}}(z) - \underline{\underline{\mathrm{E}}}_{2KP}$ is also a parallel representation of a period P time varying feedback process.

It turns out that, in principle, the detector should account for the possible interference between any pair of segments of any pair of users. This strategy which corresponds to the optimum setup is however very demanding. It is well-known that the complexity of the MMSE JD coefficient computation is roughly proportional to the third power of the spreading factor (see Table 5.1). With the multirate description described above, the spreading factor is virtually multiplied by P, which dramatically increases the computational complexity. The purpose of this section is to investigate FIR solutions of reduced complexity. The idea of reducing the complexity is to explore what happens when a few segments only interfere with each other. In such a situation, it seems logical to use only a limited number of received signal segments rather than all of them.

5.6.1 MMSE linear joint detection

From the IIR linear joint detector described above (see (5.50)), the following FIR version can be obtained :

$$\hat{\underline{\mathrm{I}}}_0^{P-1}(n) = \left[\begin{array}{ccc} \underline{\underline{\mathcal{W}}}_{-1} & \underline{\underline{\mathcal{W}}}_0 & \underline{\underline{\mathcal{W}}}_1 \end{array} \right] \left[\begin{array}{c} \underline{\mathrm{r}}_0^{P-1}(n+1) \\ \underline{\mathrm{r}}_0^{P-1}(n) \\ \underline{\mathrm{r}}_0^{P-1}(n-1) \end{array} \right]. \qquad (5.121)$$

Complexity can be further reduced by using only N_f segments of the received signal to build the estimate of the current symbol. Assuming a decision delay of Δ symbol periods, the estimation is now :

$$\hat{\underline{\mathrm{I}}}_0^{P-1}(n) = \overline{\underline{\underline{\mathcal{W}}}} \left[\begin{array}{l} \underline{\mathrm{r}}_0^{\Delta-1}(n+1) \\ \underline{\mathrm{r}}_0^{P-1}(n) \\ \underline{\mathrm{r}}_{P-N_b+L}^{P-1}(n-1) \end{array} \right] \qquad (5.122)$$

where matrix $\overline{\underline{\underline{\mathcal{W}}}}$ has non-zero entries at the positions given by the shaded area of Figure 5.6.

The number of filter taps associated with this simplified detection scheme is much lower. In fact, the span of the time-varying detector made of modules of size $2K \times M$ may now be chosen with a better granularity: the number of modules does not need to be a multiple of P or, equivalently, the span of the detector does not have to be a multiple of P. A drawback, however, lies in the need for these filters to be computed separately for each of the P segments.

The $2K$ estimates at phase p are now given by:

$$\hat{\underline{\mathrm{I}}}_p(n) = \underline{\underline{\mathrm{W}}}_p \underline{\mathrm{r}}_{p-N_b+L}^{p+\Delta}(n) \qquad (5.123)$$

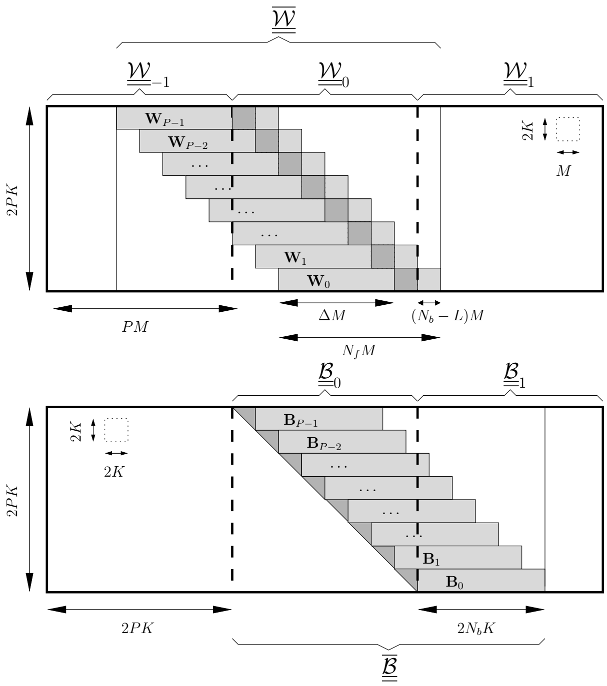

Figure 5.6: *Feedforward and feedback time-varying filters*

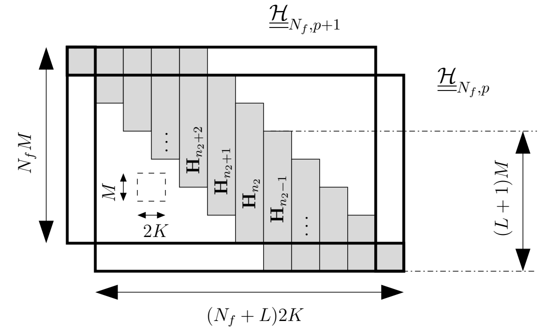

Figure 5.7: *Two successive channel matrices*

with

$$\underline{\mathrm{r}}_{p-N_b+L}^{p+\Delta}(n) = \underline{\underline{\mathcal{H}}}_{N_f,p}\,\underline{\mathrm{I}}_{p-N_b}^{p+\Delta}(n) + \underline{\mathrm{n}}_{p-N_b+L}^{p+\Delta}(n). \tag{5.124}$$

The segment-dependent channel matrix $\underline{\underline{\mathcal{H}}}_{N_f,p}$ is illustrated in Figure 4.7. The MMSE feedforward estimator for the symbols corresponding to segment p is now (see (5.93) and (5.94)) :

$$\begin{aligned} \underline{\underline{\mathrm{W}}}_p &= \sigma_I^2\,\underline{\underline{\mathrm{F}}}_\Delta\,\underline{\underline{\mathcal{H}}}_{N_f,p}^T\left(\sigma_n^2\underline{\underline{\mathrm{E}}}_{N_f M} + \sigma_I^2\underline{\underline{\mathcal{H}}}_{N_f,p}\,\underline{\underline{\mathcal{H}}}_{N_f,p}^T\right)^{-1} & (5.125)\\ &= \underline{\underline{\mathrm{F}}}_\Delta\left(\sigma_I^{-2}\underline{\underline{\mathrm{E}}}_{(N_f+L)2K} + \sigma_n^{-2}\underline{\underline{\mathcal{H}}}_{N_f,p}^T\,\underline{\underline{\mathcal{H}}}_{N_f,p}\right)^{-1}\underline{\underline{\mathcal{H}}}_{N_f,p}^T\sigma_n^{-2} & (5.126)\end{aligned}$$

where the new extraction matrix $\underline{\underline{\mathrm{F}}}_\Delta$ is

$$\underline{\underline{\mathrm{F}}}_\Delta = \left(\ \underline{\underline{0}}_{2K\times\Delta\,2K}\ \middle|\ \underline{\underline{\mathrm{E}}}_{2K}\ \middle|\ \underline{\underline{0}}_{2K\times N_b\,2K}\ \right). \tag{5.127}$$

In the case of long CIRs and detectors (i.e. $(N_f, L) \gg 1$), it is crucial to design a fast update algorithm for the computation of $\underline{\underline{\mathrm{W}}}_{p+1}$, on the basis of $\underline{\underline{\mathrm{W}}}_p$. This is possible thanks to the specific structure of the successive channel matrices $\underline{\underline{\mathcal{H}}}_{N_f,p}$ (see Figure 5.7) :

$$\begin{aligned} \underline{\underline{\mathcal{H}}}_{N_f,p} &= \begin{array}{c c} & \begin{array}{cc} \overset{N_f+L-1}{\Leftrightarrow} & \overset{1}{\leftrightarrow} \end{array} \\ \begin{array}{r} N_f-1 \Updownarrow \\ 1 \updownarrow \end{array} & \begin{pmatrix} \underline{\underline{\mathrm{H}}}_0 & \underline{\underline{0}} \\ \underline{\underline{\mathrm{h}}}_1^T & \underline{\underline{\mathrm{h}}}_0 \end{pmatrix}_p \end{array} \\ \underline{\underline{\mathcal{H}}}_{N_f,p+1} &= \begin{array}{c c} & \begin{array}{cc} \overset{1}{\leftrightarrow} & \overset{N_f+L-1}{\Leftrightarrow} \end{array} \\ \begin{array}{r} 1 \updownarrow \\ N_f-1 \Updownarrow \end{array} & \begin{pmatrix} \underline{\underline{\mathrm{h}}}_0 & \underline{\underline{\mathrm{h}}}_1^T \\ \underline{\underline{0}} & \underline{\underline{\mathrm{H}}}_0 \end{pmatrix}_{p+1} \end{array} \end{aligned} \tag{5.128}$$

where $\underline{\underline{\mathrm{H}}}_0(p+1) = \underline{\underline{\mathrm{H}}}_0(p)$. Using this property, the three steps of Algorithm 5.1 can be replaced by the following updating process.

Algorithm 5.3 *Update of the FIR linear JD coefficients :*

1. *Update the channel output correlation matrix:*

$$\begin{array}{rcl}
\underline{\underline{R}}_{rr}(p) & = & \begin{array}{rc} & \begin{array}{cc} \overset{N_f-1}{\Leftrightarrow} & \overset{1}{\leftrightarrow} \end{array} \\ \begin{array}{r} N_f-1 \Updownarrow \\ 1 \updownarrow \end{array} & \begin{pmatrix} \underline{\underline{R}}_0 & \underline{\underline{r}}_1 \\ \underline{\underline{r}}_1^T & \underline{\underline{r}}_0 \end{pmatrix}_p \end{array} \\
\underline{\underline{R}}_{rr}(p+1) & = & \begin{array}{rc} & \begin{array}{cc} \overset{1}{\leftrightarrow} & \overset{N_f-1}{\Leftrightarrow} \end{array} \\ \begin{array}{r} 1 \updownarrow \\ N_f-1 \Updownarrow \end{array} & \begin{pmatrix} \underline{\underline{r}}_0 & \underline{\underline{r}}_1^T \\ \underline{\underline{r}}_1 & \underline{\underline{R}}_0 \end{pmatrix}_{p+1} \end{array} .
\end{array} \tag{5.129}$$

Using (5.128), we get $(\underline{\underline{R}}_0)_{p+1} = (\underline{\underline{R}}_0)_p$. The update reduces to the computation of:

$$\begin{pmatrix} \underline{\underline{r}}_0 \\ \underline{\underline{r}}_1 \end{pmatrix}_{p+1} = \sigma_n^2 \begin{pmatrix} \underline{\underline{E}}_M \\ \underline{\underline{0}} \end{pmatrix} + \sigma_I^2 \begin{pmatrix} \underline{\underline{h}}_0 & \underline{\underline{h}}_1^T \\ \underline{\underline{0}} & \underline{\underline{H}}_0 \end{pmatrix}_{p+1} \begin{pmatrix} \underline{\underline{h}}_0^T \\ \underline{\underline{h}}_1 \end{pmatrix}_{p+1} . \tag{5.130}$$

2. *Update the Cholesky factor $\underline{\underline{L}}_{r,p+1}$:*

$$\begin{array}{rcl}
\underline{\underline{L}}_{r,p} & = & \begin{array}{rc} & \begin{array}{cc} \overset{N_f-1}{\Leftrightarrow} & \overset{1}{\leftrightarrow} \end{array} \\ \begin{array}{r} N_f-1 \Updownarrow \\ 1 \updownarrow \end{array} & \begin{pmatrix} \underline{\underline{L}}_0 & \underline{\underline{0}} \\ \underline{\underline{l}}_1^T & \underline{\underline{l}}_0 \end{pmatrix}_p \end{array} \\
\underline{\underline{L}}_{r,p+1} & = & \begin{array}{rc} & \begin{array}{cc} \overset{1}{\leftrightarrow} & \overset{N_f-1}{\Leftrightarrow} \end{array} \\ \begin{array}{r} 1 \updownarrow \\ N_f-1 \Updownarrow \end{array} & \begin{pmatrix} \underline{\underline{l}}_0 & \underline{\underline{0}} \\ \underline{\underline{l}}_1 & \underline{\underline{L}}_0 \end{pmatrix}_{p+1} \end{array} .
\end{array} \tag{5.131}$$

Part of the new Cholesky factor has first to be computed from scratch:

$$\begin{pmatrix} \underline{\underline{l}}_0 \\ \underline{\underline{l}}_1 \end{pmatrix}_{p+1} \left(\underline{\underline{l}}_0^T\right)_{p+1} = \begin{pmatrix} \underline{\underline{r}}_0 \\ \underline{\underline{r}}_1 \end{pmatrix}_{p+1} . \tag{5.132}$$

The remaining part, $\underline{\underline{L}}_0$, of the Cholesky factor fulfils:

$$\left(\underline{\underline{L}}_0\underline{\underline{L}}_0^T + \underline{l}_1\underline{l}_1^T\right)_{p+1} = \left(\underline{\underline{L}}_0\underline{\underline{L}}_0^T\right)_p . \tag{5.133}$$

The updated submatrix may be computed by M successive applications of the Cholesky rank-1 update algorithm [60].[2]

3. *Solve the new Wiener-Hopf equation with the updated $\underline{\underline{R}}_{rr}$ and the new $\underline{\underline{R}}_{Ir}$:*

$$\left(\underline{\underline{L}}_{p+1}\underline{\underline{L}}_{p+1}^T\right)\underline{\underline{W}}_{p+1}^T = \underline{\underline{R}}_{Ir}^T(p+1).$$

A detailed complexity analysis will be given and discussed in Section 5.6.3.

5.6.2 MMSE decision-feedback joint detection

The FIR version of the full complexity DF joint detector (see (5.60)) is given by:

$$\begin{aligned}\hat{\underline{\mathrm{I}}}_0^{P-1}(n) = &\begin{bmatrix} \underline{\underline{\mathcal{W}}}_{-1} & \underline{\underline{\mathcal{W}}}_0 & \underline{\underline{\mathcal{W}}}_1 \end{bmatrix}\begin{bmatrix} \underline{\mathrm{r}}_0^{P-1}(n+1) \\ \underline{\mathrm{r}}_0^{P-1}(n) \\ \underline{\mathrm{r}}_0^{P-1}(n-1) \end{bmatrix} \\ &- \begin{bmatrix} \left(\underline{\underline{\mathcal{B}}}_0 - \underline{\underline{\mathrm{E}}}_{2KP}\right) & \underline{\underline{\mathcal{B}}}_1 \end{bmatrix}\begin{bmatrix} \underline{\mathrm{I}}_0^{P-1}(n) \\ \underline{\mathrm{I}}_0^{P-1}(n-1) \end{bmatrix}.\end{aligned} \tag{5.134}$$

The reduced complexity decision-feedback estimation becomes:

$$\hat{\underline{\mathrm{I}}}_0^{P-1}(n) = \overline{\underline{\underline{\mathcal{W}}}}\begin{bmatrix} \underline{\mathrm{r}}_0^{\Delta-1}(n+1) \\ \underline{\mathrm{r}}_0^{P-1}(n) \\ \underline{\mathrm{r}}_{P-N_b+L}^{P-1}(n-1) \end{bmatrix} - \left(\overline{\underline{\underline{\mathcal{B}}}} - \underline{\underline{\mathcal{F}}}\right)\begin{bmatrix} \underline{\mathrm{I}}_0^{\Delta-1}(n+1) \\ \underline{\mathrm{I}}_0^{P-1}(n) \\ \underline{\mathrm{I}}_{P-N_b}^{P-1}(n-1) \end{bmatrix} \tag{5.135}$$

where $\overline{\underline{\underline{\mathcal{W}}}}$ and $\overline{\underline{\underline{\mathcal{B}}}}$ have non-zero entries at the positions given by the shaded area of Figure 5.6.

---

[2] The Cholesky rank-1 update/downdate algorithm is an efficient method of computing a lower triangular matrix $\tilde{\underline{\underline{\mathrm{L}}}}_1$ of size N_1 and a rectangular matrix $\tilde{\underline{\underline{\mathrm{L}}}}_2$ of size $N_2 \times N_1$ satisfying the relation $(\underline{\underline{\mathrm{L}}}_1^T\ \underline{\underline{\mathrm{L}}}_2^T)^T\,\underline{\underline{\mathrm{L}}}_1^T \pm (\underline{\mathrm{x}}_1^T\ \underline{\mathrm{x}}_2^T)^T\,\underline{\mathrm{x}}_1^T = (\tilde{\underline{\underline{\mathrm{L}}}}_1^T\ \tilde{\underline{\underline{\mathrm{L}}}}_2^T)^T\,\tilde{\underline{\underline{\mathrm{L}}}}_1^T$ where $\underline{\mathrm{x}}_1$ and $\underline{\mathrm{x}}_2$ are vector columns. The algorithm applies N_1 appropriate Givens rotations on an augmented version of matrix $(\underline{\underline{\mathrm{L}}}_1^T\ \underline{\underline{\mathrm{L}}}_2^T)$. Its complexity is $\mathcal{O}(N_1^2 + 2N_1N_2)$. If $\underline{\mathrm{x}}_1$ and $\underline{\mathrm{x}}_2$ are matrices and not vectors, then the result is n consecutive updates using the n columns of $\underline{\mathrm{x}}_1$ and $\underline{\mathrm{x}}_2$. $\tilde{\underline{\underline{\mathrm{L}}}}_1$ obviously appears as an updated Cholesky factor.

The $2K$ estimates at phase p are now given by:

$$\hat{\underline{I}}_p(n) = \underline{\underline{W}}_p \underline{r}_{p-N_b+L}^{p+\Delta}(n) - \left(\underline{\underline{B}}_p - \underline{\underline{F}}_\Delta\right) \underline{I}_{p-N_b}^{p+\Delta}(n). \tag{5.136}$$

The optimal feedback and feedforward matrices are now (see (5.106) and (5.107)):

$$\underline{\underline{B}}_p = \underline{\underline{F}}_\Delta \, \underline{\underline{L}}_{N_f,p}^T \tag{5.137}$$

$$\underline{\underline{W}}_p = \underline{\underline{F}}_\Delta \, \underline{\underline{D}}_{N_f,p}^{-1} \, \underline{\underline{L}}_{N_f,p}^{-1} \, \underline{\underline{\mathcal{H}}}_{N_f,p}^T \, \sigma_n^{-2} \tag{5.138}$$

with

$$\overline{\underline{\underline{R}}}_{N_f,p} = \left(\sigma_I^{-2} \, \underline{\underline{E}}_{(N_f+L)2K} + \sigma_n^{-2} \, \underline{\underline{\mathcal{H}}}_{N_f,p}^T \, \underline{\underline{\mathcal{H}}}_{N_f,p}\right) = \underline{\underline{L}}_{N_f,p} \, \underline{\underline{D}}_{N_f,p} \, \underline{\underline{L}}_{N_f,p}^T. \tag{5.139}$$

The updating algorithm for the computation of $\left(\underline{\underline{W}}_{p+1}, \underline{\underline{B}}_{p+1}\right)$, on the basis of $\left(\underline{\underline{W}}_p, \underline{\underline{B}}_p\right)$ is based on the following decomposition of the successive channel matrices:

$$\underline{\underline{\mathcal{H}}}_{N_f,p} = \begin{array}{r} \\ N_f-1 \Updownarrow \\ 1 \updownarrow \end{array} \begin{array}{c} \overset{\Delta}{\Leftrightarrow} \quad \overset{N_b}{\Leftrightarrow} \quad \overset{1}{\leftrightarrow} \\ \left(\begin{array}{ccc} \underline{\underline{H}}_0 & \underline{\underline{H}}_1 & \underline{\underline{0}} \\ \underline{\underline{h}}_1^T & \underline{\underline{h}}_2^T & \underline{\underline{h}}_0 \end{array}\right)_p \end{array}$$

$$\underline{\underline{\mathcal{H}}}_{N_f,p+1} = \begin{array}{r} \\ 1 \updownarrow \\ N_f-1 \Updownarrow \end{array} \begin{array}{c} \overset{1}{\leftrightarrow} \quad \overset{\Delta}{\Leftrightarrow} \quad \overset{N_b}{\Leftrightarrow} \\ \left(\begin{array}{ccc} \underline{\underline{h}}_0 & \underline{\underline{h}}_1^T & \underline{\underline{h}}_2^T \\ \underline{\underline{0}} & \underline{\underline{H}}_0 & \underline{\underline{H}}_1 \end{array}\right)_{p+1} \end{array} \tag{5.140}$$

where $\left(\begin{array}{cc} \underline{\underline{H}}_0 & \underline{\underline{H}}_1 \end{array}\right)_{p+1} = \left(\begin{array}{cc} \underline{\underline{H}}_0 & \underline{\underline{H}}_1 \end{array}\right)_p$. In its updating version, the filter coefficient computation algorithm (Algorithm 5.2) becomes:

Algorithm 5.4 *Update of the FIR DF-JD coefficients :*

1. *Compute the first* $2K$ *columns of the new MMSE matrix* $\overline{\underline{\underline{R}}}_{N_f,p+1}$*:*

$$\left(\begin{array}{c} \underline{\underline{r}}_0 \\ \underline{\underline{r}}_1 \\ \underline{\underline{r}}_2 \end{array}\right)_{p+1} = \sigma_I^{-2} \left(\begin{array}{c} \underline{\underline{E}}_{2K} \\ \underline{\underline{0}} \\ \underline{\underline{0}} \end{array}\right) + \sigma_n^{-2} \left(\begin{array}{c} \underline{\underline{h}}_0^T \\ \underline{\underline{h}}_1 \\ \underline{\underline{h}}_2 \end{array}\right)_{p+1} \left(\begin{array}{c} \underline{\underline{h}}_0 \end{array}\right)_{p+1} \tag{5.141}$$

with

$$\overline{\underline{\underline{R}}}_{N_f,p+1} = \begin{array}{cc} & \begin{array}{ccc} \overset{1}{\leftrightarrow} & \overset{\Delta}{\Leftrightarrow} & \overset{N_b}{\Leftrightarrow} \end{array} \\ \begin{array}{c} 1\,\updownarrow \\ \Delta\,\Updownarrow \\ N_b\,\Updownarrow \end{array} & \begin{pmatrix} \underline{\underline{r}}_0 & \underline{\underline{r}}_1^T & \underline{\underline{r}}_2^T \\ \underline{\underline{r}}_1 & \underline{\underline{R}}_0 & \underline{\underline{R}}_1^T \\ \underline{\underline{r}}_2 & \underline{\underline{R}}_1 & \underline{\underline{R}}_2 \end{pmatrix}_{p+1} \end{array} . \tag{5.142}$$

2. *Update the Cholesky factor* $\overline{\underline{\underline{L}}}_{N_f,p+1}$*:*

$$\begin{aligned} \overline{\underline{\underline{L}}}_{N_f,p} &= \begin{array}{cc} & \begin{array}{ccc} \overset{\Delta}{\Leftrightarrow} & \overset{N_b}{\Leftrightarrow} & \overset{1}{\leftrightarrow} \end{array} \\ \begin{array}{c} \Delta\,\Updownarrow \\ N_b\,\Updownarrow \\ 1\,\updownarrow \end{array} & \begin{pmatrix} \underline{\underline{L}}_0 & \underline{\underline{0}} & \underline{\underline{0}} \\ \underline{\underline{L}}_1 & \underline{\underline{L}}_2 & \underline{\underline{0}} \\ \underline{\underline{l}}_1^T & \underline{\underline{l}}_2^T & \underline{\underline{l}}_0 \end{pmatrix}_{p} \end{array} \\ \overline{\underline{\underline{L}}}_{N_f,p+1} &= \begin{array}{cc} & \begin{array}{ccc} \overset{1}{\leftrightarrow} & \overset{\Delta}{\Leftrightarrow} & \overset{N_b}{\Leftrightarrow} \end{array} \\ \begin{array}{c} 1\,\updownarrow \\ \Delta\,\Updownarrow \\ N_b\,\Updownarrow \end{array} & \begin{pmatrix} \underline{\underline{l}}_0 & \underline{\underline{0}} & \underline{\underline{0}} \\ \underline{\underline{l}}_1 & \underline{\underline{L}}_0 & \underline{\underline{0}} \\ \underline{\underline{l}}_2 & \underline{\underline{L}}_1 & \underline{\underline{L}}_2 \end{pmatrix}_{p+1} \end{array} . \end{aligned} \tag{5.143}$$

The first $2K$ *columns have to be computed from scratch:*

$$\begin{pmatrix} \underline{\underline{l}}_0 \\ \underline{\underline{l}}_1 \\ \underline{\underline{l}}_2 \end{pmatrix}_{p+1} \left(\underline{\underline{l}}_0\right)_{p+1}^T = \begin{pmatrix} \underline{\underline{r}}_0 \\ \underline{\underline{r}}_1 \\ \underline{\underline{r}}_2 \end{pmatrix}_{p+1} . \tag{5.144}$$

The $\Delta 2K$ *next columns satisfy the update relation:*

$$\begin{aligned} \begin{pmatrix} \underline{\underline{L}}_0 \\ \underline{\underline{L}}_1 \end{pmatrix}_{p+1} \left(\underline{\underline{L}}_0\right)_{p+1}^T &= \begin{pmatrix} \underline{\underline{L}}_0 \\ \underline{\underline{L}}_1 \end{pmatrix}_{p} \left(\underline{\underline{L}}_0\right)_{p}^T - \begin{pmatrix} \underline{\underline{l}}_1 \\ \underline{\underline{l}}_2 \end{pmatrix}_{p+1} \left(\underline{\underline{l}}_1\right)_{p+1}^T \\ &+ \sigma_n^{-2} \begin{pmatrix} \underline{\underline{h}}_1 \\ \underline{\underline{h}}_2 \end{pmatrix}_{p+1} \left(\underline{\underline{h}}_1\right)_{p+1}^T - \sigma_n^{-2} \begin{pmatrix} \underline{\underline{h}}_1 \\ \underline{\underline{h}}_2 \end{pmatrix}_{p} \left(\underline{\underline{h}}_1\right)_{p}^T . \end{aligned} \tag{5.145}$$

This problem is solved by $3\times 2K$ *successive applications of the Cholesky rank-*1 *update/downdate algorithm.*

3. *Update the feedforward matrix* $\overline{\underline{\underline{W}}}_{N_f,p+1}$*:*

$$
\begin{aligned}
\overline{\underline{\underline{W}}}_{N_f,p} &= \begin{array}{r c}
 & \begin{array}{cc} \overset{N_f-1}{\Leftrightarrow} & \overset{1}{\leftrightarrow} \end{array} \\
\begin{array}{r} \Delta \Updownarrow \\ 1 \updownarrow \\ N_b \Updownarrow \end{array} & \left(\begin{array}{cc} \underline{\underline{W}}_0 & \underline{\underline{0}} \\ \underline{\underline{w}}_1^T & \underline{\underline{w}}_0 \\ \underline{\underline{W}}_1 & \underline{\underline{w}}_2 \end{array} \right)_p
\end{array} \\
\overline{\underline{\underline{W}}}_{N_f,p+1} &= \begin{array}{r c}
 & \begin{array}{cc} \overset{1}{\leftrightarrow} & \overset{N_f-1}{\Leftrightarrow} \end{array} \\
\begin{array}{r} 1 \updownarrow \\ \Delta \Updownarrow \\ N_b \Updownarrow \end{array} & \left(\begin{array}{cc} \underline{\underline{w}}_0 & \underline{\underline{0}} \\ \underline{\underline{w}}_1 & \underline{\underline{W}}_0 \\ \underline{\underline{w}}_2 & \underline{\underline{W}}_1 \end{array} \right)_{p+1}
\end{array} .
\end{aligned}
\tag{5.146}
$$

There is a triangular system for the first $2K$ *columns:*

$$
\left(\begin{array}{cc} \underline{\underline{l}}_0 & \underline{\underline{0}} \\ \underline{\underline{l}}_1 & \underline{\underline{L}}_0 \end{array} \right)_{p+1} \left(\begin{array}{c} \underline{\underline{w}}_0 \\ \underline{\underline{w}}_1 \end{array} \right)_{p+1} = \sigma_n^{-2} \left(\begin{array}{c} \underline{\underline{h}}_0 \\ \underline{\underline{h}}_1 \end{array} \right)_{p+1} . \tag{5.147}
$$

The last $(N_f - 1)2K$ *columns satisfy the update equation:*

$$
\left(\underline{\underline{W}}_0^T \underline{\underline{L}}_0^T \right)_{p+1} = \left(\underline{\underline{W}}_0^T \underline{\underline{L}}_0^T \right)_p \tag{5.148}
$$

which can be incorporated into (5.145).

5.6.3 Computational complexity

In this section, we evaluate the number of operations required by the computation of the optimal filter coefficients for each code segment. Table 5.2 gives a rough order-of-magnitude estimate of the computational complexity associated with each of the three steps of the presented algorithms, assuming $N_f \gg L \gg 1$. The values given here correspond to the approximate number of complex scalar operations required for each matrix manipulation, taking the banded structure of the matrices into account [60].

Figures 5.8 and 5.9 give the exact number of real instructions required for the full computation of a new set of JD coefficients, and Figure 5.10 compares the number of instructions required for the full computation to that required for the updating procedure proposed above. To obtain these curves, a specific number of instructions was associated with each type of operation: 2 instructions for a multiply-and-add (which represents the majority of the operations required by the algorithms), and 1 instruction

Table 5.2: *Approximate complexity (in scalar operations) associated with the fast update of FIR-JD coefficients*

	Update Linear JD	Update DF-JD
1	$(2K)M^2 \quad \frac{1}{2}L^2$	$(2K)^2M \quad L$
2	$M^3 \quad 5(N_fL - \frac{1}{2}L^2)$	$(2K)^3 \quad 14(N_fL - \frac{1}{2}L^2)$
3	$(2K)M^2 \quad 2(N_fL - \frac{1}{2}L^2)$	$(2K)^2M \quad (N_fL - \frac{1}{2}L^2 + 7N_f^2)$

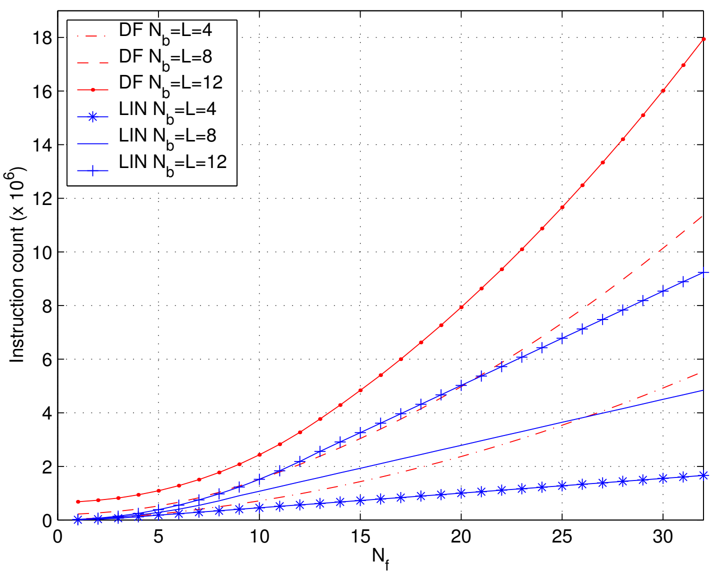

Figure 5.8: *Instruction count for computing the JD coefficients vs. N_f and $N_b = L$, with $M = K = 10$.*

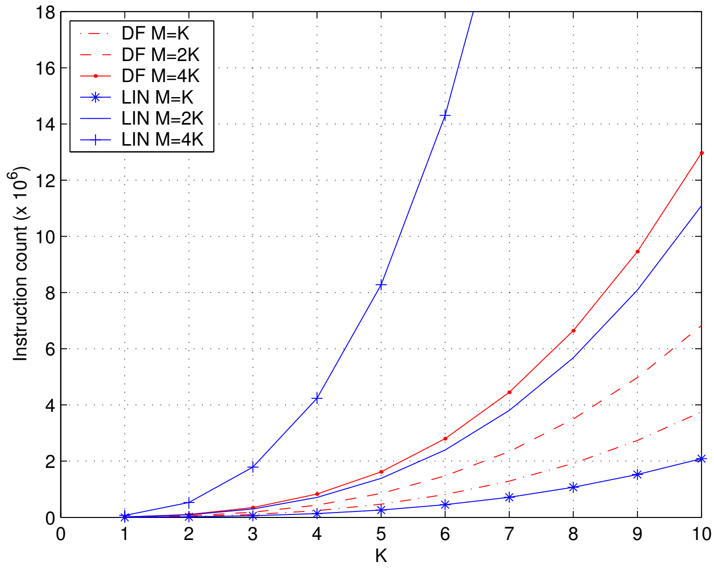

Figure 5.9: *Instruction count for computing the JD coefficients vs. K and M, with $L = 8$ and $N_f = 16$.*

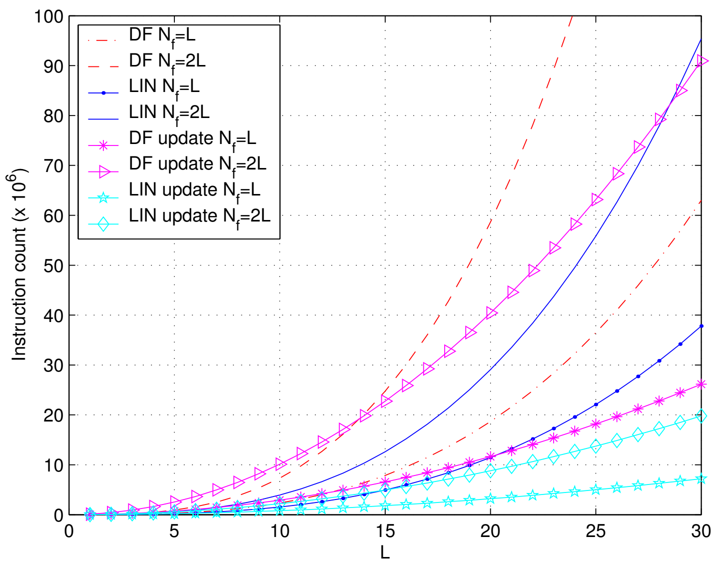

Figure 5.10: *Instruction count for computing the JD coefficients vs. $L = N_b$ and N_f, with $K = 10$ and $M = 10$.*

for the other operations. The displayed curves thus give approximately 2 times the number of scalar operations.
From these results, we can draw some general conclusions:

- When $M = K$, the computational complexity is higher for the DF-JD (roughly proportional to N_f^2) than for the linear JD (roughly proportional to N_f). This appears in Figure 5.8. The impact of the channel impulse response length L is comparable in the two cases.

- In the case of a long detector with $N_f \gg L$, the complexity associated with the computation of the feedforward section of the DF-JD (proportional to N_f^2) becomes prohibitive (Figure 5.8). The direct Equation (5.100) should be used instead.

- In some scenarios, it may be that $M \gg K$, especially for non-saturated systems ($K < N$) operating at a fractional rate ($N < M$). In that case, the complexity of the linear-JD algorithm is dramatically higher than its DF counterpart. This effect is illustrated in Figure 5.9. Equation (5.126) should be implemented instead of the direct Equation (5.125) to reduce the complexity. It should be noted that the fractional receiver oversampling factor can be chosen such that $M > N(1 + \alpha)$ and hence the classical value of $2N$ is not really necessary. In any case, considering that M is generally proportional to N, the resulting complexity increases with the third power of the spreading factor.

- The proposed update algorithms are effective for long channels only ($L \gg 1$). This is illustrated in Figure 5.10. This is a direct consequence of the Cholesky rank-1 update/downdate algorithm: the number of operations is $\mathcal{O}\left(n^2\right)$ instead of $\mathcal{O}\left(n^3\right)$ but the number of instructions associated with each of these operations is higher.

5.7 ZF equalization for Cyclic-Prefixed transmission

The cyclic-prefixed block transmission system presented in Section 4.6 is well-suited to low-complexity detection techniques exploiting the circulant channel structure induced by the cyclic prefix extension.

Let us consider a single-user system. The received signal, after removal of the CP, is given by

$$\underline{\mathrm{r}} = \underline{\underline{\mathrm{H}}}\,\underline{\mathrm{I}} + \underline{\mathrm{n}} = \underline{\underline{\mathcal{C}}}\left[\underline{\underline{\mathrm{S}}}\,\underline{\mathrm{I}}\right] + \underline{\mathrm{n}} \tag{5.149}$$

where $\underline{\underline{S}}$ is the signature matrix and $\underline{\underline{\mathcal{C}}}$ is a circulant channel matrix. The channel matrix can be factorized as follows

$$\underline{\underline{\mathcal{C}}} = \underline{\underline{W}}_N^T \, \underline{\underline{\Lambda}} \, \underline{\underline{W}}_N \tag{5.150}$$

where $\underline{\underline{W}}_N$ is the DFT matrix of size N.

In a zero-forcing context, the effect of the frequency-selective channel can be easily suppressed by equalizing the received signal in the frequency domain :

$$\underline{y} = \underline{\underline{W}}_N \, \underline{r} = \underline{\underline{\Lambda}} \, \underline{\underline{W}}_N \, \left[\underline{\underline{S}} \, \underline{I}\right] + \underline{\underline{W}}_N \, \underline{n}. \tag{5.151}$$

This equalization only requires the application of a diagonal matrix on the frequency-domain samples $\underline{y}$:

$$\hat{\underline{y}} = \underline{\underline{\Lambda}}^{-1} \, \underline{y}. \tag{5.152}$$

Returning to the time domain, the equalized signal becomes :

$$\hat{\underline{r}} = \underline{\underline{W}}_N^T \, \hat{\underline{y}} = \underline{\underline{S}} \, \underline{I} + \left[\underline{\underline{W}}_N^T \, \underline{\underline{\Lambda}}^{-1} \, \underline{\underline{W}}_N\right] \, \underline{n}. \tag{5.153}$$

The symbols are finally recovered by correlating the equalized signal with the N signature codes $s_p(n)$:

$$\hat{\underline{I}} = \underline{\underline{S}}^T \, \hat{\underline{r}} = \underline{I} + \underline{\underline{S}}^T \, \left[\underline{\underline{W}}_N^T \, \underline{\underline{\Lambda}}^{-1} \, \underline{\underline{W}}_N\right] \, \underline{n} = \underline{I} + \underline{e}. \tag{5.154}$$

The error covariance matrix is

$$\underline{\underline{R}}_{ee} = \sigma_n^2 \, \underline{\underline{S}}^T \, \left[\underline{\underline{W}}_N^T \, \underline{\underline{\Lambda}}^{-2} \, \underline{\underline{W}}_N\right] \, \underline{\underline{S}}. \tag{5.155}$$

The *arithmetic mean* of the error variances

$$\frac{1}{N} \sum_{p=1}^{N} \sigma_{e_p}^2 = \frac{1}{N} \mathrm{tr} \left[\underline{\underline{R}}_{ee}\right] \tag{5.156}$$

is constant for all orthogonal signature sets $\underline{\underline{S}}$ with $\underline{\underline{S}}^T \, \underline{\underline{S}} = \underline{\underline{E}}_N$.

What really matters, as far as the bit rate computation is concerned, is the geometrical mean of the error variances. This geometrical mean is actually different for every set of orthogonal signatures. Two extreme cases can be put forward :

- The geometrical mean of the error variances is minimum when the error covariance matrix is diagonal. Indeed, it is known that

$$\prod_{p=1}^{N} \left(\underline{\underline{\mathrm{R}}}_{ee}\right)_{pp} \geq \det\left(\underline{\underline{\mathrm{R}}}_{ee}\right) \tag{5.157}$$

  with equality if and only if $\underline{\underline{\mathrm{R}}}_{ee}$ is diagonal, and the right-hand side of (5.157) does not depend on the selected signature set. A diagonal error covariance matrix is obtained by letting $\underline{\underline{\mathrm{S}}} = \underline{\underline{\mathrm{W}}}$, i.e. by implementing a DMT system[3]. Among all CP transmission systems, DMT is then the one that minimizes the geometrical mean of error variances at the output of the linear zero-forcing receiver.

- The sum of error variances being constant, the maximum product of error variances is achieved when all variances are equal. In other words, the geometrical mean of the error variances is maximum when the error covariance matrix has a constant diagonal. This is obtained by letting $\underline{\underline{\mathrm{S}}} = \underline{\underline{\mathrm{E}}}_N$, i.e. by implementing a single-carrier system. Among all CP transmission systems, single-carrier is then the one that maximizes the geometrical mean of error variances at the output of the linear zero-forcing receiver. It also has the interesting property that all N symbols in the block have an identical SNR at the receiver output.

The other CP-based transmission schemes (like Hadamard transmission for instance) have an intermediate score.

To conclude this section, we propose to show that the fundamental reason for the difference of performance among the various CP transmission schemes is neither related to the CP technique nor to the choice of a zero-forcing equalizer, but is only due to the use of a linear receiver, which is not the optimal structure. Let us consider a zero-forcing decision-feedback (ZF-DF) receiver. In this structure, the feedforward part of the equalizer is no longer made of one tap per subchannel in the frequency domain, but is a full matrix described in the time domain. It is again assumed that the receiver first removes the cyclic prefix, so that it works with the same received vector $\underline{\mathrm{r}}$. The symbol estimates are now

$$\hat{\underline{\mathrm{I}}} = \underline{\underline{\mathrm{F}}}\,\underline{\mathrm{r}} - \left[\underline{\underline{\mathrm{B}}} - \underline{\underline{\mathrm{E}}}_N\right] \underline{\mathrm{I}} \tag{5.158}$$

[3] Actually, baseband DMT can be described by means of *real* signature codes $s_p(n)$. See a discussion about this in Section 4.2.3.

where $\underline{\underline{B}}$ is the causal feedback section, i.e. an upper triangular matrix with ones on the main diagonal. The derivation of the optimal matrices $\underline{\underline{F}}$ and $\underline{\underline{B}}$ under a ZF constraint [62] requires the following Cholesky factorization :

$$\sigma_n^{-2}\,\underline{\underline{H}}^T\,\underline{\underline{H}} = \underline{\underline{L}}\,\underline{\underline{D}}\,\underline{\underline{L}}^T. \tag{5.159}$$

The optimal matrices are then given by

$$\begin{aligned} \underline{\underline{F}} &= \sigma_n^{-2}\,\underline{\underline{D}}^{-1}\,\underline{\underline{L}}^{-1}\,\underline{\underline{H}}^T \\ \underline{\underline{B}} &= \underline{\underline{L}}^T. \end{aligned} \tag{5.160}$$

From (5.158) and (5.160), the symbol estimates are

$$\hat{\underline{I}} = \underline{I} + \sigma_n^{-2}\,\underline{\underline{D}}^{-1}\,\underline{\underline{L}}^{-1}\,\underline{\underline{H}}^T\,\underline{n}. \tag{5.161}$$

The error covariance matrix is $\underline{\underline{R}}_{ee} = \underline{\underline{D}}^{-1}$. The geometrical average of the error variances becomes

$$\frac{1}{N}\prod_{p=1}^{N}\left(\underline{\underline{R}}_{ee}\right)_{pp} = \frac{1}{N}\det\left(\underline{\underline{D}}\right)^{-1} \tag{5.162}$$

$$= \frac{1}{N}\det\left(\underline{\underline{L}}\,\underline{\underline{D}}\,\underline{\underline{L}}^T\right)^{-1} \tag{5.163}$$

$$= \frac{1}{N}\det\left(\sigma_n^{-2}\,\underline{\underline{S}}^T\,\underline{\underline{W}}_N^T\,\underline{\underline{\Lambda}}^2\,\underline{\underline{W}}_N\underline{\underline{S}}\right)^{-1} \tag{5.164}$$

$$= \frac{1}{N}\prod_{p=1}^{N}\left(\frac{\Lambda_p^2}{\sigma_n^2}\right)^{-1}. \tag{5.165}$$

At the output of a DF-ZF receiver, the geometrical mean of the error variances is thus independent of the signature set. Furthermore, it can be easily verified that the DF-ZF receiver is identical to the linear-ZF receiver in the case of DMT transmission. The same level of performance (as measured by the geometrical mean of error variances) is then accessible to all types of CP transmission schemes as soon as ZF decision-feedback equalization is performed in the receiver. This receiver, however, is rather complex, except for the case of DMT transmission, where it is identical to the simple ZF linear receiver.

5.8 Applications to the powerline channel

In this Section, the performance of a complete PLC system is analyzed, combining the multiple access techniques proposed in Chapter 4, the channel model introduced in Chapter 2, and the MMSE Joint Detector derived in Chapter 5.

The frequency band available for powerline communications is supposed to be in the range of 1 MHz to 10 MHz. Passband transmission is thus required. A maximum power spectral density of $\overline{\gamma}(f) = -60$ dBm/Hz is imposed for the transmitted signals in the whole frequency band.

A CAP-FB transmission system with a central frequency of $f_c = 5.5$ MHz, a chip rate of $1/T_c' = 9$ MHz, and an average transmission power of $P = 9$ mW, is compatible with the proposed transmission constraints. The use of a paraunitary FB with symbols of equal variance on all signatures guarantees a flat power spectral density for the transmitted signal sum. The chip shaping filters are sine- and cosine-modulated half-root Nyquist filters with a roll-off factor of $\alpha = 0.22$. Taking into account the roll-off effect, the effective bandwidth of the transmitted signals is roughly 0 to 11 MHz. The chip duration is $T_c' = 111$ ns.

The powerline network considered in the next computations is given in Figure 2.12. The $K = 5$ users in positions 2, 5, 10, 15 and 20 are simultaneously active, and the differential propagation mode is considered. Unused terminations are assumed to be left open. The computed end-to-end channel responses are illustrated in the time domain in Figure 2.22, and in the frequency domain (0-50 MHz) in the lower part of Figure 2.23. The top of Figure 3.15 also gives the channel frequency responses in the range of 0 to 10 MHz. The minimum delay between two successive paths is approximately 50 ns. Combining the significant channel paths with the cable responses and the modulated shaping filters, the global channel impulse responses have an extension of approximately 9 μs, i.e. $L_c = 81$ chips.

In the next computations, the AWGN level is chosen as $N_0 = -140$ dBm/Hz, which is a rather optimistic noise scenario.

The receiver operates at a fractional rate M/T_c' with $M = 3$. A finite-length MMSE DF-JD provides noisy estimates $\hat{I}_p(n)$ of the transmitted symbols. The SINR's ρ_p at the N detector outputs are computed assuming perfect past decisions, and the user bit rates are finally obtained according to (4.56). The SNR gap used in these computations is $\Gamma = 1$ (which corresponds to ideal transmission).

5.8.1 CAP-FB systems : OFDMA, CDMA and TDMA

Three types of FBs of length $N = 128$ are firstly compared (see Section 4.2.3) : DFT filters (CAP-OFDMA), Hadamard codes (CAP-CDMA) and single-carrier signatures (CAP-TDMA). For this choice of N, the symbol duration is $T = NT'_c = 14\mu$s. The global channel impulse responses have thus an extension of less than one symbol ($L = 1$). For this configuration, an observation window of $N_f = 3$ successive symbols, combined with a decision delay of $\Delta = 2$ symbols and a feedback section of length $N_b = 1$, is sufficient to approach the optimal performance.

Tables 5.3, 5.4 and 5.5 give the bit rates (in Mbits/s) obtained with the three CAP-FB systems. The first rows correspond to the single-user configurations, obtained when all of the N signatures are allocated to a single user. As expected, the SU rates are identical for the three filter banks. In a multiuser configuration, a balanced signature allocation should be derived, that would provide each user with a bit rate in proportion with its own potential :

- Using TDM(A), the channel can be dedicated to each user in turn, which corresponds to K successive SU configurations, with time intervals of equal duration for each user. In that scenario, each user gets 20 % of its SU bit rate. The obtained rates are given in the second rows. A better performance can be expected by using a smart signature allocation algorithm.

- In the downlink, the partial bit rates R_{kp}, obtained with the MMSE DF-JD by allocating signature p to user k, can be computed once for all. Algorithm 3.6 introduced in Chapter 3 can then be used to solve the problem of optimal subchannel assignment with balanced rate constraints. The obtained maximum balanced rates are given in the third rows.

- In the uplink, the subchannel assignment problem is much more difficult to solve. Indeed, by using the MMSE DF-JD, the partial bit rates R_{kp} for a given subchannel p actually depend on the allocation of the $N-1$ other subchannels. The following method was used to obtain a good (if not optimal) signature allocation. Starting from the optimal signature allocation for the downlink (which is easily obtained with Algorithm 3.6), some signatures are successively transferred from one user to another, until the balanced rate constraints are almost satisfied. Five quasi-balanced signature allocations can then be obtained,

Table 5.3: *CAP-OFDMA: maximum balanced rates (in Mbits/s)*

Configuration	User 2	User 5	User 10	User 15	User 20	%
SU-OFDM	218.13	195.90	156.94	123.04	92.98	100.0
TDMA-OFDM	43.63	39.18	31.39	24.61	18.60	20.0
downlink-OFDM	51.42	46.18	37.00	29.00	21.92	23.6
uplink-OFDMA	52.39	47.05	37.69	29.55	22.33	24.0
Allocation 1	52.57	47.08	38.54	26.99	24.05	
Allocation 2	53.12	48.33	36.94	28.90	22.26	
Allocation 3	51.02	46.75	39.99	28.88	22.00	
Allocation 4	51.56	50.02	38.48	27.36	22.01	
Allocation 5	52.75	46.51	36.80	30.61	22.26	

Table 5.4: *CAP-CDMA: maximum balanced rates (in Mbits/s)*

Configuration	User 2	User 5	User 10	User 15	User 20	%
SU-CDMA	218.13	195.90	156.94	123.04	92.98	100.0
TDMA-CDMA	43.63	39.18	31.39	24.61	18.60	20.0
downlink-CDMA	49.92	44.83	35.92	28.16	21.28	22.9
uplink-CDMA	50.81	45.64	36.56	28.66	21.66	23.3
Allocation 1	51.55	44.33	36.00	30.19	21.52	
Allocation 2	51.23	45.47	37.21	28.28	21.58	
Allocation 3	51.27	47.85	35.40	28.11	21.55	
Allocation 4	50.53	44.33	37.07	29.97	20.94	
Allocation 5	50.48	44.49	37.18	27.96	22.65	

Table 5.5: *CAP-TDMA: maximum balanced rates (in Mbits/s)*

Configuration	User 2	User 5	User 10	User 15	User 20	%
SU-SC	218.13	195.90	156.94	123.04	92.98	100.0
TDMA-SC	43.63	39.18	31.39	24.61	18.60	20.0
downlink-TDMA	43.63	39.18	31.39	24.61	18.60	20.0

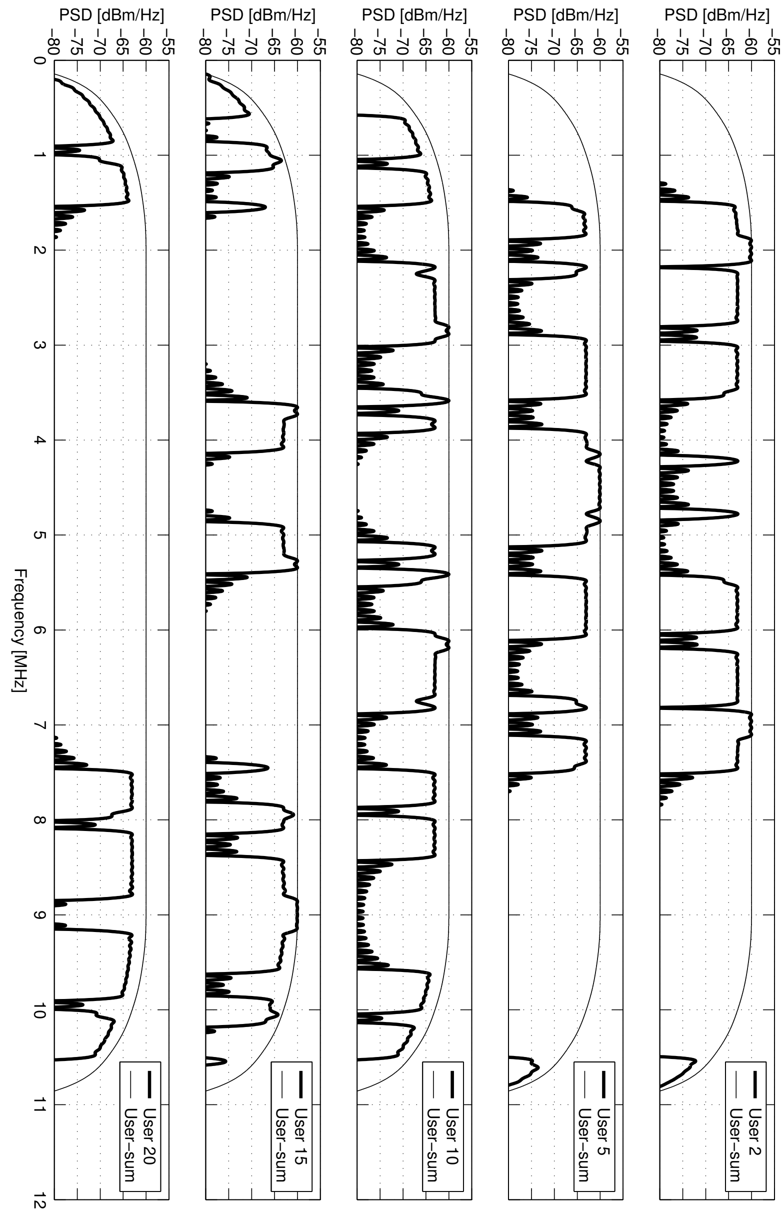

Figure 5.11: *Power spectral density of the transmitted signals, CAP-OFDMA with DFT tones of length* $N = 128$.

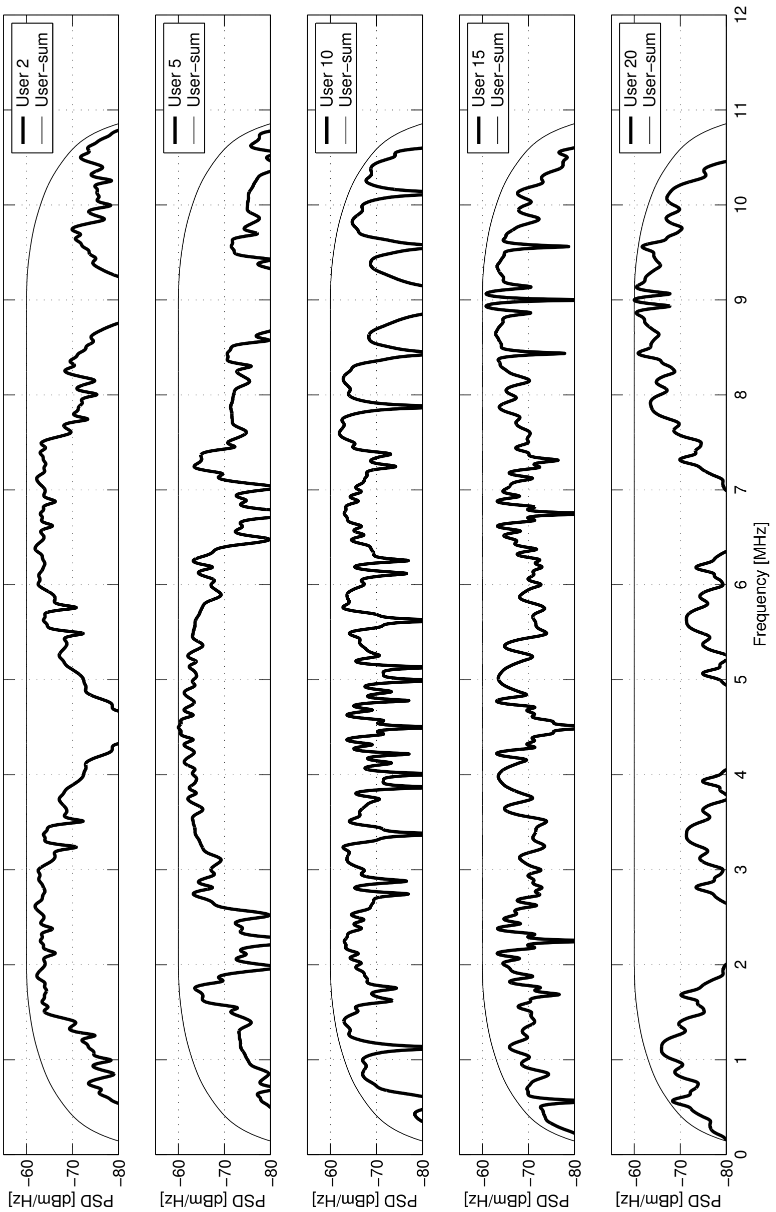

Figure 5.12: *Power spectral density of the transmitted signals, CAP-CDMA with Hadamard codes of length* $N = 128$.

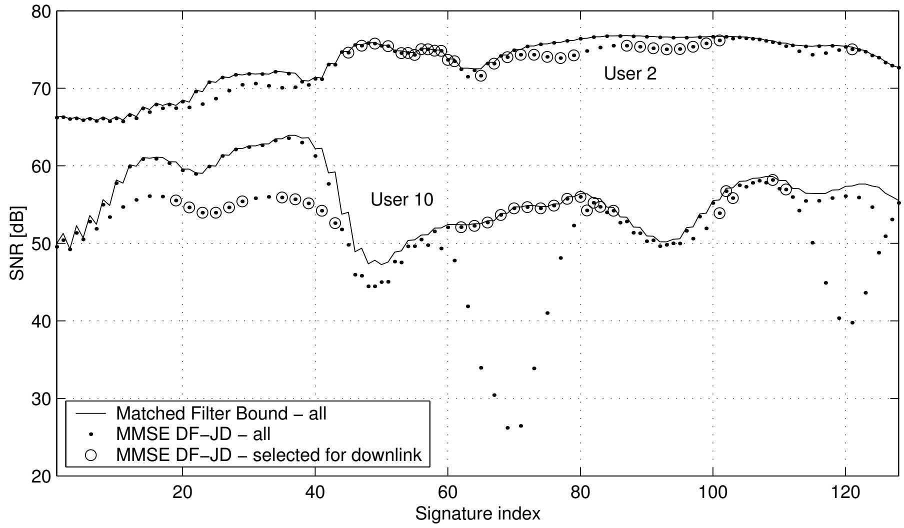

Figure 5.13: *SINR at the output of the MMSE DF-JD vs. tone index, CAP-OFDMA with* $N = 128$ *tones.*

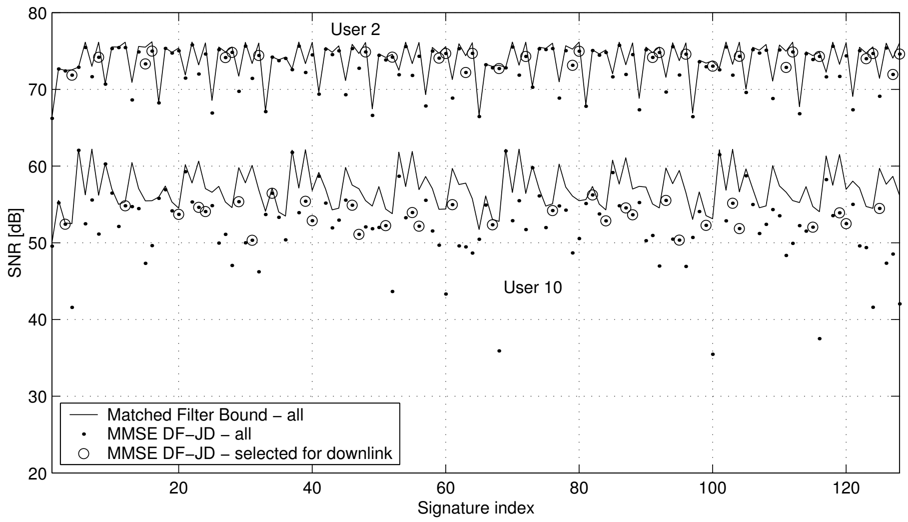

Figure 5.14: *SINR at the output of the MMSE DF-JD vs. code index, CAP-CDMA with* $N = 128$ *codes.*

Table 5.6: *CAP-CDMA with long codes: maximum balanced rates (in Mbits/s)*

Configuration	User 2	User 5	User 10	User 15	User 20	%
SU-CDMA	218.13	195.90	156.94	123.05	92.99	100
TDMA-CDMA	43.63	39.18	31.39	24.61	18.60	20
uplink-CDMA	44.29	40.10	32.02	25.90	20.85	
	20.31 %	20.47 %	20.40 %	21.05 %	22.43 %	

that differ from each other by only one subchannel. Perfectly balanced rates are finally obtained by time-sharing between the 5 proposed allocations, with appropriate sharing coefficients. The uplink balanced rates obtained with this method are given in the fourth rows, while the last rows give the user rates corresponding to the 5 discrete signature allocations.

In a multiuser configuration, the performance of the MMSE DF-JD now depends on the selected filter bank. No gain can be expected from the CAP-TDMA system (single-carrier signatures), as all signatures have an identical spectrum. A rate gain is achieved with the two other systems as they are able to shape the spectrum of the transmitted signals in accordance with the physical channels.

Figures 5.11 and 5.12 give the power spectral density (in dBm/Hz) of the transmitted signals in uplink, for the selected signature allocations in CAP-OFDMA and CAP-CDMA. These Figures also illustrate how different filter banks are able to shape the spectrum of the transmitted signals with specific degrees of freedom.

Figures 5.13 and 5.14 show the distribution of the SINRs at the output of the MMSE DF-JD vs. the signature index, for both the single-user CAP-OFDMA and CAP-CDMA systems. The continuous lines give the matched filter bound. Circles are used to denote the signatures selected for users 2 and 10 by the allocation algorithm in the downlink.

5.8.2 CAP-CDMA with long codes

For the purpose of comparison, a long-code CAP-CDMA system is considered, with short Hadamard codes of length $N = 20$, and a long-code with a periodicity of $P = 64$ segments obtained by truncating a Gold code of length 1023. For this choice of N, the symbol duration is $T = NT'_c = 2.22\mu$s. The

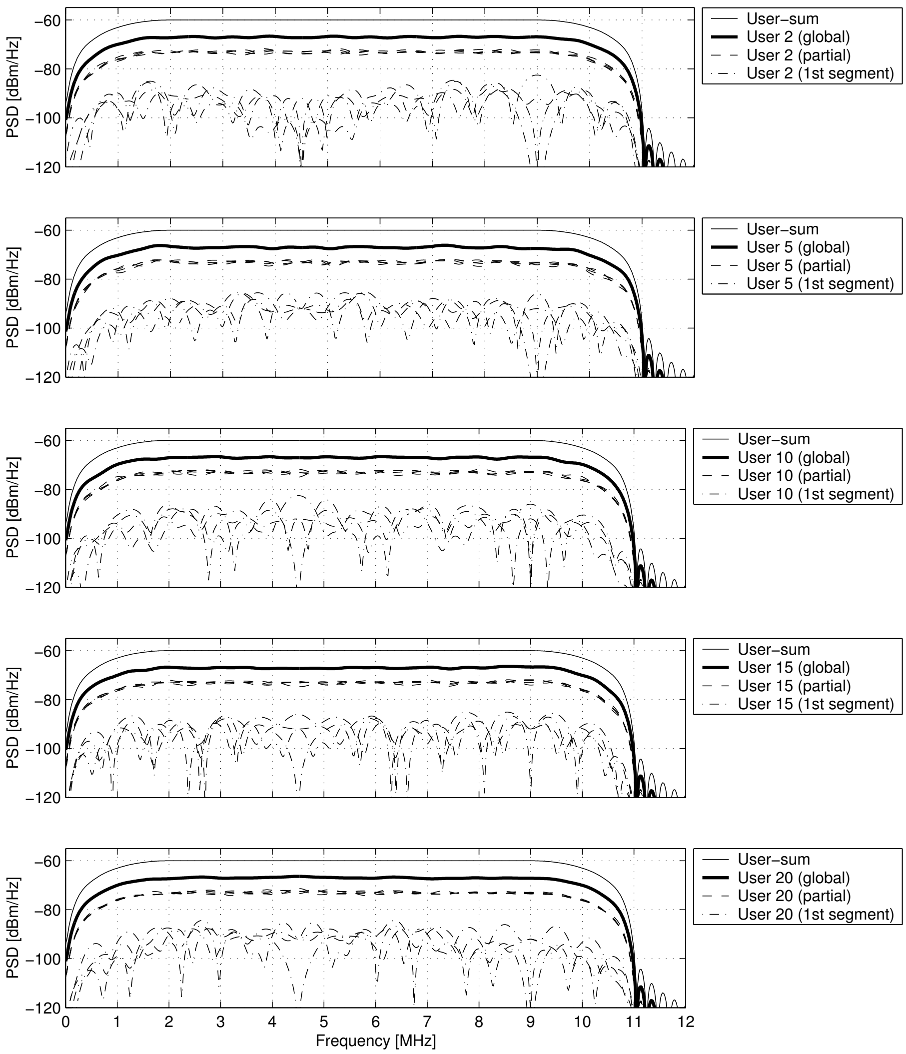

Figure 5.15: *Power spectral density of the transmitted signals, CAP-CDMA with long codes (short spreading codes: Hadamard codes of length $N = 20$, long code periodicity: $P = 64$ symbols).*

global channel impulse responses have thus an extension of $L = 5$ symbols. For this configuration, an observation window of $N_f = 12$ successive symbols, combined with a decision delay of $\Delta = 11$ symbols and a feedback section of length $N_b = 5$, is sufficient to approach the optimal performance.

Table 5.6 gives the computed user rates (in Mbits/s). The first row gives the single-user rates, obtained by allocating the $N = 20$ spreading codes to the same user. These rates are almost identical to the SU rates obtained with a paraunitary FB (and no long code). The second row gives the balanced rates obtained by time-sharing between single-user configurations. The third row gives the user rates obtained by allocating arbitrarily 4 spreading codes to each of the 5 users. These rates are not exactly balanced : a slight power control could be investigated to obtained perfectly balanced rates. Actually the rate gain with respect to the time-sharing solution is negligible.

Figure 5.15 illustrates the power spectral density of the transmitted signals, which are approximately flat in the whole frequency band. The global PSD of a given user is obtained by combining the PSDs of the 4 subchannels (4 spreading codes). The PSD of a given subchannel is then obtained by combining the PSDs associated with each of the 64 code segments.

Finally, Figure 5.16 gives the distribution of the SINR at the output of the MMSE DF-JD as a function of the code segment, for each of the 4 spreading codes of users 2, 5, 10 and 20. The horizontal dashed lines give the average SINR associated with each spreading code (obtained by considering the 64 code segments). It turns out that the different symbols associated with a given spreading code may have quite different SINRs.

5.9 Conclusion

In this Chapter, fundamental limits have been derived on the performance of the FB-based multiple access scheme presented in Chapter 4. The matched filter bound, on one hand, provides a useful information on the maximum signal to noise ratio that can be expected by allocating a given signature to a given user. This bound can be a starting point for a signature allocation algorithm. This bound, however, is not achievable in a practical system. In particular, it does not account for the mutual interference between signatures.

A more useful bound is the capacity region of the FB-based multiple access system. It differs from the general capacity region defined in Chapter 3

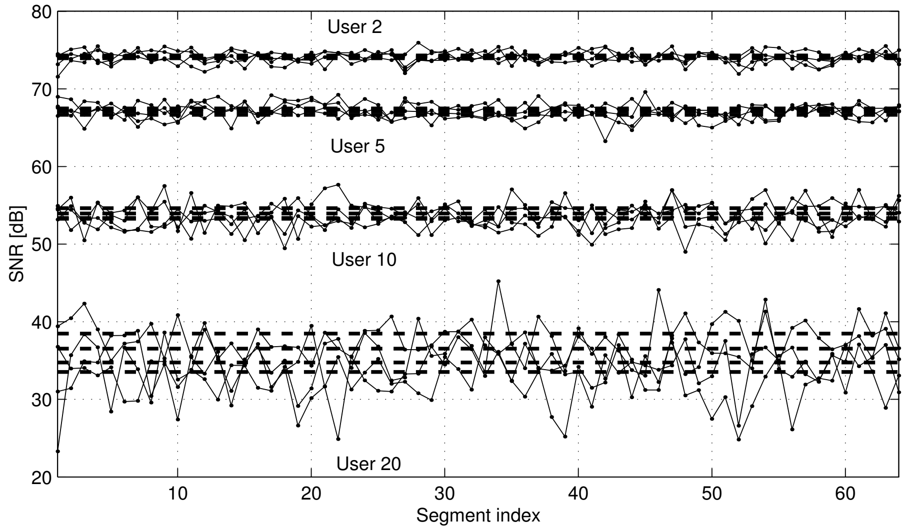

Figure 5.16: *SINR at the output of the MMSE DF-JD vs. code segment, CAP-CDMA with $N = 20$ spreading codes, and a long code periodicity of $P = 64$.*

by the fact that the power spectral density of the transmitted signals is now restricted by the selected FB. In other words, the signature allocation algorithm allows the shaping of the transmitted PSDs, but with a limited flexibility that is closely related to the nature of the FB and the number of available subchannels. For a paraunitary FB, the FB-based single-user capacity has been shown to be independent of the FB, and identical to the true (PSD-constrained) single-user capacity. The boundary of the capacity region, however, differs from one FB to another, as it depends on the flexibility with which a given FB is able to shape the PSD of the individual transmitted signals. For a given FB, the computation of the balanced capacity was shown to be extremely difficult. Lower and upper bounds have been proposed, which are easier to compute.

Linear and decision-feedback MMSE joint detectors suited to the FB-based system have been proposed as a practical and efficient solution. Infinite detectors were firstly introduced. Their performance provide an upper bound on that of the practical finite-length detectors. The arithmetic mean of the estimation error variances (for the linear JD) and the geometrical mean of the estimation error variances (for the DF-JD) were shown to be independent of the FB if the paraunitary property is satisfied. Moreover, it was shown that the single-user capacities and the sum-capacity of the multiuser channel could be achieved by means of an infinite DF-JD followed by AWGN decoders. This proves that the MMSE DF-JD is an efficient solution to transform the initial FB-based frequency-selective system into a set of parallel and independent subchannels. All points of the capacity region are not achievable with the DF-JD, however, as successive decoding among the users is generally required, which is not feasible with a causal DF-JD.

The practical computation of joint detector coefficients has been analyzed in detail as a function of the system parameters. Complex matrix manipulations are required (e.g. Cholesky factorizations), but the effective complexity of these manipulations is reduced if the banded structure of the matrices is taken into account. Anyway, the resulting complexity is still proportional to the third power of the spreading factor N (which is also the number of signatures), which restricts the feasability of the proposed system to moderate values of N. The number of subchannels should be sufficient, however, to allow the spectral shaping of the transmitted signals with a good flexibility. The final choice for the number of subchannels is thus a trade-off between performance and complexity issues.

The MMSE JD was shown to be also compatible with the long-code CAP-CDMA system. The price to pay is the need for a systematic update of the detector coefficients for every new symbol, which dramatically increases the computational complexity of the receiver. Fast update algorithms have been proposed to reduce that complexity, but the complexity reduction is rather low. For this reason, long-code CAP-CDMA is not a good candidate, and short-code CAP-CDMA with an efficient code allocation algorithm should be preferred.

Finally, the linear zero-forcing receiver has been shown to be a powerful low-complexity solution suited to the cyclic-prefixed FB-based *downlink* transmission scheme. In each receiver, the signal just needs to be equalized by a single coefficient in the frequency domain. Back to the time domain, the symbols are finally recovered by a simple correlation with the adequate signature code. This solution has a low complexity, even with large values of N. It represents an attractive alternative to the MMSE-JD for the downlink. In order to limit the rate loss induced by the cyclic prefix, however, the number of subchannels N should be very large.

Chapter 6

Performance loss in non-ideal conditions

6.1 Introduction

The performance analysis proposed in Chapter 5 has been carried out with the assumption that the joint detector is operated in ideal conditions. By this, we mean that two important hypotheses are satisfied :

- The clocks of the K transmitters and that of the unique receiver are perfectly synchronized. This implies that the received sequence of samples can be effectively modeled by the filtering of the transmitted symbol sequences by the nominal equivalent channels, plus the additive noise. In other words, *timing synchronization* is ideal.

- The equivalent channels are perfectly known by the receiver, which allows the computation of JD coefficients that are perfectly matched to these equivalent channels. In other words, *channel knowledge* is ideal.

In a practical system, these assumptions are not satisfied. Actually both the clock alignment and the channel coefficients have to be estimated and tracked. Maximum likelihood (ML) estimation techniques can be used to derive efficient estimates of these parameters on the basis of the observed noisy signal. ML timing estimation techniques are analyzed in chapter 7, while the issue of ML channel estimation is beyond the scope of this work. The parameter estimates obtained with these techniques are not ideal. It follows a timing error ε_p for each subchannel (which is actually identical for all subchannels allocated to a given user), and an estimated channel matrix $\hat{\underline{\underline{\mathrm{H}}}}(z) = \underline{\underline{\mathrm{H}}}(z) + \tilde{\underline{\underline{\mathrm{H}}}}(z)$ that differs from the true value $\underline{\underline{\mathrm{H}}}(z)$. It is important to evaluate the robustness of the proposed multiuser FB-based transmission system with respect to these timing and channel estimation errors. The performance degradation associated with these non-ideal conditions can be modeled by means of an excess mean square error (MSE) at the output of the joint detector. In the following, we assume that the timing and channel estimation errors are very small, which allows the use of first order approximation for the computation of the excess MSE. These conditions are satisfied if the system is operated at high SNR.

6.2 Excess MSE in non-ideal conditions

The symbol estimates at the output of an IIR linear MMSE JD operated in non-ideal conditions are given by

$$\hat{\underline{\mathrm{I}}}(z) = \hat{\underline{\underline{\mathrm{W}}}}(z)\, \underline{\mathrm{R}}_{\underline{\varepsilon}}(z) \tag{6.1}$$

where :

- The non-ideal JD coefficients are based on the estimated channel matrix $\hat{\underline{\underline{\mathrm{H}}}}(z)$:

$$\begin{aligned} \hat{\underline{\underline{\mathrm{W}}}}(z) &= \sigma_I^2\, \hat{\underline{\underline{\mathrm{H}}}}^H(1/z^*) \left[\sigma_n^2\, \underline{\underline{\mathrm{E}}}_M + \sigma_I^2\, \hat{\underline{\underline{\mathrm{H}}}}(z)\, \hat{\underline{\underline{\mathrm{H}}}}^H(1/z^*)\right]^{-1} && (6.2)\\ &= \underline{\underline{\mathrm{W}}}(z) + \tilde{\underline{\underline{\mathrm{W}}}}(z) && (6.3) \end{aligned}$$

  where $\underline{\underline{\mathrm{W}}}(z)$ is the optimal linear MMSE JD associated with the true channel matrix $\underline{\underline{\mathrm{H}}}(z)$.

- The asynchronous received sequences are related to the transmitted symbols by

$$\begin{aligned} \underline{\mathrm{R}}_{\underline{\varepsilon}}(z) &= \underline{\underline{\mathrm{H}}}_{\underline{\varepsilon}}(z)\, \underline{\mathrm{I}}(z) + \underline{\mathrm{N}}(z) && (6.4)\\ &= \underline{\mathrm{R}}_{\underline{0}}(z) + \tilde{\underline{\mathrm{R}}}_{\underline{\varepsilon}}(z) && (6.5) \end{aligned}$$

  where the asynchronous channel matrix $\underline{\underline{\mathrm{H}}}_{\underline{\varepsilon}}(z)$ contains the z-transformed sequences $\overline{h}_{pk}(mT + \rho T_s + \varepsilon_k)$ (see (4.38)).

The symbol estimation errors $\hat{\underline{\epsilon}}(z)$ obtained in non-ideal conditions are given by

$$\begin{aligned} \hat{\underline{\epsilon}}(z) &= \underline{\mathrm{I}}(z) - \hat{\underline{\mathrm{I}}}(z) && (6.6)\\ &\approx \underline{\epsilon}(z) - \tilde{\underline{\underline{\mathrm{W}}}}(z)\, \underline{\mathrm{R}}_{\underline{0}}(z) - \underline{\underline{\mathrm{W}}}(z)\, \tilde{\underline{\mathrm{R}}}_{\underline{\varepsilon}}(z) && (6.7) \end{aligned}$$

where $\underline{\epsilon}(z)$ is the estimation error obtained with perfect channel knowledge and timing synchronization. The mean square symbol estimation errors are

$$\Gamma_{\underline{\hat{\epsilon}}\underline{\hat{\epsilon}}}(0) = \frac{1}{2\pi} \int_{-\pi}^{\pi} \underline{\underline{\gamma}}_{\underline{\hat{\epsilon}}\underline{\hat{\epsilon}}}(e^{j\Omega})\, \mathrm{d}\Omega. \tag{6.8}$$

From (6.7), the error power spectrum contains the following contributions :

$$\begin{aligned}\underline{\underline{\gamma}}_{\underline{\hat{\epsilon}}\underline{\hat{\epsilon}}}(z) \approx \underline{\underline{\gamma}}_{\underline{\epsilon}\underline{\epsilon}}(z) + \left[\underline{\underline{\tilde{\mathrm{W}}}}(z)\, \underline{\underline{\gamma}}_{\underline{\mathrm{R}}_0\underline{\mathrm{R}}_0}(z)\, \underline{\underline{\tilde{\mathrm{W}}}}^H(\frac{1}{z^*})\right] \\ + \left[\underline{\underline{\mathrm{W}}}(z)\, \underline{\underline{\gamma}}_{\underline{\tilde{\mathrm{R}}}_\varepsilon\underline{\tilde{\mathrm{R}}}_\varepsilon}(z)\, \underline{\underline{\mathrm{W}}}^H(\frac{1}{z^*}) + \underline{\underline{\gamma}}_{\underline{\epsilon}\underline{\tilde{\mathrm{R}}}_\varepsilon}(z)\, \underline{\underline{\mathrm{W}}}^H(\frac{1}{z^*}) + \underline{\underline{\mathrm{W}}}(z)\, \underline{\underline{\gamma}}_{\underline{\tilde{\mathrm{R}}}_\varepsilon\underline{\epsilon}}(z)\right].\end{aligned} \tag{6.9}$$

The first term is the MMSE obtained in ideal conditions. The second term is the excess MSE due to channel estimation errors. The third term is the excess MSE due to timing synchronization errors. Some cross-terms have been neglected to obtain (6.9), for the following reasons :

- The cross-spectrum between $\underline{\epsilon}(z)$ and $\underline{\underline{\tilde{\mathrm{W}}}}(z)\, \underline{\mathrm{R}}_0(z)$ is exactly equal to zero thanks to the orthogonality principle.
- The cross-spectrum between $\underline{\underline{\tilde{\mathrm{W}}}}(z)\, \underline{\mathrm{R}}_0(z)$ and $\underline{\underline{\mathrm{W}}}(z)\, \underline{\tilde{\mathrm{R}}}_\varepsilon(z)$ represents the coupling between the channel estimation and timing synchronization effects. As both estimation errors are assumed to be uncorrelated, the expectation of these cross-terms is equal to zero.

6.2.1 Excess MSE due to channel estimation errors

Let us now compute how the channel estimation error $\underline{\underline{\tilde{\mathrm{H}}}}(z)$ is transformed into an error on the linear JD matrix $\underline{\underline{\tilde{\mathrm{W}}}}(z)$. Developing (6.2), we get

$$\begin{aligned}\underline{\underline{\hat{\mathrm{W}}}}(z) &\approx \sigma_I^2 \left[\underline{\underline{\mathrm{H}}}^H(\frac{1}{z^*}) + \underline{\underline{\tilde{\mathrm{H}}}}^H(\frac{1}{z^*})\right] && (6.10)\\ &\quad \cdot \left\{\underline{\underline{\gamma}}_{\underline{\mathrm{R}}_0\underline{\mathrm{R}}_0}(z) + \sigma_I^2 \left[\underline{\underline{\mathrm{H}}}(z)\, \underline{\underline{\tilde{\mathrm{H}}}}^H(\frac{1}{z^*}) + \underline{\underline{\tilde{\mathrm{H}}}}(z)\, \underline{\underline{\mathrm{H}}}^H(\frac{1}{z^*})\right]\right\}^{-1} \\ &\approx \underline{\underline{\mathrm{W}}}(z) + \sigma_I^2\, \underline{\underline{\tilde{\mathrm{H}}}}^H(\frac{1}{z^*})\, \underline{\underline{\gamma}}^{-1}_{\underline{\mathrm{R}}_0\underline{\mathrm{R}}_0}(z) && (6.11)\\ &\quad - \sigma_I^2\, \underline{\underline{\mathrm{H}}}^H(\frac{1}{z^*})\, \underline{\underline{\gamma}}^{-1}_{\underline{\mathrm{R}}_0\underline{\mathrm{R}}_0}(z)\, \sigma_I^2 \left[\underline{\underline{\mathrm{H}}}(z)\, \underline{\underline{\tilde{\mathrm{H}}}}^H(\frac{1}{z^*}) + \underline{\underline{\tilde{\mathrm{H}}}}(z)\, \underline{\underline{\mathrm{H}}}^H(\frac{1}{z^*})\right] \underline{\underline{\gamma}}^{-1}_{\underline{\mathrm{R}}_0\underline{\mathrm{R}}_0}(z)\end{aligned}$$

where the second order terms were neglected and the following matrix perturbation property was used :

$$\left(\underline{\underline{\mathrm{A}}} + \underline{\underline{\mathrm{a}}}\right)^{-1} \approx \underline{\underline{\mathrm{A}}}^{-1} - \underline{\underline{\mathrm{A}}}^{-1}\, \underline{\underline{\mathrm{a}}}\, \underline{\underline{\mathrm{A}}}^{-1} \tag{6.12}$$

for an arbitrary small perturbation $\underline{\underline{\mathrm{a}}}$ of a given matrix $\underline{\underline{\mathrm{A}}}$. The JD deviation matrix $\underline{\underline{\tilde{\mathrm{W}}}}(z)$ becomes

$$\begin{aligned}
\underline{\underline{\tilde{\mathrm{W}}}}(z) &\approx \left\{\left[\sigma_I^2\,\underline{\underline{\mathrm{E}}}_N - \underline{\underline{\mathrm{W}}}(z)\,\underline{\underline{\gamma}}_{\underline{\mathrm{R}}_0\underline{\mathrm{R}}_0}(z)\,\underline{\underline{\mathrm{W}}}^H(\frac{1}{z^*})\right]\,\underline{\underline{\tilde{\mathrm{H}}}}^H(\frac{1}{z^*})\right. \\
&- \left.\underline{\underline{\mathrm{W}}}(z)\,\underline{\underline{\tilde{\mathrm{H}}}}(z)\,\left[\sigma_I^2\,\underline{\underline{\mathrm{H}}}^H(\frac{1}{z^*})\right]\right\}\,\underline{\underline{\gamma}}^{-1}_{\underline{\mathrm{R}}_0\underline{\mathrm{R}}_0}(z) \qquad (6.13) \\
&\approx \underline{\underline{\gamma}}_{\epsilon\epsilon}(z)\,\underline{\underline{\tilde{\mathrm{H}}}}^H(\frac{1}{z^*})\,\underline{\underline{\gamma}}^{-1}_{\underline{\mathrm{R}}_0\underline{\mathrm{R}}_0}(z) - \underline{\underline{\mathrm{W}}}(z)\,\underline{\underline{\tilde{\mathrm{H}}}}(z)\,\underline{\underline{\mathrm{W}}}(z) \qquad (6.14)
\end{aligned}$$

in which (6.13) comes from the expression of the optimal linear JD in (5.53) and (6.14) comes from the expression of the optimal MMSE in (5.58).

The excess MSE due to channel estimation errors is obtained by introducing (6.14) into the second term of (6.9). This result is valid under the condition that the CE error $\underline{\underline{\tilde{\mathrm{H}}}}(z)$ is small with respect to the true channel $\underline{\underline{\mathrm{H}}}(z)$. If we make the additional assumption that the symbol estimation error $\underline{\epsilon}(z)$, obtained in the absence of a CE error, has a small variance, then the first term in (6.14) can be neglected, which provides a very tractable expression for the CE-related excess MSE :

$$\begin{aligned}
\Gamma_{\underline{\hat{\epsilon}}\underline{\hat{\epsilon}}}(0) &\approx \Gamma_{\underline{\epsilon}\underline{\epsilon}}(0) + \int_{-\pi}^{\pi}\left\{\underline{\underline{\mathrm{W}}}(e^{j\Omega})\,\underline{\underline{\tilde{\mathrm{H}}}}(e^{j\Omega})\,\left[\underline{\underline{\mathrm{W}}}^H(e^{j\Omega})\,\underline{\underline{\gamma}}_{\underline{\mathrm{R}}_0\underline{\mathrm{R}}_0}(e^{j\Omega})\,\underline{\underline{\mathrm{W}}}(e^{j\Omega})\right]\right. \\
&\quad .\ \left.\underline{\underline{\tilde{\mathrm{H}}}}^H(e^{j\Omega})\,\underline{\underline{\mathrm{W}}}^H(e^{j\Omega})\right\}\,\frac{\mathrm{d}\Omega}{2\pi} \qquad (6.15) \\
&\approx \Gamma_{\underline{\epsilon}\underline{\epsilon}}(0) + \int_{-\pi}^{\pi}\left\{\underline{\underline{\mathrm{W}}}(e^{j\Omega})\,\underline{\underline{\tilde{\mathrm{H}}}}(e^{j\Omega})\,\left[\sigma_I^2\,\underline{\underline{\mathrm{E}}}_N - \underline{\underline{\gamma}}_{\epsilon\epsilon}(e^{j\Omega})\right]\right. \\
&\quad .\ \left.\underline{\underline{\tilde{\mathrm{H}}}}^H(e^{j\Omega})\,\underline{\underline{\mathrm{W}}}^H(e^{j\Omega})\right\}\,\frac{\mathrm{d}\Omega}{2\pi} \qquad (6.16) \\
&\approx \Gamma_{\underline{\epsilon}\underline{\epsilon}}(0) + \sigma_I^2\int_{-\pi}^{\pi}\left\{\underline{\underline{\mathrm{W}}}(e^{j\Omega})\,\left[\underline{\underline{\tilde{\mathrm{H}}}}(e^{j\Omega})\,\underline{\underline{\tilde{\mathrm{H}}}}^H(e^{j\Omega})\right]\,\underline{\underline{\mathrm{W}}}^H(e^{j\Omega})\right\}\,\frac{\mathrm{d}\Omega}{2\pi}.
\end{aligned}$$

Let us model the CE error matrix $\underline{\underline{\tilde{\mathrm{H}}}}(z)$ as $M \times N$ mutually independent white Gaussian sequences of length $L+1$ and with equal variance σ_h^2. The average CE error cross-spectrum is then

$$\mathrm{E}\left\{\underline{\underline{\tilde{\mathrm{H}}}}(z)\,\underline{\underline{\tilde{\mathrm{H}}}}^H(z)\right\} = (L+1)\,N\,\sigma_h^2\,\underline{\underline{\mathrm{E}}}_M. \qquad (6.17)$$

Combining (6.15) and (6.17), the average MSE associated with the p-th subchannel is finally

$$\sigma^2_{\hat{\epsilon}_p} = \sigma^2_{\epsilon_p} + \sigma_I^2\,.\,(L+1)N\,.\,\sigma_h^2\sum_{n=-\infty}^{+\infty} w_p^2(n) \qquad (6.18)$$

where $w_p(n)$ is the p-th sequence of JD coefficients. The sum $\sum_n w_p^2(n)$ in (6.18) can be interpreted as the sensitivity of the linear MMSE JD with respect to CE errors. It is inversely proportional to the energy associated with subchannel p. If the coefficients $w_p(n)$ are large, then the channel estimation errors may be significantly magnified, resulting in large excess MSE. If, on the other hand, these coefficients are small, then we do not have significant error magnification. The CE error variance σ_h^2, that depends on the selected ML channel estimator, is proportional to the additive noise power. The product $\sigma_h^2 \sum_n w_p^2(n)$ is thus a representation of the inverse SNR available in the p-th subchannel.

These results can be extended to the decision-feedback JD. In that case, both the feedforward coefficients $\underline{\underline{\hat{W}}}_{df}(z) = \underline{\underline{W}}_{df}(z) + \underline{\underline{\tilde{W}}}_{df}(z)$ and the feedback coefficients $\underline{\underline{\hat{B}}}(z) = \underline{\underline{B}}(z) + \underline{\underline{\tilde{B}}}(z)$ can deviate from their optimal values as their computation is based on the non-ideal channel estimate $\underline{\underline{\hat{H}}}(z) = \underline{\underline{H}}(z) + \underline{\underline{\tilde{H}}}(z)$. Using the properties of the optimal DF-JD, it can be shown that the symbol error spectrum with imperfect channel knowledge is

$$\begin{aligned}\underline{\underline{\gamma}}_{\hat{\epsilon}\hat{\epsilon}}(z) = \underline{\underline{\gamma}}_{\epsilon\epsilon}(z) + \underline{\underline{B}}(z) \left[\underline{\underline{\tilde{W}}}(z)\, \underline{\underline{\gamma}}_{\underline{R}_0\underline{R}_0}(z)\, \underline{\underline{\tilde{W}}}^H(\frac{1}{z^*})\right] \underline{\underline{B}}^H(\frac{1}{z^*}) \\ + \underline{\underline{\tilde{B}}}(z)\, \underline{\underline{S}}_c^{-1}(z)\, \underline{\underline{\tilde{B}}}^H(\frac{1}{z^*}). \quad (6.19)\end{aligned}$$

where $\underline{\underline{S}}_c^{-1}(z)$ is defined in (5.56). There are two contributions to the excess MSE. The first one depends on the error on the linear MMSE JD coefficients $\underline{\underline{\tilde{W}}}(z)$, whose first-order approximation is given in (6.14). The second term involves the error on the feedback matrix coefficients $\underline{\underline{\tilde{B}}}(z)$. This error can be approximated as follows. Let $\underline{\underline{\hat{S}}}_c(z) = \underline{\underline{S}}_c(z) + \underline{\underline{\tilde{S}}}_c(z)$ be the key power spectrum (see (5.56)) based on the estimated channel $\underline{\underline{\hat{H}}}(z)$. The error on the estimated key power spectrum is

$$\underline{\underline{\tilde{S}}}_c(z) \approx \sigma_n^{-2} \left[\underline{\underline{\tilde{H}}}^H(\frac{1}{z^*})\, \underline{\underline{H}}(z) + \underline{\underline{H}}^H(\frac{1}{z^*})\, \underline{\underline{\tilde{H}}}(z)\right]. \quad (6.20)$$

The estimated feedback coefficients $\underline{\underline{\hat{B}}}(z)$ are obtained from the factorization of the estimated power spectrum $\underline{\underline{\hat{S}}}_c(z)$:

$$\underline{\underline{\hat{S}}}_c(z) = \underline{\underline{\hat{D}}}^H(\frac{1}{z^*})\, \underline{\underline{\hat{\Lambda}}}\, \underline{\underline{\hat{D}}}(z) \rightarrow \underline{\underline{\hat{B}}}(z) = \underline{\underline{\hat{D}}}(z). \quad (6.21)$$

The error on the key power spectrum $\underline{\underline{\tilde{S}}}_c(z)$ is related to the error on its spectral factor $\underline{\underline{\tilde{D}}}(z)$ as follows :

$$\underline{\underline{\tilde{S}}}_c(z) \approx \underline{\underline{D}}^H(\frac{1}{z^*})\,\underline{\underline{\Lambda}}\,\underline{\underline{\tilde{D}}}(z) + \underline{\underline{D}}^H(\frac{1}{z^*})\,\underline{\underline{\tilde{\Lambda}}}\,\underline{\underline{D}}(z) + \underline{\underline{\tilde{D}}}^H(\frac{1}{z^*})\,\underline{\underline{\Lambda}}\,\underline{\underline{D}}(z). \tag{6.22}$$

After left division of Equation (6.22) by $\underline{\underline{D}}^H(\frac{1}{z^*})$ and right division by $\underline{\underline{D}}(z)$, we get

$$\underline{\underline{D}}^{-H}(\frac{1}{z^*})\,\underline{\underline{\tilde{S}}}_c(z)\,\underline{\underline{D}}^{-1}(z) \approx \left[\underline{\underline{\Lambda}}\,\underline{\underline{\tilde{D}}}(z)\,\underline{\underline{D}}^{-1}(z)\right] + \left[\underline{\underline{\tilde{\Lambda}}}\right] + \left[\underline{\underline{D}}^H(\frac{1}{z^*})\,\underline{\underline{\tilde{D}}}^H(\frac{1}{z^*})\,\underline{\underline{\Lambda}}\right] \tag{6.23}$$

The first term in (6.23) is a strictly causal, monic and stable matrix transfer function. The zero-order term in its z-expansion is a lower triangular matrix with '0's on the main diagonal. The second term in (6.23) is a constant diagonal matrix. The third term is strictly anticausal. Actually, any power spectrum can be decomposed into a sum of three such terms. It follows the next expression for the error on the feedback JD coefficients :

$$\underline{\underline{\tilde{B}}}(z) = \underline{\underline{\tilde{D}}}(z) = \underline{\underline{\Lambda}}^{-1}\left[\underline{\underline{D}}^{-H}(\frac{1}{z^*})\,\underline{\underline{\tilde{S}}}_c(z)\,\underline{\underline{D}}^{-1}(z)\right]_+ \underline{\underline{D}}(z) \tag{6.24}$$

where $[x(z)]_+$ denotes the strictly causal part of the spectrum $x(z)$. Using (6.24) and (5.66), the second contribution to the excess MSE (last term in (6.19)) can finally be written as a function of the channel estimation error $\underline{\underline{\tilde{H}}}(z)$ as follows :

$$\underline{\underline{\tilde{B}}}(z)\,\underline{\underline{S}}_c^{-1}(z)\,\underline{\underline{\tilde{B}}}^H(\frac{1}{z^*}) \approx \underline{\underline{\Lambda}}^{-1}\left[\underline{\underline{D}}^{-H}(\frac{1}{z^*})\,\underline{\underline{\tilde{S}}}_c(z)\,\underline{\underline{D}}^{-1}(z)\right]_+ \underline{\underline{\Lambda}}^{-1} \left[\underline{\underline{D}}^{-H}(\frac{1}{z^*})\,\underline{\underline{\tilde{S}}}_c(z)\,\underline{\underline{D}}^{-1}(z)\right]_+^H \underline{\underline{\Lambda}}^{-1} \tag{6.25}$$

where $\underline{\underline{\tilde{S}}}_c(z)$ is given in (6.20).

6.2.2 Excess MSE due to timing synchronization errors

In first order approximation, one can write

$$\underline{\underline{H}}_{\underline{\varepsilon}}(z) \approx \underline{\underline{H}}_{\underline{0}}(z) + \underline{\underline{\dot{H}}}_{\underline{0}}(z)\,\mathrm{Diag}\left(\underline{\varepsilon}\right) + \frac{1}{2}\underline{\underline{\ddot{H}}}_{\underline{0}}(z)\,\mathrm{Diag}\left(\underline{\varepsilon}^2\right) \tag{6.26}$$

where Diag $(\underline{\varepsilon})$ is a $N \times N$ diagonal matrix containing the timing errors associated with the N subchannels, and $\underline{\underline{\dot{\mathrm{H}}}}_0(z)$ (resp $\underline{\underline{\ddot{\mathrm{H}}}}_0(z)$) contains the z-transformed sequences of equivalent channels first (resp. second) derivatives with respect to the sampling instant. Let us model the timing errors ε_k as zero-mean Gaussian variables with variance $\sigma^2_{\varepsilon_k}$. As the average timing errors are assumed to be equal to zero, the first-order terms are discarded in the next derivations, and only the second-order terms are considered.

The excess MSE due to timing synchronization errors is obtained by introducing (6.26) into the third term of (6.9), together with

$$\begin{aligned} \underline{\tilde{\mathrm{R}}}_{\underline{\varepsilon}}(z) &= \left[\underline{\underline{\mathrm{H}}}_{\underline{\varepsilon}}(z) - \underline{\underline{\mathrm{H}}}_0(z)\right] \underline{\mathrm{I}}(z) & (6.27)\\ \underline{\epsilon}(z) &= \left[\underline{\underline{\mathrm{E}}}_N - \underline{\underline{\mathrm{W}}}(z)\,\underline{\underline{\mathrm{H}}}_0(z)\right] \underline{\mathrm{I}}(z) + \text{additive noise.} & (6.28) \end{aligned}$$

Keeping only the second order terms, it comes

$$\begin{aligned} \gamma_{\underline{\hat{\epsilon}}\underline{\hat{\epsilon}}}(z) &\approx \gamma_{\underline{\epsilon}\underline{\epsilon}}(z) + \sigma_I^2 \left[\underline{\underline{\mathrm{W}}}(z)\,\underline{\underline{\dot{\mathrm{H}}}}_0(z)\,\mathrm{Diag}\left(\underline{\varepsilon}^2\right)\,\underline{\underline{\dot{\mathrm{H}}}}_0^H(\frac{1}{z^*})\,\underline{\underline{\mathrm{W}}}^H(\frac{1}{z^*})\right] \\ &+ \frac{1}{2}\sigma_I^2 \left\{ \left[\underline{\underline{\mathrm{E}}}_N - \underline{\underline{\mathrm{W}}}(z)\,\underline{\underline{\mathrm{H}}}_0(z)\right] \mathrm{Diag}\left(\underline{\varepsilon}^2\right)\,\underline{\underline{\ddot{\mathrm{H}}}}_0^H(\frac{1}{z^*})\,\underline{\underline{\mathrm{W}}}^H(\frac{1}{z^*}) \right. \\ &+ \left. \underline{\underline{\mathrm{W}}}(z)\,\underline{\underline{\ddot{\mathrm{H}}}}_0(z)\,\mathrm{Diag}\left(\underline{\varepsilon}^2\right) \left[\underline{\underline{\mathrm{E}}}_N - \underline{\underline{\mathrm{H}}}_0^H(\frac{1}{z^*})\,\underline{\underline{\mathrm{W}}}^H(\frac{1}{z^*})\right]\right\} \qquad (6.29) \end{aligned}$$

The third and fourth terms in (6.29) can be neglected if the nominal symbol errors $\underline{\epsilon}(z)$ are small. The timing-related excess MSE is then obtained by integrating the second term in (6.29) around the unit circle. The average symbol mean square errors are finally

$$\sigma^2_{\hat{\epsilon}_p} = \sigma^2_{\epsilon_p} + \sigma_I^2 \sum_{k'=1}^{K} \left[\sum_{n=-\infty}^{+\infty} \sum_{p' \in \mathcal{C}_{k'}} \dot{x}^2_{pp'}(n)\right] \sigma^2_{\varepsilon_{k'}} \qquad (6.30)$$

where $\dot{x}_{pp'}(n)$ are the first derivatives with respect to $\varepsilon_{k'}$ of the sequence of interference coefficients $x_{pp'}(n)$. The factor between brackets in (6.30) can be interpreted as the sensitivity of the p-th symbol error variance $\sigma^2_{\epsilon_p}$ with respect to the k'-th timing error $\varepsilon_{k'}$.

6.3 Sensitivity to timing offsets in a single-user system

The effect of a timing offset on the performance of a single-user FB-based transmission system has been analyzed in [63]. The present chapter extends these results by considering paraunitary filter banks and assuming an ideal half Nyquist pulse shaping filter in the transmitter, a static frequency selective channel, and various IIR receivers. The independence of the average timing sensitivity to the selected FB is demonstrated. This study is restricted to a single-user scenario. Actually, the results can be generalized easily to a multiuser system, but in that case, the global timing sensitivity is strongly dependent on the selected signature allocation.

6.3.1 Baseband FB modulation

6.3.1.1 Timing sensitivity

In all generality, the symbol estimate at the output of the detector can be written as :

$$\hat{I}_{p,\varepsilon}(n) = J_{p,\varepsilon}(n) + w_{p,\varepsilon}(n). \tag{6.31}$$

where $J_{p,\varepsilon}(n) = \sum_{p'=0}^{N-1} \sum_{m=-\infty}^{+\infty} x_{pp',\varepsilon}(m)\, I'_p(n-m)$ and $w_{p,\varepsilon}(n)$ represents the contribution of the additive noise.

The interference coefficients $x_{pp',\varepsilon}(m)$ may be obtained by sampling a given set of continuous-time interference waveforms $x_{pp',a}(t)$, that depend on the FB, the channel and the chosen detector, at the symbol rate, with a timing error ε:

$$x_{pp',\varepsilon}(m) = x_{pp',a}(mT + \varepsilon) \tag{6.32}$$

In the z domain, the estimation errors are:

$$\underline{\epsilon}_{\varepsilon}(z) = \hat{\underline{I}}_{\varepsilon}(z) - \underline{I}(z) = \left(\underline{\underline{X}}_{\varepsilon}(z) - \underline{\underline{E}}_N\right) \underline{I}(z) + \underline{W}_{\varepsilon}(z) \tag{6.33}$$

where matrix $\underline{\underline{X}}_{\varepsilon}(z)$ has element (p, p') given by the z-transform of the sequence $x_{pp',\varepsilon}(m)$. The error covariance matrix is given by

$$\underline{\underline{R}}_{\epsilon\epsilon}(\varepsilon) = \frac{1}{2\pi} \int_{-\pi}^{\pi} \underline{\underline{\gamma}}_{\epsilon_\varepsilon \epsilon_\varepsilon}(e^{j\Omega})\, d\Omega = \left[\underline{\underline{R}}_{JJ}(\varepsilon) + \underline{\underline{R}}_{ww}\right] + \underline{\underline{R}}_{II} - \left[\underline{\underline{R}}_{I\hat{I}}(\varepsilon) + \underline{\underline{R}}_{\hat{I}I}(\varepsilon)\right]. \tag{6.34}$$

The first two terms give the total variance of the symbol estimates built at the receiver, including the additive noise. The error variance on each output is now the sum of two contributions:

$$\sigma^2_{\epsilon_p} = x_p(\varepsilon)\, \sigma_I^2 + y_p\, \sigma_n^2 \tag{6.35}$$

The first term represents the residual interference between symbol streams, the ISI inside each symbol stream and the self-interference $(x_{pp,\varepsilon}(0) - 1)$.

The second term gives the contribution of the additive noise: its variance is independent of the timing error. The proportionality factors $x_p(\varepsilon)$ and y_p may be computed from equation (6.34). The interference factor may be decomposed into:

$$x_p(\varepsilon) = x_{p_1}(\varepsilon) + x_{p_2}(\varepsilon) + 1 \tag{6.36}$$

with the following definitions:

$$\begin{aligned} x_{p_1}(\varepsilon) &= \left(\frac{1}{2\pi} \int_{-\pi}^{\pi} \underline{\underline{\mathrm{X}}}_{\varepsilon}(e^{j\Omega}) \underline{\underline{\mathrm{X}}}_{\varepsilon}^{H}(e^{j\Omega})\, d\Omega \right)_{pp} \\ &= \sum_{m=-\infty}^{\infty} \sum_{p'=0}^{N-1} |x_{pp',\varepsilon}(m)|^2 \end{aligned} \tag{6.37}$$

$$x_{p_2}(\varepsilon) = -\left(\frac{1}{2\pi} \int_{-\pi}^{\pi} \underline{\underline{\mathrm{X}}}_{\varepsilon}(e^{j\Omega}) + \underline{\underline{\mathrm{X}}}_{\varepsilon}^{H}(e^{j\Omega})\, d\Omega \right)_{pp} = -2\, x_{pp,\varepsilon}(0) \tag{6.38}$$

For the receivers investigated in this paper, it can be shown that the $x_p(\varepsilon)$ functions are even, with a global minimum at 0. For small timing errors, the following approximation is valid:

$$x_p(\varepsilon) \approx x_p(0) + \frac{\varepsilon^2}{2} \ddot{x}_p(0), \qquad \ddot{x}_p(\varepsilon) = \frac{d^2 x_p(\varepsilon)}{d\varepsilon^2} \tag{6.39}$$

The signal to noise plus interference ratio (SINR) at the output of the p^{th} symbol stream is given by:

$$\rho_p(\varepsilon) = \frac{\sigma_I^2}{\sigma_{e_p}^2(\varepsilon)} \approx \frac{\sigma_I^2}{\sigma_I^2 \left[x_p(0) + \frac{\varepsilon^2}{2} \ddot{x}_p(0) \right] + y_p\, \sigma_n^2} \tag{6.40}$$

With the last approximation, the 3 dB loss offset is inversely proportional to the initial signal to noise ratio and to the second derivative:

$$\varepsilon_{p,3dB} \approx \sqrt{\frac{2}{\rho_p(0)\, \ddot{x}_p(0)}} \tag{6.41}$$

In the sequel, we propose to use this value $\ddot{x}_p(0)$ as a measurement of the timing sensitivity. We just need to remember that the real sensitivity also depends on the initial signal to noise ratio at perfect synchronization $\rho_p(0)$.

An interesting interpretation of this second derivative is obtained by observing that:

$$\ddot{x}_p(0) \approx 2 \sum_{p'=0}^{N-1} \sum_{n=-\infty}^{\infty} |\dot{x}_{pp',a}(nT)|^2 \tag{6.42}$$

In other words, the timing sensitivity is equal to the sum of the interference waveform squared slopes sampled at the symbol rate. The last approximation is valid if $x_{pp',a}(nT) \approx \delta(p-p')\delta(n)$, that is to say if the interference level is low.

Let us show that the coefficients $x_{p_1}(\varepsilon)$ can be expressed as the sum of a few sinusoïds. Using (6.37) and $\Omega = 2\pi fT$, we write:

$$x_{p_1}(\varepsilon) = \left(T \int_{-\frac{1}{2T}}^{\frac{1}{2T}} \underline{\underline{\mathrm{X}}}_{\varepsilon}(f) \underline{\underline{\mathrm{X}}}_{\varepsilon}^{H}(f)\, df \right)_{pp} \tag{6.43}$$

From (6.32), the discrete time spectra $\underline{\underline{\mathrm{X}}}_{\varepsilon}(f)$ are linked to the continuous time spectra $\underline{\underline{\mathrm{X}}}_{a}(f)$ by:

$$\underline{\underline{\mathrm{X}}}_{\varepsilon}(f) = \frac{1}{T} \sum_{n=-\infty}^{\infty} \underline{\underline{\mathrm{X}}}_{a}(f - \frac{n}{T})\, e^{2\pi j \varepsilon (f - \frac{n}{T})} \tag{6.44}$$

By substitution of (6.44) into (6.43), we get:

$$x_{p_1}(\varepsilon) = \left\{ \underline{\underline{\mathrm{R}}}_{xx}(0) + \sum_{\Delta n=1}^{M} 2\Re\left[e^{2\pi j \varepsilon \frac{\Delta n}{T}} \underline{\underline{\mathrm{R}}}_{xx}(\Delta n) \right] \right\}_{pp} \tag{6.45}$$

where the sequence of matrices $\underline{\underline{\mathrm{R}}}_{xx}(\Delta n)$ is defined as:

$$\underline{\underline{\mathrm{R}}}_{xx}(\Delta n) = \frac{1}{T} \int_{-\infty}^{\infty} \underline{\underline{\mathrm{X}}}_{a}(f)\, \underline{\underline{\mathrm{X}}}_{a}^{H}(f - \frac{\Delta n}{T}) df \tag{6.46}$$

and $M = \lfloor N(1+\alpha) \rfloor$. It has been explicitly assumed that the spectra $X_{pp'}(f)$, including the transmit filter, are zero for $|f| > \frac{1+\alpha}{2T_c}$.

The first contribution to the timing sensitivity is finally obtained as a sum:

$$\ddot{x}_{p_1}(0) = -(\frac{2\pi}{T_c})^2 \sum_{\Delta n=1}^{M} 2(\frac{\Delta n}{N})^2 \Re\left[\underline{\underline{\mathrm{R}}}_{xx}(\Delta n) \right]_{pp} \tag{6.47}$$

The second contribution to the timing sensitivity can also be expressed as a function of the continuous time spectra $\underline{\underline{\mathrm{X}}}_{a}(f)$:

$$\ddot{x}_{p_2}(0) = -2 \frac{d^2 x_{pp,a}(t)}{dt^2} = 2 \int_{-\infty}^{\infty} (2\pi f)^2 \left[\underline{\underline{\mathrm{X}}}_{a}(f) \right]_{pp} df \tag{6.48}$$

6.3.1.2 The matched filter receiver

The matched filter receiver has been introduced in Section 5.2. Notations are reminded here in a single-user context, and with an additional timing offset ε.

The continuous-time interference waveforms associated with a matched filter bank are

$$x_{pp'}(t) = h_p(-t) \otimes h_{p'}(t) \tag{6.49}$$

The matched filter outputs are obtained by first filtering the signal with $c(-t)$ in the analog domain and sampling the result at a rate $1/T_c$:

$$q_\varepsilon(n) = \left[r(t) \otimes c(-t)\right](nT_c + \varepsilon) \tag{6.50}$$

where ε is the timing offset caused by a non-perfect synchronization. The corresponding polyphase components $q_{\varepsilon,\rho}(n) = q_\varepsilon(nN + \rho)$ are expressed, with z transforms, as:

$$\underline{\mathrm{Q}}_\varepsilon(z) = \underline{\underline{\mathrm{G}}}_\varepsilon(z)\,\underline{\mathrm{V}}(z) + \underline{\mathrm{U}}_\varepsilon(z). \tag{6.51}$$

The polyphase matrix $\underline{\underline{\mathrm{G}}}_\varepsilon(z)$ is Toeplitz with element (i,j) given by the z transform of $g(nT + (i-j)T + \varepsilon)$. The noise vector spectrum $\underline{\underline{\gamma}}_\nu(z) = \frac{N_0}{2}\,\underline{\underline{\mathrm{G}}}_0(z)$ does not depend on the sampling phase thanks to the noise stationarity. The matched filter outputs are finally computed by passing the sequence $q_\varepsilon(n)$ through a bank of analysis filters matched to the synthesis bank:

$$\begin{aligned}
\hat{\underline{\mathrm{I}}}_\varepsilon(z) &= \underline{\underline{\mathrm{S}}}^H(\frac{1}{z^*})\,\underline{\mathrm{Q}}_\varepsilon(z) \\
&= \left(\underline{\underline{\mathrm{S}}}^H(\frac{1}{z^*})\,\underline{\underline{\mathrm{G}}}_\varepsilon(z)\,\underline{\underline{\mathrm{S}}}(z)\right)\,\underline{\mathrm{I}}(z) + \underline{\mathrm{W}}_\varepsilon(z) && (6.52)\\
&= \underline{\mathrm{J}}_\varepsilon(z) + \underline{\mathrm{W}}_\varepsilon(z) && (6.53)
\end{aligned}$$

with $\underline{\mathrm{W}}_\varepsilon(z) = \underline{\underline{\mathrm{S}}}^H(\frac{1}{z^*})\,\underline{\mathrm{U}}_\varepsilon(z)$. The matched filter estimation errors are defined by $\underline{\epsilon}_\varepsilon(z) = \hat{\underline{\mathrm{I}}}_\varepsilon(z) - \underline{\mathrm{I}}(z)$. Assuming a paraunitary FB, the error covariance spectrum writes:

$$\underline{\underline{\gamma}}_{\epsilon_\varepsilon\epsilon_\varepsilon}(z) = \underline{\underline{\mathrm{S}}}^H(\frac{1}{z^*})\left[\sigma_I^2\left(\underline{\underline{\mathrm{G}}}_\varepsilon(z) - \underline{\underline{\mathrm{E}}}_N\right)\left(\underline{\underline{\mathrm{G}}}_\varepsilon^H(\frac{1}{z^*}) - \underline{\underline{\mathrm{E}}}_N\right) + \sigma_n^2\,\underline{\underline{\mathrm{G}}}_0(z)\right]\underline{\underline{\mathrm{S}}}(z) \tag{6.54}$$

Equation (6.54) implies that the arithmetic mean of the error variances does not depend on the FB. As a consequence, we may expect that the average timing sensitivity $\frac{1}{N}\sum_{p=0}^{N-1}\ddot{x}_p(0)$ should also be independent of the FB. To check this, let us derive a more adequate form for the general results shown in (6.47) and (6.48).

The $\underline{\underline{\mathrm{R}}}_{JJ}$ covariance matrix appears to be:

$$\underline{\underline{\mathrm{R}}}_{JJ}(\varepsilon) = \frac{\sigma_I^2}{2\pi}\int_{-\pi}^{\pi} \underline{\underline{\mathrm{S}}}^H(e^{j\Omega})\left[\underline{\underline{\mathrm{G}}}_\varepsilon(e^{j\Omega})\underline{\underline{\mathrm{G}}}_\varepsilon^H(e^{j\Omega})\right]\underline{\underline{\mathrm{S}}}(e^{j\Omega})\,d\Omega \tag{6.55}$$

The channel polyphase matrix $\underline{\underline{\mathrm{G}}}_\varepsilon(e^{j\Omega})$ is derived from the analog channel transmittance $G(f)$ as:

$$\left[\underline{\underline{\mathrm{G}}}_\varepsilon(e^{j\Omega})\right]_{pq} = \frac{1}{T}\sum_{n=-\infty}^{+\infty} G(f-\frac{n}{T})\,e^{2\pi j(\varepsilon+[p-q]T)(f-\frac{n}{T})} \tag{6.56}$$

It follows:

$$\begin{aligned}
\left[\underline{\underline{\mathrm{G}}}_\varepsilon(e^{j\Omega})\,\underline{\underline{\mathrm{G}}}_\varepsilon^H(e^{j\Omega})\right]_{pq} &= \sum_{k=1}^{N}\left[\underline{\underline{\mathrm{G}}}_\varepsilon(e^{j\Omega})\right]_{pk}\left[\underline{\underline{\mathrm{G}}}_\varepsilon^*(e^{j\Omega})\right]_{qk}\\
&= \frac{1}{T^2}\sum_{k=1}^{N}\sum_{n=-\infty}^{\infty}\sum_{\Delta n=-\infty}^{+\infty} G(f-\frac{n}{T})G(f-\frac{n}{T}-\frac{\Delta n}{T})\\
&\qquad e^{2\pi j\varepsilon\frac{\Delta n}{T}}\,e^{2\pi jT_c(p-k)(f-\frac{n}{T})}\,e^{2\pi jT_c(k-q)(f-\frac{n}{T}-\frac{\Delta n}{T})}\\
&= \frac{1}{T^2}\sum_{\Delta n=-M}^{M} e^{2\pi j\varepsilon\frac{\Delta n}{T}}\left[\sum_{n=-\infty}^{\infty} G(f-\frac{n}{T})G(f-\frac{n}{T}-\frac{\Delta n}{T})\right.\\
&\qquad\left. e^{2\pi jT_c(p-q)(f-\frac{n}{T})}\left(\sum_{k=1}^{N} e^{2\pi j(k-q)(-\frac{\Delta n}{N})}\right)\right]
\end{aligned} \tag{6.57}$$

Using the following property:

$$\sum_{k=1}^{N} e^{2\pi j(k-q)(-\frac{\Delta n}{N})} = \begin{cases} N & \text{if } \Delta n = lN, l\in\mathcal{Z} \\ 0 & \text{otherwise}\end{cases}\,, \tag{6.58}$$

it appears that the non-zero terms in the last equation are limited to $\Delta n = 0, \pm N$. That is,

$$\underline{\underline{\mathrm{G}}}_\varepsilon(e^{j\Omega})\,\underline{\underline{\mathrm{G}}}_\varepsilon^H(e^{j\Omega}) = \underline{\underline{\mathrm{R}}}_{gg}(e^{j\Omega}) + e^{2\pi j\frac{\varepsilon}{T_c}}\,\underline{\underline{\mathrm{R}}}_{gg+}(e^{j\Omega}) + e^{-2\pi j\frac{\varepsilon}{T_c}}\,\underline{\underline{\mathrm{R}}}_{gg-}(e^{j\Omega}) \tag{6.59}$$

where the following polyphase matrices are defined:

- $\underline{\underline{\mathrm{R}}}_{gg}(e^{j\Omega})$ is the polyphase matrix of $\frac{1}{T_c}(g(t) \otimes g(t))$
- $\underline{\underline{\mathrm{R}}}_{gg+}(e^{j\Omega})$ is the polyphase matrix of $\frac{1}{T_c}(g(t) \otimes g(t)e^{2\pi j \frac{t}{T_c}})$
- $\underline{\underline{\mathrm{R}}}_{gg-}(e^{j\Omega})$ is the polyphase matrix of $\frac{1}{T_c}(g(t) \otimes g(t)e^{-2\pi j \frac{t}{T_c}})$

The last two matrices are non zero only if the excess bandwidth α is non zero. For parity reasons, computation of equation (6.55) simplifies into:

$$\begin{aligned}
\underline{\underline{\mathrm{R}}}_{JJ}(\varepsilon) = & \left[\frac{\sigma_I^2}{2\pi}\int_{-\pi}^{\pi} \underline{\underline{\mathrm{S}}}^H(e^{j\Omega})\,\underline{\underline{\mathrm{R}}}_{gg}(e^{j\Omega})\,\underline{\underline{\mathrm{S}}}(e^{j\Omega})\,d\Omega\right] \\
& + 2\cos(\frac{2\pi\varepsilon}{T_c})\left[\frac{\sigma_I^2}{2\pi}\int_{-\pi}^{\pi} \underline{\underline{\mathrm{S}}}^H(e^{j\Omega})\,\underline{\underline{\mathrm{R}}}_{gg_c}(e^{j\Omega})\,\underline{\underline{\mathrm{S}}}(e^{j\Omega})\,d\Omega\right] \\
& = \underline{\underline{\mathrm{R}}}_{JJ}(0) + 2(\cos(\frac{2\pi\varepsilon}{T_c}) - 1) \\
& \left[\frac{\sigma_I^2}{2\pi}\int_{-\pi}^{\pi} \underline{\underline{\mathrm{S}}}^H(e^{j\Omega})\,\underline{\underline{\mathrm{R}}}_{gg_c}(e^{j\Omega})\,\underline{\underline{\mathrm{S}}}(e^{j\Omega})\,d\Omega\right]
\end{aligned}$$

where $\underline{\underline{\mathrm{R}}}_{gg_c}(e^{j\Omega})$ is defined as the polyphase matrix of $\frac{1}{T}(g(t)\otimes g(t)\cos(2\pi\frac{t}{T_c}))$. By comparison with the general expression (6.45), we observe that the use of a paraunitary FB reduces the size of the summation to only one term.

The second derivative of the continuous time interference waveforms can be expressed as:

$$\left.\frac{d^2 x_{pp,a}(t)}{dt^2}\right|_{t=0} = \frac{1}{2\pi}\int_{-\pi}^{\pi}\left[\underline{\underline{\mathrm{S}}}^H(e^{j\Omega})\underline{\underline{\mathrm{R}}}_{\ddot{g}}(e^{j\Omega})\underline{\underline{\mathrm{S}}}(e^{j\Omega})\right]_{pp} d\Omega \tag{6.60}$$

where $\underline{\underline{\mathrm{R}}}_{\ddot{g}}(e^{j\Omega})$ is the polyphase matrix of $\ddot{g}(t)$. An alternative expression is obtained from (6.49):

$$\left.\frac{d^2 x_{pp,a}(t)}{dt^2}\right|_{t=0} = \int_{-\infty}^{\infty}(2\pi j f)^2|H_p(f)|^2\,df = -W_p^2\frac{\mathcal{E}_p}{\sigma_I^2} \tag{6.61}$$

where $\mathcal{E}_p$ and W_p^2 are the received symbol energy and mean square bandwidth defined in (4.32) and (4.33).

Using these results, we can now compute the second derivative of the error covariance matrix with respect to the timing offset, and derive the timing sensitivity for each symbol stream $\ddot{x}_p(0)$:

$$\ddot{\underline{\underline{\mathrm{x}}}}_p(0) = \mathrm{diag}\left(\frac{1}{\pi}\int_{-\pi}^{\pi}\underline{\underline{\mathrm{S}}}^H(e^{j\Omega})\left[(\frac{2\pi}{T_c})^2\underline{\underline{\mathrm{R}}}_{gg_c}(e^{j\Omega}) - \underline{\underline{\mathrm{R}}}_{\ddot{g}}(e^{j\Omega})\right]\underline{\underline{\mathrm{S}}}(e^{j\Omega})d\Omega\right) \tag{6.62}$$

From the last expression, we conclude again that the average timing sensitivity does not depend on the selected FB, as already expected.

6.3.1.3 Baseband PAM and AWGN channel

Let us analyse in more details the general result presented above on a simple example: a single baseband PAM modulation ($N = 1$, $\underline{\underline{S}}(z) = 1$) and a frequency-flat channel channel ($c(t) = \delta(t - \tau)$). In this scenario, the channel correlation corresponds to a full raised cosine filter. The corresponding spectrum $G(f)$ is recalled here for convenience:

$$G(f) = \begin{cases} T_c & |f| < f_1 \\ \frac{T_c}{2}\left(1 + \cos\left[\frac{\pi T_c}{\alpha}(|f| - f_1)\right]\right) & f_1 \le |f| \le f_2 \\ 0 & |f| > f_2 \end{cases} \tag{6.63}$$

with $f_1 = \frac{1-\alpha}{2T_c}$ and $f_2 = \frac{1+\alpha}{2T_c}$, α being the roll-off factor. The received symbol energy is $Es = \sigma_I^2 \int_{-\infty}^{\infty} G(f)\, df = \sigma_I^2$. At perfect synchronism, the interference disappears and we get $\rho(0) = \sigma_I^2/\sigma_n^2$.

Equation (6.45) becomes:

$$\begin{aligned} x_{p_1}(\varepsilon) &= \left[\frac{1}{T_c}\int_{-\infty}^{\infty} |G(f)|^2\, df\right] + 2\cos(\frac{2\pi\varepsilon}{T_c})\left[\frac{1}{T_c}\int_{-\infty}^{\infty} G(f)G^*(f - \frac{1}{T_c})\, df\right] \\ &= (1 - \frac{\alpha}{4}) + \frac{\alpha}{4}\cos(\frac{2\pi\varepsilon}{T_c}) \end{aligned} \tag{6.64}$$

where (6.63) has been used to obtain the last expression. The first contribution to the timing sensitivity is thus:

$$\ddot{x}_{p_1}(0) = -(\frac{2\pi}{T_c})^2\, \frac{\alpha}{4} \tag{6.65}$$

Equation (6.48) simplifies into:

$$\ddot{x}_{p_2}(0) = 2\int_{-\infty}^{\infty} (2\pi f)^2\, G(f)\, df = (\frac{2\pi}{T_c})^2 \left[(\frac{1}{2} - \frac{4}{\pi^2})\alpha^2 + \frac{1}{6}\right] = 2W^2 \tag{6.66}$$

using (6.63).

These results are illustrated on figure 6.1. The dotted line gives the evolution of the term (6.66) with α: it appears that the concavity of the Nyquist waveform at the origin increases with the rolloff. The continuous line gives the total timing sensitivity $\ddot{x}_p(0)$, which decreases with the rolloff. With

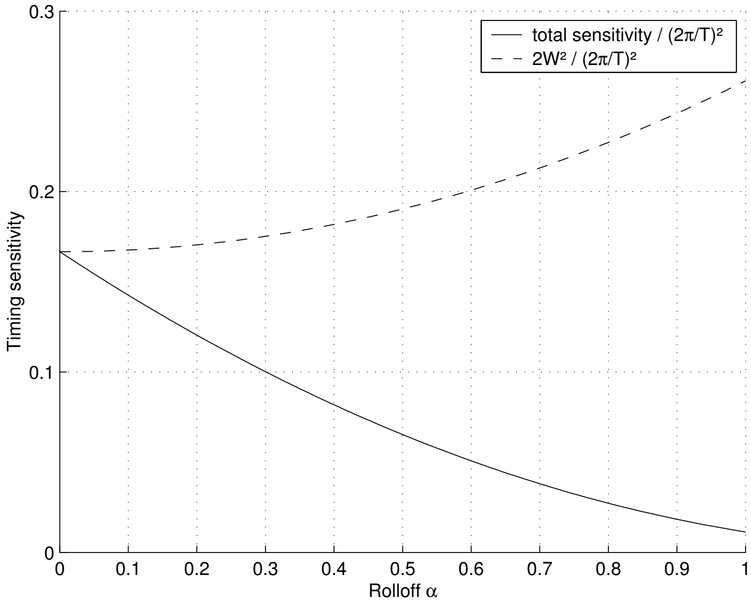

Figure 6.1: *Timing sensitivity vs. roll-off for a single PAM modulation*

the interpretation given in (6.42), this reflects the decrease of the Nyquist waveform slopes around the zero-crossing points at higher α.

Figure 6.2 gives the profile of the SINR $\rho(\varepsilon)$ as a function of the relative timing error ε/T_c. The different sets of curves correspond to various levels of additive noise: $\rho(0) = 10$ to 50 dB with a 5 dB step. Following (6.41), the timing sensitivity is highly dependent on this parameter. The different line styles correspond to distinct roll-off values: $\alpha = 0.1$, 0.3 and 0.5. A larger sensitivity at low α can be observed on the curves.

6.3.1.4 DMT and Hadamard modulations

Let us now investigate the effect of a timing error on DMT and Hadamard transmission schemes, with the simple AWGN channel.

Intuitively, we may expect a higher timing sensitivity for the higher tones and the codes with many transitions, as their spectrum is located at higher frequencies. This is true for the term $\ddot{x}_{p_2}(0) = 2W_p^2$. But concerning the first term $\ddot{x}_{p_1}(0)$, the effect is inverted: filters with higher spectral components will be more influenced by the roll-off region, and the resulting timing sensitivity is decreased. In the light of (6.42), this means that the

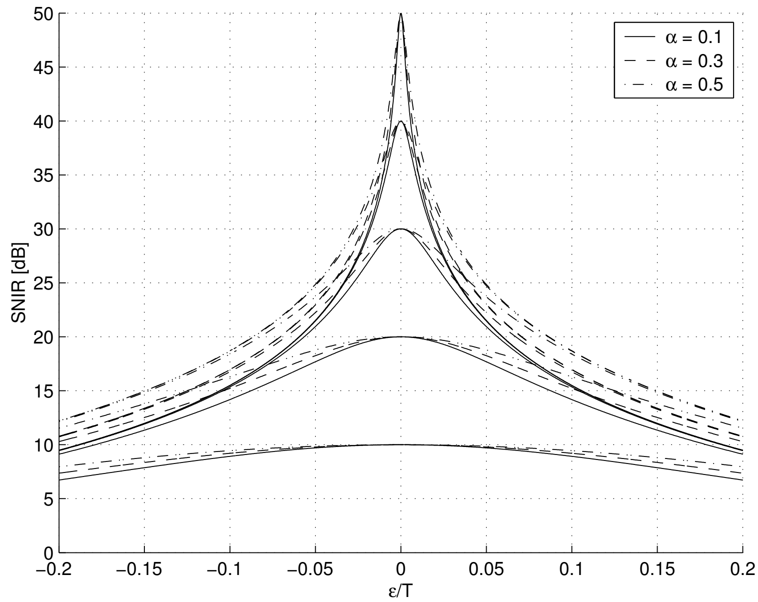

Figure 6.2: *SINR vs. timing error for a single PAM modulation*

average squared slopes of the interference waveforms actually decrease for the higher tones and the codes with more transitions, due to the roll-off effect.

Figure 6.3 gives the timing sensitivity profile vs. the tone index p for a DMT 512 transmission scheme. As expected, we observe an increase for the second term $\ddot{x}_p(0)$ (upper curves). The total sensitivity (lower curves) first increases with the tone index, and finally decreases for the higher tones. This effect appears faster at high roll-off values. The curves corresponding to sine and cosine filters are almost superimposed, with an exact matching for $p = N/2$.

Figure 6.4 gives the same results for a Hadamard 512 FB transmission scheme. The codes are ordered with their spectral content: the first code has no transition, while the last code has the highest number of transitions.

In both schemes, and for any roll-off factor α, it can be verified that the average $\ddot{x}_p$ corresponds to the single PAM value reported on figure 6.1.

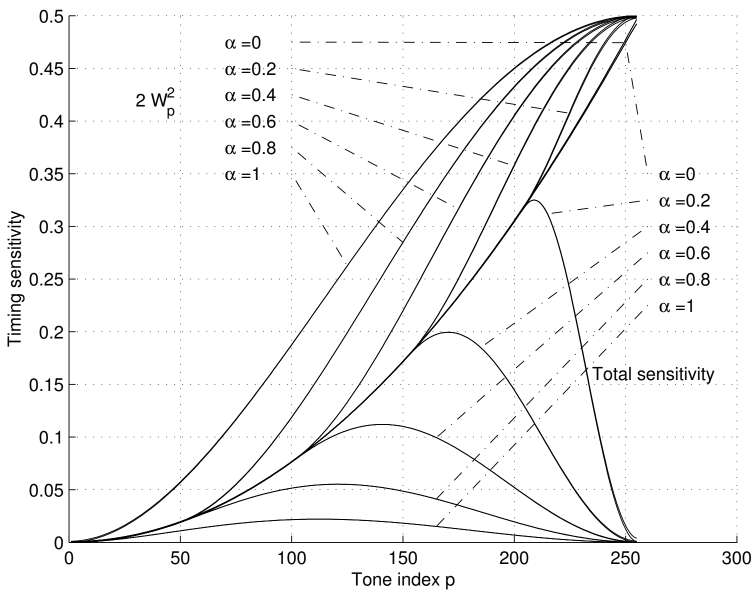

Figure 6.3: *Timing sensibility vs. tone index for a DMT 512 FB scheme*

6.3.1.5 MMSE receivers

Let us now analyze the timing error sensitivity associated with IIR MMSE equalizers. The equalizers are computed at modem start-up by assuming perfect synchronism.

For a paraunitary FB $\underline{\underline{S}}(z)$, it can be shown that the estimation error covariance spectrum writes:

$$\underline{\underline{\gamma}}_{\underline{\epsilon}_\varepsilon \underline{\epsilon}_\varepsilon}(z) = \underline{\underline{B}}(z)\, \underline{\underline{S}}^H(\frac{1}{z^*}) \left[\underline{\underline{\gamma}}^{(0)}_{\underline{\epsilon}_\varepsilon \underline{\epsilon}_\varepsilon}(z)\right] \underline{\underline{S}}(z)\, \underline{\underline{B}}^H(\frac{1}{z^*}) \tag{6.67}$$

with

$$\begin{aligned} \underline{\underline{\gamma}}^{(0)}_{\underline{\epsilon}_\varepsilon \underline{\epsilon}_\varepsilon}(z) = \Bigg[& \sigma_I^2 \left(\underline{\underline{S}}_{c_0}^{-1}(z)\, \underline{\underline{G}}_\varepsilon(z) - \underline{\underline{E}}_N\right) \left(\underline{\underline{G}}_\varepsilon^H(\frac{1}{z^*})\, \underline{\underline{S}}_{c_0}^{-1}(z) - \underline{\underline{E}}_N\right) \\ & + \sigma_n^2\, \underline{\underline{S}}_{c_0}^{-1}(z)\, \underline{\underline{G}}_0(z)\, \underline{\underline{S}}_{c_0}^{-1}(z) \Bigg] \end{aligned} \tag{6.68}$$

and

$$\underline{\underline{S}}_{c_0}(z) = \sigma_I^{-2}\, \underline{\underline{E}}_N + \frac{2}{N_0}\, \underline{\underline{G}}_0(z). \tag{6.69}$$

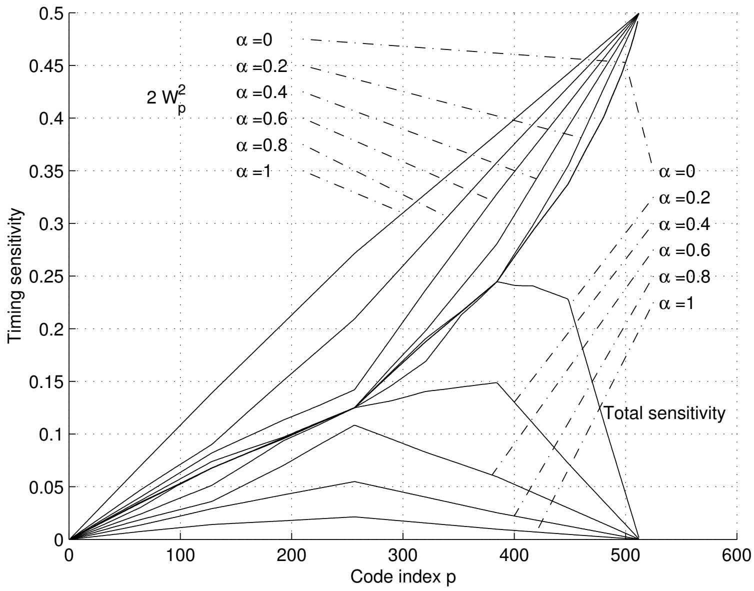

Figure 6.4: *Timing sensibility vs. code index for a Hadamard 512 FB scheme*

As pointed out in Section 1.3.3, it is known that the arithmetic mean of the error variances at the output of a linear JD ($\underline{\underline{\mathrm{B}}}(z) = \underline{\underline{\mathrm{E}}}_N$) is independent of the selected FB. Equation (6.67) shows that this property remains valid even in the presence of an arbitrary timing error ε.

We finally provide a way to compute the timing sensitivity of the presented MMSE receivers:

$$\underline{\ddot{\mathrm{x}}}_p(0) = \mathrm{diag}\left(\frac{1}{\pi}\int_{-\pi}^{\pi} \underline{\underline{\mathrm{B}}}(e^{j\Omega})\,\underline{\underline{\mathrm{S}}}^H(e^{j\Omega})\,\underline{\underline{\mathrm{S}}}_{\ddot{g}}(e^{j\Omega})\,\underline{\underline{\mathrm{S}}}(e^{j\Omega})\,\underline{\underline{\mathrm{B}}}^H(e^{j\Omega})d\Omega\right) \quad (6.70)$$

with

$$\underline{\underline{\mathrm{S}}}_{\ddot{g}}(e^{j\Omega}) = \left[(\frac{2\pi}{T_c})^2\,\underline{\underline{\mathrm{S}}}_{c_0}^{-1}(e^{j\Omega})\,\underline{\underline{\mathrm{R}}}_{gg_c}(e^{j\Omega})\,\underline{\underline{\mathrm{S}}}_{c_0}^{-1}(e^{j\Omega}) - \underline{\underline{\mathrm{S}}}_{c_0}^{-1}(e^{j\Omega})\,\underline{\underline{\mathrm{R}}}_{\ddot{g}}(e^{j\Omega})\right] \quad (6.71)$$

From (6.70), it appears that the average timing sensitivity is independent of the selected FB in the linear case.

6.3.2 Extension to CAP FB modulation

6.3.2.1 The matched filter receiver

To implement a FB-CAP matched filter receiver, the outputs of two quadrature matched filters are first sampled at a rate $1/T_c$ with a timing error ε :

$$\begin{pmatrix} q_{a,\varepsilon}(n) \\ q_{b,\varepsilon}(n) \end{pmatrix} = \left[\begin{pmatrix} c(-t) \\ \tilde{c}(-t) \end{pmatrix} \otimes r(t) \right] (nT_c + \varepsilon). \qquad (6.72)$$

The polyphase components of the sequences $q_{a,\varepsilon}(n)$ and $q_{b,\varepsilon}(n)$ are given by

$$\left[\begin{array}{c} \underline{\mathrm{Q}}_{a,\varepsilon}(z) \\ \underline{\mathrm{Q}}_{b,\varepsilon}(z) \end{array} \right] = \left[\begin{array}{cc} \underline{\underline{\mathrm{G}}}_{\varepsilon}(z) & \underline{\underline{\tilde{\mathrm{G}}}}_{\varepsilon}(z) \\ -\underline{\underline{\tilde{\mathrm{G}}}}_{\varepsilon}(z) & \underline{\underline{\mathrm{G}}}_{\varepsilon}(z) \end{array} \right] \left[\begin{array}{c} \underline{\mathrm{V}}_a(z) \\ \underline{\mathrm{V}}_b(z) \end{array} \right] + \left[\begin{array}{c} \underline{\mathrm{U}}_{a,\varepsilon}(z) \\ \underline{\mathrm{U}}_{b,\varepsilon}(z) \end{array} \right] \qquad (6.73)$$

where $\underline{\underline{\mathrm{G}}}_{\varepsilon}(z)$ and $\underline{\underline{\tilde{\mathrm{G}}}}_{\varepsilon}(z)$ are the polyphase matrices associated with the waveforms $g(t)$ and $\tilde{g}(t)$, respectively, with

$$\begin{array}{lllllll} g(t) & = & c(t) \otimes c(-t) & = & \tilde{c}(t) \otimes \tilde{c}(-t) & = & [\Gamma_f(t)\, \cos(\omega_0 t)] \otimes \Gamma_c(t) \\ \tilde{g}(t) & = & \tilde{c}(t) \otimes c(-t) & = & -c(t) \otimes \tilde{c}(-t) & = & [\Gamma_f(t)\, \sin(\omega_0 t)] \otimes \Gamma_c(t) \end{array} \qquad (6.74)$$

where $\Gamma_f(t)$ and $\Gamma_c(t)$ are the baseband Nyquist pulse and physical channel autocorrelation functions, respectively.

The matched filter outputs are finally obtained by using a bank of analysis filters:

$$\left[\begin{array}{c} \underline{\hat{\mathrm{I}}}_{a,\varepsilon}(z) \\ \underline{\hat{\mathrm{I}}}_{b,\varepsilon}(z) \end{array} \right] = \underline{\underline{\mathrm{S}}}^H(\frac{1}{z^*}) \left[\begin{array}{c} \underline{\mathrm{Q}}_{a,\varepsilon}(z) \\ \underline{\mathrm{Q}}_{b,\varepsilon}(z) \end{array} \right] = \left[\begin{array}{c} \underline{\mathrm{J}}_{a,\varepsilon}(z) \\ \underline{\mathrm{J}}_{b,\varepsilon}(z) \end{array} \right] + \left[\begin{array}{c} \underline{\mathrm{W}}_{\varepsilon}(z) \\ \underline{\tilde{\mathrm{W}}}_{\varepsilon}(z) \end{array} \right] \qquad (6.75)$$

Using the paraunitary property, the error covariance spectra write:

$$\underline{\underline{\gamma}}_{\epsilon_{a,\varepsilon}\epsilon_{a,\varepsilon}}(z) = \underline{\underline{\mathrm{S}}}^H(\frac{1}{z^*}) \left\{ \sigma_I^2 \left[\left(\underline{\underline{\mathrm{G}}}_{\varepsilon}(z) - \underline{\underline{\mathrm{E}}}_N \right) \left(\underline{\underline{\mathrm{G}}}^H_{\varepsilon}(\frac{1}{z^*}) - \underline{\underline{\mathrm{E}}}_N \right) \right.\right.$$
$$\left.\left. + \underline{\underline{\tilde{\mathrm{G}}}}_{\varepsilon}(z)\, \underline{\underline{\tilde{\mathrm{G}}}}^H_{\varepsilon}(\frac{1}{z^*}) \right] + \sigma_n^2\, \underline{\underline{\mathrm{G}}}_0(z) \right\} \underline{\underline{\mathrm{S}}}(z) = \underline{\underline{\gamma}}_{\epsilon_{b,\varepsilon}\epsilon_{b,\varepsilon}}(z) \qquad (6.76)$$

It appears again that the average error variance does not depend on the selected FB. Furthermore, for a given basis function p selected in the FB, the same error variance is obtained on each of the quadrature components a and b. An explicit expression of the $\underline{\underline{\mathrm{R}}}_{JJ}(\varepsilon)$ covariance matrix that appears in the error variance equation can be found as in the baseband scenario. The result is:

$$\underline{\underline{\mathrm{R}}}_{JJ}(\varepsilon) = \underline{\underline{\mathrm{R}}}_{JJ}(0) + 2(\cos(\frac{2\pi\varepsilon}{T_c}) - 1) \left[\frac{\sigma_I^2}{2\pi} \int_{-\pi}^{\pi} \underline{\underline{\mathrm{S}}}^H(e^{j\Omega}) \left[\underline{\underline{\mathrm{R}}}_{gg_c}(e^{j\Omega}) + \underline{\underline{\mathrm{R}}}_{\tilde{g}\tilde{g}_c}(e^{j\Omega}) \right] \underline{\underline{\mathrm{S}}}(e^{j\Omega})\, d\Omega \right] \quad (6.77)$$

The resulting timing sensitivity can be derived consequently.

6.3.2.2 Single CAP and AWGN channel

Considering a single CAP transmission scheme ($N = 1$) and a frequency flat physical channel, the channel correlation corresponds to a cosine modulated full raised cosine filter $g_c(t)$. The corresponding spectrum $G_c(f)$ and its Hilbert transform $\tilde{G}_c(f)$ are:

$$\begin{aligned} G_c(f) &= \frac{1}{2}\left[G(f - f_0) + G(f + f_0)\right] \\ \tilde{G}_c(f) &= \frac{j}{2}\left[-G(f - f_0) + G(f + f_0)\right] \end{aligned} \quad (6.78)$$

with $G(f)$ given in (6.63). This implies the following property, which can be checked easily:

$$\int_{-\infty}^{\infty} G_c(f)\, G_c(f-\Delta_f) + \tilde{G}_c(f)\, \tilde{G}_c(f-\Delta_f)\, df = \int_{-\infty}^{\infty} G(f)\, G(f-\Delta_f) \quad (6.79)$$

We first compute the noise-free estimate variance $\sigma^2_{J_p}(\varepsilon)$ as a function of the timing error:

$$\begin{aligned} x_{p_1}(\varepsilon) = \frac{\sigma_J^2(\varepsilon)}{\sigma_I^2} &= \left[\frac{1}{T_c} \int_{-\infty}^{\infty} |G_c(f)|^2 + |\tilde{G}_c(f)|^2\, df \right] \\ &+ 2\cos(\frac{2\pi\varepsilon}{T_c}) \left[\frac{1}{T_c} \int_{-\infty}^{\infty} G_c(f) G_c^*(f - \frac{1}{T_c}) + \tilde{G}_c(f) \tilde{G}_c^*(f - \frac{1}{T_c})\, df \right] \\ &= (1 - \frac{\alpha}{4}) + \frac{\alpha}{4}\cos(\frac{2\pi\varepsilon}{T_c}) \end{aligned} \quad (6.80)$$

using (6.63) and (6.79). This result is exactly the same as in the baseband PAM scenario (6.64): the CAP modulation has no influence on $\sigma_J^2(\varepsilon)$. The corresponding contribution to the timing sensitivity is given by (6.65).

The second contribution to the timing sensitivity is computed as follows:

$$\ddot{x}_{p_2}(0) = 2\int_{-\infty}^{\infty}(2\pi f)^2\, G_c(f)\, df \tag{6.81}$$

$$= (\frac{2\pi}{T_c})^2\left[(\frac{1}{2}-\frac{4}{\pi^2})\alpha^2+\frac{1}{6}\right]+2\,(2\pi f_0)^2 = 2W^2 \tag{6.82}$$

Here the effect of the CAP modulation is sensible : a new term is added, which increases the original timing sensitivity proportionally to the square of the carrier frequency. This is obvious as the modulated interference waveform contains higher spectral components.

6.4 Conclusion

In this Chapter, it has been shown how the performance computation of the MMSE joint detectors introduced in Chapter 5 could be refined to take into account the respective effects of non-ideal timing synchronization and non-ideal channel estimation. These effects translate into an excess mean square error (MSE) at the output of the joint detector. For a steady-state system operating at high SNR, these effects are just second-order effects. The derivation of the excess MSE is interesting, however, as it reflects the robustness of the considered system against timing and channel estimation errors. Equations (6.18) and (6.30) give the respective approximate excess MSE obtained at high SNR (i.e. when the nominal symbol estimation errors are small) : these expressions allow an intuitive interpretation.

The concept of timing sensitivity has been further developed in a single-user context. The variance of the symbol estimation error at the output of a given detector varies with the timing error ε, with a global minimum for $\varepsilon = 0$. The second-order derivative of this function with respect to the timing error can thus be interpreted as a timing sensitivity. The timing sensitivity has been shown to be equivalent to the sum of the interference waveform squared slopes sampled at the symbol rate. The average timing sensitivity of a given paraunitary FB-based system has been shown to be independent of the selected FB (at least for the matched filter and linear MMSE receivers). Finally, the distribution of timing sensitivities as a function of the signature index has been analyzed for the DMT and Hadamard filter banks, for different values of the shaping filter roll-off.

Chapter 7

Timing synchronization

7.1 Introduction

The problem under consideration in this chapter is that of network timing synchronization at the level of the head-end. During the acquisition phase, the joint detector is optimized for the sampling phase at which the received signal is sampled at this time, and also for the K phases at which the chip-rate sequences are transmitted by the K users. The joint detector is assumed to be non-adaptive : its coefficients are constant. During the transmission, the system is in tracking phase : a synchronization mechanism is responsible to keep the sampling phase at the receiver and the K phases of the transmitters as close as possible to the nominal values for which the joint detector has been designed. The user-specific misalignment cannot be compensated by the common receiver clock: the timing error information has to be sent back to the user modems via the downlink.

In the present chapter we design a generic decision-directed (DD) multiuser timing estimator for the maximum likelihood (ML) criterion and compute the associated Cramèr-Rao bound (CRB). We also derive practical timing error detectors (TEDs) suited to multiuser FB-based transmission. Throughout this chapter, *the decision error rate is assumed to be very low*, so that the true symbols $I_p(n)$ are used rather than the decisions. The performance of the timing error detectors considered in this chapter has then to be considered as an upper bound on the true performance that should take the effect of wrong decisions into account.

7.2 Asynchronous FB-based multiple access

In Chapter 4, the FB-based multiple access model was presented in a perfectly synchronous context, i.e. with the assumption that the K transmitter clocks and the unique receiver clock were perfectly aligned during the whole duration of the transmission. In this section, we revisit the multiple access model by introducing $K+1$ delays τ_k^t and τ^r associated with the different clocks. The delay τ^r corresponds to the receiver clock while the remaining delays τ_1^t up to τ_K^t are related to the different transmitter clocks. As these clocks are physically distributed in different locations in the network, the associated delays are a priori independent.

The continuous-time signal transmitted by each user (4.23) becomes :

$$x_{k,\tau_k^t}(t) = \sum_{n=-\infty}^{+\infty} v_k(n)\, p(t - nT_c + \tau_k^t) \tag{7.1}$$

where $v_k(n)$ is the user-specific chip rate sequence obtained at the output of the FB (see (4.3)). The delays τ_k^t are assumed to be close to their nominal values which correspond to the desired user alignments.

After propagation over the multiuser channel, the received signal is sampled at a fractional rate M/T and with an additional delay τ^r representing the alignment of the receiver clock. The cumulated timing delays are denoted by $\tau_k = \tau_k^t + \tau^r$ and are gathered in the $K \times 1$ vector $\underline{\tau}$. In the nominal mode of operations, obtained at modem start-up, the delay vector is supposed to be $\underline{\tau}_0$. The channel timing error, which corresponds to a user misalignment and/or a receiver clock offset, is denoted by $\underline{\varepsilon} = \underline{\tau} - \underline{\tau}_0$. Without loss of generality, we assume in the sequel that the nominal delay vector $\underline{\tau}_0$ is all-zero. This is equivalent to assume that the desired user alignments are incorporated in the physical channel impulse responses $c_k(t)$. The M received polyphase sequences are now :

$$\begin{aligned} r_{\rho,\underline{\varepsilon}}(m) &= \bar{r}\,(mT + \rho T_s + \tau^r) &(7.2)\\ &= \sum_{n=-\infty}^{+\infty} \sum_{k=1}^{K} \sum_{p \in \mathcal{C}_k} h_{\rho,pk,\varepsilon_k}(m-n) I_p(n) + n_{\rho,\tau^r}(m) &(7.3) \end{aligned}$$

where the filtered continuous-time received signal $\bar{r}(t)$ is given by

$$\bar{r}(t) = \sum_{k=1}^{K} \left[x_{k,\tau_k^t}(t) \otimes \bar{c}_k(t) \right] + \bar{n}(t) \tag{7.4}$$

and the MN asynchronous channel sequences $h_{\rho,pk,\varepsilon_k}(m)$ are defined by

$$h_{\rho,pk,\varepsilon_k}(m) = \sum_{n=\infty}^{+\infty} s_p(n)\bar{c}_k(mT + \rho T_s - nT_c + \varepsilon_k). \tag{7.5}$$

With FIR channels, $L+1$ asynchronous channel blocks $\underline{\underline{\mathrm{H}}}_{nk,\varepsilon_k}$ of size $M \times N_k$ can be defined for each user as in (4.45), on the basis of the asynchronous channel sequences $h_{\rho,pk,\varepsilon_k}(m)$ defined above. The corresponding asynchronous channel matrices $\underline{\underline{\mathrm{H}}}_{k,\varepsilon_k}$ are obtained as in (4.46). The matrices of channel first and second derivatives $\dot{\underline{\underline{\mathrm{H}}}}_{k,\varepsilon_k}$ and $\ddot{\underline{\underline{\mathrm{H}}}}_{k,\varepsilon_k}$, as well as the corresponding channel blocks $\dot{\underline{\underline{\mathrm{h}}}}_{k,\varepsilon_k}(n)$ and $\ddot{\underline{\underline{\mathrm{h}}}}_{k,\varepsilon_k}$, are defined in the same fashion except that the polyphase components of $h_{pk}(t)$ are replaced by the polyphase components of $dh_{pk}(t)/dt$ and $d^2h_{pk}(t)/dt^2$, respectively.

The total symbol energy received from user k (see 4.32) is given by:

$$\mathcal{E}_k = \sum_{p \in \mathcal{C}_k} \mathcal{E}_{pk} = \sigma_I^2 \frac{T}{M} \mathrm{tr}\left(\underline{\underline{\mathrm{H}}}_{k,\varepsilon_k}^T \underline{\underline{\mathrm{H}}}_{k,\varepsilon_k}\right). \tag{7.6}$$

The mean square bandwidth of the signal received from user k is defined as follows:

$$\begin{aligned} W_k^2 &= \frac{\dfrac{\sigma_I^2}{2\pi}\displaystyle\int_{-\infty}^{+\infty} \sum_{p \in \mathcal{C}_k} \omega^2 |H_{pk}(\omega)|^2 \, d\omega}{\dfrac{\sigma_I^2}{2\pi}\displaystyle\int_{-\infty}^{+\infty} \sum_{p \in \mathcal{C}_k} |H_{pk}(\omega)|^2 \, d\omega} \\ &= -\frac{\mathrm{tr}\left(\ddot{\underline{\underline{\mathrm{H}}}}_{k,\varepsilon_k}^T \underline{\underline{\mathrm{H}}}_{k,\varepsilon_k}\right)}{\mathrm{tr}\left(\underline{\underline{\mathrm{H}}}_{k,\varepsilon_k}^T \underline{\underline{\mathrm{H}}}_{k,\varepsilon_k}\right)} = \frac{\mathrm{tr}\left(\dot{\underline{\underline{\mathrm{H}}}}_{k,\varepsilon_k}^T \dot{\underline{\underline{\mathrm{H}}}}_{k,\varepsilon_k}\right)}{\mathrm{tr}\left(\underline{\underline{\mathrm{H}}}_{k,\varepsilon_k}^T \underline{\underline{\mathrm{H}}}_{k,\varepsilon_k}\right)} \end{aligned} \tag{7.7}$$

The above quantities $\mathcal{E}_k$ and W_k^2 do not depend on the timing delays ε_k even if they appear in the definitions.

The asynchronous FIR observation model relating the received samples within a length-N_fT observation window to the N transmitted symbol sequences is now

$$\left(\underline{\mathrm{r}}_{\varepsilon}\right)_{n_2}^{n_1}(n) = \sum_{k=1}^{K} \underline{\underline{\mathcal{H}}}_{N_f,k,\varepsilon_k} \left(\underline{\mathrm{I}}_k\right)_{n_2+L}^{n_1}(n) + \left(\underline{\mathrm{n}}_{\tau^r}\right)_{n_2}^{n_1}(n). \tag{7.8}$$

where the asynchronous global channel matrix $\underline{\underline{\mathcal{H}}}_{N_f,k,\varepsilon_k}$ is defined as in (4.47). The corresponding matrices of channel first and second derivatives are denoted by $\underline{\underline{\dot{\mathcal{H}}}}_{N_f,k,\varepsilon_k}$ and $\underline{\underline{\ddot{\mathcal{H}}}}_{N_f,k,\varepsilon_k}$, respectively.

One can be also interested in a FIR observation model relating a number N_f of consecutive outputs of the matched filter bank to the transmitted symbol sequences. The N_f consecutive outputs associated with the signatures allocated to the k-th user are given by

$$\left(\underline{\mathrm{y}}_{k,\underline{\varepsilon}}\right)_{n_2}^{n_1}(n) = \underline{\underline{\mathrm{F}}}_0\, \underline{\underline{\mathcal{H}}}_{N_f+L,k,0}^T \left(\underline{\mathrm{r}}_{\underline{\varepsilon}}\right)_{n_2}^{n_1+L}(n) \tag{7.9}$$

where the matrix $\underline{\underline{\mathrm{F}}}_0$ is defined by

$$\underline{\underline{\mathrm{F}}}_0 = \left(\,\underline{\underline{0}}_{N_f N\times LN} \,\middle|\, \underline{\underline{\mathrm{E}}}_{N_f N} \,\middle|\, \underline{\underline{0}}_{N_f N\times LN}\, \right). \tag{7.10}$$

In an asynchronous mode of operation, the IIR observation model becomes :

$$\underline{\mathrm{R}}_{\underline{\varepsilon}}(z) = \sum_{k=1}^{K} \underline{\underline{\mathrm{H}}}_{k,\varepsilon_k}(z)\, \underline{\mathrm{I}}_k(z) + \underline{\mathrm{N}}_{\tau^r}(z). \tag{7.11}$$

The N symbol-rate sequences obtained at the output of a bank of matched filters (5.12) are :

$$\underline{\mathrm{Y}}_{\underline{\varepsilon}}(z) = \underline{\underline{\mathrm{H}}}_{\underline{0}}^H(1/z^*)\, \underline{\mathrm{R}}_{\underline{\varepsilon}}(z) = \underline{\underline{\mathrm{X}}}_{\underline{\varepsilon}}(z)\, \underline{\mathrm{I}}(z) + \underline{\mathrm{W}}_{\tau^r}(z). \tag{7.12}$$

where the global asynchronous interference matrix $\underline{\underline{\mathrm{X}}}_{\underline{\varepsilon}}(z)$ includes $K \times K$ blocks $\underline{\underline{\mathrm{X}}}_{kk',\varepsilon_{k'}}(z)$ of size $N_k \times N_{k'}$ defined as follows :

$$\underline{\underline{\mathrm{X}}}_{kk',\varepsilon_{k'}}(z) = \frac{T}{M}\, \underline{\underline{\mathrm{H}}}_{k,0}^H(1/z^*)\, \underline{\underline{\mathrm{H}}}_{k',\varepsilon_{k'}}(z). \tag{7.13}$$

The noise cross-spectrum is $\underline{\underline{\gamma}}_w(z) = \frac{N_0}{2}\, \underline{\underline{\mathrm{X}}}_{\underline{0}}(z)$. Let $\underline{\underline{\mathrm{L}}}(z)$ be the MIMO spectral factor associated with the noise spectrum $\underline{\underline{\gamma}}_w(z)$, that is to say

$$\underline{\underline{\mathrm{X}}}_{\underline{0}}(z) = \underline{\underline{\mathrm{L}}}(z)\, \underline{\underline{\mathrm{L}}}^H(1/z). \tag{7.14}$$

A MIMO noise whitening filter $\underline{\underline{\mathrm{L}}}^{-1}(z)$ can be placed at the output of the matched filter bank, providing N filtered sequences $\tilde{y}_{p,\underline{\varepsilon}}(n)$ as follows :

$$\tilde{\underline{\mathrm{Y}}}_{\underline{\varepsilon}}(z) = \underline{\underline{\mathrm{L}}}^{-1}(z)\, \underline{\mathrm{Y}}_{\underline{\varepsilon}}(z) = \tilde{\underline{\underline{\mathrm{X}}}}_{\underline{\varepsilon}}(z)\, \underline{\mathrm{I}}(z) + \tilde{\underline{\mathrm{W}}}_{\tau^r}(z) \tag{7.15}$$

with $\underline{\underline{\tilde{X}}}_{\underline{\varepsilon}}(z) = \underline{\underline{L}}^{-1}(z)\, \underline{\underline{X}}_{\underline{\varepsilon}}(z)$ and $\underline{\underline{\tilde{X}}}_{\underline{0}}(z) = \underline{\underline{L}}^{H}(1/z)$. The noise-whitened matched filter outputs are also given by

$$\tilde{y}_{p,\underline{\varepsilon}}(n) = \sum_{m=-\infty}^{+\infty} \sum_{k=1}^{K} \sum_{p' \in \mathcal{C}_k} \tilde{x}_{pp',\varepsilon_k}(m)\, I_{p'}(n-m) + \tilde{\nu}_{p,\tau^r}(n). \tag{7.16}$$

7.3 ML-DD timing estimation and the Cramèr-Rao Lower Bound

7.3.1 Derivation of the ML-DD estimator

The log-likelihood function of the received signal is:

$$\Lambda_l\left(\underline{r}_{\underline{\varepsilon}}\,|\,\underline{I}, \hat{\underline{\varepsilon}}\right) = \kappa - \frac{1}{2\sigma_n^2}\left\|\left(\underline{r}_{\underline{\varepsilon}}\right)_{n_2}^{n_1}(n) - \sum_{k=1}^{K}\left[\underline{\underline{\mathcal{H}}}_{N_f,k,\hat{\varepsilon}_k}\right]\left(\underline{I}_k\right)_{n_2+L}^{n_1}(n)\right\|^2 \tag{7.17}$$

where κ is a constant and $\|\underline{x}\|^2$ denotes the square norm of vector $\underline{x}$. The ML-DD estimate of the delays is the vector $\hat{\underline{\varepsilon}}^*$ that maximizes this expression. In other words, the first derivative of the log-likelihood function with respect to each timing parameter:

$$\begin{aligned}\frac{\partial \Lambda_l\left[\underline{r}_{\underline{\varepsilon}}\,|\,\underline{I}, \hat{\underline{\varepsilon}}\right]}{\partial \hat{\varepsilon}_k} = \frac{1}{\sigma_n^2}&\left[\left(\underline{I}_k^T\right)_{n_2+L}^{n_1}(n)\left[\dot{\underline{\underline{\mathcal{H}}}}_{N_f,k,\hat{\varepsilon}_k}\right]^T\right.\\ &\left.\left(\left(\underline{r}_{\underline{\varepsilon}}\right)_{n_2}^{n_1}(n) - \sum_{k'=1}^{K}\left[\underline{\underline{\mathcal{H}}}_{N_f,k',\hat{\varepsilon}_{k'}}\right]\left(\underline{I}_{k'}\right)_{n_2+L}^{n_1}(n)\right)\right]\end{aligned} \tag{7.18}$$

is zero for $\hat{\varepsilon}_k = \hat{\varepsilon}_k^*$ and $k \in [1, K]$. This estimator is obviously unbiased as $\mathrm{E}_n\left\{\partial\Lambda_l/\partial\hat{\underline{\varepsilon}}\right\} = \underline{0}$ for $\hat{\underline{\varepsilon}} = \underline{\varepsilon}$. The timing estimation error is defined as $\underline{\Delta}_{\varepsilon} = \hat{\underline{\varepsilon}}^* - \underline{\varepsilon}$.

7.3.2 True Cramèr-Rao lower bound (DD-CRB)

The Fisher information matrix associated with this log-likelihood function is the $K \times K$ symmetric and positive definite matrix whose elements are defined by

$$\begin{aligned}J_{kk'}(\underline{\varepsilon}, \underline{I}) &= -\mathrm{E}_n\left\{\frac{\partial^2\Lambda_l\left[\underline{r}_{\underline{\varepsilon}}\,|\,\underline{I}, \hat{\underline{\varepsilon}}\right]}{\partial\hat{\varepsilon}_k\partial\hat{\varepsilon}_{k'}}\right\}_{\hat{\underline{\varepsilon}}=\underline{\varepsilon}} \\ &= \frac{1}{\sigma_n^2}\left(\left(\underline{I}_k^T\right)_{n_2+L}^{n_1}(n)\left[\underline{\underline{\Phi}}_{kk'}\right]\left(\underline{I}_{k'}\right)_{n_2+L}^{n_1}(n)\right)\end{aligned} \tag{7.19}$$

where $\underline{\underline{\Phi}}_{kk'} \triangleq \left[\underline{\underline{\dot{\mathcal{H}}}}_{N_f,k,\varepsilon_k}\right]^T \left[\underline{\underline{\dot{\mathcal{H}}}}_{N_f,k',\varepsilon_{k'}}\right]$. The expectation is taken with respect to the probability density function of the received signal, which is reduced here to the probability density function of the additive noise, as the symbols are assumed to be perfectly known. From the Cramèr-Rao theorem, we know that

$$\mathrm{E}_n \left\{\underline{\underline{\Delta}}_\varepsilon \underline{\underline{\Delta}}_\varepsilon^T\right\} - \underline{\underline{\mathrm{J}}}(\underline{\varepsilon}, \underline{\mathrm{I}})^{-1} \geq \underline{\underline{0}} \tag{7.20}$$

where $\geq \underline{\underline{0}}$ is interpreted as meaning that the matrix is positive semi-definite. The lower bound on the timing error variance is dependent on the specific sequence of information symbols involved in the received signal segment [64]. In a tracking mode of operation, the timing parameters are continuously estimated and the lower bound on the average timing error variance becomes:

$$\mathrm{var}(\hat{\varepsilon}_k) \geq \mathrm{E}_I \left\{\left[\underline{\underline{\mathrm{J}}}(\underline{\varepsilon}, \underline{\mathrm{I}})^{-1}\right]_{kk}\right\} \tag{7.21}$$

Equation (7.21) gives the true DD-CRB associated with the FB-based multiple access system.

7.3.3 Modified Cramèr-Rao lower bound (M-CRB)

The right-hand side of (7.21) is not easy to compute. Some simplifications are made possible by using the law of large numbers, if the length N_f of the observation interval (and the length of the corresponding sequences of symbols) is long. In that case, the diagonal elements of the Fisher information matrix are tightly distributed around a large mean, while the non-diagonal elements are tightly distributed around a zero mean:

$$\begin{aligned} J_{kk} &\sim \mathcal{N}\left[\left(N_f \frac{\sigma_I^2}{\sigma_n^2}\right) m_{kk}, \left(\sqrt{N_f}\frac{\sigma_I^2}{\sigma_n^2}\right) s_{kk}\right] \\ J_{kk'} &\sim \mathcal{N}\left[0, \left(\sqrt{N_f}\frac{\sigma_I^2}{\sigma_n^2}\right) s_{kk'}\right] \end{aligned} \tag{7.22}$$

with

$$\begin{aligned} m_{kk} &= \frac{1}{N_f}\mathrm{tr}\left(\underline{\underline{\Phi}}_{kk}\right) \\ s_{kk}^2 &= \frac{1}{N_f}\left[\sum_i \rho_i^2 \left(\underline{\underline{\Phi}}_{kk}\right)_{ii}^2 + \sum_i \sum_{j>i} \left(2\underline{\underline{\Phi}}_{kk}\right)_{ij}^2\right] \\ s_{kk'}^2 &= \frac{1}{N_f}\left[\sum_i \sum_j \left(\underline{\underline{\Phi}}_{kk'}\right)_{ij}^2\right]. \end{aligned} \tag{7.23}$$

The factor ρ_i^2 is defined by

$$\rho_i^2 = \mathrm{E}\left\{I^4\right\}/\sigma_I^4 - 1 < 4/5 \tag{7.24}$$

and depends on the PAM constellation used on the i-th symbol stream. The quantities defined in (7.23) are independent of the observation window size N_f (at least by neglecting the side-effect due to continuous transmission).

To get a tractable expression of the CRB, we have to observe two inequalities:

- The symmetric positive definite Fisher information matrix, has the property that:

  $$\left[\underline{\underline{\mathrm{J}}}^{-1}\right]_{kk} \geq \frac{1}{J_{kk}} \quad \forall\, \underline{\mathrm{I}} \tag{7.25}$$

  Inequality (7.25) becomes an equality if and only if the Fisher information matrix is diagonal. In other words, considering it as an equality is equivalent to neglecting the performance degradation due to the joint estimation process. For a long observation window, the next approximation for the matrix inversion is valid:

  $$\left[\underline{\underline{\mathrm{J}}}^{-1}\right]_{kk} \approx \frac{1}{J_{kk}}\left(1 + \sum_{k' \neq k} \frac{J_{kk'}^2}{J_{kk}\, J_{k'k'}}\right) \tag{7.26}$$

  and the average inverse of the Fisher information matrix becomes:

  $$\mathrm{E}_I\left\{\left[\underline{\underline{\mathrm{J}}}^{-1}\right]_{kk}\right\} \approx \mathrm{E}_I\left\{\frac{1}{J_{kk}}\right\}\left(1 + \frac{1}{N_f}\sum_{k' \neq k} \frac{s_{kk'}^2}{m_{kk} m_{k'k'}}\right) \tag{7.27}$$

  The last factor appears as a correction term which decreases linearly with the size of the observation window.

- The application of Jensen's inequality[1] to the convex function $f(x) = 1/x$ gives:

  $$\mathrm{E}_I\left\{\frac{1}{J_{kk}}\right\} \geq \frac{1}{\mathrm{E}_I\left\{J_{kk}\right\}} \tag{7.28}$$

[1] If $f(.)$ is a convex function and X is a random variable, then

$$\mathrm{E}\left\{f\left(X\right)\right\} \geq f\left(\mathrm{E}\left\{X\right\}\right)$$

As J_{kk} is concentrated near its mean, a second order Taylor expansion of its inverse can be used (see [65], pp. 113) to provide the following approximation:

$$\mathrm{E}_I\left\{\frac{1}{J_{kk}}\right\} \approx \frac{1}{\mathrm{E}_I\left\{J_{kk}\right\}}\left(1+\frac{1}{N_f}\frac{s_{kk}^2}{m_{kk}^2}\right) \tag{7.29}$$

The last factor appears again as a correction term which decreases linearly with the size of the observation window.

In the light of relations (7.25) and (7.28), we obtain a modified (looser) lower bound on the timing error variance:

$$\mathrm{var}(\hat{\varepsilon}_k) > \left[\mathrm{E}_I\left\{\underline{\underline{\mathrm{J}}}\left(\underline{\varepsilon}, \underline{\mathrm{I}}\right)\right\}\right]_{kk}^{-1} = \frac{1}{\mathrm{E}_I\left\{J_{kk}\right\}} \tag{7.30}$$

From a careful examination of the $\left[\dot{\underline{\underline{\mathcal{H}}}}_{N_f,k,\varepsilon_k}\right]$ matrix structure shown in (4.47), we can check that

$$m_{kk} = \frac{1}{N_f}\mathrm{tr}\left(\underline{\underline{\Phi}}_{kk}\right) = \mathrm{tr}\left(\dot{\underline{\underline{\mathrm{H}}}}_{k,\varepsilon_k}^T\,\dot{\underline{\underline{\mathrm{H}}}}_{k,\varepsilon_k}\right) \tag{7.31}$$

Using the definitions (7.6) and (7.7), the proposed modified bound is finally given by :

$$\mathrm{var}(\hat{\varepsilon}_k) > \left[\frac{2\mathcal{E}_k}{N_0}\right]^{-1}\frac{1}{N_f\,W_k^2}. \tag{7.32}$$

Note that this modified bound does not depend on the true value to be estimated $\underline{\varepsilon}$.

The bound proposed in (7.30) corresponds to the modified Cramèr-Rao bound (M-CRB) introduced for vector parameter estimation by [66]. In that reference, which corresponds to a NDA scenario, the symbols are considered as nuisance parameters. In that scenario, the symbol-dependent (exponential) likelihood function has to be averaged over the symbols distribution before the logarithm is taken. This provides the following Fisher information matrix:

$$\bar{J}_{k,k'}(\underline{\varepsilon}) = -\mathrm{E}_n\left\{\frac{\partial^2 \ln\left[\mathrm{E}_I\left\{\Lambda\left(\underline{\mathrm{r}}_{\underline{\varepsilon}}\,|\,\underline{\mathrm{I}},\hat{\underline{\varepsilon}}\right)\right\}\right]}{\partial\hat{\varepsilon}_k\partial\hat{\varepsilon}_{k'}}\right\}_{\hat{\underline{\varepsilon}}=\underline{\varepsilon}} \tag{7.33}$$

The authors showed that the M-CRB is always lower than the true NDA-CRB. We finally have the following ordering between the bounds:

$$\underbrace{\left[\left(\mathrm{E}_I\left\{\underline{\underline{\mathrm{J}}}(\underline{\varepsilon},\underline{\mathrm{I}})\right\}\right)^{-1}\right]_{kk}}_{M-CRB} \leq \underbrace{\mathrm{E}_I\left\{\left[\,\underline{\underline{\mathrm{J}}}(\underline{\varepsilon},\underline{\mathrm{I}})^{-1}\,\right]_{kk}\right\}}_{DD-CRB} \leq \underbrace{\left[\,\underline{\underline{\bar{\mathrm{J}}}}(\underline{\varepsilon})^{-1}\,\right]_{kk}}_{NDA-CRB} \tag{7.34}$$

With PAM-distributed symbols $I_p(n)$, an exhaustive survey of all possible symbol combinations should be performed to obtain the expectation E(.) appearing in the expression of the true DD-CRB (7.21). The computation of the true DD-CRB has thus a complexity that increases exponentially with $(N_f + L)N$, i.e. the number of symbols used to obtain the timing estimate, and with the size of each PAM constellation. Let us consider a simple transmission scheme with a single user ($K = 1$), a single signature ($N = 1$) and an AWGN channel ($L = 1$). The ratio of the M-CRB with the true DD-CRB becomes :

$$\begin{aligned} \frac{\text{DD-CRB}}{\text{M-CRB}} &= \left(\sigma_I^2 N_f\right) \mathrm{E}_I\left\{\frac{1}{\sum_{n=1}^{N_f} I_n^2}\right\} && (7.35) \\ &\approx 1 + \frac{\rho^2}{N_f} && (7.36) \end{aligned}$$

where ρ is defined in (7.24). Figure 7.1 illustrates the evolution of the ratio (7.35) with the length N_f of the observation window, for different values of the PAM constellation size. The solid lines give the true DD-CRB (obtained by an exhaustive computation), while the dashed lines give the asymptotic approximation (7.36). Obviously, the proposed asymptotic approximation is already tight with moderate values of N_f. Moreover, the M-CRB converges rapidly to the true DD-CRB. Extrapolating these results to the general multiuser FB scenario, we assume in the sequel that the M-CRB is a pertinent approximation of the true DD-CRB.

The M-CRB for a given user is the same as in the single user scenario, that is to say it only depends on the average matched filter bound (MFB) $2\mathcal{E}_k/N_0$ and the mean square bandwidth (MSB) W_k^2 of the considered user. However, both quantities are dependent on the individual channels and the waveforms allocated to the different users. In a FB system, the waveform allocation has thus a strong impact on the multiuser timing estimator performance: it should be matched to the different channels in such a way that the average MFB-MSB product is maximized for each user.

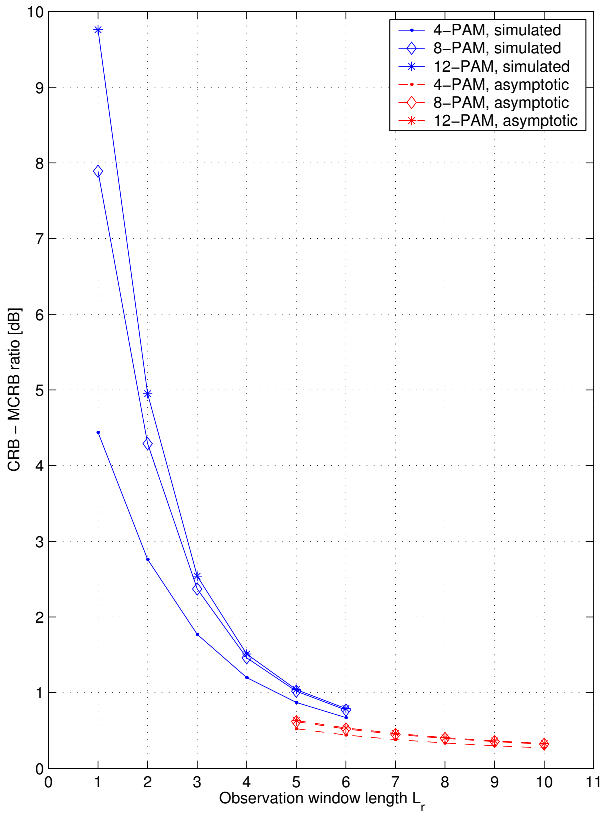

Figure 7.1: *Comparison of the true DD-CRB and the M-CRB*

In a single-user scenario, the M-CRB can be shown to be independent of the FB as long as it satisfies the paraunitary property :

$$\begin{aligned} \text{M-CRB} &= -\frac{1}{N_f}\left(\frac{\sigma_I^2}{N_0/2}\right)\left[\operatorname{tr}\left\{\int_{-\pi}^{\pi} \underline{\underline{\mathrm{S}}}^H\left(e^{j\Omega}\right) \underline{\underline{\ddot{\mathrm{G}}}}\left(e^{j\Omega}\right) \underline{\underline{\mathrm{S}}}\left(e^{j\Omega}\right) \frac{\mathrm{d}\Omega}{2\pi}\right\}\right]^{-1} \\ &= -\frac{1}{N_f}\left(\frac{\sigma_I^2}{N_0/2}\right)\sum_{p=1}^{N} \ddot{x}_{pp}(0) = -\frac{1}{N_f\, N}\left(\frac{\sigma_I^2}{N_0/2}\right)\ddot{g}(0) \end{aligned} \qquad (7.37)$$

where $g(t)$ is the channel correlation function.

7.4 Symbol-rate ML-DD timing estimation

The previous section was devoted to the performance computation of an optimal timing estimator placed at the channel output. This estimator has an access to the received signal samples at a fractional rate M/T, which represent a sufficient statistic of the continuous-time received signal.

The primary task of the receiver is to compute symbol estimates, by means of an appropriate joint detector. The JDs analyzed in Chapter 5 are firstly constituted by a bank of matched filters whose outputs are sampled at the symbol rate. The matched filter outputs are then combined through an appropriate MIMO filter (optionally with a feedback section) whose purpose is to decrease the residual interference. This MIMO filter is invertible, so there is no loss of information associated with it. The bank of matched filters, however, represent a non-invertible operation, in the sense that the channel output samples cannot be recovered from the matched filter outputs. This is not a problem regarding the process of symbol detection, as the matched filter outputs actually represent a sufficient statistic of the data symbols $I_p(n)$. But there is well a loss of information regarding the process of timing estimation.

A class of timing estimators, the so-called symbol-rate timing estimators, are intended to build estimates of the timing error on the basis of output samples produced at the symbol rate, that is to say at the output of the matched filter bank or that of the JD. The corresponding optimal performance is necessarily lower than that of a timing estimator working directly at the channel output. The purpose of this section is to derive the M-CRB associated with the symbol rate ML-DD timing estimation.

Following the observation model given by (7.9), the log-likelihood function of the received signal is now :

$$\begin{aligned}\Lambda_l\left(\underline{\mathrm{y}}_{\underline{\varepsilon}}\,|\,\underline{\mathrm{I}},\hat{\underline{\varepsilon}}\right) = \kappa - \frac{1}{2\sigma_n^2}\Bigg\{&\left[\left(\underline{\mathrm{y}}_{\underline{\varepsilon}}\right)_{n_2}^{n_1}(n) - \left[\underline{\underline{\mathrm{F}}}_0\,\underline{\underline{\mathcal{H}}}_0^T\,\underline{\underline{\mathcal{H}}}_{\hat{\underline{\varepsilon}}}\right]\,(\underline{\mathrm{I}}_k)_{n_2+L}^{n_1+L}(n)\right]^T \\ &\left[\underline{\underline{\mathrm{F}}}_0\,\underline{\underline{\mathcal{H}}}_0^T\,\underline{\underline{\mathcal{H}}}_0\,\underline{\underline{\mathrm{F}}}_0^T\right]^{-1}\left[\left(\underline{\mathrm{y}}_{\underline{\varepsilon}}\right)_{n_2}^{n_1}(n) - \left[\underline{\underline{\mathrm{F}}}_0\,\underline{\underline{\mathcal{H}}}_0^T\,\underline{\underline{\mathcal{H}}}_{\hat{\underline{\varepsilon}}}\right]\,(\underline{\mathrm{I}}_k)_{n_2+L}^{n_1+L}(n)\right]\Bigg\}\end{aligned} \quad (7.38)$$

The entries of the $K \times K$ Fisher information matrix associated with this log-likelihood function are now :

$$\begin{aligned}\overline{J}_{kk'}(\underline{\varepsilon},\underline{\mathrm{I}}) &= -\mathrm{E}_n\left\{\frac{\partial^2\Lambda_l\left[\underline{\mathrm{y}}_{\underline{\varepsilon}}\,|\,\underline{\mathrm{I}},\hat{\underline{\varepsilon}}\right]}{\partial\hat{\varepsilon}_k\partial\hat{\varepsilon}_{k'}}\right\}_{\hat{\underline{\varepsilon}}=\underline{\varepsilon}} \\ &= \frac{1}{\sigma_n^2}\left\{\left(\underline{\mathrm{I}}_k^T\right)_{n_2+L}^{n_1+L}(n)\,\left[\overline{\underline{\underline{\Phi}}}_{kk'}\right]\,\left(\underline{\mathrm{I}}_{k'}\right)_{n_2+L}^{n_1+L}(n)\right\}\end{aligned} \tag{7.39}$$

where matrix $\overline{\underline{\underline{\Phi}}}_{kk'}$ is defined by

$$\overline{\underline{\underline{\Phi}}}_{kk'} = \dot{\underline{\underline{\mathcal{H}}}}^T_{k,\varepsilon_k}\,\left(\underline{\underline{\mathcal{H}}}_{\underline{0}}\,\underline{\underline{\mathrm{F}}}_0^T\right)\,\left(\underline{\underline{\mathrm{F}}}_0\,\underline{\underline{\mathcal{H}}}_{\underline{0}}^T\,\underline{\underline{\mathcal{H}}}_{\underline{0}}\,\underline{\underline{\mathrm{F}}}_0^T\right)^{-1}\,\left(\underline{\underline{\mathrm{F}}}_0\,\underline{\underline{\mathcal{H}}}_{\underline{0}}^T\right)\,\dot{\underline{\underline{\mathcal{H}}}}_{k',\varepsilon_{k'}} \tag{7.40}$$

The M-CRB on the symbol-rate timing estimator is expressed as follows :

$$\mathrm{var}\left(\hat{\varepsilon}_k\right) > \frac{1}{\mathrm{E}_I\left\{\overline{J}_{kk}\right\}} = \left[\frac{\sigma_I^2}{\sigma_n^2}\mathrm{tr}\left(\overline{\underline{\underline{\Phi}}}_{kk}\right)\right]^{-1}. \tag{7.41}$$

From the examination of the channel matrix structure, it can be shown that for a long observation window $N_f \gg L$ the trace of $\overline{\underline{\underline{\Phi}}}_{kk'}$ can be approximated as follows :

$$\mathrm{tr}\left(\overline{\underline{\underline{\Phi}}}_{kk}\right) \approx N_f\,\mathrm{tr}\left\{\int_{-\pi}^{\pi}\underline{\underline{\Psi}}_{kk}\left(e^{j\Omega}\right)\frac{\mathrm{d}\Omega}{2\pi}\right\} \tag{7.42}$$

with

$$\underline{\underline{\Psi}}_{kk}(z) = \begin{pmatrix}\dot{\underline{\underline{\mathrm{X}}}}^H_{1k,\varepsilon_k}(\tfrac{1}{z}) & \cdots & \dot{\underline{\underline{\mathrm{X}}}}^H_{Kk}(\tfrac{1}{z})\end{pmatrix}\left[\underline{\underline{\mathrm{X}}}_{\underline{0}}(z)\right]^{-1}\begin{pmatrix}\dot{\underline{\underline{\mathrm{X}}}}_{1k,\varepsilon_k}(z) \\ \vdots \\ \dot{\underline{\underline{\mathrm{X}}}}_{Kk,\varepsilon_k}(z)\end{pmatrix} \tag{7.43}$$

An equivalent expression in the time domain can be obtained by using Parseval's relation :

$$\mathrm{tr}\left(\overline{\underline{\underline{\Phi}}}_{kk}\right) \approx N_f\,\dot{\mathcal{X}}_k^2 \tag{7.44}$$

where

$$\dot{\mathcal{X}}_k^2 \triangleq \sum_{n=-\infty}^{+\infty}\sum_{p=1}^{N}\sum_{p'\in\mathcal{C}_k}\dot{\tilde{x}}^2_{pp',\varepsilon_k}(n) \tag{7.45}$$

The minimum error variance associated with a symbol-rate timing estimator is thus inversely proportional to the sum of the noise-whitened interference waveforms squared slopes, sampled at the symbol rate.

7.5 Joint timing error tracking structures

7.5.1 Feedforward structure

In a DD feedforward mode of operations, at time m, the synchronizer tries to estimate the vector of timing errors $\underline{\varepsilon}$ on the basis of a large set of measurement data, and the knowledge of the data symbols. The vector of measurement data is denoted by $\underline{\mathrm{x}}_{\underline{\varepsilon}}$: it can be made of channel outputs, matched filter outputs, or joint detector outputs.

A given DD feedforward timing error detector is characterized by a specific timing error vector function $\underline{\mathrm{S}}\left(\underline{\mathrm{x}}_{\underline{\varepsilon}}, \underline{\mathrm{I}}, \underline{\hat{\varepsilon}}\right)$ that should be close to the null vector for $\underline{\hat{\varepsilon}} = \underline{\varepsilon}$ in the absence of noise. In the ideal case, an exhaustive search on the trial vector $\underline{\hat{\varepsilon}}$ would be performed, and the proposed estimate would be $\underline{\hat{\varepsilon}}^*$ such that:

$$\underline{\mathrm{S}}\left(\underline{\mathrm{x}}_{\underline{\varepsilon}}, \underline{\mathrm{I}}, \underline{\hat{\varepsilon}}^*\right) = \underline{0}. \tag{7.46}$$

Because of the noise, the resulting estimate will differ from the true value $\underline{\varepsilon}$.

As suggested above, the TED output for a given candidate timing vector $\underline{\hat{\varepsilon}}$ depends on the known data symbols $\underline{\mathrm{I}}$ and the measurement data vector $\underline{\mathrm{x}}_{\underline{\varepsilon}}$, which is itself a function of the data symbols, the additive noise and the true timing error vector: $\underline{\mathrm{x}}_{\underline{\varepsilon}} = f\left(\underline{\mathrm{n}}, \underline{\mathrm{I}}, \underline{\varepsilon}\right)$. The TED output can usually be expressed as the sum of three terms as follows:

$$\begin{aligned} \underline{\mathrm{S}}\left(\underline{\mathrm{x}}_{\underline{\varepsilon}}, \underline{\mathrm{I}}, \underline{\hat{\varepsilon}}\right) &= \underline{\mathrm{S}}_I\left(\underline{\mathrm{I}}, \underline{\varepsilon}, \underline{\hat{\varepsilon}}\right) + \underline{\mathrm{N}}_n\left(\underline{\mathrm{n}}, \underline{\mathrm{I}}, \underline{\varepsilon}, \underline{\hat{\varepsilon}}\right) \\ &= \underline{\mathrm{S}}_0\left(\underline{\varepsilon}, \underline{\hat{\varepsilon}}\right) + \underline{\mathrm{N}}_s\left(\underline{\mathrm{I}}, \underline{\varepsilon}, \underline{\hat{\varepsilon}}\right) + \underline{\mathrm{N}}_n\left(\underline{\mathrm{n}}, \underline{\mathrm{I}}, \underline{\varepsilon}, \underline{\hat{\varepsilon}}\right) \end{aligned} \tag{7.47}$$

where

- The first term $\underline{\mathrm{S}}_0\left(\underline{\varepsilon}, \underline{\hat{\varepsilon}}\right)$ is the so-called 'S-hypercurve' of the TED. It is the expectation with respect to both data and additive noise of the TED output.
- The second term $\underline{\mathrm{N}}_s\left(\underline{\mathrm{I}}, \underline{\varepsilon}, \underline{\hat{\varepsilon}}\right)$ is the self-noise. It represents the deviation of the TED output from the S-hypercurve due to the specific pattern of data symbols contained in the received signal. In a given sense, the first two terms-sum $\underline{\mathrm{S}}_I\left(\underline{\mathrm{I}}, \underline{\varepsilon}, \underline{\hat{\varepsilon}}\right)$ gives the instantaneous pattern-dependent S-hypercurve.
- The third term $\underline{\mathrm{N}}_n\left(\underline{\mathrm{n}}, \underline{\mathrm{I}}, \underline{\varepsilon}, \underline{\hat{\varepsilon}}\right)$ represents the contribution of the additive noise. In the DD scenario, its expectation with respect to the noise is supposed to be zero.

The S-hypercurve evaluated at the true timing error, that is to say $\underline{\mathrm{S}}_0\left(\underline{\varepsilon},\underline{\varepsilon}\right)$, gives the average bias of the TED. The term $\underline{\mathrm{S}}_I\left(\underline{\mathrm{I}},\underline{\varepsilon},\underline{\varepsilon}\right)$ is the instantaneous bias which depends on the data sequence.

To evaluate the mean square value of the estimation error, some approximations have to be done:

1. A first order expansion of the timing error vector function is performed:
$$\underline{\mathrm{S}}\left(\underline{\mathrm{x}}_{\underline{\varepsilon}},\underline{\mathrm{I}},\hat{\underline{\varepsilon}}\right) \approx \underline{\mathrm{S}}\left(\underline{\mathrm{x}}_{\underline{\varepsilon}},\underline{\mathrm{I}},\underline{\varepsilon}\right) + \left[\frac{\partial \underline{\mathrm{S}}}{\partial \hat{\underline{\varepsilon}}}\left(\underline{\mathrm{x}}_{\underline{\varepsilon}},\underline{\mathrm{I}},\underline{\varepsilon}\right)\right]\underline{\Delta}_{\varepsilon} \tag{7.48}$$
where $\left[\frac{\partial \underline{\mathrm{S}}}{\partial \hat{\underline{\varepsilon}}}\left(\underline{\mathrm{x}}_{\underline{\varepsilon}},\underline{\mathrm{I}},\underline{\varepsilon}\right)\right]$ is the $K\times K$ TED Jacobian matrix with respect to the candidate timing vector, evaluated at $\hat{\underline{\varepsilon}}=\underline{\varepsilon}$. Using (7.46) and (7.48), the correlation matrix of the estimation error becomes:
$$\begin{aligned}\mathrm{E}_n\left\{\underline{\Delta}_{\varepsilon}\underline{\Delta}_{\varepsilon}^T\right\} = \mathrm{E}_n\Bigg\{&\left[\frac{\partial \underline{\mathrm{S}}}{\partial \hat{\underline{\varepsilon}}}\left(\underline{\mathrm{x}}_{\underline{\varepsilon}},\underline{\mathrm{I}},\underline{\varepsilon}\right)\right]^{-1}\left[\underline{\mathrm{S}}\left(\underline{\mathrm{x}}_{\underline{\varepsilon}},\underline{\mathrm{I}},\underline{\varepsilon}\right)\underline{\mathrm{S}}\left(\underline{\mathrm{x}}_{\underline{\varepsilon}},\underline{\mathrm{I}},\underline{\varepsilon}\right)^T\right]\\ &\left[\frac{\partial \underline{\mathrm{S}}}{\partial \hat{\underline{\varepsilon}}}\left(\underline{\mathrm{x}}_{\underline{\varepsilon}},\underline{\mathrm{I}},\underline{\varepsilon}\right)\right]^{-T}\Bigg\}\end{aligned} \tag{7.49}$$
This linearization is valid for small timing errors only.

2. At high signal-to-noise ratios, the noisy fluctuation of the Jacobian matrix with respect to its mean value is much smaller than this mean value. From (7.46) and (7.48), the timing error vector is thus approximated as:
$$\underline{\Delta}_{\varepsilon} \approx -\left[\mathrm{E}_n\left\{\frac{\partial \underline{\mathrm{S}}}{\partial \hat{\underline{\varepsilon}}}\left(\underline{\mathrm{x}}_{\underline{\varepsilon}},\underline{\mathrm{I}},\underline{\varepsilon}\right)\right\}\right]^{-1}\underline{\mathrm{S}}\left(\underline{\mathrm{x}}_{\underline{\varepsilon}},\underline{\mathrm{I}},\underline{\varepsilon}\right) \tag{7.50}$$
$$= -\left[\frac{\partial \underline{\mathrm{S}}_I}{\partial \hat{\underline{\varepsilon}}}\left(\underline{\mathrm{I}},\underline{\varepsilon},\underline{\varepsilon}\right)\right]^{-1}\underline{\mathrm{S}}\left(\underline{\mathrm{x}}_{\underline{\varepsilon}},\underline{\mathrm{I}},\underline{\varepsilon}\right) \tag{7.51}$$
The correlation matrix of the estimation error becomes:
$$\begin{aligned}\mathrm{E}_n\left\{\underline{\Delta}_{\varepsilon}\underline{\Delta}_{\varepsilon}^T\right\} = &\left[\frac{\partial \underline{\mathrm{S}}_I}{\partial \hat{\underline{\varepsilon}}}\left(\underline{\mathrm{I}},\underline{\varepsilon},\underline{\varepsilon}\right)\right]^{-1}\mathrm{E}_n\left\{\underline{\mathrm{S}}\left(\underline{\mathrm{x}}_{\underline{\varepsilon}},\underline{\mathrm{I}},\underline{\varepsilon}\right)\underline{\mathrm{S}}\left(\underline{\mathrm{x}}_{\underline{\varepsilon}},\underline{\mathrm{I}},\underline{\varepsilon}\right)^T\right\}\\ &\left[\frac{\partial \underline{\mathrm{S}}_I}{\partial \hat{\underline{\varepsilon}}}\left(\underline{\mathrm{I}},\underline{\varepsilon},\underline{\varepsilon}\right)\right]^{-T}\end{aligned} \tag{7.52}$$

with

$$\mathrm{E}_n\left\{\underline{\mathrm{S}}\left(\underline{\mathrm{x}}_{\underline{\varepsilon}},\underline{\mathrm{I}},\underline{\varepsilon}\right)\underline{\mathrm{S}}\left(\underline{\mathrm{x}}_{\underline{\varepsilon}},\underline{\mathrm{I}},\underline{\varepsilon}\right)^T\right\}=\underline{\mathrm{S}}_I\left(\underline{\mathrm{I}},\underline{\varepsilon},\underline{\varepsilon}\right)\underline{\mathrm{S}}_I\left(\underline{\mathrm{I}},\underline{\varepsilon},\underline{\varepsilon}\right)^T + \mathrm{E}_n\left\{\underline{\mathrm{N}}_n\left(\underline{\mathrm{n}},\underline{\mathrm{I}},\underline{\varepsilon},\underline{\varepsilon}\right)\underline{\mathrm{N}}_n\left(\underline{\mathrm{n}},\underline{\mathrm{I}},\underline{\varepsilon},\underline{\varepsilon}\right)^T\right\} \quad (7.53)$$

The unbiased part of (7.52) has to be compared with the true CRB.

3. The correlation matrix obtained so far still depends on the specific symbol sequence that is contained in the signal. To obtain the mean performance of the timing detector, a statistical average has to be performed on the data symbols. To simplify the computations, we assume that the symbol-dependent fluctuation of the Jacobian matrix with respect to its mean value is much smaller than this mean value. In these conditions, the average correlation matrix of the estimation error simplifies into:

$$\mathrm{E}_{n,I}\left\{\underline{\Delta}_{\varepsilon}\underline{\Delta}_{\varepsilon}^T\right\}=\left[\frac{\partial\underline{\mathrm{S}}_0}{\partial\hat{\underline{\varepsilon}}}\left(\underline{\varepsilon},\underline{\varepsilon}\right)\right]^{-1}\left[\mathrm{E}_{n,I}\left\{\underline{\mathrm{S}}\left(\underline{\mathrm{x}}_{\underline{\varepsilon}},\underline{\mathrm{I}},\underline{\varepsilon}\right)\underline{\mathrm{S}}\left(\underline{\mathrm{x}}_{\underline{\varepsilon}},\underline{\mathrm{I}},\underline{\varepsilon}\right)^T\right\}\right] \left[\frac{\partial\underline{\mathrm{S}}_0}{\partial\hat{\underline{\varepsilon}}}\left(\underline{\varepsilon},\underline{\varepsilon}\right)\right]^{-T} \quad (7.54)$$

with

$$\mathrm{E}_{n,I}\left\{\underline{\mathrm{S}}\left(\underline{\mathrm{x}}_{\underline{\varepsilon}},\underline{\mathrm{I}},\underline{\varepsilon}\right)\underline{\mathrm{S}}\left(\underline{\mathrm{x}}_{\underline{\varepsilon}},\underline{\mathrm{I}},\underline{\varepsilon}\right)^T\right\}=\underline{\mathrm{S}}_0\left(\underline{\varepsilon},\underline{\varepsilon}\right)\underline{\mathrm{S}}_0\left(\underline{\varepsilon},\underline{\varepsilon}\right)^T + \mathrm{E}_I\left\{\underline{\mathrm{N}}_s\left(\underline{\mathrm{I}},\underline{\varepsilon},\underline{\varepsilon}\right)\underline{\mathrm{N}}_s\left(\underline{\mathrm{I}},\underline{\varepsilon},\underline{\varepsilon}\right)^T\right\} + \mathrm{E}_{n,I}\left\{\underline{\mathrm{N}}_n\left(\underline{\mathrm{n}},\underline{\mathrm{I}},\underline{\varepsilon},\underline{\varepsilon}\right)\underline{\mathrm{N}}_n\left(\underline{\mathrm{n}},\underline{\mathrm{I}},\underline{\varepsilon},\underline{\varepsilon}\right)^T\right\} \quad (7.55)$$

The use of this approximation is equivalent to the use of the M-CRB instead of the true DD-CRB. The unbiased part of (7.54) has to be compared to the M-CRB. The mean square value obtained by this expression is lower than the true mean square value of the timing error estimate.

A remaining question is the following: does the performance of the estimator depend on the true value $\underline{\varepsilon}$ to be estimated? It is not the case in the single user scenario where the timing error function $S\left(\underline{\mathrm{x}}_{\varepsilon},\underline{\mathrm{I}},\hat{\varepsilon}\right)$ only depends on the difference $\varepsilon-\hat{\varepsilon}$. In the multiuser configuration, however, the timing error vector function $\underline{\mathrm{S}}\left(\underline{\mathrm{x}}_{\underline{\varepsilon}},\underline{\mathrm{I}},\hat{\underline{\varepsilon}}\right)$ depends on all differences $\varepsilon_k-\hat{\varepsilon}_{k'}$ for every pair (k, k'). As a consequence, the performance of the multiuser timing estimator generally depends on the true value $\underline{\varepsilon}$ to be estimated. Intuitively, this can be explained by the idea that the inter-user offsets $\varepsilon_k - \varepsilon_{k'} \neq 0$ for $k \neq k'$ can have a positive or a negative impact on the joint timing estimation process.

Assuming in first-order approximation that the true value $\underline{\varepsilon}$ does not matter, the TED output only depends on the difference $\underline{\hat{\varepsilon}} - \underline{\varepsilon}$. The terms in the above expressions can then be computed for $(\underline{\hat{\varepsilon}}, \underline{\varepsilon}) = (\underline{0}, \underline{0})$ and the Jacobian matrix with respect to the candidate timing vector can be replaced by the Jacobian matrix with respect to the true timing vector:

$$\frac{\partial \underline{\mathrm{S}}}{\partial \underline{\hat{\varepsilon}}} \left(\underline{\mathrm{x}}_{\underline{\varepsilon}}, \underline{\mathrm{I}}, \underline{\varepsilon}\right) = -\frac{\partial \underline{\mathrm{S}}}{\partial \underline{\varepsilon}} \left(\underline{\mathrm{x}}_{\underline{\varepsilon}}, \underline{\mathrm{I}}, \underline{\varepsilon}\right) . \tag{7.56}$$

7.5.2 Feedback structure

In a feedback system, an instantaneous estimate of the timing error vector is computed at the symbol rate, and a timing correction is continuously applied by a feedback signal sent on the downlink to resynchronize the user transmitters.

At time n, a new block of N symbols is detected, and the TED output is computed with $\underline{\hat{\varepsilon}}(n) = \underline{0}$. In these conditions, the estimation error $\underline{\Delta}_{\varepsilon}(n)$ is equal to the true value itself, with the sign changed: $\underline{\Delta}_{\varepsilon}(n) = -\underline{\varepsilon}(n)$.

The TED output vector is then transformed into a vector of K timing corrections $\underline{\bar{\varepsilon}}(n)$ through the matrix gain $\underline{\underline{\mathrm{K}}}_c(n)$ which can be time-dependent. The timing corrections are finally filtered by means of a constant MIMO $K \times K$ loop filter $\underline{\underline{\mathrm{F}}}(z)$. The feedback loop equations are given by:

$$\underline{\varepsilon}(n+1) = \underline{\varepsilon}(n) - \underline{\bar{\varepsilon}}(n) \tag{7.57}$$

$$\underline{\bar{\varepsilon}}(n) = \underline{\underline{\mathrm{F}}}(z) \otimes \left[\underline{\underline{\mathrm{K}}}_c(n)\ \underline{\mathrm{S}}\left(\underline{\mathrm{x}}_{\underline{\varepsilon}}(n), \underline{\mathrm{I}}(n), \underline{0}\right)\right] \tag{7.58}$$

To evaluate the mean square value of the timing error $\underline{\varepsilon}$, some approximations have to be done:

1. A new Taylor expansion of the TED output is defined as follows:

$$\underline{\mathrm{S}}\left(\underline{\mathrm{x}}_{\underline{\varepsilon}}(n), \underline{\mathrm{I}}(n), \underline{0}\right) \approx \underline{\mathrm{S}}\left(\underline{\mathrm{x}}_{\underline{0}}(n), \underline{\mathrm{I}}(n), \underline{0}\right) + \left[\frac{\partial \underline{\mathrm{S}}}{\partial \underline{\varepsilon}} \left(\underline{\mathrm{x}}_{\underline{0}}(n), \underline{\mathrm{I}}(n), \underline{0}\right)\right] \underline{\varepsilon}(n) \tag{7.59}$$

The Taylor expansion proposed here is identical to the one previously proposed in (7.48), in the special cases where the TED output only depends on the difference $\underline{\hat{\varepsilon}} - \underline{\varepsilon}$, which implies (7.56).

2. The noisy fluctuation of the Jacobian matrix is supposed to be small as compared with its mean value:

$$\frac{\partial \underline{S}}{\partial \underline{\varepsilon}} \left(\underline{x}_{\underline{0}}(n), \underline{I}(n), \underline{0}\right) \approx \frac{\partial \underline{S}_I}{\partial \underline{\varepsilon}} \left(\underline{I}(n), \underline{0}, \underline{0}\right) \triangleq \underline{\underline{K}}_d(n) \tag{7.60}$$

This matrix provides the instantaneous (pattern-dependent) multiuser TED sensitivity.

3. The closed loop transfer function is time variant because the Jacobian matrix in the Taylor expansion depends on the specific sequence of symbols contained in the signal. To obtain a time-invariant system, and to ensure the decoupling between the timing errors, the matrix gain $\underline{\underline{K}}_c(n)$ can be taken as the inverse of the Jacobian matrix:

$$\underline{\underline{K}}_c(n) = \underline{\underline{k}} \cdot \underline{\underline{K}}_d(n)^{-1} \tag{7.61}$$

where $\underline{\underline{k}}$ is a diagonal matrix of constant values. In these conditions, the feedback loop equation can be expressed in the z-domain as follows:

$$\underline{\varepsilon}(n) = \underline{\underline{H}}_s(z)\, \underline{N}_t(n) \tag{7.62}$$

where the loop transfer function $\underline{\underline{H}}_s(z)$ and the equivalent noise $\underline{N}_t(n)$ are given by:

$$\begin{aligned} \underline{\underline{H}}_s(z) &\triangleq \left[(1-z)\, \underline{\underline{E}}_K - \underline{\underline{F}}(z)\, \underline{\underline{k}}\right]^{-1} \underline{\underline{F}}(z)\, \underline{\underline{k}} && (7.63) \\ \underline{N}_t(n) &\triangleq \underline{\underline{K}}_d(n)^{-1} \left[\underline{S}_0\left(\underline{0}, \underline{0}\right) + \underline{N}_s\left(\underline{I}(n), \underline{0}, \underline{0}\right)\right. \\ &+ \left.\underline{N}_n\left(\underline{n}(n), \underline{I}(n), \underline{0}, \underline{0}\right)\right] && (7.64) \end{aligned}$$

This equivalent noise is made up of three contributions (in volts): a constant bias, a pattern-dependent instantaneous bias ('self-noise'), and a contribution of the additive noise. These contributions are transformed into a vector of equivalent noise (in seconds) by the inverse of the time-variant TED sensitivity matrix $\underline{\underline{K}}_d(n)$. The correlation matrix of the timing error vector is:

$$\mathrm{E}_{I,n}\left\{\underline{\varepsilon}(n)\underline{\varepsilon}^T(n)\right\} = \frac{T}{2\pi} \int_{-\frac{\pi}{T}}^{\frac{\pi}{T}} \underline{\underline{H}}_s(e^{j\omega T})\, \underline{\underline{\gamma}}_{N_t}(e^{j\omega T})\, \underline{\underline{H}}_s^H(e^{j\omega T})\, d\omega \tag{7.65}$$

where the cross-spectrum of the equivalent noise $\underline{\underline{\gamma}}_{N_t}(e^{j\omega T})$ is the z transform of the equivalent noise correlation:

$$\underline{\underline{\Gamma}}_{N_t}(k) = \mathrm{E}_{I,n}\left\{\underline{\mathrm{N}}_t(n)\,\underline{\mathrm{N}}_t^T(n+k)\right\} \tag{7.66}$$

4. A last approximation consists in neglecting the pattern-dependent nature of the TED sensitivity. The average value $\underline{\underline{\mathrm{K}}}_d = \mathrm{E}_I\left\{\underline{\underline{\mathrm{K}}}_d(n)\right\}$ is used in the computations, which provides a simple expression for the equivalent noise correlation:

$$\underline{\underline{\Gamma}}_{N_t}(k) \approx \underline{\underline{\mathrm{K}}}_d^{-1}\left[\underline{\underline{\Gamma}}_{S_0}(k) + \underline{\underline{\Gamma}}_{N_s}(k) + \underline{\underline{\Gamma}}_{N_n}(k)\right]\underline{\underline{\mathrm{K}}}_d^{-T} \tag{7.67}$$

with

$$\underline{\underline{\Gamma}}_{S_0}(k) = \underline{\mathrm{S}}_0\left(\underline{0},\underline{0}\right)\ \underline{\mathrm{S}}_0\left(\underline{0},\underline{0}\right)^T, \tag{7.68}$$

$$\underline{\underline{\Gamma}}_{N_s}(k) = \mathrm{E}_I\left\{\underline{\mathrm{N}}_s\left[\underline{\mathrm{I}}\left(n\right),\underline{0},\underline{0}\right]\ \underline{\mathrm{N}}_s\left[\underline{\mathrm{I}}\left(n+k\right),\underline{0},\underline{0}\right]^T\right\}, \tag{7.69}$$

and

$$\begin{aligned}\underline{\underline{\Gamma}}_{N_n}(k) = \mathrm{E}_{n,I}\{&\underline{\mathrm{N}}_n\left[\underline{\mathrm{n}}(n),\underline{\mathrm{I}}(n),\underline{0},\underline{0}\right] \\ &\underline{\mathrm{N}}_n\left(\underline{\mathrm{n}}(n+k),\underline{\mathrm{I}}(n+k),\underline{0},\underline{0}\right)^T\Big\}\end{aligned} \tag{7.70}$$

This approximation is also equivalent to the use of the M-CRB instead of the true DD-CRB.

Figure 7.2 illustrates the feedback joint timing synchronizer, and Figure 7.3 gives the associated linearized model.

7.6 Multiuser timing error detectors (TED)

7.6.1 Symbol rate multiuser TED

The optimal symbol-rate multiuser TED can be derived from the log-likelihood function in (7.38). Its input is made of N_f consecutive blocks of noise-whitened matched filter outputs $\tilde{y}_{p,\underline{\varepsilon}}(n)$. The optimal TED output is given by :

$$\underline{\mathrm{T}}\left(\underline{\tilde{\mathrm{y}}}_{\underline{\varepsilon}},\underline{\mathrm{I}},\underline{\hat{\varepsilon}}\right) = \underline{\mathrm{S}}\left(\underline{\tilde{\mathrm{y}}}_{\underline{\varepsilon}},\underline{\mathrm{I}},\underline{\hat{\varepsilon}}\right) - \underline{\mathrm{S}}\left(\mathrm{E}_n\left\{\underline{\tilde{\mathrm{y}}}_{\underline{\hat{\varepsilon}}}\right\},\underline{\mathrm{I}},\underline{\hat{\varepsilon}}\right) \tag{7.71}$$

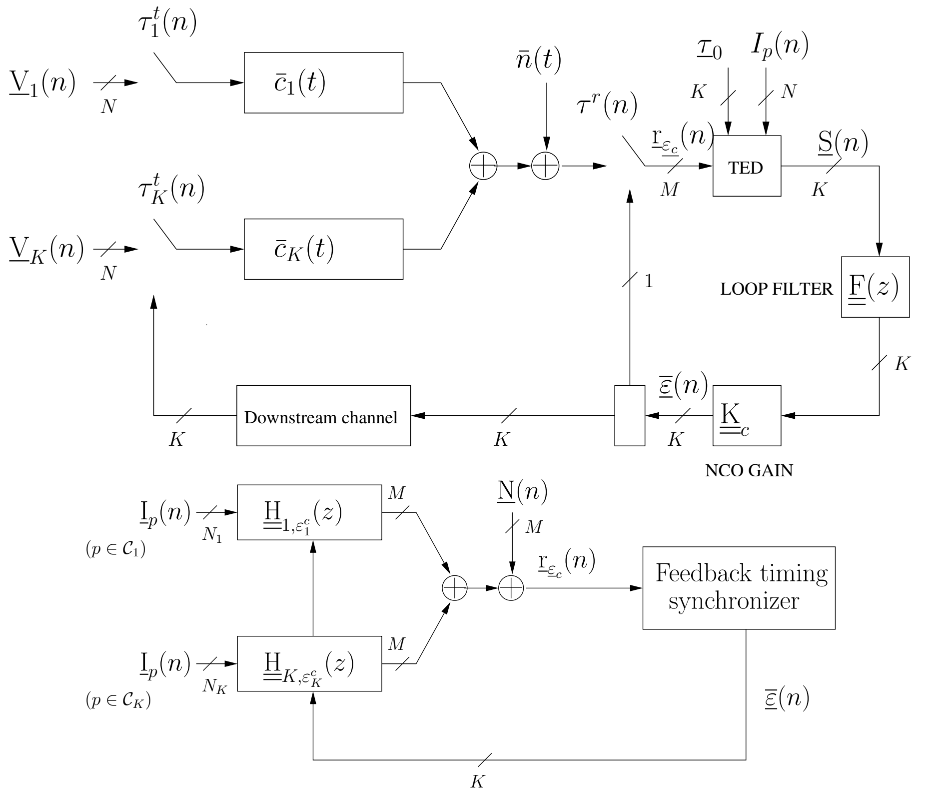

Figure 7.2: *Feedback joint timing synchronization*

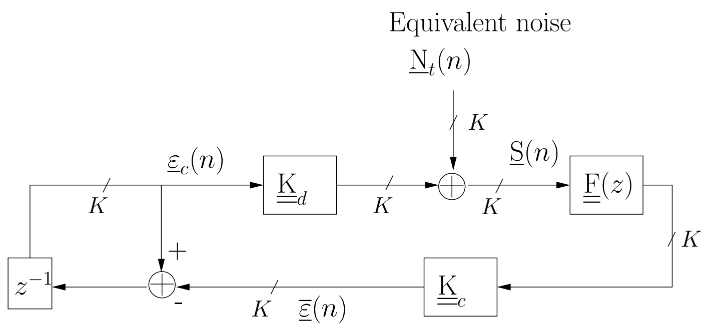

Figure 7.3: *Linearized model of the feedback joint timing synchronizer*

where the k-th element of the S-vector in last equation is given by

$$S_k\left(\underline{\tilde{\mathrm{y}}}_{\underline{\varepsilon}}, \underline{\mathrm{I}}, \underline{\hat{\varepsilon}}\right) = \sum_{n'=-n_1}^{n_2} \sum_{p=1}^{N} \tilde{y}_{p,\underline{\varepsilon}}\left(n+n'\right) \cdot \left[\sum_{m=-\infty}^{+\infty} \sum_{p' \in \mathcal{C}_k} \dot{\tilde{x}}_{pp',\hat{\varepsilon}_k}(m)\; I_{p'}\left(n+n'-m\right)\right] \quad (7.72)$$

The second term in (7.71) does not depend on the measurements $\underline{\tilde{\mathrm{y}}}_{\underline{\varepsilon}}$. This term is equivalent to the first term obtained when $\underline{\varepsilon} = \underline{\hat{\varepsilon}}$ and the additive noise is absent. It can be computed in the receiver on the basis of the known data symbols $I_p(n)$ and the known interference coefficients $x_{pp',\hat{\varepsilon}_k}(n)$ and $\dot{x}_{pp',\hat{\varepsilon}_k}(n)$, and subtracted from the first term. This correction term actually guarantees that the proposed timing estimate is unbiased for any combination of data symbols. In other words, it guarantees that the S-hypercurve is all-zero for $\underline{\varepsilon} = \underline{\hat{\varepsilon}}$, and it makes the self-noise equal to zero.

The S-hypercurve of the detector is given by

$$\begin{aligned}\left[\underline{\mathrm{S}}_0\left(\underline{\varepsilon}, \underline{\hat{\varepsilon}}\right)\right]_k &= \mathrm{E}_{n,I}\left\{S_k\left(\underline{\tilde{\mathrm{y}}}_{\underline{\varepsilon}}, \underline{\mathrm{I}}, \underline{\hat{\varepsilon}}\right)\right\} \quad (7.73)\\ &= N_f\, \sigma_I^2 \sum_{m=-\infty}^{+\infty} \sum_{p=1}^{N} \sum_{p' \in \mathcal{C}_k} \tilde{x}_{pp',\varepsilon_k}(m)\, \dot{\tilde{x}}_{pp',\hat{\varepsilon}_k}(m)\end{aligned}$$

The Jacobian matrix associated with the S-hypercurve is diagonal :

$$\frac{\partial \underline{\mathrm{S}}_0}{\partial \underline{\hat{\varepsilon}}}\left(\underline{\varepsilon}, \underline{\hat{\varepsilon}}\right) = N_f\, \sigma_I^2\, \mathrm{diag}\left\{\dot{\mathcal{X}}_k^2\right\}_{1 \le k \le K}. \quad (7.74)$$

where $\dot{\mathcal{X}}_k^2$ is defined in (7.45).

The following simplifications can be considered to obtain a practical low-complexity symbol-rate multiuser TED :

1. **Self-noise and bias mitigation.** Even if the implementation of the self-noise mitigation term (second term in (7.71)) is theoretically possible in the receiver, it increases the complexity of the TED. For this reason, it is usually discarded in practical implementations. In that case, a special attention should be paid to the possible bias associated with the S-hypercurve. In a single-user scenario, the bias and self-noise are generally equal to zero when the sequences of interference

coefficients $\tilde{x}_{pp'}(n)$ satisfy a number of symmetry properties :

$$\begin{aligned} &\tilde{x}_{pp,0}(-n) = \tilde{x}_{pp,0}(n) && \dot{\tilde{x}}_{pp,0}(0) = 0 \\ &\tilde{x}_{pp',0}(-n) = \tilde{x}_{p'p,0}(n) && \dot{\tilde{x}}_{pp',0}(-n) = -\dot{\tilde{x}}_{p'p,0}(n). \end{aligned} \tag{7.75}$$

These properties are indeed satisfied by the sequences of interference coefficients associated with the noise-whitened matched filter bank receiver, but also by those associated with the simple matched filter bank receiver and the IIR linear MMSE joint detector. The symmetry is lost in the case of a DF joint detector : in that case, a self-noise mitigation term is required to maintain a good level of performance (see a discussion in [67], for example).

In a multiuser scenario, bias and self-noise are present even in the case of symmetric sequences of interference coefficients. To show this, we rewrite the S-hypercurve (7.73) of the multiuser TED as follows :

$$\begin{aligned} [\underline{\mathrm{S}}_0\left(\underline{0},\underline{0}\right)]_k = N_f\,\sigma_I^2 \Bigg\{ &\sum_{p'\in\mathcal{C}_k} \tilde{x}_{p'p',0}(0)\,\dot{\tilde{x}}_{p'p',0}(0) \\ &+ \sum_{p'\in\mathcal{C}_k}\sum_{p\in\mathcal{C}_k,p>p'} \left[\tilde{x}_{pp',0}(0)\,\dot{\tilde{x}}_{pp',0}(0) + \tilde{x}_{p'p,0}(0)\,\dot{\tilde{x}}_{p'p,0}(0)\right] \\ &+ \sum_{m=1}^{+\infty}\sum_{p'\in\mathcal{C}_k}\sum_{p\in\mathcal{C}_k} \left[\tilde{x}_{pp',0}(m)\,\dot{\tilde{x}}_{pp',0}(m) + \tilde{x}_{p'p,0}(-m)\,\dot{\tilde{x}}_{p'p,0}(-m)\right] \\ &+ \sum_{m=-\infty}^{+\infty}\sum_{p\notin\mathcal{C}_k}\sum_{p'\in\mathcal{C}_k} \tilde{x}_{pp',0}(m)\,\dot{\tilde{x}}_{pp',0}(m) \Bigg\}. \end{aligned} \tag{7.76}$$

The first three terms in (7.76) are indeed zero when the symmetry properties in (7.75) are satisfied. The fourth term in (7.76) is not zero, however. This term is specific to the multiuser scenario. It can be shown in the same fashion that the self-noise level is increased in a multiuser scenario. Actually, the symmetry properties in (7.75) ensure that

$$\sum_{k=1}^{K}\left[\mathrm{E}_n\left\{S_k\left(\underline{\tilde{\mathrm{y}}}_0,\underline{\mathrm{I}},\underline{0}\right)\right\}\right] = 0, \tag{7.77}$$

that is to say the sum of self-noises is always zero, but the individual self-noise is non-zero. For this reason, we believe that the self-noise mitigation term should not be discarded in a multiuser configuration, in order to keep a good level of performance.

2. **Noise whitening and scaling.** The noise-whitening filter is not really implemented, as it is not useful for the primary task of the receiver, which is the detection of the information symbol sequences. So, it is preferable that the TED builds its estimate of the timing error on the basis of simple matched filter outputs, for example. The corresponding timing error variance is higher, of course. Actually the role of the noise-whitening filter is twofold :

   (a) It suppresses the correlation between successive noise samples at the output of a given matched filter branch, as well as the mutual correlation between noise samples at the output of different matched filter branches.

   (b) It normalizes the noise variance in each branch.

   While the first effect (whitening) is definitely lost when the noise-whitening filter is not implemented, the second effect (scaling) can be easily recovered by an appropriate modification of the weights associated with each symbol $I_{p'}(n+n'-m)$ in (7.72). The optimal weights can be computed easily. They are inversely proportional to the noise variance $\sigma_{w_p}^2$ at the p-th matched filter output. The modified TED output is

$$S_k\left(\underline{\mathrm{y}}_{\underline{\varepsilon}}, \underline{\mathrm{I}}, \hat{\underline{\varepsilon}}\right) = \sum_{n'=-n_1}^{n_2} \sum_{p=1}^{N} y_{p,\underline{\varepsilon}}\left(n+n'\right) \cdot \left[\sum_{m=-\infty}^{+\infty} \sum_{p' \in \mathcal{C}_k} \frac{\dot{x}_{pp',\hat{\varepsilon}_k}(m)}{\sigma_{w_p}^2} I_{p'}\left(n+n'-m\right)\right] \quad (7.78)$$

3. **Sequence truncature and selection.** The detector proposed in (7.78) correlates the received signal $y_{p,\underline{\varepsilon}}(n)$ with the N_k symbol sequences $I_{p'}(n)$ with $p' \in \mathcal{C}_k$, using appropriate weights. A further simplification can be proposed by selecting a subset of sequences $I_{p'}(n)$ and/or by truncating these sequences.

   In a single-user ($K=1$) and single-carrier ($N=1$) scenario, this truncature leads to the so-called Mueller and Müller algorithm [68]. The unique sequence of interference coefficient first derivatives $\dot{x}_0(m)$ is there approximated by its 3 central coefficients as follows :

$$\dot{x}_0(m) \approx \{\cdots, 0, +\mathbf{1}, \mathbf{0}, -\mathbf{1}, 0, \cdots\}\,. \quad (7.79)$$

This provides the well-known Mueller and Müller TED :

$$S\left(\underline{\mathrm{y}}_{\varepsilon}, \underline{\mathrm{I}}, \hat{\varepsilon}\right) = \sum_{n'=-n_1}^{n_2} y_{\varepsilon}\left(n+n'\right)\ \left[I(n+n'+1) - I(n+n'-1)\right]. \tag{7.80}$$

This approximation is effective in the single-carrier scenario as the largest part of the available energy $\sum_n \dot{x}_0^2(n)$ is indeed located in the coefficients in position ± 1.

The extension of the Mueller and Müller algorithm to the case of FB-based transmission ($N > 1$) is not trivial. Let us consider a single-user system ($K = 1$) and a paraunitary FB $\underline{\underline{\mathrm{S}}}(z)$ of size N. The polyphase matrix $\underline{\underline{\dot{\mathrm{X}}}}_0(z)$ associated with the N^2 sequences of interference coefficient first derivatives $\dot{x}_{pp',0}(n)$ is given by

$$\underline{\underline{\dot{\mathrm{X}}}}_0(z) = \underline{\underline{\mathrm{S}}}^H(z)\, \underline{\underline{\dot{\mathrm{G}}}}_0(z)\, \underline{\underline{\mathrm{S}}}(z) \tag{7.81}$$

where $\underline{\underline{\dot{\mathrm{G}}}}_0(z)$ is the Toeplitz polyphase matrix associated with $\dot{g}(nT_c)$, the channel correlation first derivative, sampled at the chip rate. The total energy associated with the sequences $\dot{x}_{pp',0}(n)$ is

$$\begin{aligned}
\dot{\mathcal{X}}^2 &= \sum_{n=-\infty}^{+\infty} \sum_{p=1}^{N} \sum_{p'=1}^{N} \dot{x}_{pp',0}^2(n) && (7.82)\\
&= \int_{-\pi}^{\pi} \mathrm{tr}\left\{ \underline{\underline{\dot{\mathrm{X}}}}_0^H(e^{j\Omega})\, \underline{\underline{\dot{\mathrm{X}}}}_0(e^{j\Omega}) \right\} \frac{\mathrm{d}\Omega}{2\pi} && (7.83)\\
&= \int_{-\pi}^{\pi} \mathrm{tr}\left\{ \underline{\underline{\dot{\mathrm{G}}}}_0^H(e^{j\Omega})\, \underline{\underline{\dot{\mathrm{G}}}}_0(e^{j\Omega}) \right\} \frac{\mathrm{d}\Omega}{2\pi} && (7.84)\\
&= N \sum_{n=-\infty}^{+\infty} \dot{g}(nT_c)^2 && (7.85)
\end{aligned}$$

where (7.84) comes from the paraunitary property of the FB. So, the quantity $\dot{\mathcal{X}}^2$ is independent of the selected FB. From (7.85), it actually depends on N, but this only reflects that the observation window associated with a burst of N_f blocks has a duration of $N_f N T_c$ which obviously increases proportionally to N. While the sequence $\dot{g}(nT_c)$ itself can be effectively restricted to the central coefficients $\dot{g}(\pm T_c)$, it is a priori unclear how the available energy $\sum_n \dot{g}^2(nT_c)$ is distributed among the various sequences $\dot{x}_{pp',0}(n)$ through Equation (7.81). This redistribution of the energy depends on the selected FB.

A determining factor is the length of the signatures $s_p(n)$ constituting the FB. Let $N' = (n_b + 1)\, N$ be the signature length, which means that each signature extends over $n_b + 1$ successive blocks of symbols. This parameter n_b is equal to 0 for the basic FBs such as Walsh-Hadamard codes or DMT basis functions (see Section 4.2.3). The FB polyphase matrix is given by

$$\underline{\underline{\mathrm{S}}}(z) = \sum_{n=0}^{n_b} \underline{\underline{\mathrm{S}}}_n\, z^{-n}. \tag{7.86}$$

Introducing (7.86) into (7.81), we get

$$\underline{\underline{\dot{\mathrm{X}}}}_0(z) = \sum_{m=-n_b}^{n_b} \left[\sum_{n=0}^{n_b} \underline{\underline{\mathrm{S}}}_n^H\, \underline{\underline{\dot{\mathrm{G}}}}_0(z)\, \underline{\underline{\mathrm{S}}}_{n-m} \right] z^{-m} \tag{7.87}$$

For large values of N, the Toeplitz polyphase matrix $\underline{\underline{\dot{\mathrm{G}}}}_0(z)$ can be approximated by the zero-order term in its z-transform expansion :

$$\underline{\underline{\dot{\mathrm{G}}}}_0(z) = \sum_{n=-\infty}^{+\infty} \underline{\underline{\dot{\mathrm{G}}}}_{0,n}\, z^{-n} \approx \underline{\underline{\dot{\mathrm{G}}}}_{0,0}. \tag{7.88}$$

It comes that

$$\underline{\underline{\dot{\mathrm{X}}}}_0(z) \approx \sum_{m=-n_b}^{n_b} \underline{\underline{\dot{\mathrm{X}}}}_{0,n}\, z^{-n} \quad \text{with} \quad \underline{\underline{\dot{\mathrm{X}}}}_{0,n} = \sum_{n=0}^{n_b} \underline{\underline{\mathrm{S}}}_n^H\, \underline{\underline{\dot{\mathrm{G}}}}_{0,0}\, \underline{\underline{\mathrm{S}}}_{n-m}. \tag{7.89}$$

The sequences $\dot{x}_{pp',0}(n)$ can thus be truncated to the interval $n \in \{-n_b, n_b\}$ without a significant loss of performance. The performance loss decreases with N. An important special case is that of FBs extending over a single block, i.e. $n_b = 0$. For these FBs, the sequences $\dot{x}_{pp',0}(n)$ can be restricted to their central coefficient $n = 0$. The corresponding energy is

$$\begin{aligned}
\sum_{p=1}^{N} \sum_{p'=1}^{N} \dot{x}_{pp',0}^2(n) &= \operatorname{tr}\left\{ \left[\underline{\underline{\mathrm{S}}}^H\, \underline{\underline{\dot{\mathrm{G}}}}_{0,0}\, \underline{\underline{\mathrm{S}}} \right]^H \left[\underline{\underline{\mathrm{S}}}^H\, \underline{\underline{\dot{\mathrm{G}}}}_{0,0}\, \underline{\underline{\mathrm{S}}} \right] \right\} && (7.90)\\
&= \operatorname{tr}\left\{ \underline{\underline{\dot{\mathrm{G}}}}_{0,0}^H\, \underline{\underline{\dot{\mathrm{G}}}}_{0,0} \right\} && (7.91)\\
&= N \left[\dot{g}^2(0) + 2 \sum_{n=1}^{N-1} \frac{N-k}{N}\, \dot{g}^2(nT_c) \right], && (7.92)
\end{aligned}$$

which rapidly converges to (7.85) for large values of N. The simplified multiuser TED incorporating the proposed truncature is given by

$$S_k\left(\underline{\mathrm{y}}_{\underline{\varepsilon}}, \underline{\mathrm{I}}, \underline{\hat{\varepsilon}}\right) = \sum_{n'=-n_1}^{n_2} \sum_{p=1}^{N} y_{p,\underline{\varepsilon}}\left(n+n'\right) \cdot \left[\sum_{p'\in\mathcal{C}_k} \frac{\dot{x}_{pp',\hat{\varepsilon}_k}(0)}{\sigma_{w_p}^2} I_{p'}\left(n+n'\right)\right] \quad (7.93)$$

for FBs with a single-block extension. A further approximation can be investigated by replacing the MF outputs $\underline{\mathrm{y}}_{\underline{\varepsilon}}$ with MMSE JD outputs $\hat{\underline{\mathrm{I}}}_{\underline{\varepsilon}}$ in the last equation, and by updating the weighting coefficients accordingly.

7.6.2 Early-late multiuser TED

The optimal multiuser TED at the channel output can be derived from the log-likelihood function in (7.17). It requires the implementation of a bank of derivated matched filters $\dot{h}_{pk}(-t)$ in the receiver. Its input is made of N_f consecutive blocks of derivated matched filter outputs $\dot{y}_{p,\underline{\varepsilon}}(n)$. The optimal TED output is given by :

$$\underline{\mathrm{T}}\left(\dot{\underline{\mathrm{y}}}_{\underline{\varepsilon}}, \underline{\mathrm{I}}, \underline{0}\right) = \underline{\mathrm{S}}\left(\dot{\underline{\mathrm{y}}}_{\underline{\varepsilon}}, \underline{\mathrm{I}}, \underline{0}\right) - \underline{\mathrm{S}}\left(\mathrm{E}_n\left\{\dot{\underline{\mathrm{y}}}_{\underline{0}}\right\}, \underline{\mathrm{I}}, \underline{0}\right) \quad (7.94)$$

where the k-th element of the S-vector in last equation is given by

$$S_k\left(\dot{\underline{\mathrm{y}}}_{\underline{\varepsilon}}, \underline{\mathrm{I}}, \underline{0}\right) = \sum_{n'=-n_1}^{n_2} \sum_{p\in\mathcal{C}_k} \dot{y}_{p,\underline{\varepsilon}}\left(n+n'\right)\, I_p\left(n+n'\right). \quad (7.95)$$

The S-hypercurve of the detector is given by

$$\left[\underline{\mathrm{S}}_0\left(\underline{\varepsilon}, \underline{0}\right)\right]_k = N_f\, \sigma_I^2 \sum_{p\in\mathcal{C}_k} \dot{x}_{pp,\varepsilon_k}(0). \quad (7.96)$$

The Jacobian matrix associated with the S-hypercurve is diagonal :

$$\frac{\partial \underline{\mathrm{S}}_0}{\partial \underline{\varepsilon}}\left(\underline{\varepsilon}, \underline{0}\right) = N_f\, \sigma_I^2\, \mathrm{diag}\left\{\sum_{p\in\mathcal{C}_k} \ddot{x}_{pp,\varepsilon_k}(0)\right\}_{1\le k\le K}. \quad (7.97)$$

The following simplifications can be considered to obtain a practical low-complexity symbol-rate multiuser TED :

1. **Self-noise and bias mitigation.** Like for the optimal symbol-rate multiuser TED, the second term in (7.94) is a self-noise mitigation term. Even with perfectly symmetrical interference waveforms, there would be a significant self-noise if that term was suppressed, due to the multiuser configuration.

2. **MMSE joint detector and scaling.** The bank of matched filters can be replaced by a joint detector designed with an MMSE criterion. The optimal linear MMSE JD is actually obtained by cascading the matched filter bank with a MIMO filter whose purpose is to reduce the residual interference. Let $w_p(t)$ be the filter associated with the MMSE-JD p-th branch. The continuous-time interference waveforms are given by $\overline{x}_{pp',\underline{\varepsilon}}(n) = \left[\bar{h}_{p'k}(t) \otimes w_p(t)\right](nT + \varepsilon)$. The idea here is thus to replace the bank of derivated matched filters $\dot{h}_{pk}(-t)$ by a bank of derivated MMSE filters $\dot{w}_p(t)$. The TED based on joint detector outputs $\hat{I}_p(n)$ is given by

$$S_k\left(\dot{\hat{\underline{\mathrm{I}}}}_{\underline{\varepsilon}}, \underline{\mathrm{I}}, \underline{0}\right) = \sum_{n'=-n_1}^{n_2} \sum_{p \in \mathcal{C}_k} \lambda_p^2 \, \dot{\hat{I}}_{p,\underline{\varepsilon}}\left(n+n'\right) \, I_p\left(n+n'\right) \qquad (7.98)$$

where the weights λ_p^2 associated with each JD branch have to be optimized. These weights are necessary as the SNR of each subchannel should be taken into account. Indeed, while the amplitudes of the matched filter outputs depend on the channel attenuation associated with each subchannel, that of the JD output are normalized. The optimal weights λ_p^2 in (7.98) can be shown to be

$$\lambda_p^2 = \frac{\ddot{\overline{x}}_{pp}(0)}{\int_{-\infty}^{+\infty} \dot{w}_p^2(t)\,\mathrm{d}t}. \qquad (7.99)$$

The optimal weights in (7.99) are effectively equal to 1 in the case where the detector filters $w_p(t)$ are identical to the matched filters $h_{pk}(-t)$.

3. **Early-late implementation.** The ultimate approximation of the optimal TED is obtained by replacing the derivative in (7.98) by a finite difference :

$$\dot{\hat{I}}_{p,\underline{\varepsilon}}\left(n\right) \approx \hat{I}_{p,\underline{\varepsilon}^+}\left(n\right) - \hat{I}_{p,\underline{\varepsilon}^-}\left(n\right) \qquad (7.100)$$

where $\varepsilon_k^+ = \varepsilon_k + T_s$ and $\varepsilon_k^- = \varepsilon_k - T_s$ for all k. The $2N$ sequences $\hat{I}_{p,\underline{\varepsilon}^+}\left(n\right)$ and $\hat{I}_{p,\underline{\varepsilon}^-}\left(n\right)$ can be obtained by feeding the bank of MMSE filters with adequately delayed or anticipated versions of the received fractional-rate sequence. The resulting early-late multiuser TED is finally

$$S_k\left(\left\{\underline{\hat{\mathrm{I}}}_{\underline{\varepsilon}^+},\underline{\hat{\mathrm{I}}}_{\underline{\varepsilon}^-}\right\},\underline{\mathrm{I}},\underline{0}\right)=\sum_{n'=-n_1}^{n_2}\sum_{p\in\mathcal{C}_k}\lambda_p^2\left[\hat{I}_{p,\underline{\varepsilon}^+}\left(n+n'\right)\right.$$
$$\left.-\hat{I}_{p,\underline{\varepsilon}^-}\left(n+n'\right)\right]I_p\left(n+n'\right) \quad (7.101)$$

The fundamental drawback associated with the early-late TED is the need to compute $3N$ different JD outputs for each block of received samples.

7.7 Asymptotic performance for an AWGN channel

In this section, the relative performance of the various TEDs are compared in a simplified scenario with a single user ($K = 1$) and a frequency-flat channel ($c(t) = \delta(t-\tau)$). The channel correlation $g(t)$ (including the shaping filter in the transmitter and the matched filter) corresponds to a full raised cosine filter with roll-off α. The variance of the timing estimate is given by

$$\sigma_\varepsilon^2=\frac{1}{N_f\,N}\left(\frac{\sigma_I^2}{N_0/2}\right)^{-1}F\left(\alpha\right). \quad (7.102)$$

The first factor in (7.102) represents the length of the observation window, expressed in number of chip durations T_c. The second factor gives the effect of the signal-to-noise ratio on the timing detection. The last factor $F\left(\alpha\right)$, that only depends on the roll-off, is specific of the selected TED.

Table 7.1 gives the expression of the inverse factor $F\left(\alpha\right)^{-1}$ for the different TEDs presented in this chapter. The second column corresponds to a single-carrier system, while the third column is for a paraunitary FB-based transmission with N subchannels. The timing error variance associated with the first three TEDs is known to be independent of the FB and independent of N. The common factor $F\left(\alpha\right)$ can thus be computed analytically in the single-carrier case as a function of α. The last line corresponds to the truncated symbol-rate TED proposed in (7.93). The associated timing error variance only depends on N and α, and can be computed numerically by using (7.92). The computed functions $F\left(\alpha\right)$ are displayed in Figure 7.4.

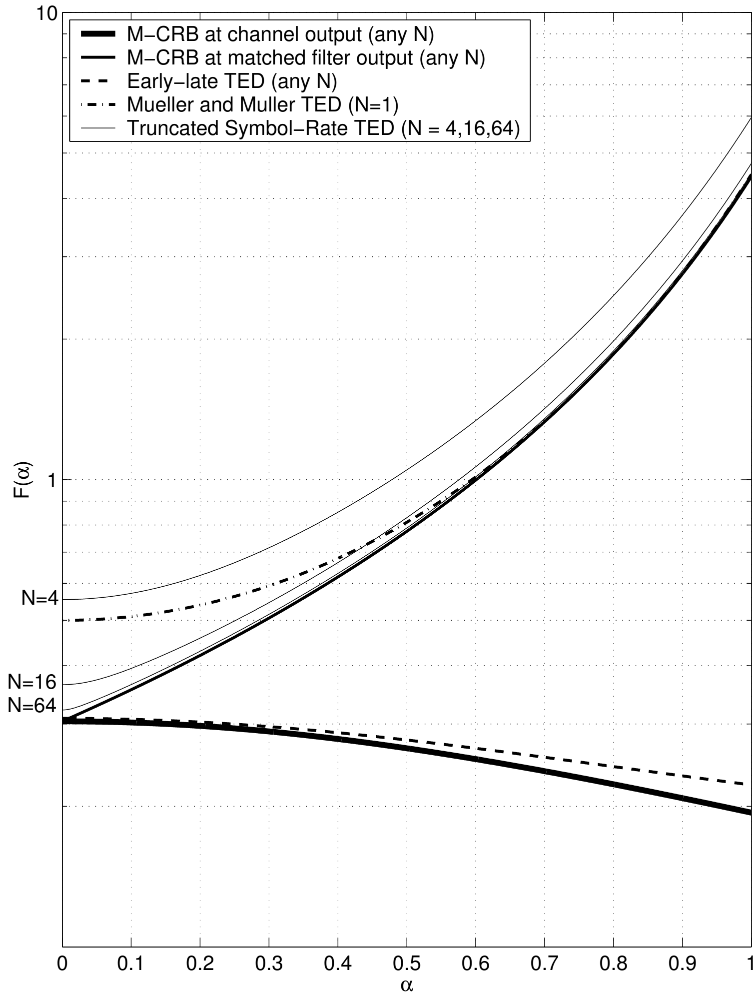

Figure 7.4: *Relative performance of various single-user TEDs for a frequency-flat channel*

Table 7.1: $F(\alpha)^{-1}$ *of various timing error detectors*

TED	$N=1$	$N>1$
ML (channel output)	$-\ddot{g}(0)$	$-\dfrac{1}{N}\sum_{p=1}^{N}\ddot{x}_{pp}(0)$
Early-late	$\dfrac{2\dot{g}^2(T_s)}{1-g(2T_s)}$	$\dfrac{2\left[\frac{1}{N}\sum_{p=1}^{N}\dot{x}_{pp}(T_s)\right]^2}{1-\frac{1}{N}\sum_{p=1}^{N}x_{pp}(2T_s)}$
ML (MF output)	$\sum_{n=-\infty}^{+\infty}\dot{g}^2(nT_c)$	$\dfrac{1}{N}\sum_{p=1}^{N}\sum_{p'=1}^{N}\sum_{n=-\infty}^{+\infty}\dot{x}^2_{pp'}(n)$
Mueller and Müller	$\sum_{n=-1}^{1}\dot{g}^2(nT_c)$	
Truncated symbol-rate		$\dfrac{1}{N}\sum_{p=1}^{N}\sum_{p'=1}^{N}\dot{x}^2_{pp'}(0)$

Table 7.2: *M-CRB for an uplink 5-user powerline channel with CAP-OFDMA and $N = 128$ tones*

	User 2	User 5	User 10	User 15	User 20
$\frac{2E_k}{N_0}$ [dB]	94.08	89.42	77.52	73.13	73.05
$\frac{1}{2\pi} W_k$ [MHz]	4.49	4.90	2.79	1.94	1.12
$N_f \frac{\sigma^2_{\varepsilon_k}}{T_c'^2}$ [dB]	-103.99	-100,09	-83,32	-75,74	-70,91

This figure provides a basic understanding of the performance loss that can be expected from :

- The implementation of a ML symbol-rate TED rather than an optimal ML TED using channel outputs.
- The early-late approximation.
- The truncature loss associated with the Mueller and Müller TED ($N = 1$).
- The truncature loss associated with the symbol rate multiuser TED proposed in this work ($N > 1$).

7.8 Applications to the powerline channel

Let us now illustrate the performance of the proposed multiuser timing error detectors with a practical example. We consider the 5-user uplink PLC system introduced in Section 5.8. The multiple access method is CAP-OFDMA with $N = 128$ tones. The power spectral density of the transmitted signals resulting from the signature allocation algorithm is presented in Figure 5.11.

Table 7.2 gives the M-CRB on the timing error variance, according to equation (7.32). The first row gives the user-specific global SNR $\frac{2\mathcal{E}_k}{N_0}$ (in dB), obtained by combining the received energy in all subchannels allocated to each user. The second row gives the mean bandwidth $\frac{W_k}{2\pi}$ (in MHz) of the received signals. Finally, the third row gives the minimum timing error variance, normalized with respect to the squared chip duration $T_c'^2$.

The performance computation of practical TEDs requires the analysis of the continuous-time interference waveforms $x_{pp'}(t)$ obtained by combining the equivalent channel $h_{p'k}(t)$ with the p-th branch of the receiver :

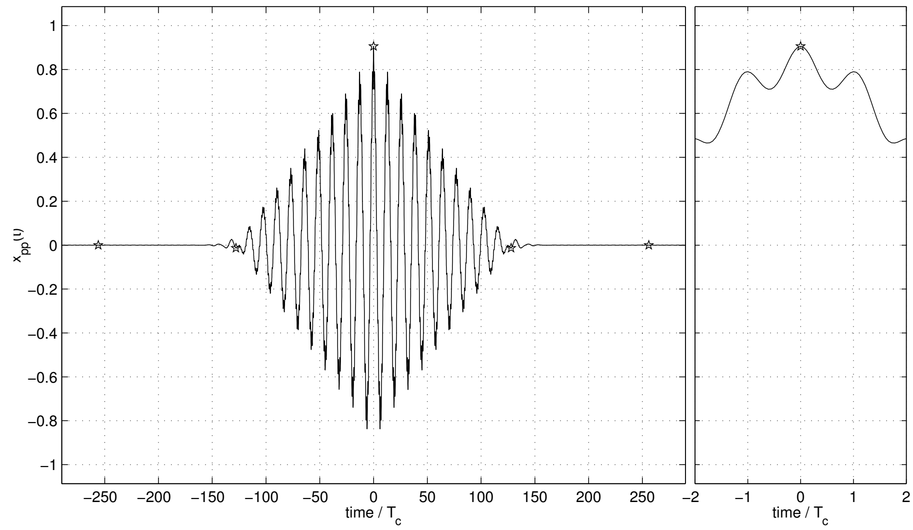

Figure 7.5: *Continuous-time interference waveform* $x_{10,10}(t)$ *(CAP-OFDMA,* $N = 128$*).*

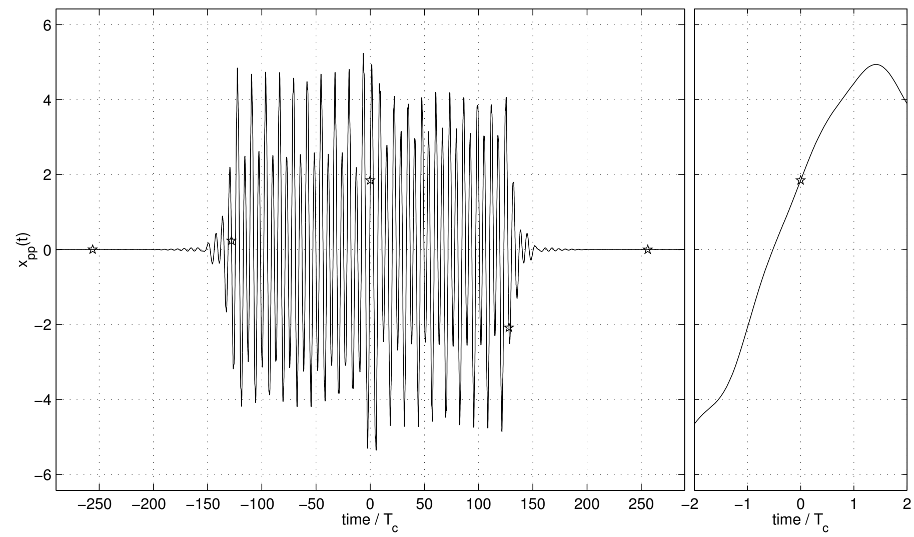

Figure 7.6: *Continuous-time interference waveform* $x_{40,20}(t)$ *(CAP-OFDMA,* $N = 128$*).*

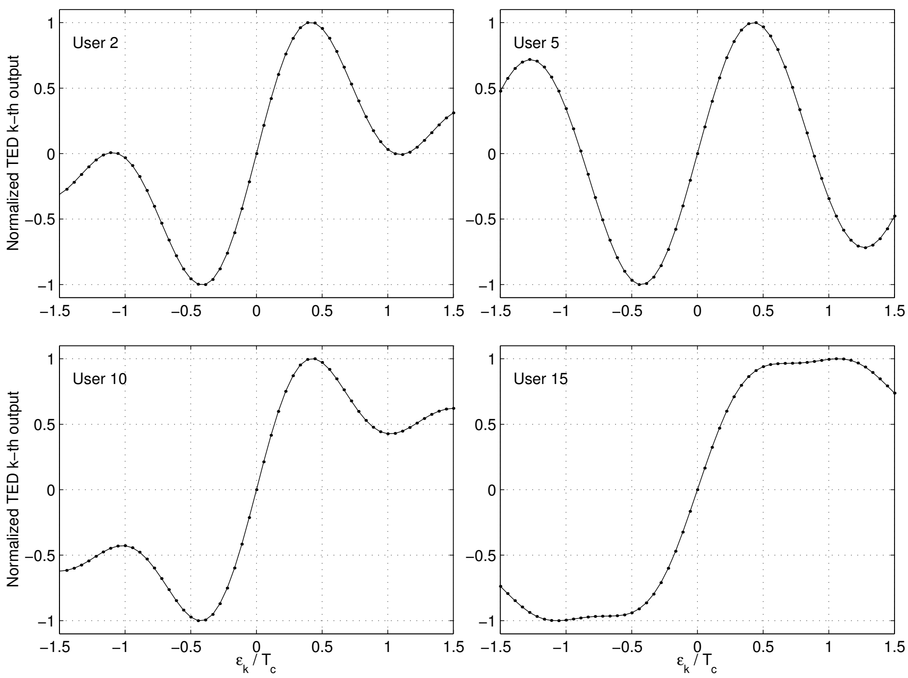

Figure 7.7: *Normalized S-curves for the Early-Late multiuser TED (CAP-OFDMA with a matched filter bank receiver).*

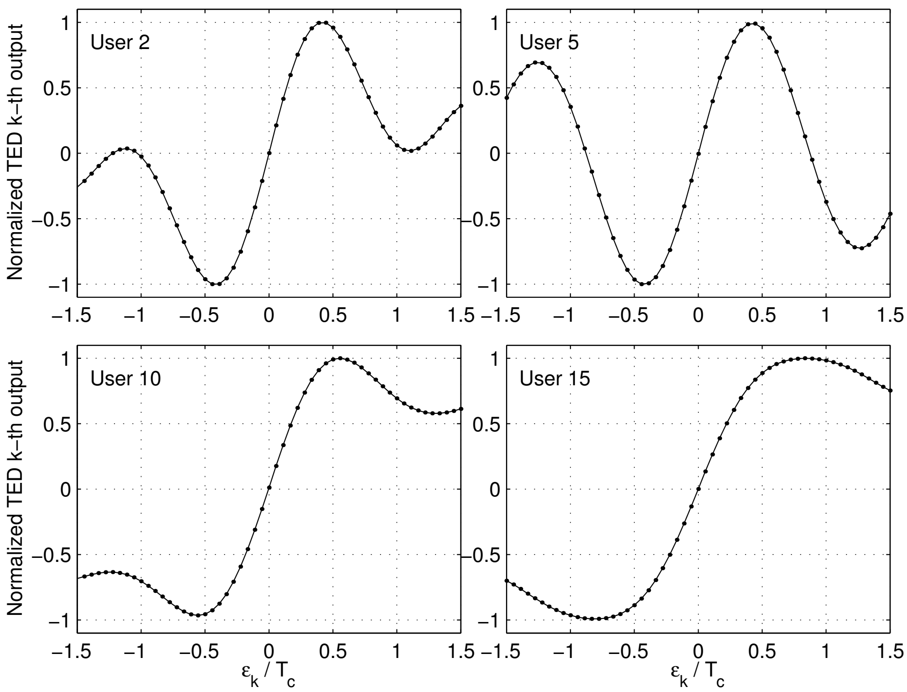

Figure 7.8: *Normalized S-curves for the Symbol-rate multiuser TED (CAP-OFDMA with a matched filter bank receiver).*

Table 7.3: *Timing error variance of the Early-Late multiuser TED vs. M-CRB [dB]*

Detector	User 2	User 5	User 10	User 15	User 20	weights
MF bank	0.08	0.01	0.20	0.09	0.21	λ_p^2
	0.15	0.04	0.29	0.45	0.38	1
MMSE-JD	**2.86**	**3.37**	**3.28**	**5.44**	**11.54**	λ_p^2
	4.15	6.77	4.47	8.14	24.52	1

- Figure 7.5 illustrates the $x_{10,10}(t)$ waveform obtained with a matched filter receiver. Signature 10 being allocated to user 15, this waveform corresponds to $h_{10,15}(t) \otimes h_{10,15}(-t)$. The stars represent the nominal interference coefficients obtained by sampling the continuous-time interference waveform at the symbol rate $1/T$, with a sampling phase equal to zero. The concavity of the waveform at the origin $\ddot{x}_{pp}(0)$, which can be evaluated on the right part of Figure 7.5, determines the contribution of the p-th subchannel to the Early-Late estimation of the k-th timing error ε_k.

- Figure 7.6 illustrates the $x_{40,20}(t)$ waveform obtained with a matched filter receiver. Signatures 20 and 40 are both allocated to user 10, so this waveform corresponds to $h_{20,10}(t) \otimes h_{40,10}(-t)$. The slope of the waveform at the origin $\dot{x}_{pp'}(0)$, which can be evaluated on the right part of Figure 7.6, determines the contribution of the p-th receiver branch and the p'-th subchannel to the Symbol-Rate estimation of the k-th timing error ε_k.

Figures 7.7 and 7.8 give the normalized S-curves for the Early-Late and Symbol-Rate multiuser TEDs, respectively, placed at the output of a matched filter bank receiver. The combination of these individual S-curves generates the global S-hypercurve. The slope of the S-curve at the origin determines the performance of the TED.

Finally, Tables 7.3 and 7.4 give the relative performance (in dB) of various Early-Late and Symbol-Rate timing error detectors as compared to the M-CRB. The timing error variance is computed according to Equation (7.54). Self-noise compensation is assumed in the computations, so the timing error variance is basically equal to the variance of the additive noise term, divided by the squared slope of the TED S-curve. In each case, two kinds of receivers are considered : a matched filter bank (which is ideal for the

Table 7.4: *Timing error variance of the Symbol-Rate multiuser TED vs. M-CRB [dB]*

Detector	User 2	User 5	User 10	User 15	User 20	weights
MF Bank	0.86	0.52	2.35	1.72	1.64	$\dot{x}_{pp'}/\sigma^2_{w_p}$
	0.84	1.78	8.93	7.36	3.28	$\dot{x}_{pp'}$
MMSE-JD	**3.89**	**3.91**	**4.29**	**5.95**	**6.51**	$\dot{x}_{pp'}/\sigma^2_{w_p}$
	26.48	22.49	5.56	6.27	8.00	$\dot{x}_{pp'}$

timing estimation but not for the symbol estimation), or a linear MMSE-JD. The performance of the proposed TEDs are found to be very close to the M-CRB as long as a matched filter bank is implemented in the receiver. The performance loss is important if the MF bank is replaced by a linear MMSE-JD, especially for the users with highly dispersive channels.

7.9 Conclusion

In this Chapter, the issue of Decision-Directed multiuser timing synchronization has been addressed, assuming perfect decisions. The FB-based multiple access system has been redefined to include user-specific timing errors ε_k.

The Cramèr-Rao bound (CRB) on the joint timing error estimator has been derived. The bound actually varies with the symbols used for transmission. The average bound (i.e. the expectation with respect to the transmitted symbols) is not easy to compute. For long observation windows, it has been shown to converge to the so-called modified CRB. The M-CRB, given by Equation (7.32), is easy to compute: it only depends on the total SNR $\frac{2\mathcal{E}_k}{N_0}$, the mean square bandwidth W_k^2, and the length of the observation window. Moreover, the timing errors related to different users are uncorrelated. In a single-user system, the M-CRB is independent of the selected FB. In a multiuser system, however, the signature allocation algorithm has a strong impact on the distribution of the user-specific timing error variances.

Another M-CRB can be computed by considering the problem of timing estimation at the symbol rate, i.e. at the output of a matched filter bank. The symbol-rate M-CRB has been derived. It is higher than the M-CRB computed at the channel output.

Feedforward and feedback *multiuser* timing error tracking structures have been analyzed in detail. A number of approximations have been identified, providing a tractable expression (7.54) for the correlation matrix of the joint timing estimation error.

Two practical multiuser TEDs have been proposed. The first one (7.93) is derived from the maximum-likelihood symbol-rate multiuser TED (7.71). Two major approximations are proposed : the noise-whitening filter is discarded and replaced by a well-chosen set of weights, and the sequences of interference waveform slopes are truncated to their central coefficient. The second one (7.101) is derived from the maximum-likelihood multiuser TED at channel output (7.94). The proposed approximations are the use of an MMSE joint detector (with an appropriate set of weights) rather than the matched filter bank, and the early-late implementation of the first-order derivative.

The performance of the proposed TEDs has been tested with the 5-user PLC channel. The performance loss with respect to the M-CRB is acceptable, and comparable for both systems.

Chapter 8

Conclusions

8.1 Achievements

This work was devoted to the analysis of high-speed multiuser communication systems suited to frequency-selective channels. The initially aimed application was the powerline outdoor access network, that is to say a strongly branched wired distribution network, intended to provide a simultaneous link with a network head-end to multiple subscribers physically distributed along the main cable. The results obtained in this work have a large scope, however, and are not restricted to the powerline scenario.

The starting point was the derivation of realistic models for the channel transfer functions. This task (and only this one) was performed in the specific powerline context. The multiconductor transmission line theory (MTL) has been applied to various cable structures which are commonly used in power distribution networks. Several modes of propagation, the so-called eigenmodes, have been identified : they correspond to fixed distributions of voltages and currents in the conductors, that propagate with their own propagation factor $e^{-\gamma z}$ along the multiconductor structure. The fundamental characteristics of these eigenmodes (voltage and current distribution, characteristic impedance, phase velocity, attenuation factor) have been analyzed in a wide frequency range (0.5 to 25 MHz) and related to the fundamental cable characteristics (geometry, size, materials). This made it possible to model accurately the transfer function of a complete access network including a high number of cable segments, derivations, and terminations. A specific multi-dimensional scattering matrix algebra was developed to achieve that goal. The obtained channel transfer functions were also analyzed in the light of a simple multipath model, which allowed an intuitive interpretation. As expected, the channel responses are highly frequency-selective, with deep notches at some frequencies. Furthermore, the channel attenuation increases dramatically, not only with the distance of the subscriber with respect to the head-end, but also and above all with the number of taps between transmitter and receiver. Finally, the different contributions to the end-to-end channel impulse responses have been identified.

The issue of multiuser channel capacity has then been addressed, with an original approach aiming at providing fair data rates to every subscriber. The concept of balanced capacity has been proposed as an efficient way to satisfy fairness constraints among K users with different channel qualities. Ranging through the K-dimensional capacity region is achieved by modifying the power allocation among the users, and the decoding order in a successive decoding strategy. The optimal power allocation with balanced rates constraints was shown to be obtained in two steps: a first power allocation is computed, that maximizes a linear combination of individual data rates, then the weights of the linear combination (the so-called 'relative priorities') are iteratively updated until the balanced rates constraints are satisfied. Closed-form solutions for the first step have been derived for a memoryless multiuser channel, as a function of the channel gains and the user relative priorities. Specific power allocations have been obtained for the downlink and the uplink. Then a Newton-Raphson based algorithm has been proposed for the iterative updating of the relative priorities. It was shown to converge within a few iterations. These results have been extended to the case of frequency-selective multiuser channels. Different types of power constraints have been considered (PSD-sum, power-sum, individual power). The critical scenario is that of an individual power constraint : in that case, both power and rate constraints have to be satisfied simultaneously by every user, which makes the convergence of the proposed algorithm very slow. An alternative method, based on the Iterative Multiuser Water-Filling algorithm, has been proposed for that scenario. Finally, the issue of the optimal FDMA balanced rates computation has been addressed, with a simple constraint on the PSD-sum. An efficient subchannel allocation algorithm has been proposed. The balanced capacities obtained with these algorithms represent useful bounds on the effective bit rates that can be expected from practical transmission systems. They provide guidelines about the appropriate way of shaping the spectral density of the different transmitted signals as a function of the channel frequency responses, and also about the optimal joint decoding strategy.

A general transmission scheme was called for, that was able to shape the signal power spectral density with a high degree of flexibility. The proposed solution is the implementation of a paraunitary filter bank in the transmitters. Every user is provided with the ability to modulate any subset of filters with mutually independent sequences of PAM symbols. Furthermore, adaptive modulation can be used, i.e. the size of every PAM constellation can be adapted to the subchannel conditions. The maximal power spectral density of the transmitted signals is easily controlled as the sum of the modulated signature waveforms represents a flat PSD in the whole bandwidth. The classical modulation methods proposed in the powerline community (single-carrier, OFDM, CDMA) are obtained by selecting the appropriate FB (unit matrix, DFT filters, Hadamard codes). A further improvement lies in the combination of FB transmission with the CAP (Carrierless Amplitude-Phase) technique, which provides a flexible passband transmission scheme that is required if the available bandwidth does not extend down to the zero frequency. For a given choice of the implemented FB, the optimization of the transmission scheme is performed by selecting the appropriate signature allocation among the users, the appropriate power allocation among the different signatures, and the appropriate constellation size in each subchannel. The potential performance of different FBs can be compared. It basically depends on the flexibility offered by the FB : this flexibility increases with the number of subchannels and with the frequency-selectivity of the FB. An alternative solution lies in the use of CDMA with periodic long codes. With this solution, the optimization of the transmitter is not required any more as the average PSD of the transmitted signals is flat. So, every user is ensured to get an average performance, whatever the transfer function of its channel. User inequalities can be compensated by using a simple power control. The overall system complexity is reduced, at the price of a reduced bit rate performance. The choice for this solution rather than another depends on the trade-off between performance and complexity. Actually another argument disqualifies the choice of the long-code CDMA technique : the need to update the coefficients of the joint detector at the symbol rate. The complexity of the receiver is indeed dramatically increased in the long-code scenario.

MMSE linear and decision-feedback joint detectors have been derived in the general context of FB-based multiuser transmission. Infinite detectors have been firstly derived, as their performance provide an upper bound on the performance that can be expected from their FIR counterparts. In particular, it has been shown that the sum-capacity of the frequency-selective multiuser channel could be achieved by means of an infinite DF-JD followed by ideal AWGN decoders. The DF-JD thus provides an efficient way, from an information-theoretical point of view, of transforming a frequency-selective multiple access channel into a set of independent subchannels. The choice of the implemented paraunitary FB does not affect the achievable capacity in a single-user system. In a multiuser system, however, the achievable bit rates strongly depend on the signature allocation, and the flexibility associated with this allocation is related to the choice of the FB. The complexity associated with the derivation of practical FIR MMSE joint detectors has been analyzed in detail, with a particular attention for time-varying JDs suited to CDMA with periodic long codes.

The various reasons for which the practical bit rates that can be achieved with the proposed transmission (FB-based modulation) and detection (MMSE DF joint detection) system are lower than those offered by the true capacity region are now summarized :

1. *The power spectral density of the transmitted signals is constrained by the selected FB.* Furthermore, in a practical system, every signature in the FB should be allocated to a single user, which reduces the power allocation process to an integer optimization problem.

2. *The IIR DF-JD can only remove the causal interference.* Successive decoding among the users is not possible with the proposed joint detection structure. This does not affect the sum-capacity of the multiuser channel, but the global capacity region is reduced.

3. *Practical implementations of the MMSE JD suffer from an excess MSE* due to :

    - The use of a finite size (FIR) JD rather than the optimal IIR version.
    - The residual timing offset and/or jitter that remains after non-ideal timing synchronization.
    - Imperfect channel knowledge in the receiver, resulting in the derivation of JD coefficients that are not perfectly matched to the true channel responses.

4. *A finite-complexity decoder is used in every subchannel.* This is modeled by the SNR-gap $\Gamma > 1$ used to compute the bit rate that can be expected for a given received SINR. With a perfect decoder, the SNR-gap would be equal to 1. Actually the concept of capacity (which

implies error-free transmission) is here replaced by that of maximum bit rate for a given error probability.

5. *Error propagation must be taken into account.* Decision errors reduce the performance of both the DF-JD and the decision-directed channel estimator and timing synchronizer, which results into an increased MSE.

6. *The transmitted symbols do not have a Gaussian distribution - The size of the PAM constellation associated with every subchannel must be an integer.*

All these performance degradations must be taken into account in the derivation of a fair signature allocation among the users.

The sensitivity of the multiuser FB-based transmission scheme to channel estimation errors and timing synchronization errors has been derived. Using first-order approximations, closed-forms expressions have been obtained.

Finally, the issue of decision-directed maximum-likelihood timing synchronization has been properly extended to the multiuser scenario, assuming perfect decisions. The modified Cramèr-Rao bound has been derived and has been shown to be a simple extension of the single-user bound. Both timing estimation based on channel output and symbol-rate timing estimation have been investigated, and the associated bounds have been compared. Popular timing error detector structures (Early-late, Mueller and Müller) have been extended to the multiuser FB-based transmission scheme.

8.2 Perspectives

This thesis covered a number of important aspects related to the design of an efficient multiuser communication system : channel modeling, power allocation, multiuser capacity, modulation and multiple access, joint detection, robustness against channel estimation errors, and timing synchronization. There remains several issues that can be used as starting points for future studies. Here is a non-exhaustive list of items that would deserve a specific treatment in the prolongation of the present work :

- Transmission over multiconductor cables can be modeled as a *Multi-Input Multi-Output (MIMO)* system if all conductors are available up to the customer premises. Several sources could be used to couple the signal onto the system, and several sensors could be used to recover it at the opposite end. This concept of 'multiconductor diversity' has the potential to increase the capacity of powerline access networks. It is closely related to the concept of antenna diversity in wireless communication systems.

- The issue of *optimal duplexing* can be addressed. Rather than considering the global system as the concatenation (in different time slots) of a broadcast channel (downlink) and a multiple access channel (uplink), the transmission in both directions could be simultaneous, and a global optimal power allocation could be derived, possibly with fairness constraints among the users and among both directions of transmission.

- Concerning the issue of multiuser capacity associated with frequency-selective channels, different *power constraints* have been considered separately : power-sum vs. individual power, power itself vs. power spectral density. In a practical system, the effective constraint could be mixed : a global power budget $\bar{P}$ would have to be allocated to all users, with a maximum individual power $P_k > \bar{P}/K$ for every user, a maximum individual PSD γ_k at every frequency, and a maximum PSD-sum $\bar{\gamma} > \bar{P}/B$. A generalized power allocation algorithm with balanced rates constraints could be derived in this context.

- The introduction of *repeaters* in the network has the potential to increase the global capacity of the PLC system. The number of repeaters, and their position along the distribution cable, have to be optimized according to the network configuration. The balanced capacity of the system can be selected as the optimization variable. The power re-transmitted by the repeaters has to be taken into account in the global power budget.

- *Filter Bank design* can be investigated to improve the global system performance. In this work, the flexibility was restricted to the signature allocation among the users for a fixed signature set.

- The issue of *channel coding* has been discarded in this work. The decoder has been considered as a black box offering a fixed coding gain that was incorporated in the expression of the SNR-gap. The effect of a simple coding scheme on the proposed system performance should be modeled more accurately. Furthermore, joint modulation and coding techniques can be investigated to improve the global system performance.

- Maximum likelihood *channel estimation* techniques have to be designed and analyzed properly in the proposed multiuser FB-based context.

- The *time-varying* characteristic of the channel has not been considered. It has been assumed that the channel responses were sufficiently stable within periods of several seconds or even minutes, which enables the use of fixed joint detectors that can be computed explicitly on the basis of the channel estimates. Adaptive structures must be investigated if the channel changes are faster.

- Finally, the *noise scenario* used in this work is not representative of the powerline channel. A complete system should be robust against narrowband and impulsive noise, and incorporate specific features aimed at mitigating these types of noises.

Curriculum vitae

Thierry Sartenaer
Born in Namur, Belgium, on November, 21st 1974.

Education

1992 - 1997 : Electrical Engineer, Université catholique de Louvain.
Orientation : Telecommunications.
Master thesis : "Analyse des données altimétriques Topex-Poséidon obtenues en cas de pluie."

Professional background

1997-1998 : Modem design engineer, Alcatel ETCA, Charleroi, Belgium. Collaborations with Alcatel Bell (Antwerp, Belgium) and Alcatel Espace (Toulouse, France).

1998-2004 : Teaching assistant, Communications and Remote Sensing Laboratory, Université catholique de Louvain.

Research

1998-2004 : PhD in Applied Sciences, Université catholique de Louvain.
Subject : "Multiuser communications over frequency selective wired channels and applications to the powerline access network."

List of publications

Journal papers

- Thierry Sartenaer, Luc Vandendorpe, "Resource allocation for frequency-selective multiple access channels with adaptive QAM modulation", *Revue HF Tijdschrift (Belgian Journal of Electronics and Communications)*, n° 1 / 2001, pp. 51-63.

- Jérôme Louveaux, Luc Vandendorpe, Thierry Sartenaer, "Cyclic prefixed single carrier and multicarrier transmission : bit rate comparison", *IEEE Communications Letters*, Volume 7, N° 4, April 2003, pp. 180-182.

- Jérôme Louveaux, Luc Vandendorpe, Thierry Sartenaer, "Early-late timing recovery with decision-feedback equalizers", *IEEE Communications Letters*, Volume 7, N° 7, July 2003, pp. 332-334.

- Thierry Sartenaer, Luc Vandendorpe, "Linear and DF joint detectors for DS-CDMA communications using periodic long codes", *IEEE Transactions on Signal Processing*, Volume 52, N°7, July 2004, pp. 2080-2091.

- Thierry Sartenaer, Jérôme Louveaux, Luc Vandendorpe, "Balanced capacity of downlink and uplink wireline multiuser channels", submitted to *IEEE Transactions on Communications*, February 2004.

Conferences papers

- Thierry Sartenaer, François Horlin, Luc Vandendorpe, "DMT-FDMA as a multiple access technique for wideband upstream powerline communications", ISPLC'2000 - International Symposium on Powerline Communications, April 5-7, 2000, Limerick, Ireland, pp. 89-96.

- Thierry Sartenaer, François Horlin, Luc Vandendorpe, "Multiple access techniques for wideband upstream powerline communications: CAP-CDMA and DMT-FDMA ", ICC'2000 - IEEE International Conference on Communications, New Orleans, USA, June 18-22, 2000, Vol. 2, pp. 1064-1068.

- Thierry Sartenaer, Luc Vandendorpe, "Resource allocation for frequency-selective multiple access channels with adaptive QAM modulation", SCVT 2000 - IEEE Symposium on Communications and Vehicular Technology, October 19, 2000, Leuven, Belgium, pp. 178-185.

- Thierry Sartenaer, Luc Vandendorpe, "Resource allocation for frequency-selective multiple access channels with adaptive QAM modulation", Proceedings URSI Forum 2000, December 2000, Brussels, Belgium.

- Thierry Sartenaer, Paul Delogne, "Powerline cables modelling for broadband communications", ISPLC'2001 - International Symposium on Powerline Communications, April 4-6, 2001, Malmö, Sweden, pp. 331-337.

- Luc Vandendorpe, François Horlin, Thierry Sartenaer, "FSLE and FDSF joint detectors for long code DS-CDMA codes", ICASSP'01 - IEEE International Conference on Acoustics, Speech and Signal Processing, May 7-11, 2001, Salt Lake City, USA, Vol. 4, pp. 2261-2264.

- Luc Vandendorpe, François Horlin, Thierry Sartenaer, "Linear and DF joint detectors for DS-CDMA communications using periodic long codes", ICC'2001 - IEEE International Conference on Communications, June 11-15, 2001, Helsinki, Finland, Vol. 3, pp. 821-825.

- Fawzi Issa, Thierry Sartenaer et al., "Analysis of power line communication networks using a new approach based on scattering parameters matrix", IEEE International Symposium on Electromagnetic Compatibility, August 19-23, 2002, Minneapolis, USA, Vol. 2, pp. 1043-1047.

- Thierry Sartenaer, Luc Vandendorpe, "About the sensitivity of FB modulations to timing offsets", ICC'2002, IEEE International Conference on Communications, April 28 - May 2, 2002, New York, USA, Vol. 3, pp. 1485-1489.

- Thierry Sartenaer, Luc Vandendorpe, "ML DA timing estimation for multiuser FB uplink transmission over static time dispersive channels", EUSIPCO'2002 - XI European Signal Processing Conference, September 3-6, 2002, Toulouse, France, Vol. II, pp. 35-38 (Invited paper).

- Jérôme Louveaux, Luc Vandendorpe, Thierry Sartenaer, "Cyclic prefixed single carrier and multicarrier transmission : bit rate compari-

son", SCVT'02 - IEEE Symposium on Communications and Vehicular Technology, Louvain-la-Neuve, Belgium, October 2002, pp. 61-64.

- Thierry Sartenaer, Luc Vandendorpe, "Balanced capacity of wireline multiaccess channels", EUSIPCO'2004 - XII European Signal Processing Conference, September 7-10, 2004, Vienna, Austria.

COST contributions

- Thierry Sartenaer, François Horlin, Luc Vandendorpe, "Multiple access techniques for wideband upstream powerline communications: CAP-CDMA and DMT-FDMA ", COST 262 - 4th Management Commitee Meeting, Barcelona, Spain, November 22-23, 1999, TD020.

- Thierry Sartenaer, Paul Delogne, "Powerline cables modelling for broadband communications", COST 262 - 2nd PLCs Group Meeting, Malmö, Sweden, April 4-6, 2001, TD054.

Reports

- Luc Vandendorpe, François Deryck, Gaetan Castelein, Thierry Sartenaer, "Study of Peak-to-Average power Ratio (PAR) reduction techniques in DMT systems", Confidential Report with Alcatel Bell, September 1998, 81 pp.

Bibliography

[1] K. Dostert, *Powerline communications.* Upper Saddle River: Prentice Hall, 2001.

[2] *Proc. 3rd International Symposium on Powerline Communications and its applications (ISPLC'99)*, (Lancaster, UK), March 30 - April 1 1999.

[3] M. Zimmermann and K. Dostert, "A multipath model for the powerline channel," *IEEE Transactions on Communications*, vol. 50, pp. 553–559, April 2002.

[4] S. Galli and T. C. Banwell, "Modeling the indoor power line channel: new results and modem design considerations," in *Proc. IEEE Consumer Communications and Networking Conference, CCNC'04*, (Las Vegas, USA), January 2004.

[5] T. Sartenaer and P. Delogne, "Powerline cables modelling for broadband communications," in *Proc. International Symposium on Powerline Communications, ISPLC'2001*, (Malmö, Sweden), pp. 331–338, April 2001.

[6] M. Zimmermann and K. Dostert, "Analysis and modeling of impulsive noise in broadband power line communications," *IEEE Transactions on Electromagnetic Compatibility*, vol. 44, pp. 249–258, February 2002.

[7] IEC 61000-3-8, *Electromagnetic Compatibility (EMC) - Part 3: Limits - Section 8: Signaling on Low-Voltage Electrical Installations - Emission Levels, Frequency Bands and Electromagnetic Disturbance Levels.* IEC, Geneva, Switzerland, 2002.

[8] CISPR Publication 22, *Information Technology Equipment - Radio Disturbance Characteristics - Limits and Methods of Measurements.* CISPR, Geneva, Switzerland, 2002.

[9] CENELEC EN50065-1, *Signaling on Low Voltage Electrical Installations in the Frequency Range 3 kHz to 148.5 kHz.* CENELEC, Brussels, Belgium, 2002.

[10] CENELEC and ETSI, *Draft, Questionnaire to the National Standardization Organizations on Setting the Limits of Permissible Radiated Disturbance Emissions from Telecommunication Networks.* CENELEC, Brussels, Belgium, 2002.

[11] FCC, *Code of Federal Regulations Title 47 Telecommunication: Chapter I FCC Part 15 - Radio Frequency Devices.* Washington, DC, USA, 2002.

[12] M. Götz, M. Rapp, and K. Dostert, "Power line channel characteristics and their effect on communication system design," *IEEE Communications Magazine*, vol. 42, pp. 78–86, April 2004.

[13] E. Biglieri, "Coding and modulation for a horrible channel," *IEEE Communications Magazine*, vol. 41, pp. 92–98, May 2003.

[14] J. Fox and M. S. Obaidat, *International Journal of Communication Systems - Special Issue: Powerline Communications and Applications*, vol. 16. Wiley InterScience, June 2003.

[15] W. Liu, H. Widmer, and P. Raffin, "Broadband PLC access systems and field deployment in European power line networks," *IEEE Communications Magazine*, vol. 41, pp. 114–118, May 2003.

[16] G. Jee, R. D. Rao, and Y. Cern, "Demonstration of the technical viability of PLC systems on medium- and low-voltage lines in the United-States," *IEEE Communications Magazine*, vol. 41, pp. 108–112, May 2003.

[17] F. Issa and T. S. et al., "Analysis of power line communication networks using a new approach based on scattering parameters matrix," in *Proc. IEEE International Symposium on Electromagnetic Compatibility 2002*, (Minneapolis, USA), pp. 1043–1047, August 2002.

[18] T. Sartenaer and L. Vandendorpe, "Balanced capacity of wireline multiaccess channels," in *Proc. EUSIPCO 2004*, (Vienna, Austria), September 2004.

[19] T. Sartenaer and L. Vandendorpe, "Resource allocation for frequency-selective multiple access channels with adaptive QAM modulation," *Revue HF Tijdschrift (Belgian Journal of Electronics and Communications)*, no. 1, pp. 51–63, 2001.

[20] J. Louveaux, L. Vandendorpe, and T. Sartenaer, "Cyclic prefixed single carrier and multicarrier transmission : bit rate comparison," *IEEE Communications Letters*, vol. 7, pp. 180–182, April 2003.

[21] T. Sartenaer and L. Vandendorpe, "Linear and DF joint detectors for ds-cdma communications using periodic long codes," *IEEE Transactions on Signal Processing*, vol. 52, July 2004.

[22] T. Sartenaer, F. Horlin, and L. Vandendorpe, "DMT-FDMA as a multiple access technique for wideband upstream powerline communications," in *Proc. ISPLC'2000*, (Limerick, Ireland), pp. 89–96, April 2000.

[23] T. Sartenaer, F. Horlin, and L. Vandendorpe, "Multiple access techniques for wideband upstream powerline communications : CAP-CDMA and DMT-FDMA," in *Proc. IEEE ICC'2000*, (New-Orleans), pp. 1064–1068, June 2000.

[24] T. Sartenaer and L. Vandendorpe, "Resource allocation for frequency-selective multiple access channels with adaptive QAM modulation," in *Proc. IEEE SCVT 2000 Benelux*, (Leuven, Belgium), pp. 178–185, October 2000.

[25] L. Vandendorpe, F. Horlin, and T. Sartenaer, "FSLE and FDSF joint detectors for long code DS-CDMA codes," in *Proc. IEEE ICASSP'01*, (Salt Lake City, USA), pp. 2261–2264, May 2001.

[26] L. Vandendorpe, F. Horlin, and T. Sartenaer, "Linear and DF joint detectors for DS-CDMA communications using periodic long codes," in *Proc. IEEE ICC'2001*, (Helsinki, Finland), pp. 821–825, June 2001.

[27] J. Louveaux, L. Vandendorpe, and T. Sartenaer, "Cyclic prefixed single carrier and multicarrier transmission : bit rate comparison," in *Proc. IEEE SCVT 2002 Benelux*, (Louvain-la-Neuve, Belgium), pp. 61–64, October 2002.

[28] T. Sartenaer and L. Vandendorpe, "About the sensitivity of FB modulations to timing offsets," in *Proc. IEEE ICC'2002*, (New-York, USA), p. 2002, April-May 2002.

[29] T. Sartenaer and L. Vandendorpe, "ML DA timing estimation for multiuser FB uplink transmission over static time dispersive channels," in *Proc. EUSIPCO 2002*, (Toulouse, France), pp. 35–38, September 2002.

[30] C. R. Paul, *Analysis of Multiconductor Transmission Lines.* Wiley-Interscience, 1994.

[31] T. Bostoen and O. V. de Wiel, "Modeling the low-voltage power distribution network in the frequency band from 0.5 to 30 MHz for broadband powerline communication," in *IEEE Transactions on Signal Processing*, (Zürich, Switzerland), February 2000.

[32] P. Delogne, "Calcul des paramètres d'une ligne multiconducteurs," tech. rep., Communications and Remote Sensing Laboratory, Université catholique de Louvain, October 1999.

[33] P. Delogne, "The twisted pair as a transmission channel," tech. rep., Communications and Remote Sensing Laboratory, Université catholique de Louvain, August 1998.

[34] R. A. Horn and C. A. Johnson, *Matrix analysis.* Cambridge University Press, 1985.

[35] A. VanderVorst, *Transmission, propagation et rayonnement.* De Boeck Université, Bruxelles, 1995.

[36] M. R. Spiegel, *Formules et tables de mathématiques.* McGraw-Hill, Paris (série Schaum), 1993.

[37] A. VanderVorst, *Electromagnétisme - champs et circuits.* De Boeck Université, Bruxelles, 1994.

[38] C. Y. Wong, R. S. Cheng, K. B. Letaief, and R. D. Murch, "Multiuser OFDM with adaptive subcarrier, bit, and power allocation," *IEEE Journal on Selected Areas in Communications*, vol. 17, pp. 1747–1758, October 1999.

[39] S. Verdú, "Multiple-access channels with memory with and without frame synchronism," *IEEE Transactions on Information Theory*, vol. 35, pp. 605–619, May 1989.

[40] R. S. Cheng and S. Verdú, "Gaussian multiaccess channels with ISI : capacity region and multiuser water-filling," *IEEE Transactions on Information Theory*, vol. 39, pp. 773–785, May 1993.

[41] D. N. C. Tse and S. V. Hanly, "Multiaccess fading channels - part I : Polymatroid structure, optimal resource allocation and throughput capacities," *IEEE Transactions on Information Theory*, vol. 44, pp. 2796–2815, November 1998.

[42] C. Zeng, L. M. C. Hoo, and J. M. Cioffi, "Efficient water-filling algorithms for a Gaussian multiaccess channel with ISI," in *Proc. IEEE VTC Fall'2000*, (Boston, USA), pp. 1072–1077, September 2000.

[43] C. Zeng, L. M. C. Hoo, and J. M. Cioffi, "Optimal water-filling algorithms for a Gaussian multiaccess channel with intersymbol interference," in *Proc. IEEE ICC'2001*, (Helsinki, Finland), pp. 2421–2427, June 2001.

[44] W. Yu, W. Rhee, S. Boyd, and J. M. Cioffi, "Iterative water-filling for Gaussian vector multiple access channels," in *Proc. IEEE ISIT'2001*, (Washington, USA), p. 322, June 2001.

[45] W. Yu, W. Rhee, S. Boyd, and J. M. Cioffi, "Iterative water-filling for Gaussian vector multiple-access channels," *IEEE Transactions on Information Theory*, vol. 50, pp. 145–152, January 2004.

[46] W. Yu and J. M. Cioffi, "FDMA capacity of Gaussian multiple-access channels with ISI," *IEEE Transactions on Communications*, vol. 50, pp. 102–111, January 2002.

[47] S. Diggavi, "Multiuser DMT : a multiple access modulation scheme," in *Proc. IEEE Globecom 1996*, (London, UK), pp. 1566–1570, November 1996.

[48] S. O. Ohno, P. A. Anghel, G. B. Giannakis, and Z. Q. Luo, "Multicarrier multiple access is sum-rate optimal for block transmission over circulant ISI channels," in *Proc. IEEE ICC'2002*, (New-York, USA), pp. 1656–1660, May 2002.

[49] P. Viswanath and D. N. C. Tse, "Sum capacity of the vector Gaussian broadcast channel and uplink-downlink duality," *IEEE Transactions on Information Theory*, vol. 49, pp. 1912–1921, August 2003.

[50] N. Jindal, S. Vishwanath, and A. Goldsmith, "On the duality of Gaussian multiple-access and broadcast channels," *IEEE Transactions on Information Theory*, vol. 50, pp. 768–783, May 2004.

[51] T. M. Cover, "Broadcast channels," *IEEE Transactions on Information Theory*, vol. 18, pp. 2–14, January 1972.

[52] T. Cover and J. Thomas, *Elements of Information Theory.* New York: Wiley Interscience, 1991.

[53] S. Barbarossa and G. Scutari, "On the maximum common rate in multiple access channels," in *Proc. EUSIPCO 2002*, (Toulouse, France), September 2002.

[54] W. Rhee and J. M. Cioffi, "On the capacity of multiuser wireless channels with multiple antennas," *IEEE Transactions on Information Theory*, vol. 49, pp. 2580–2595, October 2003.

[55] F. Horlin, *Channel adapted precoding for interference free uplink burst transmission.* PhD thesis, Communications and Remote Sensing Laboratory, Université catholique de Louvain, September 2002.

[56] H. Holma and A. Toskala, *WCDMA for UMTS.* Wiley, 2000.

[57] R. Gray, "On the asymptotic eigenvalue distribution of Toeplitz matrices," *IEEE Transactions on Information Theory*, vol. 18, pp. 725–730, November 1972.

[58] P. E. Caines, *Linear stochastic systems.* Wiley, 1988.

[59] Y. A. Rozanov, *Stationary random processes.* New York: Holden-Day, 1967.

[60] G. H. Golub and C. F. V. Loan, *Matrix computations.* The Johns Hopkins University Press, 1996.

[61] N. Al-Dhahir and A. H. Sayed, "The finite-length multi-input multi-output MMSE DFE," *IEEE Transactions on Signal Processing*, vol. 48, pp. 2921–2936, October 2000.

[62] A. Klein, G. Kaleh, and P. Baier, "Zero forcing and minimum mean square error equalization for multiuser detection in code division multiple access channels," *IEEE Transactions on Vehicular Technology*, vol. 45, pp. 276–287, May 1996.

[63] J. Louveaux, L. Vandendorpe, L. Cuvelier, and T. Pollet, "Bit-rate sensitivity of filter-bank-based VDSL transmission to timing errors," *IEEE Transactions on Communications*, vol. 49, pp. 375–384, February 2001.

[64] Y. Jiang, S. Feng-Wen, and J. S. Baras, "On the true Cramèr-Rao lower bound for the DA joint estimation of carrier phase and timing offsets," in *Proc. IEEE ICC'2000*, (New-Orleans, USA), pp. 331–335, June 2000.

[65] A. Papoulis, *Probability, random variables, and stochastic processes.* New York: McGraw-Hill, 1991.

[66] F. Gini, R. Reggiannini, and U. Mengali, "The modified Cramèr-Rao bound in vector parameter estimation," *IEEE Transactions on Communications*, vol. 46, pp. 52–60, January 1998.

[67] J. Louveaux, L. Vandendorpe, and T. Sartenaer, "Early-late timing recovery with decision-feedback equalizers," *IEEE Communications Letters*, vol. 7, pp. 332–334, July 2003.

[68] K. H. Mueller and M. Müller, "Timing recovery in digital synchronous data receivers," *IEEE Transactions on Communications*, vol. 24, pp. 516–531, May 1976.

[69] J. Proakis, *Digital Communications.* New York: McGraw-Hill, 1989.

[70] R. Gallager, *Information theory and reliable communication.* New York: Wiley, 1968.

[71] P. Vaidyanathan, *Multirate systems and filter banks.* Prentice Hall Signal Processing Series, 1993.

[72] H. Meyr, M. Moeneclaey, and S. A. Fechtel, *Digital communications receivers: Synchronization, Channel estimation and Signal processing.* New York: Wiley Series in Telecommunications and Signal Processing, 1998.

[73] R. D. Gitlin, J. F. Hayes, and S. B. Weinstein, *Data communications principles.* Plenum Press, 1992.

[74] S. Haykin, *Adaptive filter theory.* Prentice Hall, 1991.

[75] L. Vandendorpe and J. Louveaux, "About ML-DA timing estimation for filter bank based MC transmission," *IEEE Communications Letters*, vol. 3, pp. 106–108, April 1999.

[76] B. Farhang-Boroujeny and G. Mathew, "Nyquist filters with robust performance against timing jitter," *IEEE Transactions on Signal Processing*, vol. 46, pp. 3427–3431, December 1998.

[77] K. M. Wong, J. W. Davidson, and T. Q. Jin, "Wavelet packet division multiplexing and wavelet packet design under timing error effects," *IEEE Transactions on Signal Processing*, vol. 45, pp. 2877–2890, December 1997.

[78] M. Luise, M. Marelli, and R. Reggiannini, "Clock synchronization for wavelet-based multirate transmissions," *IEEE Transactions on Communications*, vol. 48, pp. 1047–1054, June 2000.

[79] F. Daneshgaran and M. Mondin, "Wavelet-based signal design for reduced jitter timing-recovery," *IEEE Transactions on Communications*, vol. 45, pp. 1523–1526, December 1997.

[80] L. Vandendorpe, J. Louveaux, B. Maison, and A. Chevreuil, "About the asymptotic performance of MMSE MIMO DFE for filter-bank based multicarrier transmission," *IEEE Transactions on Communications*, vol. 47, pp. 1472–1475, October 1999.

[81] R. Lupas and S. Verdú, "Linear multiuser detectors for synchronous code-division multiple-access channels," *IEEE Transactions on Information Theory*, vol. 35, pp. 123–126, January 1989.

[82] S. Verdú, "Minimum probability of error for asynchronous Gaussian multiple-access channels," *IEEE Transactions on Information Theory*, vol. 32, pp. 85–96, January 1986.

[83] A. Duel-Hallen, "Equalizers for multiple input-multiple output channels and PAM systems with cyclostationary input sequences," *IEEE Journal on Selected Areas in Communications*, vol. 10, pp. 630–639, April 1992.

[84] A. Duel-Hallen, "A family of multi-user decision-feedback detectors for asynchronous CDMA channels," *IEEE Transactions on Communications*, vol. 43, pp. 421–434, April 1995.

[85] X. Wang and H. V. Poor, "Iterative (turbo) soft interference cancellation and decoding for coded CDMA," *IEEE Transactions on Communications*, vol. 47, pp. 1046–1061, July 1999.

[86] Z. Xu and M. K. Tsatsanis, "Blind channel estimation for long code multiuser CDMA systems," *IEEE Transactions on Signal Processing*, vol. 48, pp. 988–1001, April 2000.

[87] C. J. Escudero, U. Mitra, and D. Slock, "A Toeplitz displacement method for blind multipath estimation for long code DS/CDMA signals," *IEEE Transactions on Signal Processing*, vol. 49, pp. 654–665, March 2001.

[88] S. Bhashyam and B. Aazhang, "Multiuser channel estimation and tracking for long-code CDMA systems," *IEEE Transactions on Communications*, vol. 50, pp. 1081–1090, July 2002.

[89] S. Buzzi and H. V. Poor, "Channel estimation and multiuser detection in long-code DS/CDMA systems," *IEEE Journal on Selected Areas in Communications*, vol. 19, pp. 1476–1487, August 2001.

[90] D. Guo, L. R. Rasmussen, and T. J. Lim, "Linear parallel interference cancellation in long code CDMA multiuser detection," *IEEE Journal on Selected Areas in Communications*, vol. 17, pp. 2074–2081, December 1999.

[91] Z. Yang and X. Wang, "Blind turbo multiuser detection for long-code multipath CDMA," *IEEE Transactions on Communications*, vol. 50, pp. 112–125, January 2002.

[92] S. Parkvall, "Variability of user performance in cellular DS-CDMA - long versus short spreading sequences," *IEEE Transactions on Communications*, vol. 48, pp. 1178–1187, July 2000.

[93] M. C. Jeruchim, "Techniques for estimating the bit error rate in the simulation of digital communication systems," *IEEE Journal on Selected Areas in Communications*, vol. 2, pp. 153–170, January 1984.

[94] A. N. Akansu, P. Duhamel, P. X. Lin, and M. de Courville, “Orthogonal transmultiplexers in communication: a review,” *Proc. 2000 International Zurich Seminar on Broadband Communications*, vol. 46, pp. 979–995, April 1998.

[95] C. N. Georghiades and M. Moeneclaey, “Sequence estimation and synchronization from nonsynchronized samples,” *IEEE Transactions on Information Theory*, vol. 37, p. 1649, November 1991.

[96] S. Galli, A. Scaglione, and K. Dostert, “Broadband is power: Internet access through the power line network,” *IEEE Communications Magazine*, vol. 41, pp. 82–83, May 2003.

[97] M. Gebhardt, F. Weinmann, and K. Dostert, “Physical and regulatory constraints for communication over the power supply grid,” *IEEE Communications Magazine*, vol. 41, pp. 84–90, May 2003.

[98] H. Dai and H. V. Poor, “Advanced signal processing for power line communications,” *IEEE Communications Magazine*, vol. 41, pp. 100–107, May 2003.

[99] H. A. Latchman and L. W. Yonge, “Power line local area networking,” *IEEE Communications Magazine*, vol. 41, pp. 32–33, April 2003.

[100] N. Pavlidou, A. J. Vinck, J. Yazdani, and B. Honary, “Power line communications: state of the art and future trends,” *IEEE Communications Magazine*, vol. 41, pp. 34–40, April 2003.

[101] F. J. Canete, J. A. Cortes, L. Diez, and J. T. Entrambasaguas, “Modeling and evaluation of the indoor power line transmission medium,” *IEEE Communications Magazine*, vol. 41, pp. 41–47, April 2003.

[102] S. Baig and N. D. Gohar, “A discrete multitone transceiver at the heart of the PHY layer of an in-home power line communication local area network,” *IEEE Communications Magazine*, vol. 41, pp. 48–53, April 2003.

[103] Y. J. Lin, H. A. Latchman, R. E. Newman, and S. Katar, “A comparative performance study of wireless and power line networks,” *IEEE Communications Magazine*, vol. 41, pp. 54–63, April 2003.

[104] J. A. et al., “Extending the power line LAN up to the neighborhood transformer,” *IEEE Communications Magazine*, vol. 41, pp. 64–70, April 2003.

[105] A. P. Liavas, "On the robustness of the finite-length MMSE-DFE with respect to channel and second-order statistics estimation errors," *IEEE Transactions on Signal Processing*, vol. 50, pp. 2866–2874, November 2002.

[106] A. Chockalingam, K. R. S. Kumar, and L. B. Milstein, "Performance of an LMS type receiver for interference suppression in long code DS-CDMA on rayleigh fading channels," in *Proc. IEEE ICC'2000*, (New-Orleans, USA), June 2000.

[107] D. T. M. Slock and I. Ghauri, "Blind maximum SINR receiver for the DS-CDMA downlink," in *Proc. IEEE ICASSP'2000*, (Istanbul, Turkey), June 2000.

[108] A. Chevreuil and L. Vandendorpe, "MIMO MMSE-DFE: a general framework," in *Proc. 9th IEEE Signal Processing Workshop on Statistical Signal and Array Processing*, (Portland, Oregon, USA), pp. 368–371, September 1998.

[109] *Proc. 4th International Symposium on Powerline Communications and its applications (ISPLC'2000)*, (Limerick, Ireland), April 5-7 2000.

[110] *Proc. 5th International Symposium on Powerline Communications and its applications (ISPLC'2001)*, (Malmö, Sweden), April 4-6 2001.

[111] *Proc. 6th International Symposium on Powerline Communications and its applications (ISPLC'2002)*, (Athens, Greece), March 27-29 2002.

[112] P. Delogne, "Justification de la théorie des lignes en HF," tech. rep., Communications and Remote Sensing Laboratory, Université catholique de Louvain, February 2000.

[113] F. Issa, *Analyse et Modélisation du réseau électrique basse tension aux fréquences courants porteurs de la gamme 1 MHz - 30 MHz.* PhD thesis, Université Paris XI Orsay, April 2002.

[114] J. Louveaux, *Filter bank based multicarrier modulation for xDSL transmission.* PhD thesis, Communications and Remote Sensing Laboratory, Université catholique de Louvain, May 2000.